ChemInform Abstract: Ionically Conducting Ceramics as Active Catalyst Supports

11 AUTHORS, INCLUDING:

M. N. Tsampas

Dutch Institute for Fundamental Energy Resea…

48 PUBLICATIONS   **259** CITATIONS

SEE PROFILE

Dimitrios Tsiplakides

Aristotle University of Thessaloniki

51 PUBLICATIONS   **885** CITATIONS

SEE PROFILE

Ionically Conducting Ceramics as Active Catalyst Supports

Philippe Vernoux,*,[†] Leonardo Lizarraga,[†] Mihalis N. Tsampas,[†] Foteini M. Sapountzi,[†] Antonio De Lucas-Consuegra,[‡] Jose-Luis Valverde,[‡] Stamatios Souentie,[§] Costas G. Vayenas,[§,‖] Dimitris Tsiplakides,[⊥] Stella Balomenou,[⊥] and Elena A. Baranova[#]

[†]Université de Lyon, Institut de Recherches sur la Catalyse et l'Environnement de Lyon, UMR 5256, CNRS, Université Claude Bernard Lyon 1, 2 Avenue A. Einstein, 69626 Villeurbanne, France
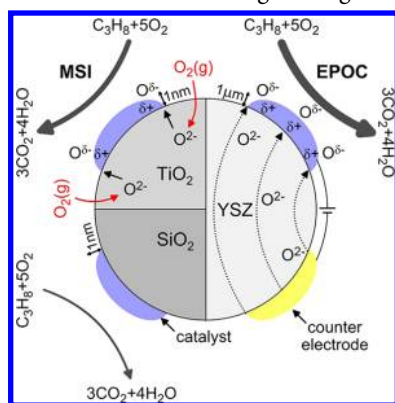
[‡]Departamento de Ingeniería Química, Facultad de Ciencias y Tecnologías Químicas, Universidad de Castilla-La Mancha, Avenida Camilo José Cela 10, 13005 Ciudad Real, Spain

[§]LCEP, Caratheodory 1 Street, Department of Chemical Engineering, University of Patras, Patras GR-26500, Greece

[‖]Division of Natural Sciences, Academy of Athens, Panepistimiou 36 Avenue, GR-10679, Athens, Greece

[⊥]Chemical Process Engineering Research Institute (CPERI), Centre for Research and Technology—Hellas (CERTH), Thessaloniki, Greece

[#]Department of Chemical and Biological Engineering, University of Ottawa, 161 Louis-Pasteur Ottawa, Ontario K1N 6N5, Canada

CONTENTS

1. INTRODUCTION

Electrochemistry and heterogeneous catalysis on metals are usually treated as different branches of physical chemistry, while similar concepts are developed to model their kinetics,[1−4] and similar surface science techniques are used to investigate their fundamental aspects at the atomic level.[1−8] There is thus increasing evidence that they are much more closely related than originally thought.[8] The situation is to some extent analogous to that existing between electrochemistry and corrosion science many decades ago. The urgent need for developing economically viable fuel cells[9,10] has brought the electrochemical and catalytic communities closer than ever before. Ionically conducting ceramics have played and will play a significant role in this direction.

Ionically conducting ceramics have the ability to selectively transport ions in a wide temperature range between 25 and 1000 °C. Many ceramics are still ionic conductive at even higher temperatures; the temperature of 1000 °C can be considered as an upper limit for practical catalytic applications. Solid electrolytes with conducting ions of O^{2-}, H^+, Li^+, K^+, Na^+, Ag^+, F^-, Cu^+, or Cl^- have been reported in the last decades.[4,9]

Ionically conducting ceramics can be implemented into solid electrolyte cells in contact with two electrodes: an anode and a cathode (Figure 1). This kind of cells exhibits multiple present
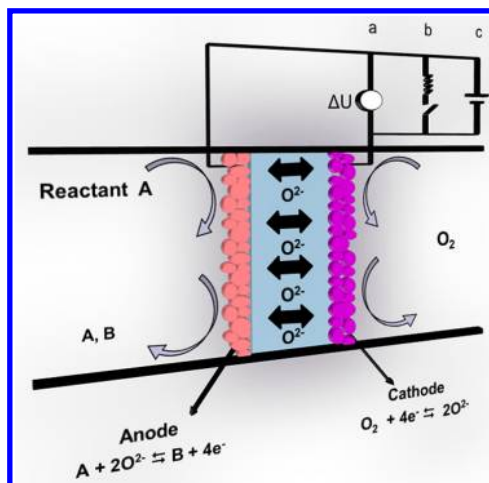
Figure 1. The three modes of operation of solid electrolyte cells: (a) as oxygen activity sensors, (b) as fuel cells, and (c) as electrolyzers or electropromotion reactors.

and future applications. The main commercial use concerns the area of sensor technology.[11] For instance, potentiometric gas sensors are based on the measurement of the potential difference between the two electrodes of a solid electrolyte cell. The first one is exposed to the gas mixture of interest (e.g., exhaust gas in the case of the lambda sensor), while the second electrode in kept under a reference atmosphere (Figure 1). In potentiometric sensors, the electrical current passing through the electrochemical cell is very small, typically less than 1 μA. In lambda sensors, which utilize O^{2-} conducting ceramics, such as Y_2O_3-stabilized-ZrO_2 (YSZ), the oxygen chemical potential (μ_{O_2}) or thermodynamic activity in the gas mixture (a_{O_2}) can be computed from the Nernst equation:

$$\Delta U = \frac{1}{4F}(\mu_{O_2} - \mu_{O_2,R}) = \frac{RT}{4F}\ln(a_{O_2}/a_{O_2,R}) \tag{1}$$

where $\mu_{O_2,R}$ and $a_{O_2,R}$ are, respectively, the chemical potential and the thermodynamic activity of O_2 in the reference gas.[12,13]

Amperometric gas sensors are also currently used. The detection is based on the measurement of the current crossing the solid electrolyte cell under the application of a known potential difference (voltage). Under conditions where the gas diffusion of the component to be measured (e.g., O_2) is rate limiting, one can link the value of this limiting current with the gaseous concentration or partial pressure of O_2 in the mixture. Similar devices can also be used for measuring the activity of oxygen in melts[14] or in solid solutions.[15]

The second application of ceramic ionic conductors is in the area of solid oxide fuel cells (SOFC), as depicted in Figure 1b.[16] The electromotive force that can be induced by a high gradient of oxygen partial pressure between the two electrode compartments generates a current and then electrical energy. The ionically conducting ceramic is the heart of SOFCs combining properties of dense membranes to ensure the tightness between the electrodes as well as the transfer of the oxygen ions from the cathode to the anode. This area could become of very large commercial importance for stationary power applications if the

stack fabrication cost can be brought below \$450/KW.[17] During the last three decades, there has been a very intense R&D effort worldwide for this purpose.

A third application is the use of ionically conducting ceramics as active catalyst supports (Figure 1c). In this case, one of the electrodes of the solid electrolyte cells is also a catalyst. The electrochemical cell is then called "electrochemical catalyst". Gaseous reactant mixture (e.g., a mixture of C_2H_4 and O_2) is fed over the catalyst–electrode. Considering an oxygen conducting ceramic, the application of a potential (± 2 V) between the catalyst and a counter electrode induces the migration of oxygen ions, O^{2-}, which are in situ supplied or removed from the catalyst during the catalytic experiments. It has been found that, rather surprisingly, this "oxygen pumping" operation can lead over a wide temperature range (220–550 °C) to very pronounced and non-Faradaic reversible modifications in the catalytic activity (changes that are not proportional to the current), frequently accompanied by very significant changes in product selectivity.

This phenomenon is known in the literature either as non-Faradaic electrochemical modification of catalytic activity (NEMCA effect) or, more commonly in recent years, as electrochemical promotion of catalysis (EPOC).[18−23]

As discussed in section 4, EPOC has been investigated by a variety of techniques, which merge to the conclusion that this process is due to electrochemically controlled migration (spillover or reverse spillover) of promoting or poisoning ionic species from the ceramic support to the catalyst surface. These ionic species are accompanied by their image charge in the metal, thus forming overall neutral dipoles, which "decorate" the catalyst surface.[22,23] In situ electrochemically supplied ions act as promoting or inhibiting agents for the reaction.

The EPOC mechanism is functionally identical to and only operationally different from the mechanism of classical promotion of catalyst nanoparticles. In addition, this Review will also discuss the comparison between EPOC and metal–support interactions (MSI). These two concepts are, at a first glance, independent phenomena, which can dramatically affect the activity of metal and metal oxide catalysts. Nevertheless, the phenomenon of spillover–backspillover of ionic species could merge the three phenomena: the promoting species being supplied chemically (for the classical promotion), electrochemically (electrochemical promotion), or via self-driven O^{2-} spillover (metal–support interactions) form a double layer at the metal–gas interface, which affects the strength of chemisorptive bonds of reactants and intermediates, thus affecting catalytic activity (Figure 2). One of the most important advantages of EPOC is the direct in situ control of the promoter amount on the catalyst surface.[23]

It is therefore not surprising that during the last 30 years there has been a gradual replacement of the common catalyst supports with negligible oxygen ion mobility (e.g., SiO_2, Al_2O_3) with new anionic or mixed anionic–electronic supports, where the same nanodispersed catalytic material can exhibit significantly higher catalyst activity.[8]

Therefore, ionically conducting ceramics present a new and very promising category of catalyst supports of finely dispersed and stabilized metallic nanoparticles to improve and tailor their performance.

This Review summarizes the main families of ionically conducting ceramics and describes the mechanism of their bulk ionic mobility. Recent studies of their utilization in heterogeneous catalytic processes are reported acting as a dense membrane (EPOC) in an electrochemical cell (electro-
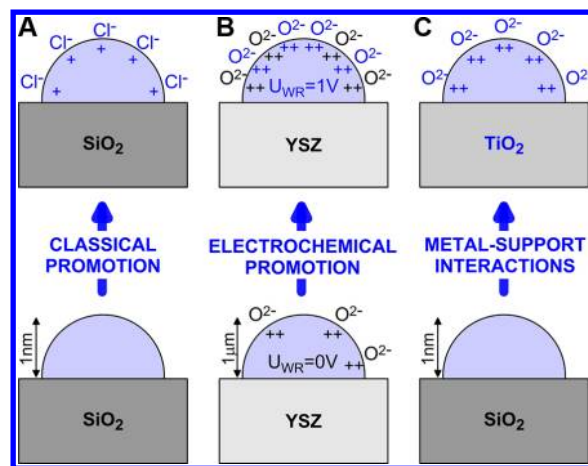
Figure 2. Schematic of the unpromoted and promoted states of metal-supported catalysts: (A) via classical promotion of common supports (electronegative promoter addition of long lifetime), (B) via EPOC (potential or current controlled O^{2-} backspillover), and (C) via MSI (self-driven O^{2-} backspillover obtained when passing from a low to a high oxygen mobility support).

chemical catalyst) or as a conventional support for dispersing catalytic metallic nanoparticles. New findings and developments in EPOC are detailed in terms of both the understanding of the phenomena and in the quest of applications. Recent studies on conventional dispersed catalysts involving oxygen ionic conducting supports then are reported and discussed regarding the comparison between theories of metal/support interactions and EPOC rules.

2. IONIC CONDUCTING CERAMICS

Michael Faraday was first to observe in 1834 that solid PbF_2, when heated at 500 °C, becomes an electrical conductor. It took almost a century to explain this observation and establish that PbF_2 is a F^- ion conductor. In the meantime, other solid electrolytes such as AgI, an Ag^+ conductor, had been discovered by Tubandt and Strock, and it soon became apparent that ions can diffuse as rapidly in some solids as in aqueous salt solutions. The atomistic interpretation of ionic conduction in solids was largely established by the pioneering work of Joffé, Frenkel, Wagner, and Schottky in the 1920s and early 1930s.[24] These works established that ion conduction can take place either by hopping of ions through a series of interstitial sites (Frenkel disorder) or by hopping of vacancies among lattice positions (Schottky disorder).

Today, the term solid electrolyte or fast ionic conductor or, sometimes, superionic conductor is used to describe solid materials whose conductivity is wholly due to ionic displacement. The main commercial application of solid electrolytes is in gas sensors, batteries, and solid oxide fuel cells.[25−32]

This section provides a short introduction to the electrical transport properties of solid electrolytes and mainly concerns the readers who are not familiar with material science. The ionic or electronic conductivity describes a bulk property of the materials and cannot be directly linked with the surface characteristics of a catalyst. Nevertheless, this section explains the different mechanisms of ionic bulk mobility in materials that can be used as catalytic supports (section 5).

2.1. General Concepts

Extensive research on solid electrolytes started in the 1960s when novel electrolytes were synthesized with sufficiently high

conductivity at temperatures lower than room temperature.[33,34] In general, solid electrolytes are solid-state materials where the predominant charge carriers are ions. The use of solid electrolytes in many cases has several advantages as compared to ionic solutions or molten salts, largely due to the simplicity and robustness of the electrochemical cell design. Moreover, the majority of solid electrolytes have unipolar type of conductivity; thus a number of undesirable effects related to the simultaneous transport of different kinds of ions are avoided. Finally, the use of solid electrolytes allows operation in a broad range of temperatures, which is of great importance, for instance, in thermodynamic studies and, of course, in catalytic studies.[33,34]

The transport properties of solid electrolytes are well studied.[25,26] The theory of electrical transport in solids is based on the defects of the crystalline lattice and was initially developed in the fundamental works of Frenkel, Schottky, and Wagner.[24,35,36]

A significant step in understanding the mechanism of electrical transport in solids was done by Frenkel in 1926.[35] He showed that at any given temperature (above absolute zero) defects or imperfections should exist in the crystal due to heat fluctuations. According to Frenkel, disorder in the crystal lattice is achieved when atoms change their position from the regular crystallite lattice to interstitial sites. Later, Schottky suggested another model of disordering with equivalent quantities of vacancies in cation and anion sublattices.[25,36] According to this model, the formation of vacancies is accompanied by the migration of the corresponding ion or atom to the surface of the crystal. Such disorders greatly affect the overall properties of the solid. Thus, defects in the lattice are considered as the most important aspect of the solid state because it is impossible to avoid defects at the atomic level. Two factors are involved: the entropy effect and the presence of impurities in any given solid.

Therefore, the type of the defects in the crystal lattice of solid electrolytes, which determines their transport properties, can be divided into three groups:[25,34]

(i) solid electrolytes with intrinsic disordering;
(ii) solid electrolytes with extrinsic (impurity) disordering; and
(iii) solid electrolytes with structural disordering.

2.2. Defect Chemistry of Ceramics

2.2.1. Solid Electrolytes with Intrinsic Disordering. In a three-dimensional solid, there are three major types of intrinsic defects, having one, two, or three dimensions.[34] One-dimensional defects are called "point" defects and are changes at atomistic levels. Important point defects in solids, which determine their physicochemical properties, are interstitial atoms (ions) and vacancies in the lattice.

Figure 3 presents the main types of single intrinsic point defects that can be encountered in binary compounds. The point defects of such compounds usually affect a sublattice for each independent compound constituent. However, in addition to vacancies and interstitials associated with each sublattice, antisite defects can be also present in multicomponent compounds. For a simple binary AB compound, an antisite defect corresponds to the abnormal occupation of one crystal site; that is, atom A occupies a lattice site regularly occupied by atom B, or inversely atom B occupies a site normally occupied by atom A. Such antisite defects are mainly observed in intermetallic and covalent compounds; they cannot be stable in ionic compounds because of the large and repulsive electrostatic interactions that they would induce.[37]
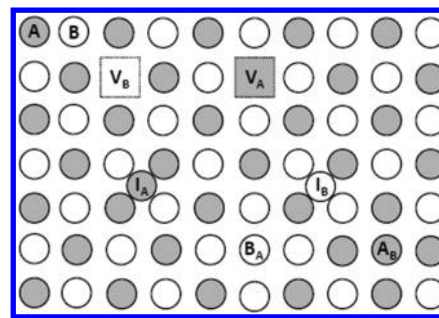
Figure 3. Intrinsic point defects in a compound AB: V_A, V_B and I_A, I_B are, respectively, vacancies and interstitials of sublattices A and B. A_B and B_A correspond to antisite defects.

For fully ionized defect description, the Kröger−Vink notation is commonly used.[38] This notation is a symbolic representation of structure elements of defective crystals. A structure element is an atom, ion, molecule, or else vacancy or interstitial located on a specified lattice site of the perfect crystal lattice. The Kröger−Vink notation provides the following information on any kind of structure element:[37]

(i) the nature of the chemical species occupying one given lattice site in the real crystal;

(ii) the nature of the regular occupant of this given lattice site in the perfect crystal;

(iii) and the effective electrical charge of the structure element.

The type of defects is given by a corresponding capital letter M or X for ions and V for vacancies. A subscript indicates the location of the defect (sublattice M or X or interstitial i).

Effective charge of the defect is indicated by a dot (˙) for a positive excess charge, and by a prime (′) for a negative excess, while (×) is used for a null effective charge. The effective charge of a structure element is the difference between its charge in the real crystal and that in the neutral perfect crystal lattice. Thus, cation vacancy with effective charge $-2e$ is represented as V_M'', and for interstitial cation and anion as symbol $M_i^{\cdot}$ and X_i'', respectively (Table 1).[39]

Ionic lattices, in the absence of macroscopic electric fields, are required to be electrically neutral. This overall charge neutrality requires that a charged defect must be compensated by a number of defects, summing a complementary charge of opposite sign. The charges of the defects and of the regular lattice particles are

Table 1. Kröger−Vink Notation for Point Defects in Crystals[a]

type of defect	symbol	remarks
vacant M site	V_M''	divalent ions are chosen as an example with MX as compound formula
vacant X site	$V_X^{\cdot\cdot}$	M^{2+}, X^{2-}: cation and anion
ion on lattice site	$M_M^{\times}$, $X_X^{\times}$	×: uncharged
L on M site	L_M'	L^+ dopant ion
N on M site	$N_M^{\cdot}$	N^{3+} dopant ion
free electron	e'	
free (electron) hole	$(h^{\cdot})$	
interstitial M ion	$M_i^{\cdot\cdot}$	·: effective positive charge
interstitial X ion	X_i''	′: effective negative charge

[a]Reprinted with permission from ref 39. Copyright 2012 Elsevier.

only important with respect to the neutral, unperturbed (ideal) lattice. Thus, in the following discussion, the charges of point defects are all given relative to the neutral unperturbed lattice.

In stoichiometric ionic solids, where electron disorders do not exist, there are four common types of point ionic defects:[26,34] (i) Frenkel defects usually occur in the cation sublattice. Frenkel disorders are not commonly observed in the anion sublattice (anti-Frenkel disorders), due to the (commonly) larger size of anions compared to cations. The formation of Frenkel defects can occur anywhere in the crystal, when a cation obtains sufficient energy due to heat fluctuation, and thus moves from the normal lattice site to the neighboring interstitial. This process can be represented as follows:

$$M_M^\times + V_i^\times \rightleftarrows M_i^{\cdot\cdot} + V_M'' \tag{2}$$

(ii) Anti-Frenkel defects are anion vacancies $V_X^{\cdot\cdot}$ and anions incorporated in interstitial sites, X_i''. This combination differs from the previous one only by the effective charge of the defects:

$$X_X^\times + V_i^\times \rightleftarrows V_X^{\cdot\cdot} + X_i'' \tag{3}$$

(iii) Schottky defects involve equivalent amounts of cation and anion vacancies $(V_M''$ and $V_X^{\cdot\cdot})$ in the lattice. In this case, the ions, which left their regular lattice sites, cannot be relocated in the interstitial sites, but emerge in the crystal surface by rebuilding the crystallite lattice. Therefore, formation of the Schottky defects usually occurs at the crystal surface, as well as at the inner surfaces, for instance, at the crystal planes of polycrystals. This process can be represented by the quasi-chemical reaction:

$$M_M^\times + X_X^\times \rightleftarrows V_X^{\cdot\cdot} + V_M'' + (MX)_{defect} \tag{4}$$
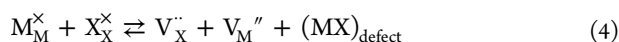
(iv) Anti-Schottky defects are interstitial cations and anions $(M_i^{\cdot\cdot}$ and $X_i'')$. In this case, ions are transferred from the surface to interstitial sites, resulting in the decrease of the amount of crystal lattice sites:

$$(MX)_{defect} \rightleftarrows M_i^{\cdot\cdot} + X_i'' \tag{5}$$

The formation energies of interstitials are larger than those for vacancies, in particular for the larger negatively charged anion interstitials. Therefore, Anti-Schottky defects are not the dominating defect type; however, they are always present in the crystal but in very low concentrations. Examples of solids with intrinsic disordering are compounds with the type of NaCl, for example, NaF, KCl, KI, AgBr, etc., or solids having the cubic fluorite structure of CaF_2 type $(SrF_2, BaF_2, CeO_2, ThO_2)$.[40]

2.2.2. Solid Electrolytes with Extrinsic Disordering. Doping of ionic crystals with foreign ions (substitutional ions or foreign ions present on interstitial sites) with a valence different from that of the host ion leads to the formation of extrinsic disordering. In most cases, the formation of the solid solutions occurs by substitution, when aliovalent ions (impurities or dopes) are placed in the lattice sites of the main compound. Obviously, for sufficiently low concentrations, such doping ions can be considered as point defects in the lattice of the main compound, and they can also be called substitutional defects. Electroneutrality requires that the excess charge of aliovalent ions in the solid solution is compensated by the opposite sign defects. In semiconductors or non-stoichiometric compounds, excess electrons or holes realize such compensation. In solid electrolytes without significant electronic conductivity, the excess charge is compensated by one of the intrinsic defects: interstitial ions or vacancies that exist in the given compound in the pure state.

Therefore, the type of compensation is strongly associated with the type of intrinsic disordering in the lattice of the host compound.

2.2.3. Solid Electrolytes with Structural Disordering. The crystal structure of such electrolytes is quite versatile; however, the common difference of these compounds is the presence of considerable excess of crystallographic positions, in which mobile ions can be located. In most of the cases, the number of existing positions is several times higher than the number of ions, which guarantees the mobility freedom and results in higher conductivity. Investigation of solid electrolytes with structural disorder started from the discovery of the high conductivity of α-AgI.[41] β-Alumina is a typical example of solid electrolytes with structural disordering. One of the important properties of β-alumina is its high unipolar conductivity at low temperatures for a number of single charged cations.[42−45]

2.3. Electrical Conductivity

The charge transport mechanisms for the electrical conduction modes in ceramic materials vary greatly, because the transport of current may be due to the motion of electrons, electron holes, or ions. Crystal structure may also significantly affect the mobility of charged species. The total electrical conductivity σ of a solid is the sum of the partial conductivities of ionic and electronic charge carriers:

$$\sigma = \sum_i \sigma_i = \sum_i q_i u_i c_i \tag{6}$$

In this equation, q_i is the charge, u_i is the mobility, and c_i is the concentration of the charge carrier i (with conductivity σ_i).

Transference/transport number is a dimensionless parameter, which informs about the contribution of the particular charged species present in the electrolyte (ions and electrons) to the overall charge transport across the cell:

$$t_i = \sigma_i/\sigma \tag{7}$$

By definition, the value of t_i lies between 0 and 1.0. The compound ZrO_2-CeO_2 is an example of variable transference number. The ionic transference numbers for this compound can vary from 0.03 to 1.0, depending on temperature, composition, and the activity of the lattice components.[46]

2.3.1. Ionic Conduction: Hopping Model. For an ion to move through a crystalline lattice, there must be an equivalent vacancy or interstitial lattice site available, and it must acquire sufficient thermal energy to surmount the free energy barrier, between the equivalent sites. Ionic conduction that occurs through the transport of charge by mobile ions is, therefore, a diffusion activated process. Assuming Boltzmann statistics for this thermally activated ion hopping, the diffusion coefficient D_i is a function of the jump distance, l, the characteristic attempt frequency, ν_o, and the Gibbs free energy of migration $\Delta_{migr}G = \Delta_{migr}H - T\Delta_{migr}S$:

$$D_i = \gamma l^2 \nu_o \exp(-\Delta_{migr}G/kT) \tag{8}$$

The factor γ takes into account geometrical and so-called correlation effects, and k is Boltzmann's constant. For example, the backward jump of an ion has a slightly higher probability than the forward jump, but, on the other hand, cooperative motion can lead to higher diffusion coefficients as compared to isolated jumps. In the classical model of ionic transport in solids, typical jump attempt frequencies ν_o are of the order of 10^{13} s^{-1} and are often identified with the Debye frequency. Enthalpies of migration, which determine the temperature dependence of

ion mobility, show large variations with typical values for solid ionic conductors between 0.2 and 2 eV (about 20−200 kJ/mol). Low values are observed for interstitial mechanisms, whereas vacancy mechanisms are generally characterized by higher activation barriers.[47]

The Nernst−Einstein equation relates the ionic mobility u_i to the diffusion coefficient D_i:

$$u_i = D_i q_i / kT \tag{9}$$

Using eqs 6, 8, and 9, the ionic conductivity can be expressed as:

$$\sigma_{ion} = (q_i^2/kT)c_i\gamma l^2 \nu_o \exp(\Delta_{migr}S/k) \exp(-\Delta_{migr}H/kT) \tag{10}$$

A general equation (Arrhenius type) representing the ionic conductivity can thus be written with a preexponential factor, σ_o:

$$\sigma_{ion} = (\sigma_o/T) \exp(-\Delta_{act}H/kT) \tag{11}$$

Most crystalline and amorphous fast ion conductors (the latter below their glass transition temperature) satisfy this equation. The activation enthalpy $\Delta_{act}H$ can contain different contributions: (i) If the concentration of mobile ionic defects is fixed by charged background impurities and dopants, as in the case of Y_2O_3-stabilized ZrO_2, the activation enthalpy $\Delta_{act}H$ is equal to the defect migration enthalpy $\Delta_{migr}H$.

(ii) Assuming a thermally activated defect creation, the carrier concentration $[i]$ is temperature dependent:

$$c_i = c_i^{\circ} \exp(-\Delta_{form}H^{\circ}/2kT) \tag{12}$$

The factor 2 comes from the fact that defect pairs are always formed. In this "intrinsic" case, $\Delta_{act}H$ is the sum of the defect migration $\Delta_{migr}H$ and $\Delta_{form}H^{\circ}$ formation enthalpies ($\Delta_{act}H = \Delta_{migr}H + \Delta_{form}H^{\circ}/2$).

(iii) If deviations from stoichiometry are observed, the activation enthalpy can be related to reaction enthalpies, such as the oxidation enthalpy for metal-deficient oxides or the reduction enthalpy for oxygen-deficient oxides.

(iv) Defect association can be observed at low temperatures. This issue was discussed by Lidiard.[48] Dreyfus and Nowick investigated the point defects association in doped sodium chloride.[49] At low temperatures, defects association due to Coulomb interactions between the oppositely charged defects begins to predominate. In the temperature domain in which association occurs, the conductivity has an effective activation enthalpy ($\Delta_{act}H = \Delta_{migr}H + \Delta_{ass}H/2$, where $\Delta_{ass}H$ is the association enthalpy). There are other important experimental consequences from such association. The formation of vacancy−dopant pairs leads to a weaker overall enhancement of conductivity. The pairs act as dipoles and contribute to dielectric relaxation processes. Haven established the presence of loss peaks due to defect pairing in 1953.[50] In addition to the formation of defect pairs, Lidiard showed that long-range defect interactions also play a role and adapted the Debye−Huckel theory of aqueous electrolytes to the case of ionic crystals.[48] The electrostatic interactions are also the origin of the frequency dependence of the ionic conductivity and dielectric permittivity of structurally disordered solid electrolytes.[51,52]

2.3.2. Ionic and Electronic Conductivity. In any solid electrolyte material, there are in principle non-zero electronic and ionic conductivities. Materials for which the ionic conductivity, σ_{ion}, is more than 2 orders of magnitude larger than the electronic conductivity, σ_n, are characterized as purely ionic conductors, while the term mixed ionic−electronic

conductors (MIECs) is used for materials in which the difference between σ_{ion} and σ_n is less than 2 orders of magnitude. It is also usual to use the term MIEC when σ_{ion} and σ_n are not too low (σ_{ion}, $\sigma_n \geq 10^{-5}\ \Omega^{-1}\ cm^{-1}$).[53,54]

The total electrical conductivity σ_t of a solid is the sum of the conductivities due to ions (σ_{ion}), electrons (σ_n), and holes (σ_p):

$$\sigma = \sigma_{ion} + \sigma_p + \sigma_n \tag{13}$$

At elevated temperatures, mixed conductors of the type M_aX_b (where the symbols X and M denote, respectively, the non-metal and metal components of the conductor) exhibit an ionic conductivity, which is virtually X_2 partial pressure, P_{X2}, independent, while in contrast their electron and (positive) hole conductivities are proportional to $P_{X_2}^{-1/n}$ and $P_{X_2}^{1/n}$, respectively. According to Patterson,[53] the partial conductivities can be expressed as:

$$\sigma_{ion} = A_{ion}^{\circ} \exp(-\Delta_{act}H_{ion}/kT) \tag{14}$$

$$\sigma_p = A_h^{\circ}P_{X_2}^{1/n} \exp(-\Delta_{act}H_h/kT) \tag{15}$$

$$\sigma_n = A_e^{\circ}P_{X_2}^{-1/n} \exp(-\Delta_{act}H_e/kT) \tag{16}$$

where X_2 is gas (O_2 in case of oxides), P_{X2} is the partial pressure of the gas, A° is the pre-exponential factor, $\Delta_{act}H$ is the activation energy, and n is the factor determined by a predominant defect structure.

The conduction domains are determined by using eqs 14−16, and they are schematically shown in Figure 4. In the case of
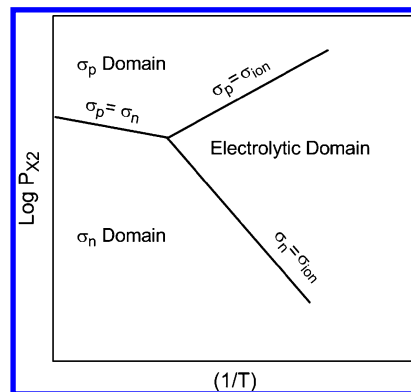
Figure 4. Relationship between the electrolytic and electronic domains in the log Px_2, versus $1/T$ plane.

oxygen ion conductors, the electrolytic domain is determined by measuring the transference number of the ion, t_{ion}, according to:

$$t_{ion} = q_{ion}/kT(\partial E/\partial \log P_{O2}) \tag{17}$$

where E is the open-circuit electromotive force (EMF) of the solid-state electrochemical cell, and P_{O2} is the partial pressure of oxygen.

The electrolytic domain corresponds to the range of oxygen chemical potential and temperature, where the ionic contribution to the total conductivity (eq 10) of a solid electrolyte is higher than 99% and the ion transference number (t_i) equals 0.99.

2.4. Ionic Conductivity Measurement Techniques

The conductivity theory shown in section 2.3 implies homogeneity of the solid electrolyte structure and is applicable to monocrystals. In practice, samples are usually prepared by pressing and sintering powders to form dense pellets.

Homogeneous specimens having the equilibrium phase or phases at the sintering temperature are often difficult to achieve. Polycrystalline samples usually possess regions of varying conductivity such as grain boundaries, internal surfaces due to porosity, and particle-to-particle contacts.

Several methods are used for measuring solid electrolytes conductivity: electrochemical impedance spectroscopy, the four-point dc technique, transference measurements, the Hebb−Wagner technique, EMF measurements, the voltage relaxation method, and the charge transfer technique. Among them, the most frequently used is electochemical impedance spectroscopy (EIS), and for this reason its operation principles will be described in detail in the following section.[26,55−57]

2.4.1. Electrochemical Impedance Spectroscopy (EIS). EIS studies the impedance of an electrochemical cell or electrodes as a function of frequency of the ac signal source. The equivalent resistance and capacitance values can be interpreted theoretically in terms of interfacial phenomena. The impedance, Z, is a generalized resistance that links voltage E and current I in phasor notation:

$$\tilde{E} = \tilde{I}Z \tag{18}$$

where $\tilde{E}$ is the phasor of the electrode potential and $\tilde{I}$ is the phasor of applied current. This equation is a generalized Ohm's law. It is convenient to represent phasors in complex notation. Component along the ordinate is regarded as imaginary and $j = \sqrt{-1}$, whereas component along the abscissa is regarded as real, therefore:

$$Z(\omega) = Z_{Re}(\omega) - jZ_{Im}(\omega) \tag{19}$$

where Z_{Re} and Z_{Im} are the real and imaginary parts of impedance, respectively.[58,59]

Useful information can be derived from the variation of impedance with frequency, which can be displayed in different ways. One of the common representations of impedance data is the Nyquist plot, where the value of Z_{Im} is plotted as a function of Z_{Re} for different values of frequency (ω) (Figure 5).

During EIS the steady-periodic linear response of a cell to a sinusoidal current or voltage perturbation is measured and analyzed in terms of gain and phase shift as a function of frequency (ω). Results are usually expressed in terms of the impedance (Z), the complex ratio of voltage displacement to current displacement (often reported on a Nyquist or Bode plot). Ideally, each charge-transfer-limiting process (electrolyte, electrode process 1, electrode process 2, etc.) is only manifest below a distinct characteristic frequency, resulting in separate features or "arcs" in the impedance diagram of magnitude R_e, R_1, R_2, etc. (Figure 5, top). Because EIS is a linear response technique, the time-response of individual processes is often modeled in terms of equivalent circuit elements, with resistance representing charge transfer and capacitance (C_1, C_2, etc.) representing charge polarization. This description is often extended to noninterfacial processes by introduction of additional empirically or theoretically derived circuit elements (Figure 5, bottom).[58,59]

The Nyquist plot of the oxygen concentration cell of the type

$$O_2, Pt/((ZrO_2)_{0.91}\text{-}(Y_2O_3)_{0.09})/Pt, O_2 \tag{20}$$
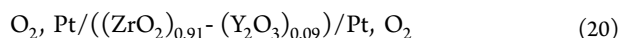
is shown in Figure 6. The first semicircle at high frequencies corresponds to the bulk properties of the solid electrolyte, in particular, the conductivity. R_1 represents the intergrain resistance. The second semicircle represents the effect of the grain boundaries. The value ($R_2 - R_1$) corresponds to the
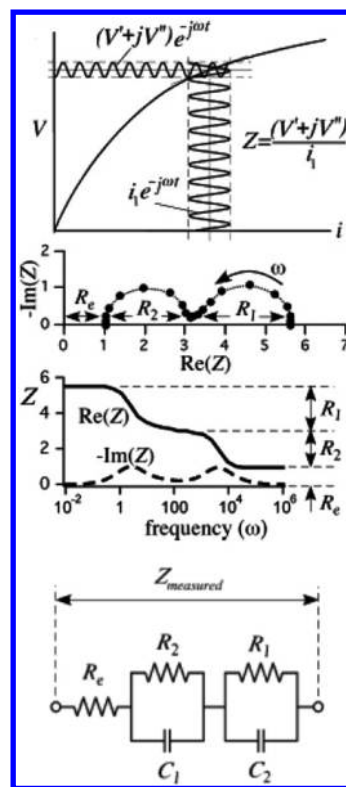
Figure 5. (top) The steady-periodic linear response of a cell to a sinusoidal current or voltage perturbation during EIS and the Nyquist and Bode plots. (bottom) EIS equivalent circuit elements, with resistance representing charge transfer and capacitance (C_1, C_2, etc.) representing charge polarization. Reprinted with permission from ref 59. Copyright 2012 American Institute of Physics.
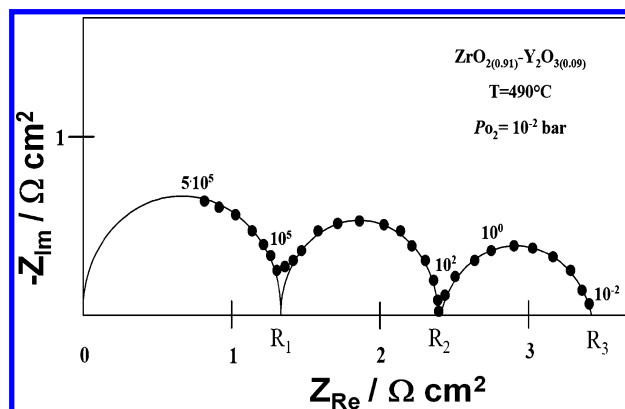
Figure 6. Complex impedance diagram. Numbers on the semicircles are the excitation frequencies in Hz. Reprinted with permission from ref 52. Copyright 2012 Elsevier.

contribution of the grain contacts to the total electrolyte resistance. The third semicircle represents processes occurring in the electrodes.

The number and shape of the semicircles in a Nyquist plot (Figure 6) depend on the working temperature and cell configuration. The first two semicircles at high frequencies are simulated by two parallel RC electric circuits in series, while the third one is more complex and corresponds to electrode processes.[60,61]

As was already mentioned, EIS ionic conductivity measurements are mostly performed on dense samples, such as pellets.

EIS measurements give the bulk ionic conductivity, which is used, for instance, to predict the flow of promoting ions that can be supplied on the catalyst−electrode during EPOC experiments. Nevertheless, no data in the literature concern the surface ionic conductivity, which plays a crucial role in catalytic mechanisms on ionic conductor-based catalysts.

3. IONIC CONDUCTING CERAMICS FOR CATALYTIC APPLICATIONS

The development of ionic conducting ceramics or solid electrolytes has been mainly driven by their commercial application in gas sensors, batteries, and solid oxide fuel cells. The minimum ionic conductivity value of a solid electrolyte for practical fuel cell applications is $0.1−1$ S cm^{-1} in the operational temperature range of SOFCs, that is, 800−1000 °C. This places very stringent restrictions on the choice of material. However, for catalytic (promotional) and sensor applications, much lower conductivity values ($\sim 10^{-4}$ S cm^{-1}) are usually sufficient. This permits the use of a large variety of solid electrolytes over a very wide temperature range (from room temperature to 700 °C). In the last years, solid electrolyte cell reactors have been used for the investigation of a wide variety of catalytic systems as described in detail in several reviews.[22,23,31,62−72]

The use of solid electrolytes in heterogeneous catalysis was first proposed in 1970 by Wagner,[73] who suggested the use of solid electrolyte cells for the measurement of oxygen activity on metal and metal oxide catalysts. This technique was used for the investigation of the mechanism of SO$_2$ oxidation on noble metals,[74] and was subsequently called solid electrolyte potentiometry (SEP).[75] It allows for the "in situ" investigation of the thermodynamic activity of oxygen adsorbed on metal electrodes deposited on solid electrolytes during catalytic reactions. After these pioneering works, the use of ionic conductors in heterogeneous catalysis has been extended through the development of other kinds of applications and configurations, which allow one to take advantage of the selective conduction of ions through the solid electrolyte by electrochemically supplying one of the reactants of the catalytic process, for example, O$_2$, through the use of an O^{2-} ionic conductor for an oxidation reaction (oxy-combustion process), or improve the activity and/or the selectivity of the catalyst film deposited on the solid electrolyte by the electrochemically promoting ions through EPOC, as detailed in section 4.

For such different applications, a wide variety of solid electrolytes have been used. In this section, a general description of the main refractory ionic conductors (ceramic conductors) is presented that according to their properties can be or have been used as catalysts or catalysts supports. Their applicability and efficiency for catalytic applications should be considered with caution because these materials have been designed and developed to fulfill the specific requirements of high temperature electrochemical processes.

3.1. Anionic Conductors

3.1.1. Fluorite-type Electrolytes. Oxygen−ion conductors are of the most common anionic conducting ceramics used in heterogeneous catalysis. The most conventional fast oxide−ion conducting materials have fluorite-type crystal structure, AO$_2$, where A is a tetravalent cation.[76] In this structure, illustrated in Figure 7, the cations occupy face-centered positions in a cubic unit cell with anions in the eight tetrahedral sites between them. The most widely used and intensively studied type are solid solutions of the type AO$_2$−A′O or AO$_2$−A$_2''$O$_3$, where A = Zr,
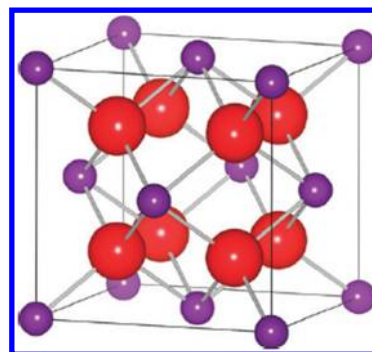

Figure 7. The fluorite crystal structure (AO$_2$). The large red spheres represent the O^{2-} oxygen ion sites, and the purple spheres are for the A^{4+} cation sites.[82] Reproduced with permission from ref 82. Copyright 2010 The Royal Society of Chemistry (http://dx.doi.org/10.1039/B915141A).

Hg, Ce, Th; A′ = Ca, Sr, Ba; A′′ = Sc, Y, or lanthanides,[77] with A′ and A′′ being lower than A valent cations.

The best known fluorite-type oxide−ion conductor is acceptor doped ZrO$_2$. Pure zirconia has poor ionic conductivity, and only adopts the cubic fluorite symmetry above 2300 °C.[78] To stabilize the cubic structure at lower temperatures and to increase the concentration of oxygen vacancies (which are required for ionic conduction via vacancy hopping), acceptor dopants are introduced into the cation sublattice.[79,80]

Typical subvalent dopants (i.e., acceptors) are Ca^{2+} and Y^{3+}, producing calcia-stabilized zirconia (CSZ) and yttria-stabilized zirconia (YSZ), respectively, the latter exhibiting high oxide−ion conductivity at temperatures above 700 °C. YSZ is the most common oxygen ion conductive electrolyte used for catalytic applications in solid electrolyte cell reactors[23] and has been the mainstay of progress toward commercially viable SOFCs. YSZ is a material with unique characteristics, with enhanced chemical stability as compared to other ceramic conductors, and thus is suitable also for liquid phase applications. YSZ membranes can maintain a stable cubic fluorite structure between room temperature and 2700 °C. As a result, the use of YSZ is more promising for high temperature applications, such as membrane reactors and gas separation by Knudsen flow. The YSZ membranes also exhibit considerable high oxygen ionic conductivity and extremely low thermal conductivity at high temperatures.[81] The conductivity of YSZ for different temperatures is presented in Figure 8 (together with several other materials, which will be discussed later).[82]

The major defects in pure ZrO$_2$ are oxygen vacancies $V_O^{\cdot\cdot}$ and electrons e$^-$, both present at low concentrations. Lower-valent oxides such as Y$_2$O$_3$, CaO, and MgO[83] when added to ZrO$_2$ raise its oxygen vacancy concentration, leading to a much higher ionic conductivity. ZrO$_2$-based solid electrolytes show the maximum in ionic conductivity when the concentration of dopant ions is close to the minimum necessary to stabilize the cubic fluorite-type phase. For instance, the highest conductivity levels in Zr$_{1-x}$Y$_x$O$_{2-x/2}$ and Zr$_{1-x}$Sc$_x$O$_{2-x/2}$ ceramics are observed at $x = 0.08−0.11$ and $0.09−0.11$, respectively. Increasing the doping level decreases the ionic conductivity due to the higher association of oxygen vacancies and dopant cations into complex defects of low mobility.[84−88] Analogous trends explain the conductivity variation in numerous perovskite, fluorite, and pyrochlore compounds.[89,90]

As was already mentioned, in solid electrolytes based on tetravalent Zr, Hg, and Ce oxides with fluorite structure, the high
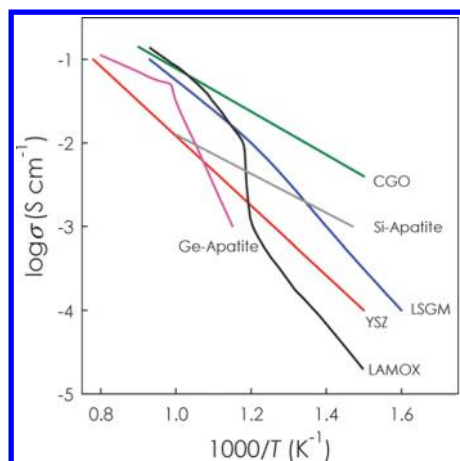
Figure 8. Ionic conductivity of several anionic conductors as a function of inverse temperature: YSZ, $(ZrO_2)_{0.92}(Y_2O_3)_{0.08}$; CGO, $Ce_{0.8}Gd_{0.2}O_{1.9}$; LSGM, $La_{0.9}Sr_{0.1}Ga_{0.8}Mg_{0.2}O_{2.85}$; LAMOX, $La_2Mo_2O_{9,64}$; Si-apatite, $La_{10}(SiO_4)_6O_{3,84}$; and Ge-apatite, $La_{10}(GeO_4)_6O_{3.84}$.[82] Reproduced with permission from ref 82. Copyright 2010 The Royal Society of Chemistry (http://dx.doi.org/10.1039/ B915141A).

ionic conductivity is realized by doping them using bi- and trivalent metal oxides, such as Y, Sr, Ca, Sc, Ln. As a result, the exceeding charge is compensated by the formation of oxygen vacancies, which are highly mobile at elevated temperatures. Moreover, for Zr and Hg oxides, the doping by low-valent ions (several mol % and higher) results not only in the creation of highly mobile oxygen vacancies, but also in the stabilization of the cubic fluorite structure, which in undoped oxides is stable only at elevated temperatures.[88] Therefore, the origin of the high oxygen ion conductivity of the fluorite lattice is the combination between its ability to accept high concentrations of vacancies and the fact that these vacancies are mobile at high temperatures.

It is well established that solid electrolytes with the fluorite-type structure show a maximum in the conductivity isotherms versus aliovalent ion content around 5−15 mol % (this value largely depends on temperature, preparation route, prehistory, purity, etc). Figure 9 shows the ionic conductivity as a function of the dopant concentration for ceria-based electrolytes.

One of the reasons of the observed decrease in the conductivity at high dopant concentrations is the change in the
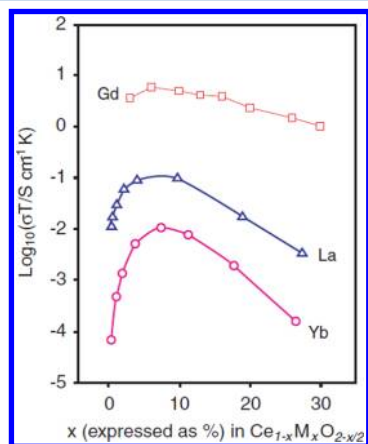

Figure 9. The isothermal conductivity of some ceria-based solid electrolytes at temperatures close to 200 °C. Reprinted with permission from ref 90. Copyright 2012 Elsevier.

character of the interaction between defects, leading to the formation of complex defects of low mobility. An empirically confirmed rule shows that at dopant concentrations close to the maximum there is a minimum in the conductivity activation energy. For the majority of ionic conductors, the conductivity activation energy (E_a) consists of two parts, the enthalpy of ion migration (ΔH_m) and any terms caused by the interaction of the point defects and/or by the charge carrier formation. The second part might be due to the formation of defect associates between the oxygen vacancy and the substitutional cation(s). For instance, at low concentration of trivalent aditives in ceria, the second term of E_a may be represented by the association enthalpy ΔH_a. In the simplified case of a simple dimer, or associated pair, the activation energy for conductivity would be given by the sum $(\Delta H_a + \Delta H_m)$.[88] Irrespective of the association type, vacancy concentrations can be defined as (i) the stoichiometric concentration, which is determined by the electroneutrality condition; and (ii) the mobile or free vacancy concentration given by the association equilibria. Only the mobile or free vacancies contribute significantly to oxygen ionic transport.

It is generally recognized[91] that the most effective aliovalent addition appears to be defined by the relationship between the anionic radii of the additive and parent lattice.[92−94] However, there is still discrepancy to understand the relationship between the dopant properties and the ionic conductivity. Kilner[95] has suggested that a better means of evaluating the relative ion mismatch of dopant and host would be to compare the cubic lattice parameter of the host oxide and that of the pseudocubic lattice parameter of the corresponding dopant oxide. In this way, it has been explained why Gd and Sc are excellent dopants in ceria and zirconia, respectively.[95] Kim[96] proposed the concept of the critical dopant ionic radius for which lattice parameters are not modified as compared to those of the undoped electrolyte.[96] Kilner et al.[97] and Gatlow[98] explained that a smaller ionic size mismatch between the host and the dopant was preferable for obtaining a high conductivity. Ionic conductivity of ZrO_2 doped with a trivalent metal oxide is the highest in the case of Sc^{3+}, because its ionic radius is most identical to that of Zr^{4+}.[99] However, cost considerations make Y_2O_3 a better choice.

Arrhenius plots are often used to compare the ionic conductivity among various solid electrolytes and to estimate the activation energy of the ionic transport. Figure 10 compares the ionic conductivity of some selected solid electrolytes.[100−105]

In the low temperature range (300−500 °C), ceramics with extremely different ionic conductivity levels (3 orders of magnitude) can be selected for catalytic applications.

3.1.2. Perovskite-Structured Oxides. Mixed metal oxides with the ABO_3 perovskite structure can be also considered as promising anionic ceramic materials for catalytic applications. This family of oxides is already widely used in heterogeneous catalysis and solid-state electrochemistry both as electrodes and electrolytes. The catalytic and electrocatalytic properties of perovskites can be tuned by varying the nature of A and B cations and/or by the insertion of dopings in the structure.[106−119]

We report in this section the perovskites compositions used as electrolytes in solid electrolyte cells. In the ABO_3 perovskite structure, the large A cation is coordinated to 12 anions, with the B cation occupying a six-coordinate site, forming a network of corner-sharing BO_6 octahedra (Figure 11).

An ideal perovskite consists of ABO_3 units, but the chemical composition can vary depending on the valency of the A- and B-site cations. Combinations such as $A^{1+}B^{5+}O_3$, $A^{2+}B^{4+}O_3$, and $A^{3+}B^{3+}O_3$ are commonly used. In most cases, the A site is
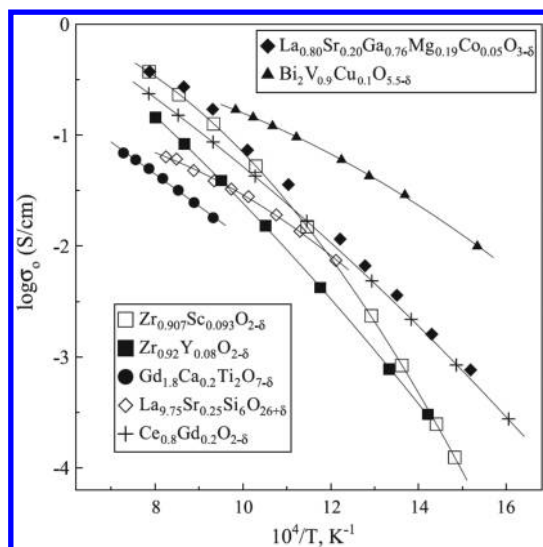
Figure 10. Arrhenius plots of oxygen ionic conductivity of various solid-electrolyte materials. Reprinted with permission from ref 89. Copyright 2012 Elsevier.
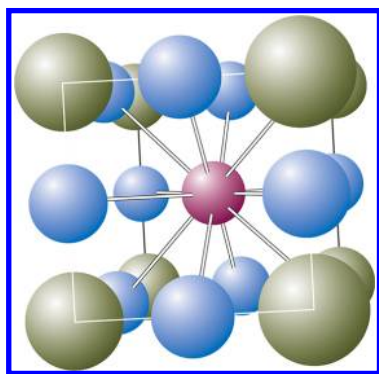

Figure 11. The perovskite (ABO_3) structure, where the red sphere represents the A-cation, the green spheres represent the B-cations, and the small blue spheres are oxygen ions. Reprinted with permission from ref 90. Copyright 2012 Elsevier.

generally occupied by 2+ large alkali earth metals, Ba, La, or Sr, and the B site by 4+ smaller first-row transition elements such as Ce, Co, or Fe. Although the same structure is maintained, the properties can be very different. For example, the $BaCoO_3$ and $SrCoO_3$ oxides exhibit oxygen conductivity, while the $BaCeO_3$ and $SrCeO_3$ materials are proton conductors. In perovskites, the most important parameter controlling the oxide ion conductivity is the degree of distortion from the fully symmetric and stress-free lattice, in which the oxide vacancy has the highest mobility and the lowest activation energy for the vacancy hopping. The $A^{3+}B^{3+}O_3$ type of perovskite has the lowest oxide−B-ion interaction and therefore the highest oxide vacancy mobility.[120]

The perovskite structured lanthanum-transition metal oxides substituted by alkaline earth metals are technologically important due to their electrical, magnetic, and catalytic properties.[121] Of particular interest are Sr and Mg doped $LaGaO_3$ (LSGM) materials, with oxide ion conductivity higher than that of YSZ as observed in Figure 8. In addition, these materials exhibit relatively low thermal expansion, similar to that of stabilized zirconia,[89] which is of great importance for the design of catalytic reactors. The high ionic conductivity of (Sr,Mg)-doped $LaGaO_3$, of the general formula $La_{1−x}Sr_xGa_{1−y}Mg_yO_{3−\delta}$, was first reported in 1994 by Ishihara et al.,[122] and by Feng and Goodenough.[123]

Rather surprisingly, the introduction of small amounts of cations with variable valence, such as cobalt, onto the gallium sites increases the ionic conduction in LSGM, and causes only a small increase in the electronic conductivity.[124] However, the concentration of transition metal dopants should be limited to values below 3−7%, as further addition leads to increased electronic and decreased ionic conductivity. Other perovskites known to exhibit oxide−ion conductivity comparable to that of YSZ include $NdGa_{0.9}Mg_{0.1}O_{2.95}$[125] and $Gd_{0.85}Ca_{0.15}AlO_{2.925}$.[126] The wide range of solid solubilities and the variety of compositions make these and other perovskite systems warrant for further investigation. Work is also being carried out on perovskite-related oxides of the K_2NiF_4 ($A_2BO_{4+\delta}$) structure such as $Ln_2NiO_{4+\delta}$ (where Ln = La, Nd, Pr).

3.1.3. Others Materials. In the last years, intensive research in the field of solid-state ionics has motivated the appearance of new anionic conducting materials of improved properties, described in detail in a very recent review.[82] Among these novel materials, the ones that have been studied mainly as alternative SOFC electrolytes are: (a) $La_2Mo_2O_9$ (LAMOX), a new family of fast oxide−ion conductors discovered in 2000 by Lacorre.[127] This compound exhibits a first-order phase transition from the non-conductive monoclinic phase (α) to the highly conductive cubic phase (β) at around 580 °C, with the latter having an ionic conductivity of 6×10^{-2} S cm^{-1} at 800 °C. Conductivity data for pure LAMOX are included in Figure 8. Doping pure LAMOX with alkaline (e.g., K and Rb) and alkaline-earth (e.g., Ca, Sr, and Ba) cations on the La site stabilizes the cubic phase at room temperature without significantly affecting the conductivity.[128]

(b) Next is apatite-type oxides. The general chemical formula of apatite oxides can be written as $M_{10}(XO_4)_6O_{2\pm y}$, where M is a rare-earth or alkaline-earth cation, X is a p-block element such as P, Si, or Ge, and y is the amount of oxygen non-stoichiometry. These materials are isostructural with the well-known hydroxyapatite biomaterials found in bones and teeth. Since the discovery of fast oxide−ion conductivity in silicate-based apatites ($Ln_{9.33}(SiO_4)_6O_2$, where Ln is typically a large lanthanide ion such as La^{3+} or Nd^{3+}) in the mid-1990s, a large number of experimental and computational studies have clarified the structure−property relationship in both Si- and Ge-based systems[129,130]

(c) Mayenite, with nominal composition of $Ca_{12}Al_{14}O_{33}$, was first reported as a fast oxide−ion conductor 20 years ago,[131] and nowadays is once again attracting attention as a cost-effective electrolyte for numerous applications. The crystal structure of this material (space group $I\overline{4}3d$, Z = 2, a = 11.98 Å) consists of 64 oxygen ions per unit cell fixed in a Ca−Al−O framework forming 12 "cages" and two oxygen ions (called extra-framework oxygen) randomly occupying one-sixth of the "cages".[130]

(d) Materials based on δ-Bi_2O_3, which although they display extremely high oxide−ion conductivity, suffer from phase stability problems, particularly under reducing atmospheres. A more stable and better ion-conducting family of oxides is based on a related system, with parent oxide $Bi_4V_2O_{11}$.[132] This family of solid electrolytes is known as the BIMEVOX family, where BI stands for bismuth, ME for metal, V for vanadium, and OX for oxygen.[133,134] The most common dopants added to BIMEVOXs are Cu, Ni, Co, and Mg, which not only stabilize the highly conductive structure at lower temperatures, but also result in an ionic transport number close to 1.0 for temperatures up to about 630 °C.[135] Interest in the BIMEVOX compounds is still active because of their high ionic conductivity, although problems with

high chemical reactivity, reducibility, and low mechanical strength have to be adequately addressed.

3.2. Alkaline Conductors

3.2.1. β-Alumina Electrolytes. The β-alumina family, a series of compounds in the $Na_2O-Al_2O_3$ system, is one of the most important groups of solid electrolytes, not only because it is practically useful for advanced batteries, but also because it is a typical two-dimensional ionic conductor, from which or by analogy with which various kinds of solid electrolyte materials can be derived.[26] The principal members are the β and β'' phases, the ideal compositions of which are $Na_2O\cdot11Al_2O_3$ ($NaAl_{11}O_{17}$) and $Na_2O\cdot5.33Al_2O_3$, although they are usually non-stoichiometric. For β-alumina, the non-stoichiometry is generally represented by $Na_{1+x}Al_{11}O_{17+x/2}$, where x is typically about 0.2. On the other hand, the β'' phase in the binary $Na_2O-Al_2O_3$ system is unstable, and incorporation of aliovalent cations such as Mg^{2+} is needed for stabilization; then, the composition is represented, for example, by $Na_{1+x}Mg_xAl_{11-x}O_{17}$, where x is typically 2/3. The crystal structure of β-alumina was verified in 1937,[42] 30 years before the discovery of its high Na^+ conductivity in 1967.[44,136] It is based on a hexagonal unit cell ($a = 5.58$ Å, $c = 22.5$ Å, space group: $P6_3/mmc$), where the $Al_{11}O_{16}$ blocks are in a spinel-like arrangement (spinel block) and the NaO^+ layers are stacked alternately along the c-axis. The β'' structure ($a = 5.59$ Å, $c = 33.95$ Å, $z = 3$, space group: $R3m$) is constructed of a similar alternate stacking of the spinel blocks and NaO layers, but the sequence of the oxygen layers in the spinel block is different.[137] The β-alumina group of oxides is characterized by structures of alternating closely packed slabs and loosely packed layers. The loosely packed layers, which contain mobile sodium ions, are called conduction planes. In these conduction planes, sodium ions are free to move under an electric field. The closely packed oxide slabs are comprised of four layers of oxygen ions with aluminum ions in both octahedral and tetrahedral interstices. In both phases, migration of Na^+ takes place in the NaO layers, which is often expressed by a honeycomb arrangement.[26]

Sodium ions in either the β or the β'' phase can be easily exchanged for various cations because of fast ionic diffusion in the layer. Ion exchange is usually carried out by immersing sample crystals in a fused salt of the cation to replace Na^+. For instance, Na^+ in β-alumina is totally replaced by fusing K^+ in KNO_3 at $300-350$ °C; the as-obtained K-β-alumina shows a K^+ conductivity of 6.5×10^{-4} S cm^{-1} at 25 °C.

Several factors influence the conductivity of polycrystalline β/β''-Al_2O_3, including: (i) composition; (ii) relative proportion of the two phases; and (iii) microstructure (grain size, porosity, impurities, etc.). As was mentioned earlier, for undoped and doped β-Al_2O_3, the accommodation of excessive sodium atoms in the interstitial sites could significantly improve the conductivity. In the case of doped β-Al_2O_3, the structure change to β''-Al_2O_3 offers accommodation of higher levels of sodium, which further increase the conductivity. Pure β'' phase, therefore, appears to be the most desired phase. However, the relatively low mechanical strength and moisture sensitivity prohibit it from being used solely as electrolyte material. In practice, a two-phase mixture of either β and β''-Al_2O_3 or ZrO_2-incorporated β''-Al_2O_3 is preferable for sufficient conductivity along with satisfactory mechanical properties.[138] On the other hand, this family of ionic conductors seems to be very attractive for low temperature catalytic reactions. As discussed in section 4, EPOC can be implemented at low temperatures (<200 °C) on this kind of oxides due their relatively high conductivity as compared to O^{2-}

conducting ceramics. In addition, Na^+ or K^+ are well-known to be effective chemical promoters of metal-supported catalysts.

3.2.2. NASICON. The NASICON family is another important series of Na^+ conductors, discovered in 1976 through careful structural examination of oxyacid salt frameworks with three-dimensional tunnels.[139] It is a solid solution in the $NaZr_2(PO_4)_3-Na_4Zr_2(SiO_4)_3$ system and can be represented by $(1-x/3)NaZr_2(PO_4)_3\cdot(x/3)Na_4Zr_2(SiO_4)_3$ or $Na_{1+x}Zr_2P_{3-x}Si_xO_{12}$. A variety of modified NASICONs have been synthesized by replacing Zr with, for example, Co, Ti, V, and/or by substituting As or Ge for P or Si.[140] The general formula of NASICON composition can be written as $A M\ddot{M}P_3O_{12}$, where the site A can be occupied by alkali ions (Li^+, Na^+, K^+, Rb^+, and Cs^+), alkaline earth ions (Mg^{2+}, Ca^{2+}, Sr^{2+}, and Ba^{2+}), H^+, H_3O^+, NH_4^+, Cu^+, Cu^{2+}, Ag^+, Pb^{2+}, Cd^{2+}, Mn^{2+}, Co^{2+}, Ni^{2+}, Zn^{2+}, Al^{3+}, Ln^{3+} (Ln = rare earth), Ge^{4+}, Zr^{4+}, Hf^{4+}, and also it can be vacant. The M and $\ddot{M}$ are occupied by di (Zn^{2+}, Cd^{2+}, Ni^{2+}, Mn^{2+}, Co^{2+}), tri (Fe^{3+}, Sc^{3+}, Ti^{3+}, V^{3+}, Cr^{3+}, Al^{3+}, In^{3+}, Ga^{3+}, Y^{3+}, Lu^{3+}), tetra (Ti^{4+}, Zr^{4+}, Hf^{4+}, Sn^{4+}, Si^{4+}, Ge^{4+}), and penta (V^{5+}, Nb^{5+}, Ta^{5+}, Sb^{5+}, As^{5+}) valent transition metal ions to balance the charge suitably. Depending on the composition, the crystal structure can be rhombohedral (for many NASICON systems), monoclinic, triclinic, orthorhombic, Langbeinite, Garnet, SW type (orthorhombic scandium wolframate $Sc_2(WO_4)_3$), and corundum-like.

The rhombohedral structure consists of a three-dimensional rigid framework with $M(\ddot{M})O_6$ octahedra and $PO_4(SiO_4)$ tetrahedra sharing common corners.[139] This 3D framework contains interconnected channels in which the mobile conducting ions are encapsulated at the A site. The interstitial space of the tunnels provides the conduction pathway for the mobile ion. Structures of orthorhombic, monoclinic, triclinic, and corundum-like NASICON polymorphs are given in Figure 12.

The conductivity of NASICON-type materials is comparable to that of β''-alumina as depicted in Figure 13, and furthermore they exhibit low thermal expansion.[141]

Many studies have been presented in the literature using NASICONs, which for brevity can be categorized based on (i) kind of the mobile ion (mono valent ions Li^+, Na^+, H^+, Cu^+, Ag^+ and di, tri, and tetra valent ions) and (ii) kind of applications such as (a) low thermal expansion materials (Ca, Sr, Ba at the site A), (b) insertion/extraction materials (presence of reducible ions like Cu^{2+}, Fe^{3+}, V^{5+}, Ti^{4+}, Nb^{5+} and a vacancy), (c) immobilization of radio active waste, (d) catalyst supports (Cu and Ag NASICONs), and (e) sensors and ion selective electrodes.

Finally, it is important to note the NASICON type Li^+ conductors (LISICON). LISICON ($Li_{14}ZnGe_4O_{16}$) and related systems ($Li_{2+2x}Zn_{1-x}GeO_4$) were first described by Bruce and West.[142] The LISICON framework is related to the γ-Li_3PO_4 crystal structure. However, even in doped compounds (for example, γ-$Li_{14.4}V_{1.6}Ge_{2.4}O_{16}$), the ionic conductivity remains relatively low (about 10^{-6} S cm^{-1} at room temperature). Furthermore, LISICON $Li_{14}ZnGe_4O_{16}$ is highly reactive with metallic lithium and atmospheric CO_2, and its conductivity decreases with time.

3.2.3. Other Materials. Other related Na^+ and K^+ conductors are (a) hollandite family materials. Hollandite is a mineral with a composition of $Ba_xMn_8O_{16}$ ($x \leq 2$), in which Ba^{2+} ions are located in one-dimensional tunnels formed along the c-axis of a pseudotetragonal framework structure composed of MnO_6 octahedra. Mixed titanates, $A_x(B,Ti)_8O_{16}$ (priderite, A, alkaline metal, B, Mg, Al, Ga, etc.), are isostructural and exhibit
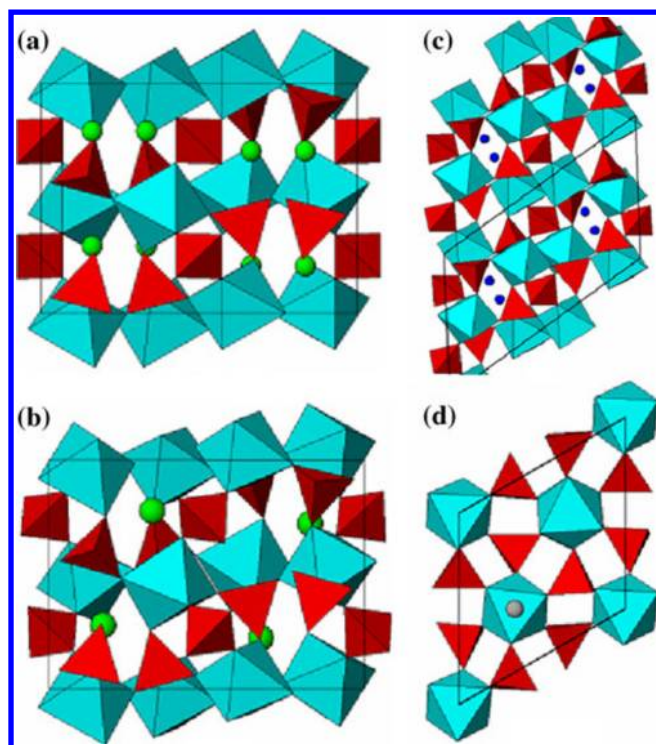
Figure 12. Structures of NASICON polymorphs: (a) orthorhombic, (b) monoclinic, (c) triclinic, and (d) corundum-like.[140] Reproduced with permission from ref 140. Copyright 2011 Springer Science and Business Media.
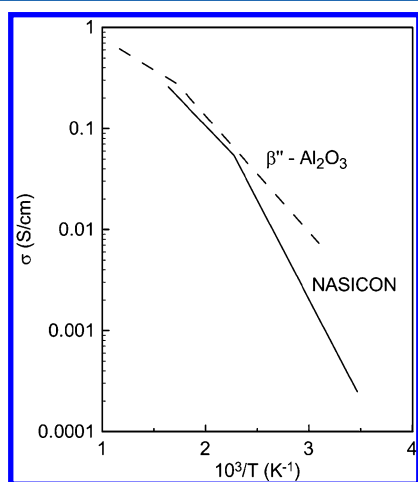

Figure 13. Conductivity of NASICON and sintered β''-alumina as a function of $1/T$. Reprinted with permission from ref 141. Copyright 2012 Elsevier.

one-dimensional ionic conduction along the tunnel. For example, a single crystal sample of $K_x(Mg,Ti)_8O_{16}$ (KMTO) shows K^+ conductivity as high as 0.1 S cm^{-1} at 293 K along the c-axis in the very high-frequency region, although it rapidly decreases as the measuring ac frequency is lowered. Analogous compounds, such as $K_xGa_8Ga_{8+x}Ti_{16-x}O_{56}$, show higher conductivity.

(b) Lithium ion conductors is another example. The simplest example is LiI, which shows not an excellent, but still considerable conductivity of $\sim 5 \times 10^{-7}$ S cm^{-1} at room temperature, while other lithium halides are almost insulators, likely due to the less polarizable nature of their halogen ions. It is

noteworthy that LiI was the first practical solid electrolyte used in a Li/I$_2$-complex cell in 1972, in which a layer of LiI was formed by contact of the negative and the positive electrodes. The layer was so thin that the resistance was small enough for low current uses, such as in a cardiac pacemaker. Another Li$^+$ conductor binary compound is Li$_3$N, the crystal structure of which is built up of Li$_2$N layers in hexagonal arrangement stacked along the c-axis with the rest of the Li in between. Intralayer migration of the latter Li$^+$ (Li$_2$) is responsible for ionic conduction. Thus, its single crystal shows highly anisotropic conductivity, that is, 1.2×10^{-3} S cm^{-1} at 25 °C along the layers, while it is about 2 orders of magnitude lower along the c-axis.[143] The conductivity of polycrystalline samples is typically 7×10^{-4} S cm^{-1} at room temperature. However, the reported conductivity values of this compound depend on the synthesis method or sample history, suggesting structure sensitivity, that is, involvement of defects in the Li$_2$ conducting layer. In fact, Li$_3$N intentionally doped with hydrogen exhibits higher conductivity due to defects of Li$_2$ introduced by partial reduction of N^{3-} to NH^{2-}. It has also been reported that Li$_3$N, which is carefully prepared so as not to be contaminated, shows conductivity values in the order of 10^{-5} S cm^{-1} regardless the crystallographic direction.[144]

3.3. Protonic Conductors

3.3.1. Perovskite-Based Electrolytes. The first report of high-temperature proton conductivity in an oxide material dates back to the 1980s when Iwahara and co-workers observed this feature in doped strontium and barium cerates.[145] After more than 20 years of active research, the perovskite-type cerates and zirconates have become well-established proton conducting systems.[146−149] The crystal structure of these materials is based on the perovskitic structure, described in section 3.1.2. Protonic defects are formed by the dissociative absorption of water at the surface, which requires the presence of oxide−ion vacancies. Water from the gas phase dissociates into a hydroxide ion and a proton, with the hydroxide ion filling an oxide−ion vacancy and the proton forming a covalent bond with lattice oxygen. Pure SrCeO$_3$, BaCeO$_3$, CaZrO$_3$, and SrZrO$_3$ exhibit only low proton incorporation unless doped with subvalent cations. In the BaCeO$_3$ system, for example, replacement of Ce^{4+} ions with M^{3+} cations (typically Y^{3+}) is charge-compensated by the formation of an oxygen vacancy.

The process of water incorporation in such systems has been found (both experimentally and theoretically) to be exothermic for doped and undoped cerates and zirconates,[150,151] which is consistent with the observation that proton uptake in perovskite oxides increases with decreasing temperature. Furthermore, incorporation of water in doped systems is more exothermic than that in undoped systems. A typical conductivity versus inverse temperature curve for 10 mol % Y-doped BaCeO$_3$ and for other proton conductors discussed in this section is shown in Figure 14.

The detailed mechanism of proton conduction in these perovskite-type compounds is still controversial. Recent infrared spectroscopy studies have shown that protons exist in their structure as OH species. However, the O to H distance is considerably longer than usual, suggesting a contribution of hydrogen bonding.[152] It is of interest a comparison with H$_x$ReO$_3$, which is built up of a structurally equivalent framework and exhibits very fast proton transport, although electronic conduction is significant. According to neutron diffraction, its hydrogen atoms are statistically located at 72 equivalent sites, which are on a sphere about 1 Å apart from each oxygen atom. It
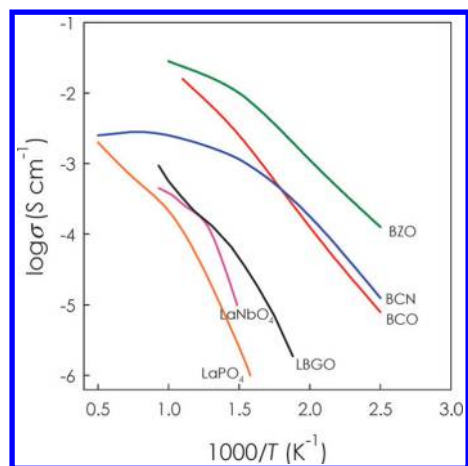
Figure 14. Total conductivities of some well-known proton conductors as a function of inverse temperature: $BaCe_{0.9}Y_{0.1}O_3$ (BCO); $BaZr_{0.8}Y_{0.2}O_3$ (BZO); $La_{0.9}Sr_{0.1}PO_4$; $Ba_3Ca_{1.18}Nb_{1.82}O_{8.73}$ (BCN); $La_{0.99}Ca_{0.01}NbO_4$; $La_{0.8}Ba_{1.2}GaO_{3.9}$ (LBGO).[82] Reproduced with permission from ref 82. Copyright 2010 The Royal Society of Chemistry (http://dx.doi.org/10.1039/ B915141A).

is thus reasonable to assume that protons in a ReO_3- or perovskite-type framework are transported by hopping from an OH group to one of the nearest oxygens.

Perovskite cerates and zirconates are mutually soluble; therefore, for the development of electrolytes with adequate proton conductivity and good chemical stability under conditions typically encountered during fuel cell operation, cerate–zirconate solid solutions are under investigation.[153] Proton conducting cerates and zirconates thus represent the most promising and actively investigated groups of solid electrolytes.

3.3.2. Other Materials. The synthesis of cation-off stoichiometric perovskites seems to be promising for the development of materials with high proton conductivity. The charge imbalance caused by the cation non-stoichiometry is compensated by protons. One of the best-known materials of this kind is $Ba_3Ca_{1.18}Nb_{1.82}O_{8.73}$ (also known as BCN18). The amount of water uptake in BCN18 per equivalent perovskite unit is comparable to that found for the cerates and zirconates.[154] Other high-temperature proton conductors receiving attention include: (a) $Ba_2In_2O_5$. Although initially proposed as an oxide–ion conductor,[155] its ability to conduct protons has also come under scrutiny.[156] The brownmillerite structure can be viewed as a perovskite-type structure, in which one-sixth of the oxide ions are missing.

(b) Second are phosphates without structural protons, such as $LaPO_4$. This compound was proposed as a candidate proton conductor in the early 1990s, and is interesting due to its unusual dissolution and proton transport mechanism.[157] Ca- and Sr-doped $LaPO_4$ have been demonstrated to exhibit predominantly protonic conductivity up to 800 °C, but with relatively low absolute conductivity values of 6×10^{-5} and 3×10^{-4} S cm^{-1}, respectively. In these materials, protons are considered to enter the crystal from ambient water vapor in the form of extrinsic positive defects, compensating the acceptor dopants and replacing the intrinsic positive defects, presumably oxygen vacancies in the form of pyrophosphate groups.[158]

(c) Next are compounds in the β-alumina family. These materials also exhibit proton conductivity when the Na$^+$ ions are exchanged with H_3O^+ and/or NH_4^+. Derivatives from the β''-

phase usually exhibit higher conductivity than those from the β phase. The highest conductivity of 10^{-4} S cm^{-1} has been reported for the compound $(NH_4)(H_3O)_{2/3}Mg_{2/3}Al_{31/3}O_{17}$, which was synthesized by soaking β''-alumina in fused ammonium salt for a long time.[159] Ionic conduction in this class of compounds, of course, occurs within layers between the spinel blocks, but it is still unclear whether protons are transported by a Grotthus-type mechanism or by a "vehicular" mechanism in which they are assumed to migrate as multiatomic ions such as H_3O^+ or NH_4^+. Gallium analogues of β- or β''-alumina are ion exchanged more smoothly, and NH_4-β gallates thus formed show higher conductivity than their alumina counterparts, likely due to the wider spacing of the conduction plane of these compounds.[160]

(d) For the case of low temperature protonic conductors, inorganic solid acids show high protonic conductivity at moderate temperatures (120–300 °C). These materials are solid acid compounds such as $CsHSO_4$ and CsH_2PO_4.[161] Their structures are usually comprised of oxyanions, XO_4, such as SO_4 or PO_4, linked together by hydrogen bonds.

3.4. Mixed Ionic–Electronic Conductors

Solid mixed ionic–electronic conductors (MIECs) can exhibit both ionic and electronic (electron/hole) conductivity. In any material, there are in principle non-zero electronic and ionic conductivities (σ_e, σ_{ion}). It is usual to limit the use of the name MIEC to materials in which σ_{ion} and σ_e do not differ by more than 2 orders of magnitude. The term MIEC is concerning materials with not too low values of σ_{ion} and σ_e (σ_{ion}, $\sigma_e \geq 10^{-5}$ S cm^{-1}). MIECs are candidates for high temperature electrochemical applications, such as electrodes or electrocatalysts, and ceramic membranes for oxygen separation or partial oxidation of light hydrocarbons. The mixed ionic–electronic conductivity allows one to induce migration of charging species (electrons in one direction, ions in the other one) inside the material without any electrical connection. This property can be used for catalytic membrane reactors as well in wireless EPOC configurations (see section 4).

3.4.1. CeO$_2$-Based Electrolytes. Among the most common mixed conductors are ceria-based materials, which offer very good mixed conducting properties. The stability of CeO_2-based materials is more sufficient, and it is well-known that these materials exhibit mixed conductivity under reducing atmospheres. These materials can also present mixed conductivity under oxidizing or inert atmospheres due to the addition of oxides with mixed valence, including bulk modifications with lanthanides.

As was already reported, CeO_2-based electrolytes are fluorite-type conducting materials,[87,161–163] which are increasingly used as catalyst supports in heterogeneous catalysis. Typical dopants of these materials include Gd_2O_3 (producing gadolinia-doped ceria, GDC, also known as cerium–gadolinium oxide, CGO) and Sm_2O_3 (producing samaria-doped ceria, SDC, also known as cerium–samarium oxide, CSO).

The conductivity of these solid solutions is significantly higher than that of YSZ, particularly at lower temperatures (500–700 °C). In addition, at low oxygen partial pressures and temperatures above 600 °C, the conductivity of these materials is not purely ionic, with a non-negligible proportion of electronic (n-type) conductivity, consistent with the partial reduction of Ce^{4+} to Ce^{3+}.[164] For instance, the electronic conductivity of gadolinia-doped ceria is about 1 order of magnitude larger than that of yttria-stabilized zirconia (about 0.1 S cm^{-1} at 800 °C).[83] However, it should be noted that the magnitude of electronic

M

dx.doi.org/10.1021/cr4000336 | *Chem. Rev.* XXXX, XXX, XXX–XXX

conductivity and the stability under reducing atmospheres for ceria-based oxides are greatly dependent on the kind and quantity of doping elements.

The widespread interest in the catalytic properties of ceria results from its application in automotive catalysis, where its ability to be reduced and reoxidized provides high "oxygen storage capacity".[165−169] Because of these redox properties (the ability of cerium to cycle between Ce^{3+} and Ce^{4+}), ceria can greatly enhance catalytic activities for a number of important reactions when it is used as a support for transition metals. For example, in reactions that use steam as an oxidant (e.g., the water−gas shift reaction and steam reforming of hydrocarbons), rates for ceria-supported metals can be several orders of magnitude higher than that for ceria or the transition metal alone. Besides the aforementioned applications, ceria and ceria-supported metals are finding new application in catalyzing many reactions including redox reactions, synthesis gas production, organic synthesis, catalytic abatement of organic pollutants, and so on. Understanding the interaction between the support (CeO_2) and the transition metal may offer significant opportunities for modifying and improving the catalytic performance of ceria-based catalysts, and, thus, it is the basis for the development of improved catalysts.

Fluorite solid solutions $Ce_{1−y}Pr_yO_{2−\delta}$ are also very interesting mixed conductive materials. They undergo extensive and fast oxygen stoichiometry changes with adequate stability under repeated redox cycles, which may be applicable in oxygen storage, electrocatalytic processes, etc. However, the mixed conductivity of $Ce_{1−y}Pr_yO_{2−\delta}$ is still lower than that of the best perovskite-type materials, which will be analyzed below.

3.4.2. Perovskite-Based Electrolytes. Perovskite-based electrolytes are well-known mixed conductors commonly used as cathode materials in solid oxide fuel cells (SOFCs). These materials that combine mixed ionic−electronic conductivity along with intrinsic catalytic properties can be categorized into different groups.

3.4.2.1. Manganites. Perovskite-type manganites (Ln,A)-$MnO_{3\pm\delta}$ (Ln = La−Yb or Y; A = Ca, Sr, Ba, Pb) and their derivatives possess a high electronic conductivity and substantial electrocatalytic activity toward oxygen reduction at temperatures above ∼750 °C.[170,171] Although the total conductivity of manganites is lower as compared to their Co- and Ni-containing analogues, the latter perovskite families exhibit other important disadvantages, including excessively high TECs and/or limited thermodynamic stability even under oxidizing conditions.[172] In fact, lanthanum− strontium manganites (LSM) and composites are still considered as state-of-the-art cathode materials for SOFCs operating at 800−1000 °C. All perovskite-related manganites exhibit predominant electronic conduction in combination with low oxygen ion diffusivity; their transport properties and electrochemical activity are strongly dependent on the oxygen non-stoichiometry.

3.4.2.2. Ferrites. These primarily include perovskite-like (Ln,A)$FeO_{3\pm\delta}$ and their derivatives existing in all Ln−A−Fe−O systems, $A_2Fe_2O_{5\pm\delta}$ brownmillerites, (Ln,A) $Fe_5O_{12\pm\delta}$ garnets in the compounds with relatively small Ln^{3+} cations, Ruddlesden−Popper series (Ln,A)$_{n+1}Fe_nO_z$, and a variety of other intergrowth compounds such as $Sr_4Fe_6O_{13\pm\delta}$. However, because of structural constraints and defect chemistry, features limiting electronic transport are observed; in most cases, an extensive iron substitution is necessary to achieve total conductivity values higher than 10−30 S cm^{-1} at temperatures above 400 °C.

3.4.2.3. Cobaltites. In comparison with the ferrite-based materials, perovskite related cobaltites possess considerably better cathodic and transport properties, but also higher thermal and chemical expansion.[173] As for the Manganite and ferrite electrodes, the primary attention for potential electrochemical applications is drawn to perovskite-type (Ln, Sr)$CoO_{3−\delta}$ and solid solutions on their base. At the same time, relatively high mixed conductivity and fast exchange kinetics result in an increased interest to the layered cobaltites, where the state of Co cations is often more stable with respect to disordered perovskite analogue; important compositional families are $LnBaCo_2O_{5+\delta}$ (Ln = Pr, Gd−Ho, Y), and $LnBaCo_4O_{7+\delta}$ (Ln = Dy−Yb, Y).

Other related perovskite mixed conductive materials are the nickelates and cuprates family. In ternary Ln−M−O (Ln = La, Pr, Nd; M = Ni, Cu) systems, the K_2NiF_4-type compounds are most stable under oxidizing and moderately reducing atmospheres.[174]

3.4.3. TiO$_2$-Based Electrolytes. Titanium dioxide, TiO_2, is a well-known material, which shows mixed conductivity properties and has been used in a wide range of applications, including catalysis (as a catalyst or a support[175−177]), chemical gas sensors, photocatalysts, and coatings for self-cleaning building materials.[178−181] TiO_2 is known as a n-type semiconductor, that its mainly donor-type defects, including oxygen vacancies and titanium interstitials, are responsible for the n-type conductivity and the non-stoichiometry, resulting in the apparent deficit of oxygen $TiO_{2−x}$. Among the three titanium dioxide polymorphs (rutile, anatase, and brookite), rutile and anatase have been most widely investigated. They both crystallize in a tetragonal lattice, and their bulk structure can be described basically in terms of a three-dimensional arrangement of TiO_6 octahedra. The two polymorphs differ by the degree of distortion of each octahedral unit and by the manner in which the TiO_6 building blocks are spatially assembled.

These structural differences result in different physicochemical properties, such as density (4.250 g cm^{-3} for rutile and 3.894 g cm^{-3} for anatase) and stability (rutile is more stable than anatase by about 4.9 kJ mol^{-1}). TiO_2 itself is a versatile heterogeneous catalyst suitable for reactions ranging from formation of esters, amides, and transamidations, to oxidation reactions, comproportionation reactions, and primarily in photocatalytic reactions.[182] Because of its physical properties and its unique strong metal support interaction (SMSI) properties[183] (migration of ionic species from the support onto the catalyst particle surface),[184] titanium dioxide has been further used as an excellent catalyst−support for Au and Pt in heterogeneous catalysis, in applications such as the hydrodesulfurization process, the polymer electrolyte membrane fuel cells, as well as the water−gas shift reaction.

3.5. Applications

Solid electrolytes due to their unique properties have found widespread application in several areas of modern technology. The major commercial application of solid electrolytes is in gas sensors.[28] Solid oxide fuel cells (SOFCs)[29] are promising candidates for commercialization in the near future.

Other areas of growing interest are solid-electrolyte potentiometry (SEP),[30] solid-electrolyte membrane reactors (SEMRs),[31] solid-state batteries,[32] and, of course, EPOC.[23]

3.5.1. Gas Sensors. Electrochemical sensors based on solid electrolytes are particularly attractive due to their robustness and simple realization. Moreover, the measured chemical quantities (concentration) are directly transduced in electrical signals (current or potential). Two types of electrochemical sensors can

be found: "active" sensors, which generate voltage change (potentiometric sensors), and passive sensors, for which an electrical source is necessary to apply a signal, the response of which is analyzed afterward (amperometric, coulometric, and conductometric sensors). Potentiometric sensors can detect ions (ionic sensors) or gases (gas sensors or electrochemical gauges), and their operation is based on the existence of equilibrium at the interface between a solid ionic conductor and the analyzed medium, by exchange of electrochemical species. Generally, these sensors operate according to a reaction of the first kind, for example, O_2 using an oxide conductor; I_2, Cl_2, and Br_2 using the respective halide conductor; and H_2 using a protonic conductor.[26] Wide applications have been found for oxygen sensors with ZrO_2-based electrolytes, which operate in the temperature range 750−1100 °C,[185] as well as for sensors based on $PbSnF_4$ and LaF_3 ionic conducting ceramics, which allow operation at lower temperatures (300−520 °C).[186,187]

3.5.2. Solid-State Batteries. Several reviews on the development of solid electrolyte batteries have been published.[188−191] Batteries are of three general types: (1) The first is solid-state batteries in which the anode, the electrolyte, and the cathode are solids. A typical example of this battery type is the $Ag/RbAg_4I_5/RbI_3$ cell. Generally, solid-state batteries are small primary or reserve batteries, which operate at ambient temperature. (2) Next is solid electrolyte batteries with a liquid metal anode and/or a liquid cathode. These batteries can be ambient temperature systems, for example, using a Na/Hg amalgam anode. (3) Last is ionic cathode batteries in which the cathodes are being developed mostly for use with liquid electrolytes, in particular for lithium batteries.[26]

3.5.3. Solid Oxide Fuel Cells (SOFCs). In SOFCs the chemical energy of a fuel is converted to electricity with high efficiency. The required properties of electrolytes used in SOFCs are mainly fixed by the high operating temperature, which dictates constraints of different types: (i) electrochemical, high ionic conductivity (>0.1 S cm^{-1} at 1000 °C), low electronic transference number (<10^{-3}), and large electrolytic domain; (ii) chemical, electrolyte must be stable with respect to electrode materials, oxygen, and fuel gas; (iii) thermal, phase stability and a good match of thermal expansion coefficient with other cell components; and (iv) mechanical, fracture toughness (>400 MPa at room temperature) and gas tightness.

The above-mentioned constraints have restricted the choice to oxide-based ceramics where the charge carrier is an ion associated with the oxidant (O_2) or the fuel (H_2, hydrocarbons). The most investigated oxide-conducting solid electrolytes for potential use in SOFCs belong to the fluorite-type solid solutions with the general formula MO_2−$M'O$ or MO_2−M''_2O_3, where MO_2 is the basic oxide and $M'O$ or M''_2O_3 the dopant with M = Zr, Hf, Ce; M' = Ca; M'' = Sc, Y, Ln (rare earth). After a long period of research aimed at finding suitable electrolytes for SOFCs, doped zirconia has been selected as one of the most suitable electrolytes for SOFCs.[26,29]

SOFCs can also be used for steam electrolysis,[26] which is an interesting area. Besides steam electrolysis, Gur and Huggins were first to use solid electrolyte cells to carry out other electrolytic reactions such as NO electrolysis.[192,193]

4. ELECTROCHEMICAL PROMOTION OF CATALYSIS (EPOC)

4.1. Phenomenology

4.1.1. Catalytic Rate and Selectivity Modification. The idea of using an electronically conductive metal or metal oxide porous film simultaneously as a catalyst and as an electrode can be traced to the last works of Wagner.[194] This led not only to the passive technique of solid electrolyte potentiometry (SEP) for measuring in situ the chemical potential of oxygen on catalyst−electrodes,[78] via eq 1, but, more importantly, to the discovery of the effect of electrochemical promotion of catalysis (EPOC) or non-Faradaic electrochemical modification of catalytic activity (NEMCA effect).[18−21,23,63,195−200]

The basic phenomenology of this effect when using O^{2-} and H^+-conducting solid electrolytes is shown in Figures 15 and 16.
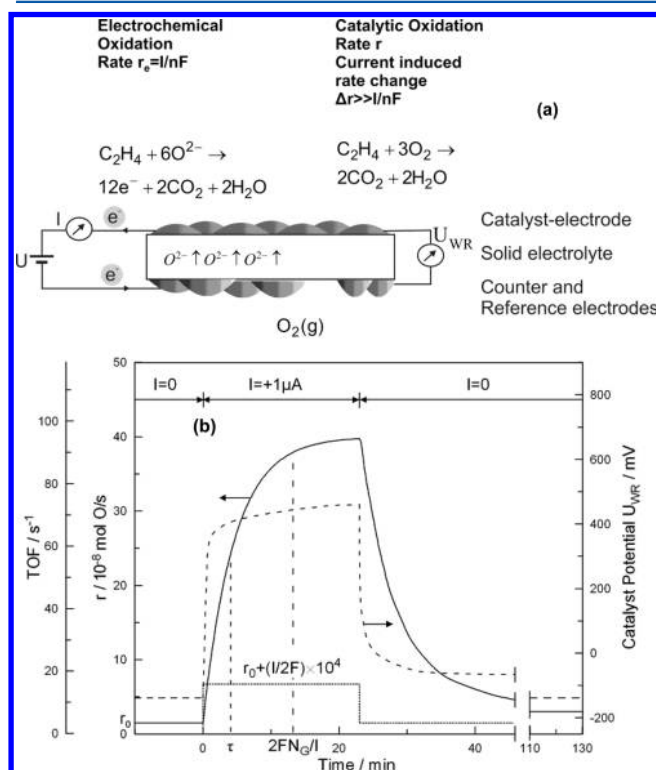
Figure 15. (a) Basic experimental setup and operating principle of EPOC with O^{2-} conducting supports. (b) Catalytic rate, r, and turnover frequency, TOF, response of C_2H_4 oxidation on Pt deposited on YSZ, an O^{2-} conductor, upon step changes in applied current. T = 370 °C, p_{O_2} = 4.6 kPa, $p_{C_2H_4}$ = 0.36 kPa. Also shown (dashed line) is the catalyst−electrode potential, U_{WR}, response with respect to the reference, R, electrode. The catalytic rate increase, Δr, is 25 time larger than the rate, r_0, before current application and 74 000 times larger than the rate, $I/2F$, of O^{2-} supply to the catalyst−electrode. N_G is the Pt/gas interface surface area, in mol Pt, and TOF is the catalytic turnover frequency (mol O reacting per surface Pt mol per s). Reprinted with permission from refs 198 and 273. Copyright 2012 Elsevier.

The (usually porous) metal catalyst−electrode, typically 0.05−2 μm thick, is deposited on the solid electrolyte and under open-circuit conditions (I = 0, no electrochemical rate) produces a catalytic rate r_0 for, for example, C_2H_4 oxidation[198,201] (Figures 15 and 16).

Application of an electrical current, I, or potential (±2 V) between the catalyst and a counter electrode causes very
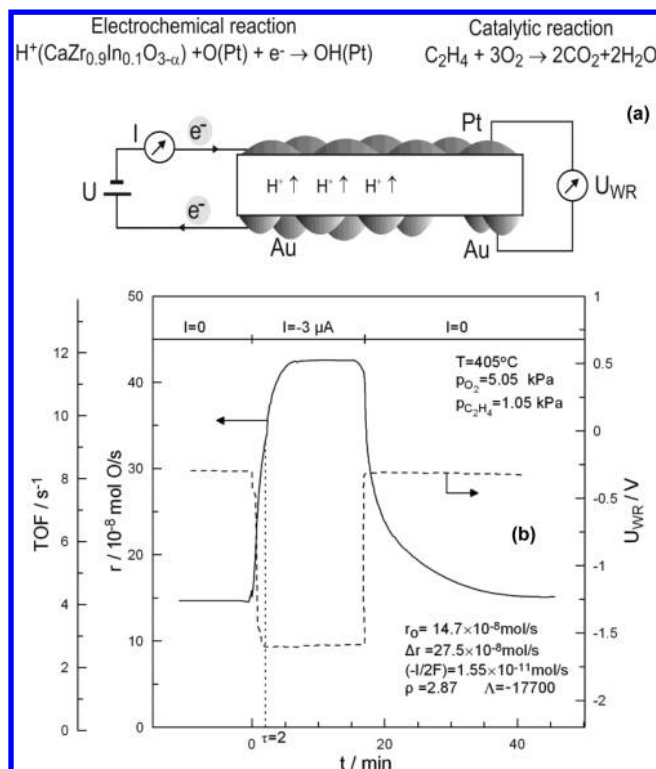
Figure 16. (a) Basic experimental setup and operating principle of electrochemical promotion using a H$^+$ conductor during C$_2$H$_4$ oxidation on Pt deposited on CaZr$_{0.9}$In$_{0.1}$O$_{3-\alpha}$. (b) Catalytic rate, r, catalytic turnover frequency, TOF, and catalyst potential response to step changes in applied current. The increase in O consumption, Δr, is 17 700 times larger than that anticipated from Faraday's law and corresponding rate, $-I/F$, of proton transfer to the Pt catalyst. Reprinted with permission from ref 201. Copyright 2012 Springer.

pronounced and non-Faradaic (i.e., $|\Delta r| \gg |I/2F|$) (being $\Delta r = r - r_o$) alterations to the catalytic rate, r, and, quite often, to the product selectivity, for example, Figure 17.[23,202] The rate of the catalytic reaction, r, can become up to 1400 times larger than the open-circuit rate, r_o,[203,204] and up to 3×10^5 times larger than the Faradaic rate ($I/2F$ for O^{2-}, $-I/F$ for Na$^+$ and H$^+$) of ion supply (or removal) to (or from) the catalyst−electrode.[23,63]
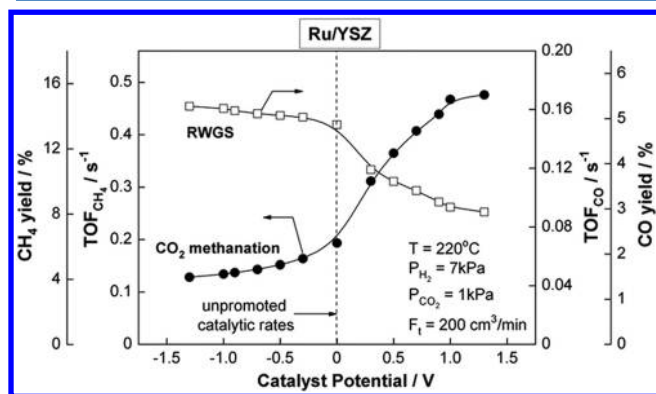
Figure 17. Electrochemical promotion of the methanation of CO$_2$ on Ru/YSZ. Increasing catalyst potential enhances the rate and TOF (turnover frequency) of methanation and suppresses the rate and TOF of the competing reverse water−gas shift reaction (RWGS). The yields (Y) of CH$_4$ and CO are also shown. Reprinted with permission from ref 202. Copyright 2012 American Chemical Society.

The Faradaic efficiency, Λ, defined from:

$$\Lambda \equiv \Delta r(\text{catalytic})/(I/nF) \qquad (21)$$

where n is the ion charge, can thus reach values up to 3×10^5 or down to -10^4.[23,63]

Electrocatalysis deals with Faradaic or subFaradaic processes, which are based on charge transfer reactions. This electrode reaction rate, within a fully effective Faradaic process without any loss (ohmic and kinetic), is proportional with the current, that is, $r_{el} = I/nF$. Therefore, by definition, the maximum Faradaic efficiency value of electrocatalytic reactions is equal to 1. This is the main difference between electrocatalysis ($|\Lambda| \leq 1$) and EPOC ($|\Lambda| \gg 1$).

A second parameter commonly used to describe the magnitude of electrochemical promotion is the rate enhancement ratio, ρ, defined from:

$$\rho \equiv r/r_o = (r_o + \Delta r)/r_o \qquad (22)$$

where r_o is the open-circuit unpromoted catalytic rate.

The maximum Λ and ρ values obtained in the experiments of Figures 15 and 16 are $\Lambda = 74\,000$ and $\rho = 26$ for C$_2$H$_4$ oxidation on Pt/YSZ (Figure 15) and $\Lambda = -17\,700$ and $\rho = 2.87$ for C$_2$H$_4$ oxidation on Pt/CaZr$_{0.9}$In$_{0.1}$O$_{3-\alpha}$ (Figure 16).

A noteworthy aspect of the galvanostatic (constant current I) rate transients depicted in Figure 15 is that the characteristic time, τ, required for the rate to reach 63% of its steady-state value is of the order of $2FN_G/I$:

$$\tau \approx 2FN_G/I \qquad (23)$$

where N_G (expressed in mol) is the metal catalyst surface area and F is Faraday's constant (96 460 C/mol). Thus, the parameter $2FN_G/I$ expresses the time required for the formation of a monolayer of O^{2-} species on the catalyst surface when O^{2-} is supplied at a rate $I/2F$ according to Faraday's law.

Similar is the situation when using proton conductors (Figure 16). The time constant of the catalytic rate transient is again of the order FN_G/I. These observations provided the first indications that EPOC is due to the formation and catalytic promoting action of a monolayer of ionic species migrating (i.e., spilling over) under the influence of the applied current from the bulk of the solid electrolyte to the metal/gas interface. This view has now been confirmed by a large number of surface science and electrochemical techniques.

As it turns out, these monolayers are overall neutral, because the promoting spillover ionic species (e.g., O^{2-}) is compensated by its image charge in the metal, thus forming adsorbed dipoles and an overall neutral double layer. This double layer, which resides at the catalytically active metal/gas interface, is termed "effective" double layer.

Electrochemical promotion can affect not only catalyst activity but also product selectivity. An example is shown in Figure 17 for the case of CO$_2$ hydrogenation on Ru/YSZ.[202] One observes that increasing catalyst potential causes a 4-fold increase in the rate of CO$_2$ methanation:

$$CO_2 + 4H_2 \rightarrow CH_4 + 2H_2O \qquad (24)$$
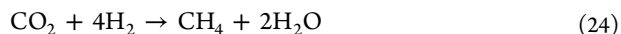
and at the same time a 2-fold decrease in the rate of the competing reverse water−gas shift reaction (RWGS):

$$CO_2 + H_2 \rightarrow CO + H_2O \qquad (25)$$

The selectivity to CH$_4$ increases from 42% to 82%.

Another example of selectivity modification is presented in Figure 18 for the isomerization of 1-butene to *cis-* and *trans-*2-butene on Pd/C using Nafion as the electrolyte.[23,205]
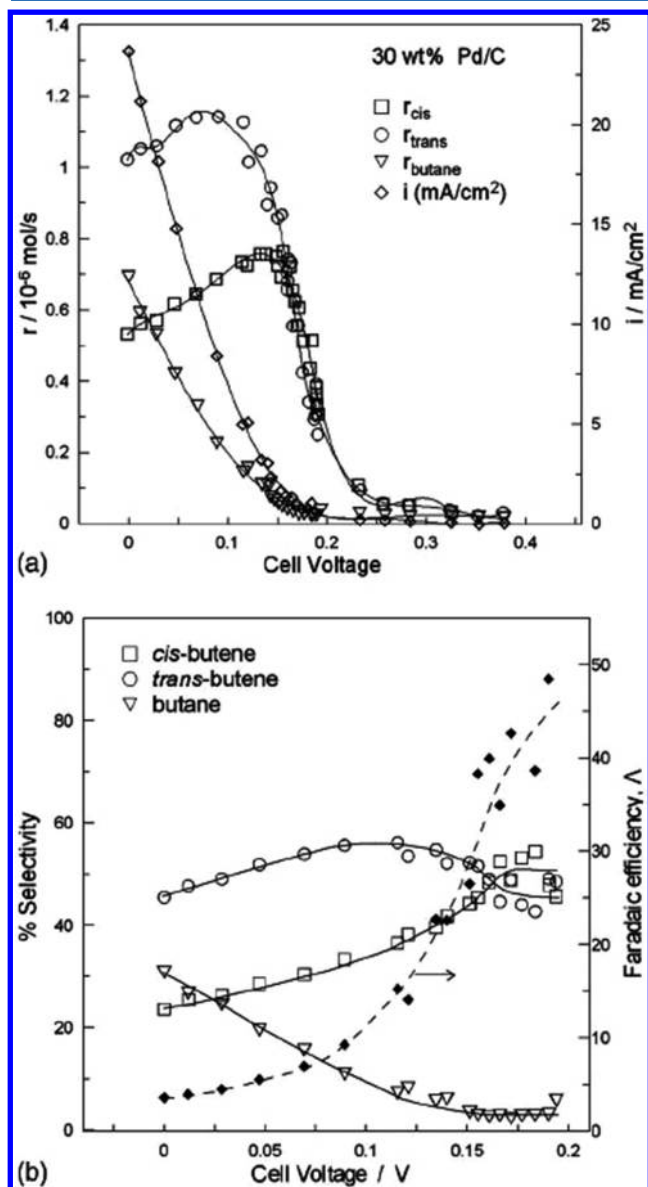
Figure 18. (a) Electrochemical promotion of an isomerization reaction. Steady-state effect of cell potential on the cell current, *I*, and on the rates of formation of *cis-*2-butene, *trans-*2-butene, and butane produced from 1-butene supplied over a dispersed Pd/C catalyst−electrode deposited on Nafion, a H^{+} conductor at room temperature. (b) Corresponding effect of cell potential on the selectivities to *cis-*2-butene, *trans-*2-butene, and butane and on the apparent Faradaic efficiency, Λ, defined as $\Delta r_{total}/(I/F)$. Thus, each proton catalyzes the isomerization of roughly 50 molecules of 1-butene to *cis-* and *trans-*2-butene. Reprinted with permission from ref 205. Copyright 2012 American Chemical Society.

Until recently,[206−208] more than 100 different catalytic reactions (oxidations, hydrogenations, dehydrogenations, isomerizations, decompositions, reformings)[23,202,205,209−212] have been electrochemically promoted on Pt, Pd, Rh, Ag, Au, Ni, IrO$_2$, RuO$_2$ catalysts deposited on O[2−] (YSZ), Na^{+} (β''-Al$_2$O$_3$),[213] K^{+} (β''-Al$_2$O$_3$),[214,215] H^{+} (CaZr$_{0.9}$In$_{0.1}$O$_{3−\alpha}$, Nafion, La$_{0.99}$Sr$_{0.01}$NbO$_{4−\delta}$), F^{−} (CaF$_2$), aqueous,[216,217] molten salt,[218] and mixed ionic−electronic (TiO$_2$,[219] CeO$_2$[220]) conductors.

Clearly EPOC is a general phenomenon, not limited to any particular class of conductive catalyst, catalytic reaction, or ionic support.

From a general point of view, both acronyms (EPOC and NEMCA) are used to characterize electrochemical activation of catalysis involving ions containing in the electrolytic support. However, the term NEMCA only refers to studies where the ionic promoting species can also take part in an electrochemical reaction (i.e., O[2−], H^{+}) while EPOC is a more general term and includes also promoting species such as K^{+} and Na^{+}.

4.1.2. Rate Dependence on Catalyst Potential. It is evident from Figures 19−21, but also from Figure 22, that upon varying the catalyst potential U_{WR} ("W" stands for the catalyst, which is the working electrode, and "R" stands for a reference electrode), there exist reactions where the rate increases with increasing catalyst potential and reactions where the rate increases with decreasing catalyst potential. In the former case, the reaction is termed electrophobic and is promoted by anion (e.g., O[2−]) supply to the catalyst. In the latter case, the reaction is termed electrophilic and is promoted by cation (e.g., Na^{+}, H^{+}) supply to the catalyst.

This is also shown by the steady-state results of Figure 19a and b.[201,221] One observes in these figures that over wide ranges of catalyst potential the catalytic rate varies exponentially with potential, that is:

$$\ln(r/r_o) = \alpha e \Delta U_{WR}/k_b T = \alpha F \Delta U_{WR}/RT \quad (26)$$

where *e* is the electron charge and α is a parameter, such that $|\alpha| \leq 1$ with $\alpha > 0$ for electrophobic reactions and $\alpha < 0$ for electrophilic ones.[23]

As shown in Figure 19c and d, two other types of *r* versus U_{WR} potential exist, that is, volcano type (Figure 19c), where the rate exhibits a maximum, and inverted volcano type (Figure 19d), where the rate exhibits a minimum upon varying the catalyst potential.[213,222]

4.1.3. Electrocatalytic Kinetics and the Prediction of |Λ|. The observed exponential variation in catalytic rate with potential (eq 26) is very similar to the high field approximation of the fundamental Butler−Volmer equation of electrochemistry,[3,23] that is:

$$\ln(I/I_o) = \alpha_j e \Delta U_{WR}/k_b T = \alpha_j F \Delta U_{WR}/RT \quad (27)$$

where α_j is the anodic (>0) or cathodic (<0) charge transfer coefficient ($|\alpha_j| \leq 1$), and I_o is the exchange current of the metal−electrolyte interface. The value of I_o is usually proportional to the length of the metal−gas−electrode interface called a three-phase boundary (tpb).[23]

Figure 20 shows the dependence of $\ln(r/r_o)$ and $\ln(I/I_o)$ on U_{WR} for the case of CO oxidation on Pt/YSZ.[223] The data are in good agreement with eqs 26 and 27. In view of eqs 26 and 27 and of the definition of Λ (=$2F\Delta r/I$ for O[2−] conductors (eq 21)), it follows that when $|\alpha| \approx |\alpha_j|$ and $\Delta r \gg r_o$, then:

$$|\Lambda| = 2F\Delta r/I \approx 2Fr/|I| \approx 2Fr_o/I_o \quad (28)$$

This equation can be used to estimate a priori the order of magnitude of the absolute values, |Λ|, of the Faradaic efficiency Λ for different reactions. Thus, eq 28 has been shown to provide a good qualitative estimation of the order of magnitude of |Λ| for different reactions on the basis of r_o and I_o only.[23,63] Equation 28 shows that polarizable (low I_o, thus low tpb length) metal−electrolyte interfaces are necessary for obtaining large Faradaic efficiency values.
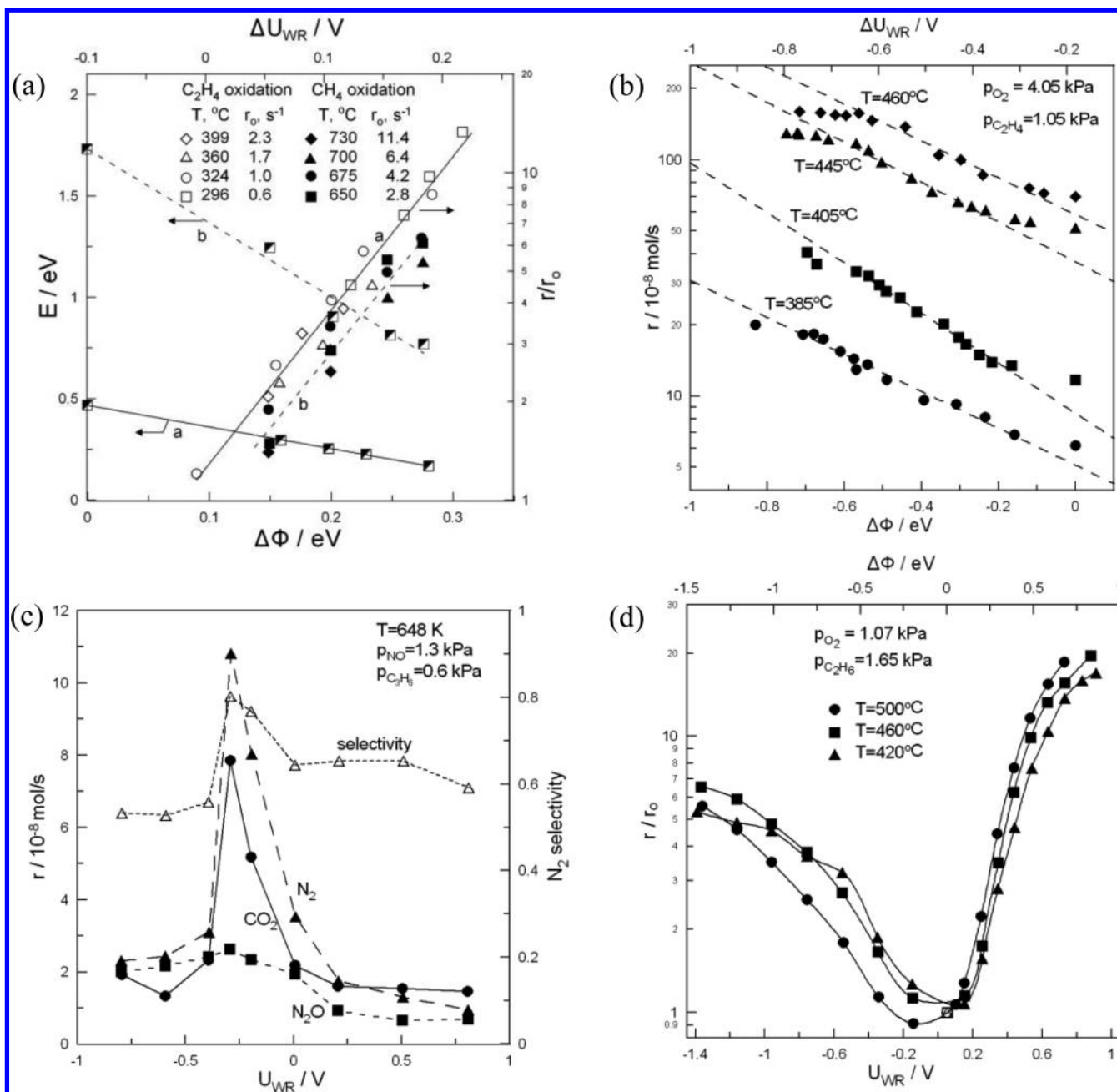
Figure 19. (a) Electrophobic behavior: Effect of catalyst potential and work function change $\Delta\Phi$ on the activation energy E and catalytic rate enhancement ratio r/r_o for C_2H_4 oxidation on Pt, p_{O2} = 4.8 kPa, p_{C2H4} = 0.4 kPa; and CH_4 oxidation on Pt, p_{O2} = 2.0 kPa, p_{CH4} = 2.0 kPa. Reprinted with permission from ref 221. Copyright 2012 Elsevier. (b) Electrophilic behavior: Effect of catalyst potential and work function change $\Delta\Phi$ on the rate of C_2H_4 oxidation on a Pt film deposited on $CaZr_{0.9}In_{0.1}O_{3-\alpha}$ H$^+$ conductor. Reprinted with permission from ref 201. Copyright 1996 Springer Science and Business Media. (c) Volcano type behavior: Effect of U_{WR} on the rates of CO_2, N_2, N_2O formation and on the selectivity to N_2 during NO reduction by propene on Pt/β''-Al$_2$O$_3$. Reprinted with permission from ref 213. Copyright 2012 Elsevier. (d) Inverted volcano behavior: Effect of catalyst potential and work function on the rate of C_2H_6 oxidation on Pt/YSZ. p_{O_2} = 1.07 kPa, $p_{C_2H_6}$ = 1.65 kPa. Reprinted with permision from ref 222. Copyright 2012 Elsevier.

4.1.4. Activation Energy Dependence on Catalyst Potential.

The above exponential catalytic rate dependence on potential (eq 26) is usually accompanied by linear variations of the catalytic activation energy, E, with potential, that is:

$$E = \alpha_E e\Delta U_{WR} \qquad (29)$$

where $|\alpha_E|$ is of the order 1, as was also shown in Figure 19a.[23]

Another example is shown in Figure 21 for the complete oxidation of propane on Pt deposited on Na-β''-Al$_2$O$_3$, a Na$^+$ conductor.[224] In addition to the linear decrease of E with increasing potential U_{WR} (Figure 21a), one observes the appearance of the compensation effect, that is, an exponential decrease in preexponential factor k with decreasing E (Figure 21b).

The observation that the catalyst potential plays as important a role in describing the electropromoted catalytic kinetics (eq 27) as in the case of electrocatalytic kinetics (eq 27) is noteworthy, as it strongly suggests a close relationship between U_{WR} and the
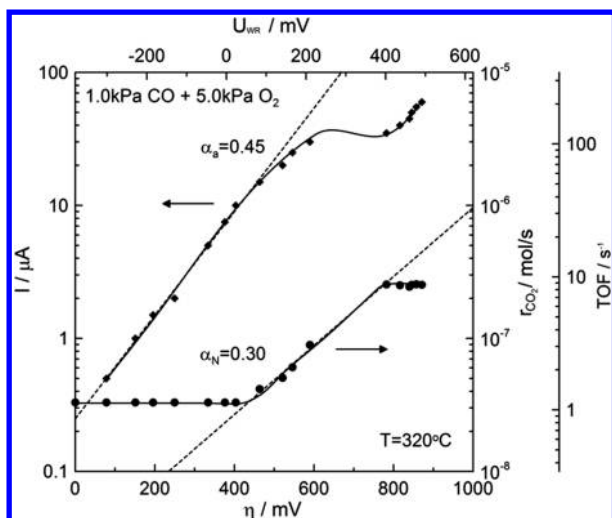
Figure 20. Effect of catalyst potential, U_{WR}, and overpotential, η, on the current and on the catalytic rate of CO oxidation on Pt/YSZ. Reprinted with permission from ref 223. Copyright 2012 Elsevier.
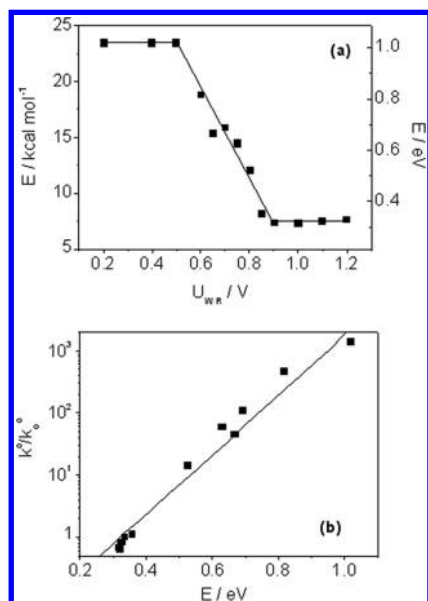
Figure 21. (a) Effect of catalyst potential U_{WR} on the apparent activation energy E. (b) Dependence of the apparent pre-exponential factor k° on the apparent activation energy E; $k_o^\circ = 2.3 \times 10^{-4}$ mol O s^{-1} corresponds to the sodium-clean catalyst. Conditions: $P_{O_2} = 1$ kPa, $P_{C_3H_8} = 0.2$ kPa. Temperature is varied between 320 and 440 °C.[224] Reprinted with permission from ref 224. Copyright 2007 Springer Science and Business Media.

state of the catalytically active metal−gas interface where the catalytic reaction takes place.

4.1.5. Work Function−Potential Equivalence under the Action of Spillover. The close relationship between the catalyst potential, U_{WR}, and the catalytically active metal−gas interface, where the catalytic reaction takes place, was first established from in situ work function measurements via the Kelvin probe technique[20,23,225] or via UPS.[23,226]

These measurements showed that over a wide range of temperatures (roughly 280−460 °C for YSZ, 180−420 °C for β''-Al$_2$O$_3$),[20,23,225] there is a one-to-one correlation between applied potential and change in work function at the metal−gas interface, that is:

$$e\Delta U_{WR} = \Delta\Phi_W \tag{30}$$

as shown in Figure 22. Furthermore, measurements utilizing two Kelvin probes simultaneously[225] showed that:

$$eU_{WR} = \Phi_W - \Phi_R \tag{31}$$

These results are identical to those obtained in aqueous electrochemistry when using emersed electrodes.[227] The existence of a neutral double layer at the metal−gas interface of both the working (W) and the reference (R) electrode results from eq 31 as follows. The potential difference between any two electrodes is given in general[3,23] by:

$$eU_{WR} = \bar{\mu}_R - \bar{\mu}_W = (\Phi_W - \Phi_R) + e(\Psi_W - \Psi_R) \tag{32}$$

where Ψ_W and Ψ_R are the Volta potentials (or vacuum levels in surface science terminology) of the gas-exposed surfaces of the two electrodes. From eqs 30−32, it follows:

$$\Psi_W = \Psi_R; \qquad \Delta\Psi_W = 0 \tag{33}$$

which in view of Gauss's law[23] implies $\Psi_W = \Psi_R = 0$, thus manifesting the existence of a neutral double layer at the metal−gas interface when eq 30 or 31 is satisfied experimentally.

The density of this double layer and thus the work function of the catalytic surface can be controlled via potential application according to eq 30. A necessary condition for this is that the temperature is high enough so that ion spillover/backspillover is fast and low enough so that desorption of the double layer to the gas phase does not take place.

These considerations dictate the above-mentioned temperature limits of validity of eqs 30 and 31. Outside these temperature limits or at very high positive or negative potentials, the double layer becomes unstable, and deviations from eqs 30 and 31 are observed[225,228] (Figure 22).

4.2. Investigations of the Origin of EPOC

As was already noted, eqs 30 and 31 lead unambiguously to eq 33, and the latter describes the formation of an overall neutral double layer at the metal−gas interface via the spillover of ions from the solid electrolyte to the catalytically active metal−gas interface (Figure 23).

The establishment of this double layer as well as kinetics of its creation and desorption have been studied by a variety of surface spectroscopic and electrochemical techniques.[23,208] These studies have provided strong evidence both for the migration (spillover) of promoting species from the solid electrolyte to the catalyst/gas interface and also for the sacrificial promoter model of EPOC when using O^{2-} conducting solid electrolytes such as YSZ.

4.2.1. The Sacrificial Promoter Mechanism. This mechanism of EPOC is based on the assumption that electrochemical supply of O^{2-} species (in the case of oxygen ionic conductors) on a catalyst surface already nearly saturated with normally adsorbed oxygen (e.g., the well-known O(2 × 2) adlattice on Pt(111)) forms a second more ionic and more strongly adsorbed species, denoted O$^{\delta-} - \delta^+$, which is overall neutral, as the charge δ^- is compensated by the image charge, δ^+, in the metal. The reaction leading to the formation of this species can be written as:

$$O^{2-}(YSZ) \rightarrow (O^{\delta-} - \delta^+) + 2e^- \tag{34}$$
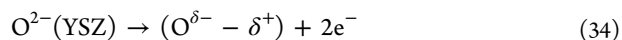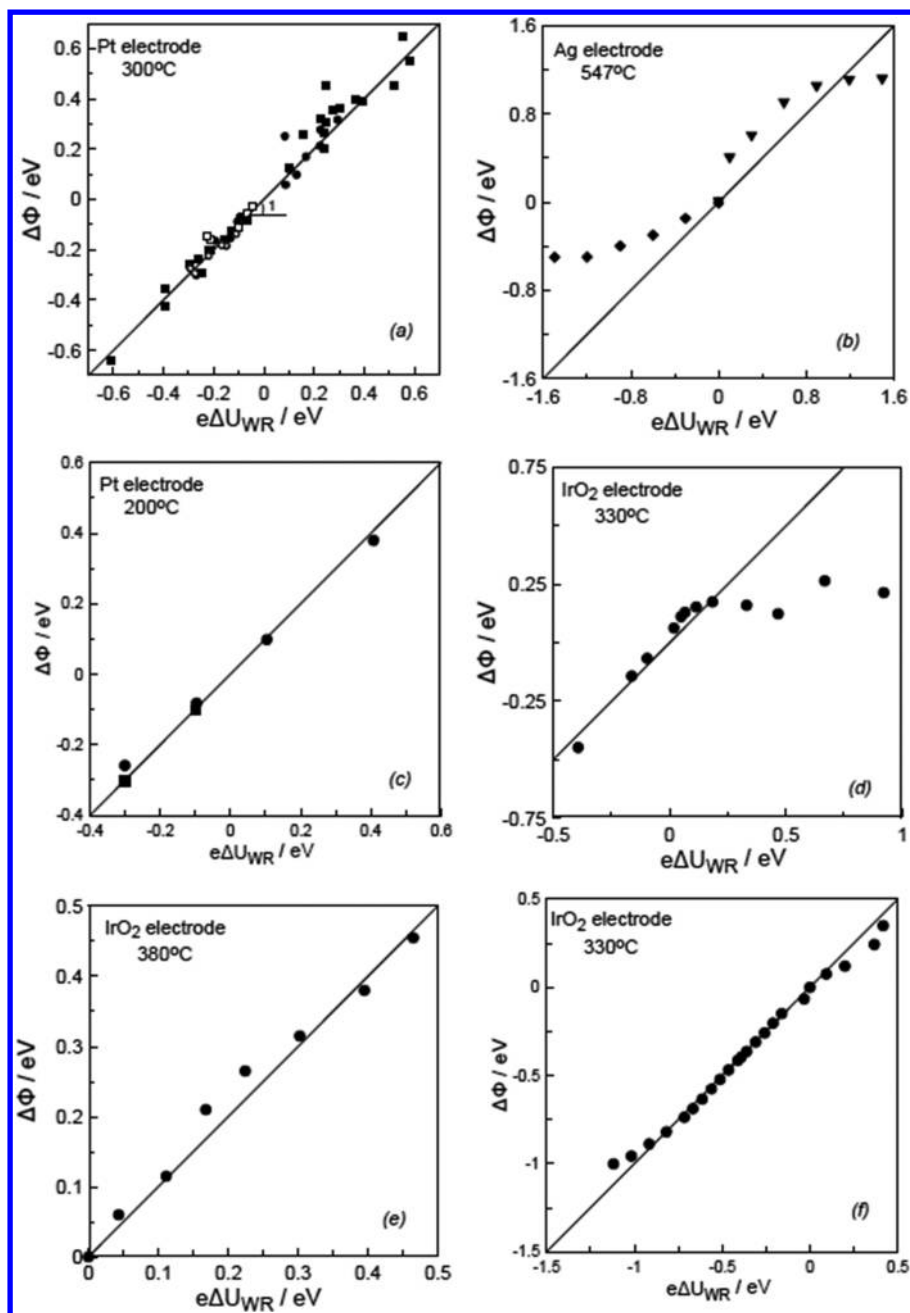
Figure 22. Effect of catalyst−electrode potential U_{WR} on the work function Φ of the gas exposed catalyst−electrode surface: (a) Pt/YSZ, $T = 300\ °C$ (squares), Pt/β''-Al$_2$O$_3$, $T = 240\ °C$ (circles); filled symbols, closed-circuit operation; open symbols, open-circuit operation, O$_2$, C$_2$H$_4$/O$_2$, and NH$_3$/O$_2$ mixtures. (b) Ag/YSZ, $T = 547\ °C$, (c) Pt/β''-Al$_2$O$_3$, $T = 200\ °C$, (d) IrO$_2$/YSZ, $T = 330\ °C$, air, (e) IrO$_2$/YSZ, $T = 380\ °C$, $p_{O2} = 15$ kPa, $p_{C2H4} = 5 \times 10^{-2}$ kPa, (f) IrO$_2$/β''-Al$_2$O$_3$, $T = 330\ °C$, air. Reproduced with permission from ref 225. Copyright 2012 The Electrochemical Society.

The spillover species O$^{\delta-}$ − δ^+ can act as a promoter for catalytic oxidations due to its repulsive lateral interactions with normally coadsorbed oxygen, O(ad), and its attractive lateral interactions with coadsorbed electropositive adsorbates, for example, carbonaceous species resulting from C$_2$H$_4$ or other hydrocarbon adsorption.

The mechanism is called "sacrificial promoter" mechanism because the promoting O$^{\delta-}$ − δ^+ species can also react with the oxidizable reactant, for example, C$_2$H$_4$, and thus has a finite mean residence time, τ_p, on the catalyst surface. This residence time is a factor of Λ larger than the residence time, τ_r, of the key reactant on the catalyst surface. It thus follows that when $\Delta r \approx r$, that is, for high ρ values, it is:[23]

$$\Lambda = \frac{\Delta r}{(I/2F)} = \frac{\text{TOF}_r}{\text{TOF}_p} = \frac{\tau_p}{\tau_r} \tag{35}$$

An experimental demonstration of eq 35 can be obtained from practically all published EPOC transients, as is shown by the example of Figure 24. This figure shows that Λ can be computed not only from its definition, that is, $\Lambda = \Delta r/(I/2F)$, but also from the ratio τ_p/τ_r or, equivalently, TOF$_r$/TOF$_p$. Thus, Figure 24 provides a straightforward proof of the validity of the sacrificial promoter mechanism.

Recently, Tsampas et al.[229] conducted isotopic labeling experiments for investigating the sacrificial promoter mechanism. The aim of this study was to operando distinguish the

T

dx.doi.org/10.1021/cr4000336 | *Chem. Rev.* XXXX, XXX, XXX−XXX
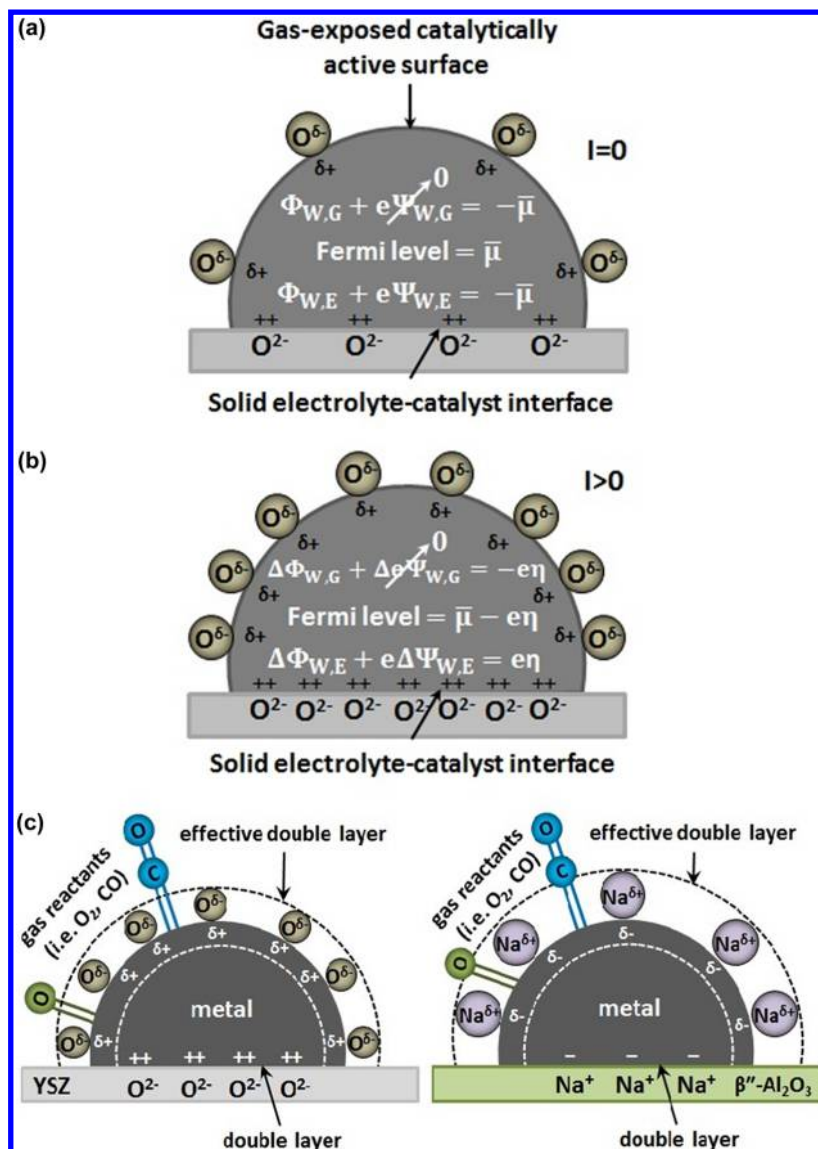
Figure 23. (a) Schematic representation of a metal crystallite deposited on YSZ and (b) of the changes induced in its electronic properties upon polarizing the catalyst–solid electrolyte interface and changing the Fermi level (or electrochemical potential of electrons) from an initial value $\bar{\mu}$ to a new value $\bar{\mu} - e\eta$. (c) Schematic representation of a metal electrode deposited on a O^{2-}-conducting (left) and on a Na^+-conducting (right) solid electrolyte, showing the location of the metal–electrolyte double layer and of the effective double layer created at the metal–gas interface due to potential-controlled ion migration (backspillover). The interaction is also depicted between the effective double layer and the adsorbed reactants during CO oxidation.

oxygen species coming from the solid electrolyte (promoting ionic oxygen) with those from the gas phase during an electrochemically activated catalytic process (at atmospheric conditions). To achieve this goal, a two-compartment tubular Pt/YSZ electrochemical catalyst with a three-electrode (Pt) configuration was utilized. The reaction compartment of the tubular Pt/YSZ catalyst was exposed to propane and isotopic oxygen, while the other compartment was fed with air for replenishing the electrolyte with normal oxygen ($^{16}O_2$). In this configuration, promoting ionic species reaction with propane will form $C^{16}O_2$, while propane combustion with oxygen coming from the gas phase will lead to formation of $C^{18}O_2$. Therefore, analysis of the reaction products can give an insight into mechanisms involved in electropromotion of propane combustion on Pt/YSZ.

Catalytic activity measurements, under positive polarizations (Figure 25), have confirmed that the oxidation of propane with gaseous oxygen can be strongly electropromoted ($C^{18}O_2$ production) with total Faradaic efficiencies up to 45, while the $C^{16}O2$ production can be only attributed to the (sub)Faradaic electrochemical oxidation of propane ($\Lambda \approx 1$).

Another important observation is the production of $C^{16}O^{18}O$. This latter was attributed to surface oxygen exchange, at triple phase boundaries, which seems to generate active oxygen species because no $^{18}O_2$ was detected in the gas phase and therefore desorbs from the surface. This $C^{16}O^{18}O$ production rate and then the oxygen exchange rate can also be electropromoted but to a lesser extent than that of $C^{18}O_2$ (Figure 25). These results suggest that the presence of ionic sacrificial promoting species onto the catalyst surface generates more reactive oxygen species coming from the gas phase, either directly adsorbed on Pt or through the YSZ support.

4.2.2. Temperature-Programmed Desorption (TPD). The use of TPD has clearly shown the existence of two oxygen

U

dx.doi.org/10.1021/cr4000336 | *Chem. Rev.* XXXX, XXX, XXX–XXX
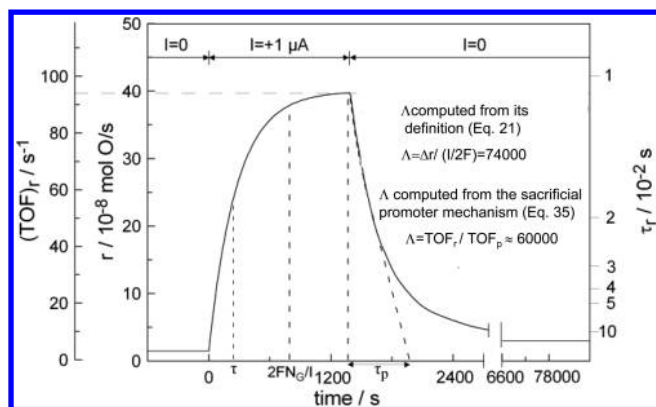
Figure 24. Demonstration of the sacrificial promoter mechanism of electrochemical promotion (eq 35) for the galvanostatic rate transient of Figure 15. The figure shows the definitions of the promoter lifetime, τ_p, and of the average reactant lifetime, $\tau_r(=(TOF)_r^{-1})$, and shows that the Λ value computed from eq 35, that is, $\Lambda = \tau_p/\tau_r$, is in good qualitative agreement with the Λ value computed from its defining eq 21, that is, $\Lambda = \Delta r/(I/2F)$. Adapted from Figure 15.

species under anodic polarization[230−232] (Figure 26, bottom). In these experiments, the sample is first exposed to O_2 and polarized at the operating temperature (350−400 °C), and then the polarization is stopped and the sample is cooled rapidly to room temperature followed by the TPD run.[230−232] The anionic backspillover species peak increases to saturation over a time period of $2FN_G/I$ and pushes, due to lateral repulsive interactions, the normally adsorbed (gas supplied) oxygen to a more weakly bonded, and thus more reactive, state (Figure 26).

These findings have been recently confirmed[233,234] also using gas supplied $^{18}O_2$ (Figure 27) and atmospheric pressure TPD under reaction conditions[235] (Figure 27). One observes in Figure 27 that indeed the strongly bonded promoting spillover oxygen species (peak β_3) is lattice oxygen (^{16}O), while the weakly bonded state (peak β_2) corresponds to gas supplied oxygen (^{18}O). One also observes that there is some oxygen isotopic scrambling leading to the appearance of an $^{16}O^{18}O$ peak, but this scrambling is not sufficient to obscure the very clear sacrificial promoter picture shown in Figures 27 and 28. The appearance of the two oxygen peaks has been also clearly manifested by using TPD in real conditions (Figure 28), that is, adsorption of oxygen at atmospheric pressure under polarization. Finally, cyclic voltammetry,[230] as shown in Figure 29, also evidenced an additional cathodic peak at low overpotentials, linked with strongly adsorbed backspillover ionic species.

Interestingly, the O_2 TPD spectrum of an electropromoted Pt film deposited on YSZ is practically identical to that obtained with nanodispersed Pt/YSZ catalysts[233,234] (e.g., Figure 30, which shows for comparison the $^{16}O^{18}O$ desorption spectra). This strongly indicates that the same promoting backspillover oxygen species is responsible for the effect of metal−support interactions (MSI) leading to enhanced activity for oxidation reactions when using supports with high ionic mobility (YSZ, CeO_2, TiO_2).[23] The only difference is that with the nano-dispersed powder Pt/YSZ samples, the weakly bonded oxygen state β_2 is also mainly formed by lattice oxygen,[233] apparently due to the very high three-phase boundary (tpb) length and concomitant fast thermal migration of lattice oxygen to the metal−gas interface.[23,233,234]

4.2.3. XPS and STM. The use of in situ XPS with an electrically polarized high-vacuum exposed Pt/YSZ catalyst
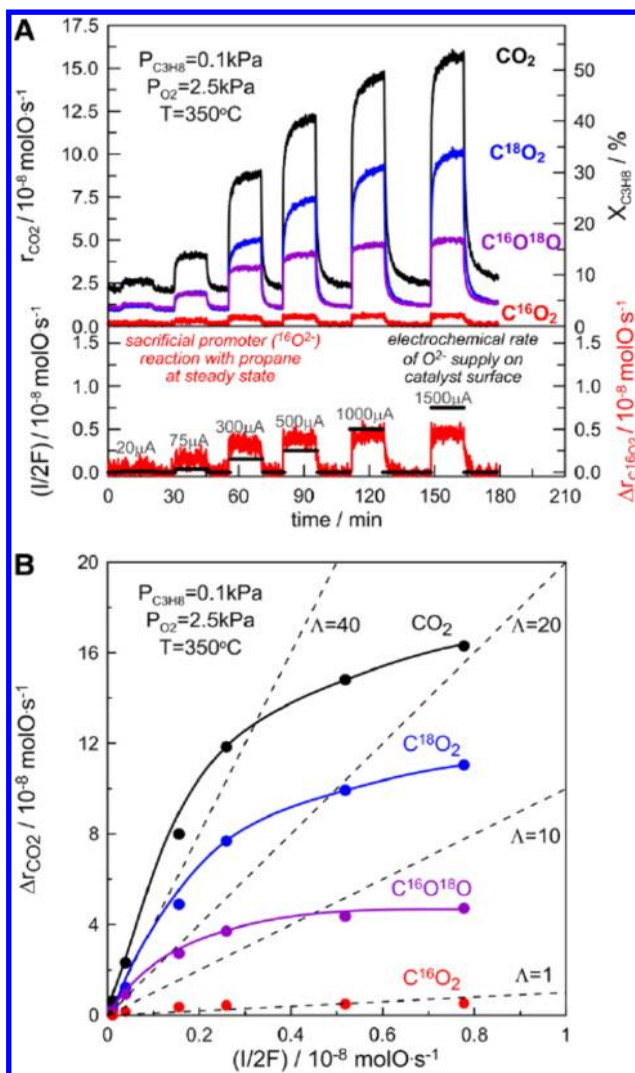
Figure 25. (A) Catalytic rate responses to step changes of various applied positive currents during C_3H_8 oxidation on Pt/YSZ. (B) Effect of electrochemical rate of O^{2-} supply on the CO_2 production rate increase. Dashed lines correspond to Faradaic efficiency values equal to 1, 10, 20, and 40. Reprinted with permission from ref 229. Copyright 2012 Elsevier.

played an important role in confirming the ion backspillover mechanism of electrochemical promotion and in providing useful information about the nature of the backspillover species. Some of the key results are shown in Figure 31 for the case of Pt/YSZ catalyst electrodes.[236]

Upon applying a positive potential to the catalyst electrode ($U_{WR} = 1$ V), the area of the O1s peak increases reversibly by 40%, positively confirming the backspillover of oxygen from YSZ onto the catalyst surface. At the same time, the O1s spectrum shifts to lower binding energies, developing a new peak centered at 528.8 eV. The low binding energy of this peak (vs ∼530 eV for normally adsorbed gas-supplied oxygen on Pt) shows the anionic character of the spillover oxygen species. Very similar results have been obtained by practically all groups who have used XPS to investigate NEMCA with YSZ supports,[226,237,238] but there has been some discussion[238] as to whether the O1s spectra under electrochemical promotion conditions show clearly the existence of two distinct oxygen species (gas supplied and spill-over).[226,237,238] The observed small differences in the XPS
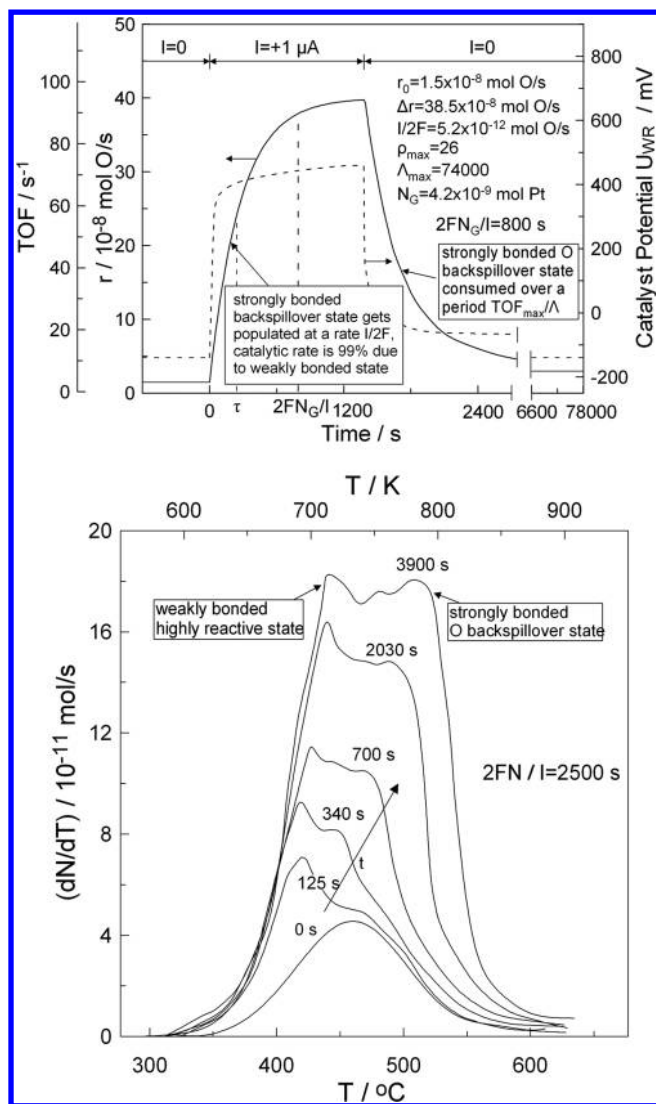
Figure 26. NEMCA and its origin on Pt/YSZ catalyst electrodes. Top: Transient effect of the application of a constant current on the rate, r, of C_2H_4 oxidation on Pt/YSZ (Figure 15 also showing the corresponding U_{WR} transient). Bottom: The O_2 TPD spectrum on Pt/YSZ after current ($I = 15\ \mu A$) application for various times t. N_G is the catalyst−electrode surface area expressed in moles of metal. Reprinted with permission from ref 230. Copyright 2012 American Chemical Society.

spectra can be safely attributed to oxygen coverage effects. This is because the backspillover oxygen species is known[23] to rapidly transform to normally adsorbed oxygen when the coverage of the latter is not near saturation.[23,226,236−238] The use of XPS has also confirmed the Na^+ backspillover mechanism of EPOC when using Na^+ conducting electrolytes.[239,240]

In addition to XPS, the reversible spillover−backspillover of oxygen between electropromoted Pt surfaces interfaced with YSZ has also been imaged ex situ using STM.[241] The latter technique has also been used to image the Na^+ backspillover on Pt(111) surfaces from β''-Al_2O_3 conductors.[239]

4.2.4. PEEM. The technique of photoemission electron spectroscopy (PEEM) is a particularly attractive and important one for spatially resolved work function measurements, as both the Kelvin probe technique and the UPS are integral methods with very poor (~mm) spatial resolution. The PEEM technique, pioneered in the area of catalysis by Ertl,[242−244] Block,[245,246] and Imbihl,[247] has been used successfully to study catalytic oscillatory
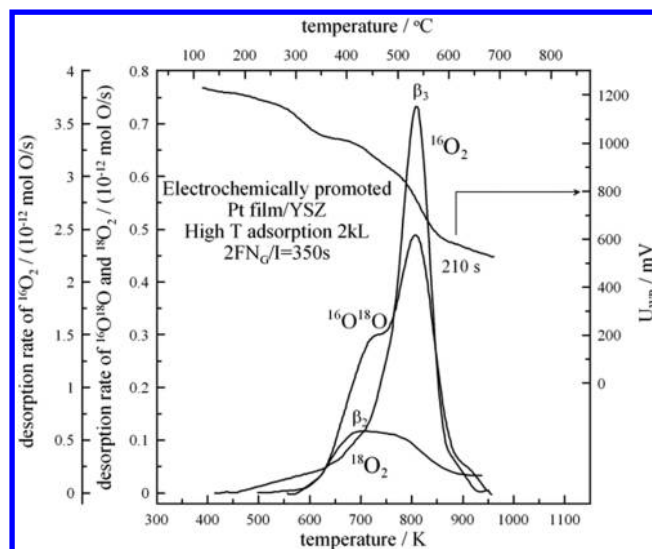
Figure 27. Oxygen thermal desorption spectra from an electrochemically promoted Pt/YSZ film, after gaseous $^{18}O_2$ adsorption at 275 °C at $P_{18O2} = 10^{-6}$ mbar for 45 min (exposure 2 kL) followed by electrochemical $^{16}O^{2-}$ supply for 210 s with a constant current of +15 μA. Also shown is the catalyst potential, U_{WR}, variation during the TPD run. Desorption was performed with linear heating rate, $\beta = 0.5$ °C/s. Reprinted with permission from ref 233. Copyright 2012 Elsevier.
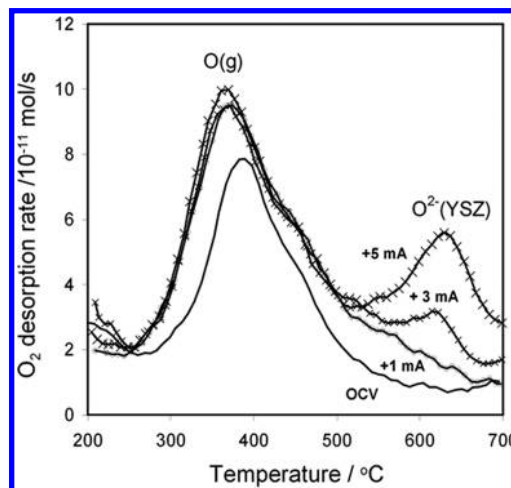
Figure 28. Atmospheric pressure O_2-TPD spectra after oxygen adsorption at 400 °C for 1 h under anodic polarization with different positive currents: +1, +3, and +5 mA. Operating conditions during oxygen adsorption: reactive mixture, O_2 1% in He; flow rate, 10 L h^{-1}.[235] Reprinted with permission from ref 235. Copyright 2007 Springer Science and Business Media.

phenomena on noble metal surfaces.[243−246] It was first employed to investigate NEMCA by Imbihl and co-workers.[247] Both porous Pt paste films and evaporated microstructured Pt electrodes prepared by microlithography were investigated. These microstructured electrodes were typically 500 Å thick (Figure 32).

Assuming that the local gray values, $G(x,t)$, of a PEEM image in Figure 32 are proportional to the photocurrent, I, and the relationship between I and work function, Φ, is given by the Fowler equation ($I \propto \Phi^2$) one can directly relate the changes in brightness with changes in work function. Figure 32 shows a Pt electrode (light) deposited on YSZ (dark). There are three circular areas of bare YSZ connected via very narrow bare YSZ
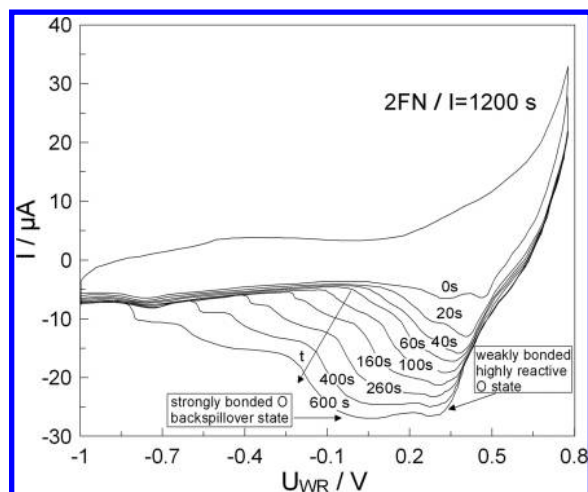
Figure 29. Cyclic voltammograms of Pt/YSZ after holding the potential at U_{WR} = 0.8 V for various times t. Reprinted with permission from ref 230. Copyright 2012 American Chemical Society.
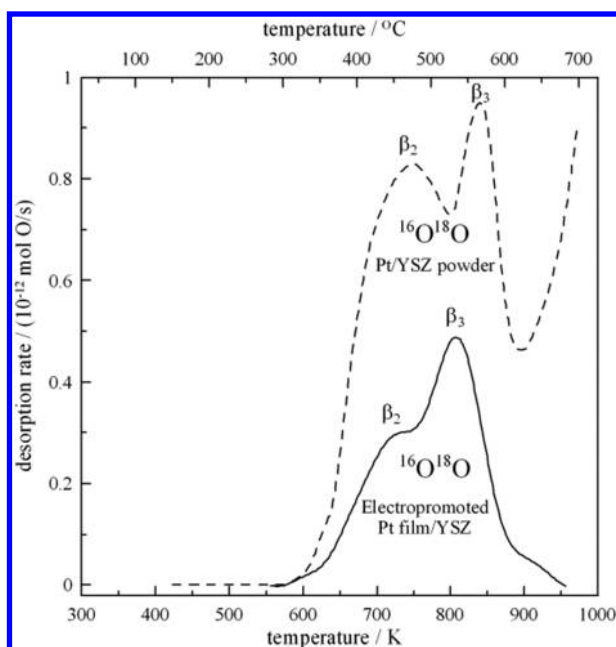
Figure 30. Comparison of oxygen thermal desorption spectra ($^{16}O^{18}O$ desorption) from nanodispersed Pt/YSZ catalyst (1%Pt/YSZ) and from Pt/YSZ film taken under UHV conditions. Desorption was performed with linear heating rate, β = 0.5 °C/s. Reprinted with permission from ref 233. Copyright 2012 Elsevier.

Figure 31. Effect of electrochemical O^{2-} pumping to a Pt/YSZ catalyst at 673 K on the O 1s XPS spectrum. Grounded working Pt/YSZ catalyst electrode. Reprinted with permission from ref 236. Copyright 2012 American Chemical Society.
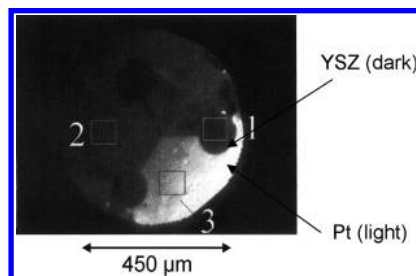
Figure 32. PEEM image of the Pt/YSZ microstructure showing three circular YSZ domains connected via channels, which are surrounded by a Pt film. Inside the window marked from 1 to 3 the digitized PEEM intensity has been integrated for the measurements displayed in Figure 33. Reprinted with permission from ref 247. Copyright 2012 Deutsche Bunsen-Gesellschaft für Physikalische Chemie.

channels. The rest of the surface is Pt. Note that the Fermi levels of the Pt film and of the YSZ solid electrolyte in the vicinity of the Pt film are equal. The YSZ, however, appears in the PEEM images much darker than the Pt film because YSZ has a negligible density of states at its Fermi level in comparison to a metal like Pt.

Following this analysis, Figure 33 shows the observed variations in PEEM intensity, and thus local work function, within three marked squares on a Pt/YSZ sample (1 is mostly on YSZ, 2 and 3 are on Pt) during electrochemical pumping (positive and negative polarizations) at T = 695 K. As shown in this figure, the local work function (which increases with decreasing local brightness) follows the imposed variation in U_{WR}. Increasing U_{WR} increases Φ, thus causing local darkening as expected, while decreasing U_{WR} decreases Φ, according to eq 30.

Therefore, PEEM has shown conclusively that Φ follows reversibly the applied potential and has provided the basis for space- and time-resolved ion spillover studies of electrochemical promotion.

With both types of electrodes, paste and evaporated films, Imbihl and co-workers[247,248] found good agreement with the work function–change potential–change equality (eq 30) previously obtained via Kelvin probe and UPS measurements.[23] They also found variations in the Fermi level of the YSZ upon potential application, which is an important and quite logical observation, because the Fermi level of YSZ in the vicinity of the metal electrode is pinned to the Fermi level of the electrode.[23,236]

Figure 34 shows clearly how the application of potential changes the brightness and thus the work function Φ of the grounded Pt catalyst–electrode (windows 2 and 3) and of the YSZ surface (window 1), in accordance with the above-discussed alignment (pinning) of the two Fermi levels.

Figure 33 shows the observed variations in local work function within the three marked squares (1 is mostly on YSZ, 2 and 3 are on Pt). As is shown in this figure and also in Figure 34, the local
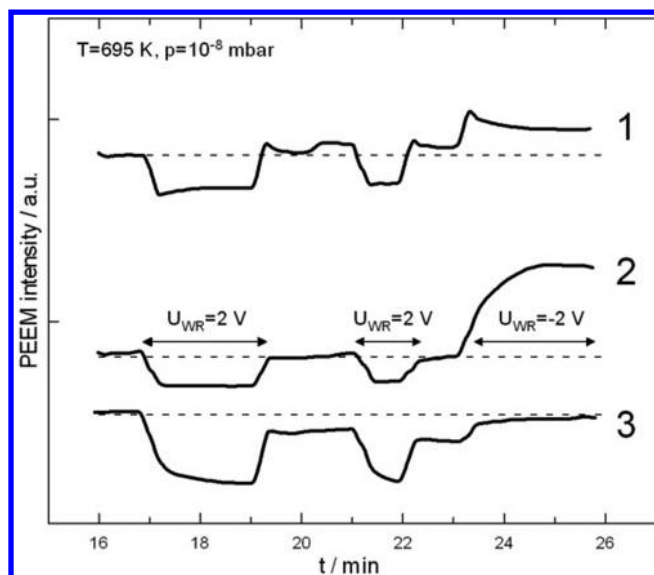
Figure 33. Local brightness variations in the three windows marked in Figure 32 during electrochemical pumping at T = 695 K. Reprinted with permission from ref 247. Copyright 2012 Deutsche Bunsen-Gesellschaft für Physikalische Chemie.
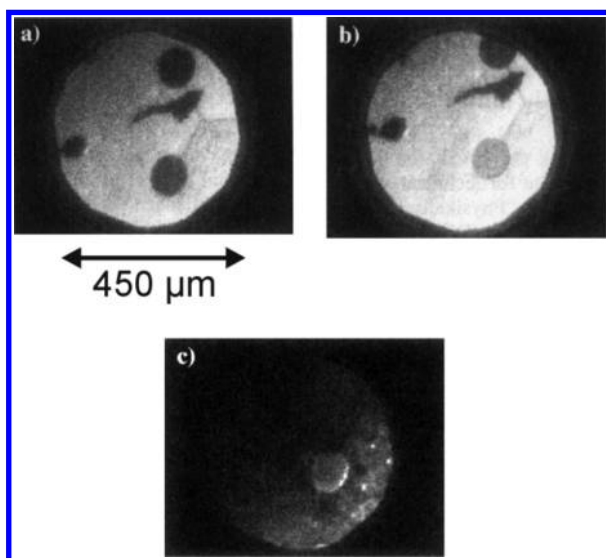
Figure 34. (a) PEEM image at U_{WR} = 0 V and T = 695 K. The irregularly shaped island close to the upper YSZ circle represents probably a defect in the Pt film. (B) Surface after electrochemical pumping with U_{WR} = −2 V for 2 min. (c) Surface during electrochemical pumping with U_{WR} = 2 V for 2 min at T = 737 K. Note the pronounced increase/decrease in brightness in (b) and (c) caused by the applied negative/positive potential on the grounded Pt electrode manifesting the pronounced decrease/increase in the work function Φ not only of the Pt surface but also of the YSZ solid electrolyte due to the Fermi level pinning at the Pt/ YSZ interface. Reprinted with permission from ref 247. Copyright 2012 Deutsche Bunsen-Gesellschaft für Physikalische Chemie.

work function (which increases with decreasing local brightness) follows the imposed variation in U_{WR}. Increasing U_{WR} increases Φ, according to eq 30, and thus causes local darkening (less electrons are emitted) as expected (Figure 34c). Decreasing U_{WR} decreases Φ, again according to eq 30 as expected (Figure 34b).

In that pioneering study,[247] it was not possible to obtain a time-resolved distribution of the backspillover oxygen species despite the fast, 40 ms, time resolution of the video-frames. If the spillover distance is 100 μm, this implies surface spillover oxygen diffusivities as high as 10^{-3} cm^2/s. If, however, microcracks exist in the film, which is very likely, then the spillover distance is much shorter, and thus much lower diffusivities would suffice to escape time-dependent detection.

The significant point is that PEEM, as is clearly presented in Figures 32−34, has shown conclusively that Φ follows reversibly the applied potential and has provided the basis for space- and time-resolved ion spillover studies of electrochemical promotion. It has also shown that the Fermi level and work function of the solid electrolyte in the vicinity of the metal electrode follow the Fermi level and work function of the metal electrode.

Subsequent PEEM work by Imbihl, Janek, and co-workers[249−251] has extracted a diffusion coefficient value of D_o = (9.2 ± 1.8)10^{-4} cm^2 s^{-1} at 670 K for the O spillover species, which is interestingly a factor of 10^3 higher than that of normally adsorbed oxygen on Pt(111).[252] More recently, the group of Janek has found an activation energy of 50 kJ/mol for the O spillover species.[251,253−255] An example of a PEEM observation of the spreading of spillover oxygen on a dense Pt electrode is given in Figure 35. Also, very recently Imbihl's group[256] has studied in detail the microstructure of sputtered Pt electrodes on YSZ.

4.3. Permanent/Persistent EPOC

One of the most interesting and potentially important from a practical viewpoint aspect of electrochemical promotion is the "permanent EPOC" effect first discovered and studied by Comninellis and co-workers at Lausanne.[200,257−262]

A typical example is shown in Figure 36, which depicts a galvanostatic EPOC transient during C$_2$H$_4$ oxidation on IrO$_2$.[257] The authors, in addition to monitoring the rate, r, and the catalyst potential, U_{WR}, were also in situ monitoring via a Kelvin probe the change, $\Delta\Phi$, in the IrO$_2$ surface work function, which at steady state nicely conforms to the fundamental eq 30. Upon positive current application, the rate of C$_2$H$_4$ oxidation increases by a factor of 2.2. The important aspect of the figure is that upon current interruption neither the rate nor Φ return to their initial open-circuit values (Figure 36). There is a permanent rate enhancement, accompanied by a permanent change in Φ. Comninellis and co-workers[257,258] defined a "permanent" rate enhancement ratio γ from:

$$\gamma = r_{per}/r_0 \tag{36}$$

which in the case of Figure 36 equals 1.5.

Some other examples of permanent NEMCA behavior were observed in the case of C$_2$H$_4$ oxidation on IrO$_2$−TiO$_2$ mixtures deposited on YSZ, the first NEMCA study utilizing an oxide catalyst (IrO$_2$) and in fact in contact with a mixed electronic− ionic conductor (TiO$_2$). These measurements of Nicole[263] provided the first basis for establishing the mechanistic equivalence of NEMCA and metal−support interactions.[264]

Permanent EPOC behavior has been also observed in the case of NO reduction by propene[265−267] or CO[268] in presence of O$_2$ on Rh/YSZ, a system of great technological interest. In the former case[265] (C$_3$H$_6$, T = 380 °C), ρ is 52 and γ is 6, but in the latter case (CO, T = 270 °C), ρ is 17 but γ is near 14. There is a very pronounced permanent enhancement of the Rh catalyst activity and selectivity. This could lead to practical applications utilizing EPOC during catalyst preparation.

What is the cause of permanent EPOC? Comninellis and co-workers had found strong evidence that it is due to the electrochemical creation and stabilization of a promoting superoxide on the catalyst surface or, more likely, due to

Y

dx.doi.org/10.1021/cr4000336 | Chem. Rev. XXXX, XXX, XXX−XXX
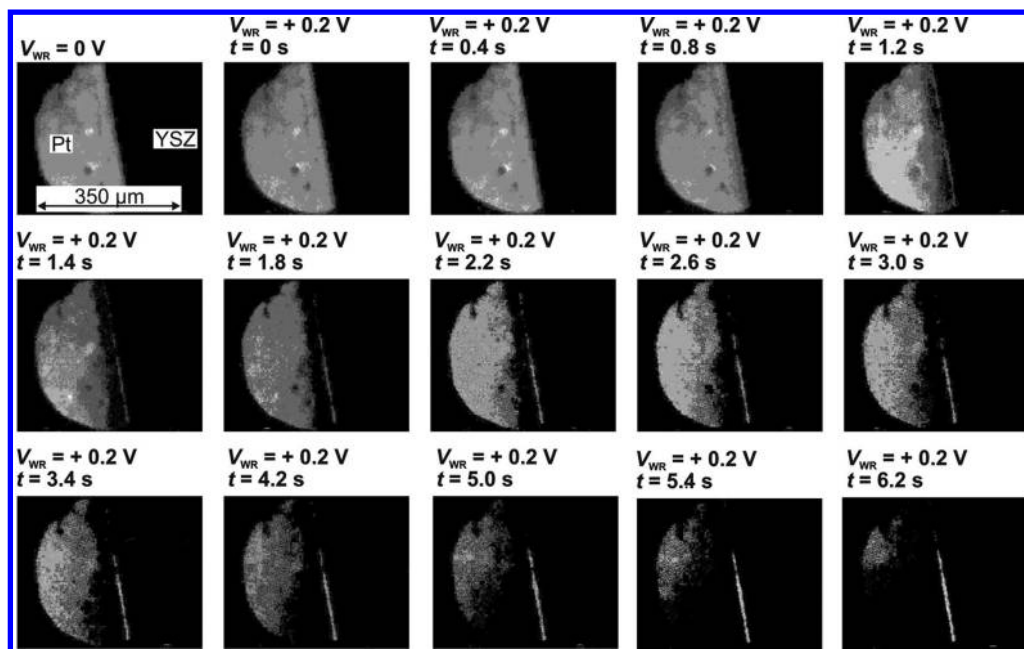
Figure 35. Sequence of PEEM images showing the spreading of spillover oxygen taken during anodic (U_{WR} = +0.2 V) polarization of a dense Pt electrode at T = 670 K (base pressure, p = 1 × 10^{-9} mbar). Oxygen adsorbed on platinum is observed as a dark area.[251] Reprinted with permission from ref 251. Copyright 2006 Wiley.
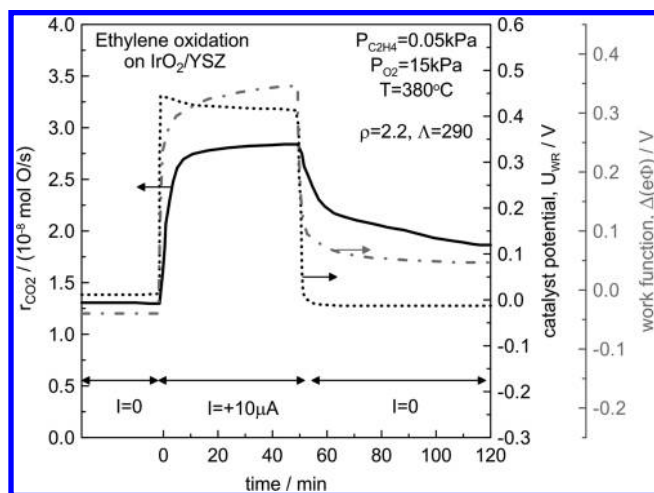
Figure 36. Transient effect of constant applied current (I = +10 μA) on the rate (r) of C_2H_4 oxidation on IrO_2/YSZ, on catalyst work function ($\Delta\Phi$), and on catalyst potential (U_{WR}). Conditions: T = 380 °C, P_{O2} = 15 kPa, and P_{C2H4} = 0.05 kPa. Reproduced with permission from ref 259. Copyright 2012 The Electrochemical Society.

promoting oxygen storage at the metal/YSZ interface. This is supported by the fact that permanent EPOC appears to be more frequent with metal oxides where the metal has multiple valence states, thus the ability to form several different oxides. It is also supported by the observation that the initial catalyst activity and work function can be restored only after prolonged catalyst exposure to the reacting gas mixture.[265,266]

For example, in the case of ethylene oxidation on Rh/YSZ,[268] it is possible that the initial state corresponds to surface Rh_2O_3,[268] the high activity EPOC state corresponds to O^{2-}-decorated reduced Rh,[268] and the permanent EPOC state corresponds to O^{2-}-decorated surface Rh_2O_3. This interesting subject is certainly worth further investigation. More recent work by Souentie, Comninellis, and co-workers[269] with Pt/YSZ catalysts

has provided strong support for the earlier hypothesis of Comninellis that permanent EPOC (or P-EPOC) is due to the storage of promoting $O^{\delta-}$ species at the Pt/YSZ interface.[269]

The mechanism proposed by Comninellis and collaborators is well supported by studies on thick Pt films, where the P-EPOC state disappears after some hours of current interruption depending on the anodic charge supplied (polarization time). After the release of all stored oxygen promoting species, the catalytic rate returns to its initial value. Therefore, the phenomenon is more persistent than permanent. However, long-term stable P-EPOC states were observed on thin sputtered Pt films interfaced with YSZ upon short anodic polarization times (few minutes).[270] This interesting result can be explained through the electrochemical formation of a thermodynamically stable interfacial PtO_x species at the Pt/YSZ interface, which it is not in contact with the reactive gas mixture. The P-EPOC effect, in this case, was only removed by applying cathodic currents, which decompose PtO_x species. This interfacial PtO_x layer increases the oxygen chemical potential gradient across the Pt/YSZ interface and then promotes the thermal migration of $O^{\delta-}$ promoting species from the electrolyte to the metal/gas interface. This effect can be analyzed as a self-driven EPOC mechanism as permanent effects observed in wireless NEMCA transients.[271]

Recent work by Mutoro et al.[272] using Pt(111)/YSZ(111) and Pt-FeO_x/YSZ(111) catalyst−electrodes prepared via pulsed laser deposition (PLD) has provided some interesting additional information regarding permanent EPOC.[272]

The main observations can be summarized as follows:

(1) Blocking Pt(111)/YSZ(111) films showed, as expected, no EPOC behavior.

(2) Partly porous Pt(111)/YSZ(111) films gave rise to reversible EPOC behavior (Figure 37).

(3) Pt−FeO_x/YSZ(111) films were the only that showed permanent EPOC behavior, which was accompanied by significant morphological changes (Figure 38).
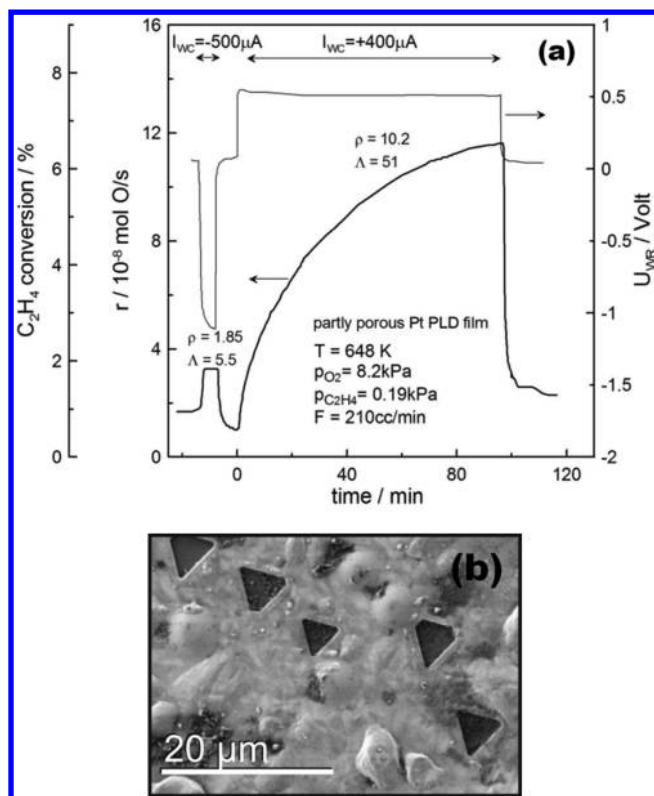
Figure 37. Galvanostatic transient experiments for a partly porous Pt PLD film (Pt3) at 648 K (a) and SEM image (b) of the film after the electropromotion experiments (dark areas are holes). Reprinted with permission from ref 272. Copyright 2012 Elsevier.

Figure 38. Transient effect of imposed currents for covering a Pt−Fe catalyst (PtFe3) at T = 648 K and SEM image of the catalyst film after the electropromotion experiments (b). Reprinted with permission from ref 272. Copyright 2012 Elsevier.

Thus, the extent of the observed reversible EPOC can be explained by morphology, that is, mainly by the length of the tpb. Its important role as the location where spillover oxygen is generated becomes apparent. The fact that iron-doped covering Pt films lead to permanent EPOC was unexpected, because iron-free covering films showed no measurable EPOC effect. The origin of this difference is yet unclear. An explanation for this could be that the presence of iron/iron oxide dopants either influences the microstructure or acts as a reservoir for oxygen.

4.4. Rules of Electrochemical and Chemical Promotion

As was already noted, the study of the electropromotion of more than 100 catalytic systems has shown that there are four main types of rate versus work function dependence (Figure 19):[23]

(a) electrophobic behavior, that is, $\partial r/\partial\Phi > 0$;

(b) electrophilic behavior, that is, $\partial r/\partial\Phi < 0$;

(c) volcano behavior, where r exhibits a maximum upon varying Φ;

(d) inverted volcano behavior, where r exhibits a minimum upon varying Φ.

Quite often, the same reaction can switch from one type of behavior to the other upon changing the catalyst or the experimental conditions (temperature, gas composition).

The first step in extracting the rules that govern the r versus Φ dependence of a catalytic system is to realize that in practically all bimolecular catalytic reactions one adsorbate, termed electron acceptor adsorbate and labeled A, has stronger propensity to accept electrons from the metal catalyst than the second adsorbate, termed electron donor adsorbate and labeled D, which has a stronger propensity for donating electrons to the metal.[23,273]

The characterization of an adsorbate on a metal surface as electron acceptor or electron donor−acceptor is not arbitrary but is strictly defined by whether its adsorption on the given metal surface causes an increase (A) or a decrease (D) in the work function, Φ, and thus on the potential (U_{WR}) of the metal surface. The potential, U_{WR}, is directly measurable under open-circuit or under electropromotion conditions in all experimental setups for the study of EPOC. In case that both reactant adsorbates are found to cause an increase or decrease in Φ, then the one causing the larger increase or the smaller decrease is termed A and the other is termed D.[23]

With these strict operational definitions of A and D, the following simple promotional global rules (G1−G4) have been extracted both for electrochemical and for chemical (ex situ) promotion:[23,273,274]

(G1) A reaction is electrophobic ($\partial r/\partial\Phi > 0$) when the reaction rate is positive order in D ($\partial r\partial p_D > 0$) and zero or negative order in A ($\partial r\partial p_A \leq 0$).

(G2) A reaction is electrophilic ($\partial r/\partial\Phi < 0$) when the reaction rate is positive order in A ($\partial r\partial p_A > 0$) and zero or negative order in D ($\partial r\partial p_D \leq 0$).

(G3) A reaction is volcano type when r passes through a maximum with varying p_A and p_D.

(G4) A reaction is inverted volcano type when the rate is positive order both in A and D.

An alternative way to express these rules is the following:

(G1) Strong adsorption of A causes electrophobic behavior.

(G2) Strong adsorption of D causes electrophilic behavior.

(G3) Strong adsorption of both A and D causes volcano-type behavior.

(G4) Weak adsorption of both A and D causes inverted volcano-type behavior.

These observations form the rules of EPOC and are summarized schematically in Figure 39a, in terms of the catalytic
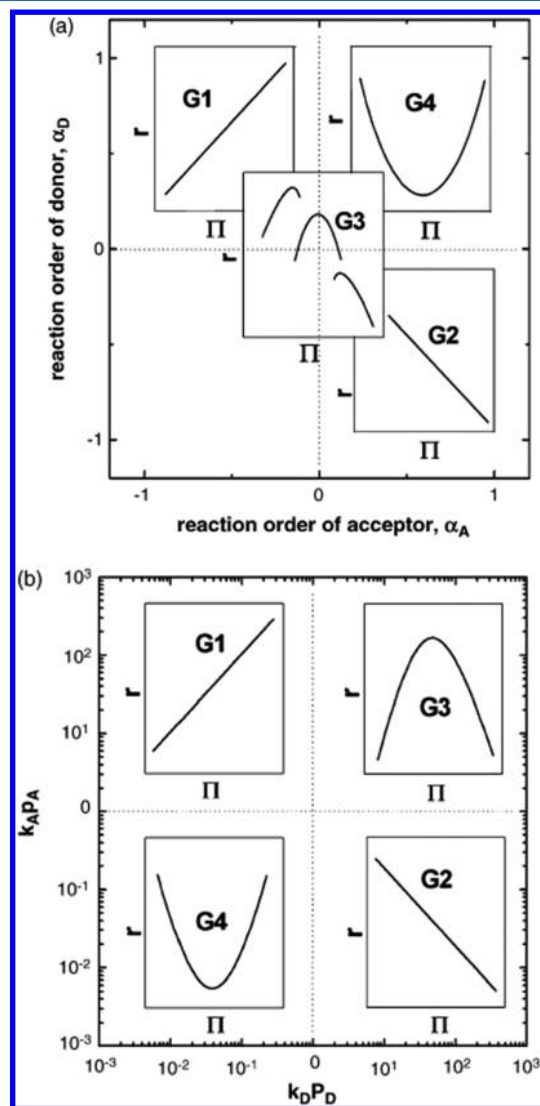
Figure 39. Effect of reaction orders a_A and a_D with respect to the electron acceptor (A) and electron donor (D) reactant on the observed rate dependence on changing catalyst work function F (electrophobic, electrophilic, volcano, and inverted volcano), and range of validity of the corresponding promotional rules G1, G2, G3, and G4. (b) Effect of the magnitude of adsorption equilibrium constants k_D, k_A and corresponding partial pressures p_D and p_A, of the electron donor and electron acceptor reactant, respectively, on the observed rate dependence on changing catalyst work function F (electrophobic, electrophilic, volcano, and inverted volcano) and range of validity of the corresponding promotional rules G1, G2, G3, and G4. Reprinted with permission from ref 274. Copyright 2012 Elsevier.

reaction rate orders with respect to the electron acceptor (A) reactant (a_A) and with respect to the electron donor (D) reactant (a_D). The reaction orders a_A and a_D are defined, as usual, from:

$$a_A = \partial \ln r / \partial \ln P_A \tag{37}$$

$$a_D = \partial \ln r / \partial \ln P_D \tag{38}$$

Figure 39b schematically shows the aforementioned rules in terms of the magnitude of the adsorption equilibrium constants k_D and k_A, multiplied by the corresponding reactant partial pressures P_D and P_A.

The above four rules are supplemented by three additional ones (G5−G7),[23,273] which address the case of monomolecular reactions, as well as the effect of electron donicity of the reactants on the magnitude of the observed promotional effect.

(G5) The above rules G1−G4 apply also when D and A are either electron acceptors or electron donors. In this case, D is always the stronger electron donor or weaker electron acceptor, and A is always the weaker electron donor or stronger electron acceptor.

(G6) A monomolecular reaction is electrophobic for an electron donor adsorbate and electrophilic for an electron acceptor adsorbate.

(G7) The maximum rate modification obtained under electrochemical promotion conditions increases for any fixed overpotential, or fixed promoter coverage, with increasing difference in the electron acceptor−electron donor character of the two reactants fundamental rules F1 and F2.

All of these rules can be derived[23,273] from the two fundamental rules F1 and F2, which simply state that at constant gas composition, the coverage of an electron acceptor (or donor) reactant decreases (or increases) with increasing work function Φ.

F1:

$$(\partial \theta_D / \partial \Phi)_{PA,PD} \geq 0 \tag{39}$$

F2:

$$(\partial \theta_A / \partial \Phi)_{PA,PD} \leq 0 \tag{40}$$

It must be noted that, depending on the experimental conditions (temperature, gas composition), the same catalytic reaction (e.g., C_2H_4 oxidation on Pt, or NH_3 synthesis on Fe) can switch between electrophobic, electrophilic, volcano, and inverted volcano behavior.[23,273] This is also clear from Figure 39a by noting that the reaction orders vary with temperature and gas composition, or from Figure 39b by noting that k_A and k_D are temperature-dependent, and, obviously, the products $k_A p_A$ and $k_D p_D$ are both temperature- and gas composition-dependent.

Thus, catalytic oxidations on metals are typically[23,273] electrophobic under fuel-lean conditions (i.e., high oxygen to fuel ratios), electrophilic under fuel-rich conditions (i.e., high fuel to oxygen ratios), volcano-type at low temperatures and intermediate O_2 to fuel ratios, and inverted volcano at high temperatures where both k_A and k_D are small (Figure 39b).

One should also note that, obviously, that all of the promotional rules discussed here are applicable under conditions of kinetic control and cannot be used under conditions of mass transfer or equilibrium limitations. The rules, in their present form, are also not applicable to cases where the promoter coverage is so high (e.g., more than ~0.2) that site blocking of the catalyst surface becomes dominant. These rules can clearly be used for promoter selection (eqs 39 and 40).

(1) In case of strong adsorption of A, electronegative promoters are needed.

(2) In case of strong adsorption of D, electropositive promoters are needed.

AB

dx.doi.org/10.1021/cr4000336 | Chem. Rev. XXXX, XXX, XXX−XXX

Table 2. Catalyst−Electrode Preparation Techniques Used for EP Studies

	catalyst−electrode preparation	catalyst−electrode/electrolyte system	reaction under study	P		$|\Lambda|$		ref
1	calcination of unfluxed organometallic pastes (Pt paste A1121, Engelhardt)	Pt/YSZ	C_2H_4 oxidation	55		3×10^5		23
2a	sputtering	Rh/YSZ/Pt and	C_2H_4 oxidation NO	1.45		77		275
	Rh and Pt on YSZ plates	Rh/YSZ/Au	reduction by C_2H_4	NO	1.33	1.65		
	Rh and Au on YSZ plates			CO_2	1.44	27		
2b	sputtering	Ir/YSZ	NO reduction by propene	N_2 yield 38−64%		Ir-40-HP		276
	Ir-deposited on YSZ			propene conversion 47−60%		N_2	570	
						C_3H_6	66	
3a	impregnation	Pt-A/YSZ	C_2H_4 oxidation	3		704		277
	Pt film preparation by thermal decomposition of a H_2PtCl_6 solution							
3b	impregnation	Pt/K-β''-Al$_2$O$_3$	CO oxidation	up to 11				279
	Pt film preparation by thermal decomposition of a H_2PtCl_6 solution							
3c	impregnation	Pt/Na-β''-Al$_2$O$_3$	NO reduction by propene	NO 1.4				278
	Pt film preparation by thermal decomposition of a H_2PtCl_6 solution							
4	nitrate impregnation	Ag/YSZ	C_7H_8 oxidation	1.6		13 000		280
	AgNO$_3$ deposition on YSZ							
5	spray deposition in C matrix	Pt−C/K-β''-Al$_2$O$_3$	CO and C_3H_6	CO	1.2			281
	Pt/C film via spraying on K-β''-Al$_2$O$_3$		oxidation	C_3H_6	4.8			
6a	electrostatic spray deposition	Pt/YSZ	NO reduction by	N_2	2.0	48		282
	Pt films deposition by ESD on YSZ, Pt(NH$_3$)$_4$(OH)$_2$(H$_2$O, or Pt(acac)$_2$		propene	CO_2	2.3			
6b	thermal decomposition technique, Ir precursor deposition on YSZ	IrO$_2$/YSZ	C_2H_4 oxidation	2.6				283
6c	Ru precursor deposition on YSZ	RuO$_2$/YSZ	C_2H_4 oxidation	11		170		284
			C_7H_8 oxidation	8		12		
7	pulsed laser deposition (PLD)	Pt(111)/YSZ(111)	C_2H_4 oxidation	5.8		42		272
	pulsed laser deposition (PLD)	Pt-FeO$_x$/YSZ(111)	C_2H_4 oxidation (permanent EPOC)	2.2		77		

(3) In case of volcano or inverted volcano type of kinetics, both electropositive and electronegative promoters can enhance the rate.[23]

The experimentally demonstrated validity of these rules underlines the importance of the electrostatic ("via the vacuum") interactions in heterogeneous catalysis.

4.5. Catalyst−Electrode Preparation

Practically all of the earlier studies of EPOC have utilized porous metal catalyst−electrode films prepared via the calcination of unfluxed organometallic pastes and, in particular, of Engelhardt Pt paste A1121 (Table 2).[23] However, in more recent years, a large variety of other techniques[209,272,275−284] have been used, including wet impregnation, electrostatic spray deposition, thermal decomposition, sputtering, and pulsed laser deposition (PLD) as shown in Table 2.

In general, the mode of preparation affects significantly the morphology of the catalyst film and thus the catalyst surface area and the length of the three-phase boundaries (tpb). Thus, as expected from, for example, eq 8, significant variations in Λ, but also in ρ, are observed, as shown in Table 2 Nevertheless, the basic character of electropromotion of a given catalytic system (electrophobic or electrophilic behavior) is in general not affected.

For instance, Lizarraga et al.[209] studied the propane combustion on Pt-sputtered deposited on YSZ and made a comparison with Pt-pasted films. They concluded that the sputtered films present higher Pt dispersion and significantly higher intrinsic catalytic activity. The performance in both systems was electrochemically promoted and followed electrophobic behavior; however, the sputtered films exhibit higher EPOC magnitude.

4.6. The Quest for EPOC of Dispersed Catalysts

A first and obvious utilization of EPOC is in the understanding of catalytic mechanisms thanks to the predictive rules defined in Figure 39. For a given reaction, the behavior of the catalytic performance upon polarization can give indications on the coverages of reactants, on the adsorption equilibrium constants, as well as on the reaction orders. In addition, EPOC experiments can be used to predict the impact of chemical promoters on the catalytic activity of classical supported catalysts. There have been already several demonstrations of this idea.[23,273,274] However, the ultimate direct utilization of electrochemical promotion in commercial reactors (in the chemical industry and in automotive exhaust catalysis) will depend on several technical and economical factors, among which the material cost minimization is considered as the most important. The main consideration here is the problem of efficient catalyst material utilization, which requires the use of thin (e.g., 10 nm thick) catalyst electrodes or dispersed catalysts.[23]

These anticipated technical challenges have been the subject of intensive research in this decade, and the latest progress in modeling, materials development, and reaction engineering has been impressive, pointing out that the main obstacles for practical utilization can be overcome.[252] In this section, we
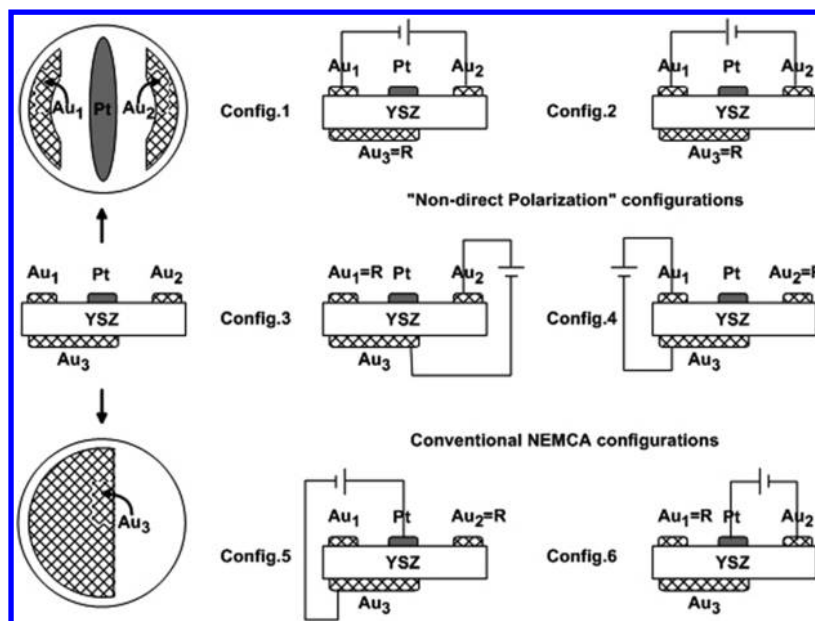
Figure 40. Pt and Au electrode geometry (left); corresponding electrical connection in four "bipolar configurations" (non-direct polarizations) and two conventional NEMCA configurations (right). Reprinted with permission from ref 285. Copyright 2012 Elsevier.

present a series of critical technological developments in EPOC studies toward material cost minimization.

4.6.1. Non-direct Polarization of Catalysts. The non-direct polarization configuration of the electrochemical catalyst (Figure 40) was the first significant improvement for scaling up electrochemical promotion in terms of catalyst dispersion. These configurations correspond to situations where the catalytic material is not used as an electrode, that is, is not connected to the external circuit.[285,286] The polarization is then applied between two electrodes, which are catalytically inert. This fact permits to facilitate the design of an EPOC reactor, because only two electrical wires become sufficient to polarize the two inert electrodes. Furthermore, the catalytic layer does not need to be electronically conductive, and thus nanoparticles or clusters of catalyst, electronically isolated, can be implemented. This can strongly improve the dispersion of the catalytic material. In addition, the EPOC reactor is a one-chamber cell because the inert electrodes and the catalytic layer can be exposed to the same reactive mixture.

Figure 40 shows the bipolar configuration that was first used by Marwood and Vayenas.[285] In their system, a Pt stripe was deposited between two gold electrodes onto a YSZ plate (Figure 44). In this configuration, the catalytic layer (film of Pt) is not directly polarized. Part of the catalytic material is polarized with a positive charge, while the other part is polarized with a negative charge. In this way, one part of the catalyst acts as an anode and the other as a cathode. There is no uniform catalyst work function as in the case where Pt is used as a working electrode and is directly polarized. The increase in the catalytic activity is the result of the simultaneous negative and positive polarization of the catalytic material. Therefore, reactions that exhibit both electrophobic and electrophilic behavior are the more appropriate to be used in this kind of bipolar configurations.[276] For instance, Marwood and Vayenas[285] and Balomenou et al.[276] have demonstrated that the rate of the ethylene catalytic combustion on the Pt stripe can be electropromoted by applying a current between the two gold electrodes.

Pliangos et al.[287] have devoloped a bipolar electrochemically promoted reactor using Rh as the catalytic material and have studied the reduction of NO by C_3H_6 in presence of oxygen. A small increase in catalytic activity was detected without direct electrical connections to the catalyst, proving that this type of reactor could be easier adapted to commercial exhaust units.

Xia et al.[288,289] have utilized this configuration to investigate CO oxidation over nanodisperded Pt particle supported on YSZ in vacuum. Figure 41A shows the size distribution of Pt nanoparticles. A SEM image of Pt nanoparticles is also shown (Figure 41A). The nanoparticles have a mean diameter value of 40 nm (Figure 41B). Figure 41C and D shows the comb like structure, where the gold electrodes supply the electric field for the polarization of the Pt clusters. This study has proven that nanodispersed Pt particles can be strongly electrochemically promoted using a non-direct polarization.

The non-direct polarization configuration was also studied in a monolithic solid electrolyte support in a plug flow reactor by Wodiunig et al.[290] Two symmetrical gold electrodes were deposited onto the external surface of the YSZ monolith (Figure 41E) to polarize the catalytic active phases (dispersed RuO_2/Au), which were deposited inside the channels. This configuration (Figure 41E) opens new opportunities for practical applications of EPOC.

It was shown[290] that the complete oxidation of C_2H_4 to CO_2 on RuO_2 catalyst dispersed on YSZ monoliths can be promoted by applying a potential or current, even at high C_2H_4 conversion. During a potentiostatic step of 30 V, an increase in the ethylene conversion from 36% to 50.5% was observed. The effect of different parameters was investigated, and it was found that the promotion is strongly affected by the cell potential, ethylene partial pressure, and temperature. The ethylene conversion increases with the applied cell potential reaching a plateau above 2 V, while a maximum Λ factor of 90 was observed at 5 V. The promoting effect passes through a maximum with increasing ethylene partial pressure and temperature. These maxima can be explained by the limitation of the rate of oxygen adsorption.
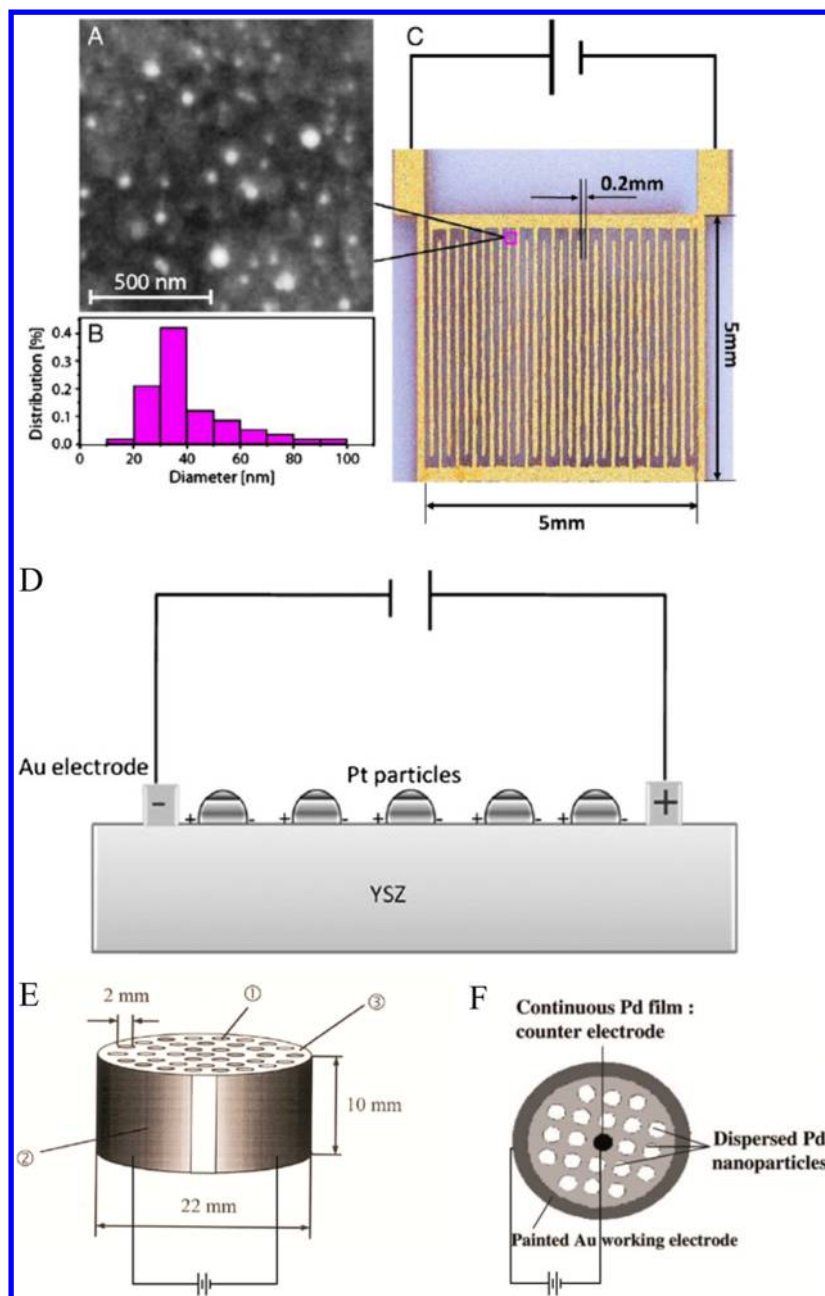
Figure 41. (A) SEM image (taken on YSZ between the Au electrodes) of dispersed Pt nanoparticles deposited by sputter deposition on YSZ followed by calcination at 973 K for 4 h. (B) Histogram of the particle size distribution. (C) The bipolar configuration of electrochemical cell showing the two Au electrodes and the polarized Pt particles deposited on YSZ solid electrolyte. (D) Cross section of the bipolar configuration presented in (C). (E) YSZ-monolith: (1) channels with RuO_2 catalyst film inside; (2) Au feeder electrodes; and (3) YSZ-monolith. (F) Right cross-section view of the honeycomb monolithic electrochemical catalyst, Pd/YSZ. Reprinted with permission from refs 288−292. Copyright 2012 Elsevier.

The promotion obtained in all of the EPOC studies using the non-direct polarization was notably lower than those obtained with the conventional monopolar configuration with a direct polarization on an electronically conducting layer of catalyst. This has been attributed to a current bypass and to the non-uniform work function distribution in the bipolar catalyst−electrode.

Wodiunig et al.[291] estimated the current bypass of a tubular cell with one bipolar element and from the current−voltage curves of a monolith with several bipolar elements. A current bypass of 11.5% was found in the tubular cell and a current bypass of 34% in the monolithic configuration, both at high cell voltages. The current bypass did not show an important influence on the

electrochemical promotion. A much more important influence was found due to the bipolar polarization of the catalyst. The non-uniform distribution of the work function led to a smaller increase of the ethylene conversion during the bipolar polarization than during the direct anodic polarization.

Roche et al.[292] validated the concept of EPOC by using, for the first time, Pd isolated particles dispersed on the channels surface of a YSZ dense honeycomb monolith for the deep oxidation of methane (Figure 41F). The transport of ions in the honeycomb monolith solid electrolyte was demonstrated by the electrochemical production of CO_2 and CO upon polarization in 5% methane in helium. Non-Faradaic effects were observed under

both anodic and cathodic polarization for methane oxidation with a maximum Faradaic efficiency of 47 (at −2 V).

A recent innovative design of non-direct polarizations, which combines an extremely lower Pt loading (around 5 $\mu g/cm^2$) with high dispersion (~15%), was recently proposed by Kambolis et al.[293] Pt nanoparticles were finely dispersed in the porosity of a mixed ionic electronic conductor (MIEC) thin film interfaced on a dense pellet of gadolinium doped ceria (CGO, $Ce_{0.9}Gd_{0.1}O_{1.95}$; see Figure 42), an O^{2-} ionic conductor.
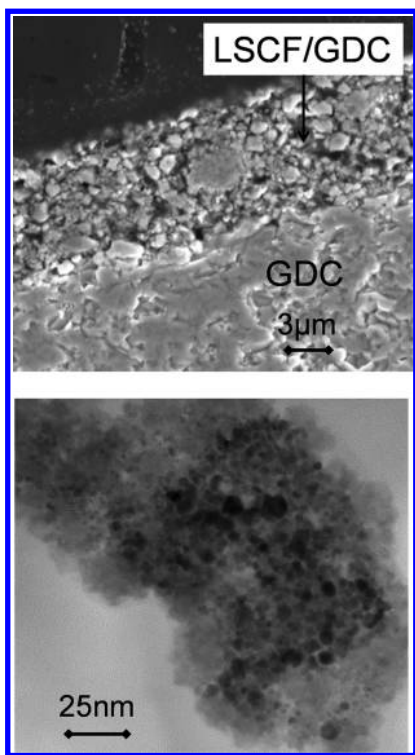
Figure 42. SEM (left) and TEM (right) images of the LSCF/CGO// CGO electrochemical catalyst.[293] Copyright 2012 Elsevier.

The electronic conductivity of the catalyst−electrode was not ensured by the Pt nanoparticles but by the MIEC film based on a composite between LSCF ($La_{0.6}Sr_{0.4}Co_{0.2}Fe_{0.8}O_{3-\delta}$) and CGO without noble metal. Pt nanoparticles, observed by transmission electronic microscopy, exhibited a size range between 3 and 20 nm, with average size of 8 nm, which is similar to that of conventional industrial Pt-supported catalysts.

Small positive polarization can strongly increase (38% enhancement) the catalytic performance of Pt nanoparticles for propane deep oxidation at low temperatures (200−300 °C) with apparent Faradaic efficiency values up to 85. Figure 43 shows the effect of small positive current application (200 μA) on the catalytic acitivity and on the catalyst potential. Rate enhancement ratio values of 1.35 and 1.38 were obtained at 307 and 267 °C, respectively, and the corresponding values were 19.4 and 4 for 307 and 267 °C, respectively.

This study clearly demonstrated that the catalytic activity of metallic nanoparticles dispersed in the porosity of a mixed ionic electronic conducting electrode can be strongly electropromoted without a direct polarization. Moreover, with this design it is possible to extend the reaction zone into a thick layer, thus increasing the specific surface area of the support (i.e., LCSF/ CGO composite).[293]
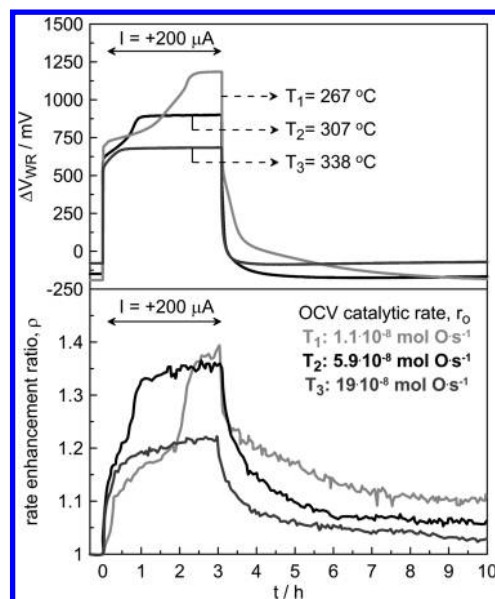
Figure 43. Impact of a positive current of +200 μA on the potential (top) and the rate enhancement ratio ρ (bottom) at 267, 307, and 338 °C. Reactive mixture: C_3H_8/O_2, 3880 ppm/2.2%. Reprinted with permission from ref 293. Copyright 2012 Elsevier.

4.6.2. EPOC in a Catalytic Membrane Reactor. Another approach for utilizing the concept of decoration of catalyst with ionic species and overcoming problems regarding electrical connections of EPOC was proposed by the group of Metcalfe.[271,294−296] This concept is based on the utilization of catalytic membrane reactors (Figure 44a) using a mixed ionic electronic conductor (MIEC) membrane.

During this kind of experiment, one of the reactor chambers is fed with the reaction mixture denoted as the reaction side, and the other is fed with pure He, H_2/He, O_2/He, or the reactive mixture denoted as the sweep side. By controlling the feed in the sweep side (Figure 44), a driving force for oxygen ions to migrate across the MIEC membrane and backspillover onto the catalyst surface can be established. Therefore, in this concept the driving force of migration is the oxygen chemical potential difference across the MIEC membrane and not the electrical polarization.

In this way, the reaction is promoted according to EPOC rules by the formation of a double layer of oxide ions on the catalyst surface. The electronic conductivity of the membrane material eliminates the need for an external circuit to pump the promoting oxide ion species through the membrane and onto the catalyst surface. Nevertheless, the catalytic layer exposed to the reaction mixture must be an electronic conductor. This excludes the utilization of non-percolated catalytic nanoparticles.

Figure 45 displays the example of ethylene oxidation on a Pt film interfaced with a dense MIEC pellet of $La_{0.6}Sr_{0.4}Co_{0.2}Fe_{0.8}O_{3-\delta}$.[271] The catalytic rate of the reaction side was monitored as a function of the sweep side feed. Initially both reaction and sweep chambers were fed with the reactive mixture (symmetrical sweep operation). When the sweep chamber was fed with O_2/He (high oxygen chemical potential), a noticeable increase in the catalytic activity in the reaction side chamber was observed. This operation is equivalent with positive polarization in convential EPOC studies with pure anionic solid electrolytes (O^{2-} conductors), as in both cases oxygen ions migrate through the membrane onto the catalyst surface promoting the reaction. Upon changing the feed from O_2/He

AF

dx.doi.org/10.1021/cr4000336 | Chem. Rev. XXXX, XXX, XXX−XXX
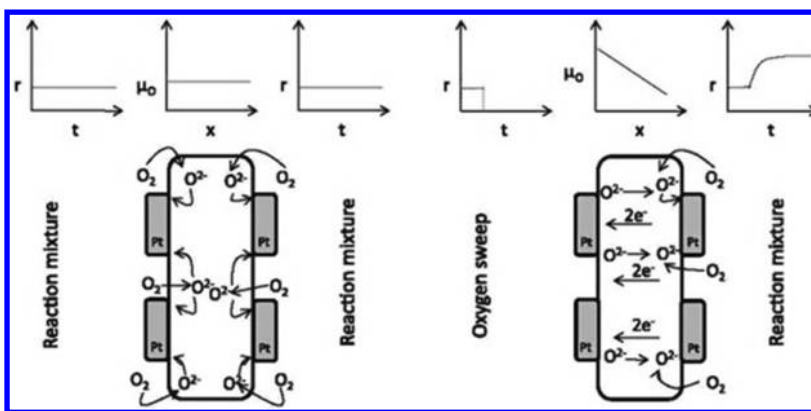
Figure 44. Schematic representation of the catalyst modification on a dual chamber MIEC pellet supporting a metallic catalyst. Left: Symmetrical operation; under identical reaction conditions, no oxygen chemical potential difference should exist across the pellet. Right: Operation under an oxygen chemical potential difference using an oxygen sweep; a driving force for the migration of oxygen across the pellet is created that increases the oxygen spillover from the bulk of the membrane and increases the reaction rate on the reaction side to a new steady-state value, while the reaction rate on the sweep side disappears. Reprinted with permission from ref 271. Copyright 2012 Elsevier.
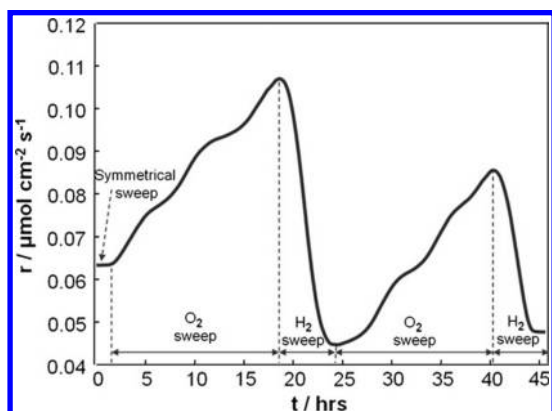
Figure 45. Reaction rate transient for a wireless experiment at 410 °C for two symmetrical O_2–H_2 sweep cycles. Experimental conditions: symmetrical sweep (both sides), $p(O_2) = 2.8$ kPa, $p(C_2H_4) = 1$ kPa, $f = 100$ mL min^{-1}; oxygen sweep (sweep side), $p(O_2) = 20$ kPa, $f = 100$ mL min^{-1}; hydrogen sweep (sweep side), $p(H_2) = 5$ kPa, $f = 100$ mL min^{-1}. Reprinted with permission from ref 271. Copyright 2012 Elsevier.

to the H_2/He in the sweep side, the catalytic activity decreases, showing the reversibility of the process. This operation is equivalent with one observed during negative polarizations in a classical EPOC experiment with pure anionic solid electrolytes (O^{2-} conductors).[296]

Poulidi et al.[271] have discussed the mechanistic origins of the phenomenon, and they stressed that an oxygen chemical potential difference across the membrane can modify both the local and the remote spillover processes on either side of the membrane. Under the influence of an oxygen chemical potential difference across the membrane, the reaction side of the catalyst becomes the receiver or the donor (depending on the sign of the oxygen chemical potential difference) of promoting oxygen species via the remote spillover process. However, the imposed oxygen chemical potential difference across the membrane may not only affect remote spillover but also the local spillover. The migration of ionic oxygen species through the membrane is very slow resulting in a prolonged operation time period to promote the reaction (in comparison with classical EPOC experiments upon polarization). The most important advantage is that this

design can be utilized to design EPOC reactors without any electrical connections.

4.7. Recent EPOC Studies

This section summarizes recent findings in the EPOC field, which are focused on catalytic processes improvement mainly in terms of activity. They are classified according to the nature of ions containing in the solid electrolyte, which is governing the EPOC behavior.

4.7.1. New Findings with Oxygen Ionic Conductors.

The recent advances related to the use of oxygen ion conductors in EPOC studies are presented in this section. This family of electrolytes appear to be promising because it is composed of ionic conducting ceramics, which are chemically and thermally stable in a wide temperature range and in both oxidizing and reducing atmospheres. In addition, the oxygen ions tank of these ceramics can be easily replenished if the investigated chemical reaction involves oxygen or water.

4.7.1.1. Oxidation of Hydrocarbons. Combustion of alkanes is the most intensively studied family of oxidation reactions, first because it is related to clean energy production and second because effective catalysts (noble metals) and their activity temperature window are suitable for the O^{2-} ionic conductivity level of ceramics such as YSZ (Figure 8). EPOC of methane deep oxidation has been extensively investigated during the past few years over a wide temperature window (250–600 °C) using Pd films deposited on YSZ with organometallic paste or by wet impregnation.[297–300] In the temperature range 470–600 °C and under oxidizing conditions, the catalytic activity of the impregnated Pd film on YSZ for methane oxidation can be increased over 160% under positive polarization.[297] Even in excess of oxygen and at lower temperature (320 °C), EPOC can affect the catalytic oxidation of methane when a small concentration of ethylene is cofed in the reaction mixture. Values for the rate enhancement ratio, ρ, for CH_4 consumption of ~18 with apparent Faradaic efficiencies of ~1400 were reported (Table 3).[300] When a CeO_2 interlayer was added between the Pd impregnated catalyst and the YSZ electrolyte, high open-circuit catalytic activity was achieved (2-fold increase in methane conversion at 400 °C), but further improvement in the activity under polarization was not observed.[299]

Roche et al.[301] investigated the same reaction on Pd films deposited by physical vapor deposition (PVD) on YSZ. Very thin layers of Pd were achieved between 11 and 75 nm. The impact of

Table 3. Recent EPOC Studies on Alkane Oxidation

electrochem catalyst	preparation technique	reactants	T, °C	EPOC behavior	unpromoted catalytic activity	ρ	Λ	P, $\mu W\,cm^{-2}$	ref
Pd/CeO$_2$/YSZ	wet im-pregn	P_{O2}/P_{CH4} = 3	560	electrophobic	CH$_4$ conversion 1% at 560 °C	5.6	764	24	298
Pd/YSZ pre-treated in C$_2$H$_4$/O$_2$	wet im-pregn	P_{O2}/P_{CH4} = 3.1	320−450	electrophobic permanent EPOC at high temp	CH$_4$ conversion 10% at 400 °C	1.7	63	100	299
Pd/YSZ	wet im-pregn	1.3% CH$_4$, 0.3% C$_2$H$_4$, 4% O$_2$	320−350	electrophobic	CH$_4$ conversion 0.3% at 330 °C	19	1400	3	300
Pd/YSZ	phys vapor depos	P_{O2}/P_{CH4} = 5	500−600	electrophobic	CH$_4$ conversion 0.8% with 11 nm thick film at 500 °C	2.6	258	52	301
Rh/YSZ	orgmet paste	P_{O2}/P_{CH4} = 1.1	350−550	electrophobic poisoning permanent EPOC observed after cathodic polarization	CH$_4$ conversion 2.6% at 430 °C	3	170	191	302
Rh/YSZ	orgmet paste	P_{O2}/P_{CH4} = 2	350−550	electrophobic poisoning permanent EPOC observed after cathodic polarization	CH$_4$ conversion 2% at 420 °C	3	100	134	303
Pt/YSZ	orgmet paste	P_{O2}/P_{C3H8} = 1	350−500	inverted volcano	pretreatment for >72 h under the reaction mixture at 550 °C led to very poor catalytic activity due to carbon depos	600	1200	4	203
		P_{O2}/P_{C3H8} = 3	350	inverted volcano		1400	180	∼400	203
Ag/YSZ	orgmet paste	P_{O2}/P_{C3H8} = 1	350−500	electrophobic	TOF = 3 × 10^{-4} s^{-1} at 500 °C	3.5	7	∼500	304
Pd/YSZ	orgmet paste	P_{O2}/P_{C3H8} = 1	350−500	inverted volcano	TOF = 8 × 10^{-3} s^{-1} at 500 °C	1.02	0.9	∼250	304

the polarization on the methane conversion was investigated between 500 and 600 °C to get sufficient activity under open-circuit conditions. It was found that the catalytic activity can be in situ tuned under anodic polarization (thus supplying oxygen ions at the catalyst surface). An example of these experiments is given in Figure 46. A current of +100 μA was applied at 500 °C to the catalyst, leading to a sharp increase in the conversion of methane from 0.8% to 2.1% (183% of conversion gain), with a Λ value of 258 demonstrating the ability of these catalysts to be electro-promoted (Table 3).

Methane deep oxidation was also investigated on Rh (pasted)/YSZ electrochemical catalyst[302] in the temperature range of 350−550 °C. It was found that the effect of electropromotion decreases with increasing partial pressure of oxygen and temperature. Under reducing conditions at 430 °C, positive current application caused a 3-fold increase in the catalytic rate, while the Faradaic efficiency was 170 (Table 3). Negative current application caused a 57% decrease in the catalytic rate, and a permanent poisoning effect was observed after negative current interruption attributed to the formation of a surface oxide layer.

The application of EPOC in the propane oxidation also received attention recently.[203,303,304] Bebelis and Kotsionopou-los[303] studied EPOC of propane combustion on Pt/YSZ and Rh/YSZ electrochemical catalysts (prepared by organometallic paste painting) at 425−520 °C and under substoichiometric O$_2$ to propane ratios. Inverted volcano behavior was observed because application of either positive or negative polarization resulted in non-Faradaic increase of the catalytic rate, by up to a factor of 4 in the case of Rh and of 1350 for Pt. Figure 47 shows the effect, obtained with the Pt/YSZ electrochemical catalyst at 480 °C, of a

Figure 46. Effect of application of +1 V potential on the methane conversion at 500 °C. Reactive mixture: CH$_4$/O$_2$ 2%/10%. Total flow rate: 10 L h^{-1}. Electrochemical catalyst: Pd (PVD, 10 nm-thick)/YSZ.[301] Reprinted with permission from ref 301. Copyright 2008 Springer Science and Business Media.

Figure 47. Catalytic rate, turnover frequency, rate enhancement ratio, Faradaic efficiency, and catalyst potential response to a step change in applied positive current. T = 480 °C; feed composition, P_{O2} = 4.7 kPa, P_{C3H8} = 1.4 kPa; flow rate, 483 cm^3 (STP) min^{-1}. Reprinted with permission from ref 303. Copyright 2012 Elsevier.

constant positive current on the catalytic rate of propane oxidation, turnover frequency (TOF), as well as on the parameters ρ and Λ and catalyst potential. Upon current application, the rate increases to a value that is 1350 times higher than its open-circuit value, while this increase is 141 times larger than the rate of O^{2-} supply to the catalyst.

Kokkofitis et al.[203,304] studied the case of electrochemically promoting propane oxidation at 350−500 °C under reducing conditions on Pt, Pd, and Ag catalyst−electrodes paste deposited on YSZ (Table 3). Inverted volcano type of EPOC was observed with Pt. At positive potentials, the intrinsic reaction rate can be enhanced by up to a factor of 1400, which corresponds to the maximum ρ value reported in EPOC literature.[203] On the other hand, on Pd, the phenomenon was sub-Faradaic (Λ values below unity). A moderate NEMCA behavior was reported on Ag, where the catalytic rate was increased only under negative polarizations (electrophilic behavior).[304]

Combustion of traces of volatile organic compounds (VOCs) at low temperatures for air cleaning is also a challenge for the catalysis community. EPOC could be used to increase the performance of noble metals to achieve catalysts effective for domestic applications. EPOC on toluene combustion has been carried out at 400−500 °C using RuO_2 films pasted on YSZ.[283] Promotional effects were found for both anodic and cathodic polarization, enhancing the rate of toluene oxidation by factors of 8 and 4, respectively. These effects were non-Faradaic demonstrating that EPOC could be used as well in this field.[283] The same reaction was electropromoted at lower temperatures (300−330 °C) using Ag films impregnated on YSZ.[280,305,306] Toluene conversion into CO_2 and H_2O on such a catalyst can be also significantly electrochemically promoted (ρ = 5.3 and Λ = 9600) upon negative polarizations, that is, oxygen removal from the catalyst surface, and this promotional effect increases with the temperature. The EPOC behaviors strongly depend on toluene and oxygen concentrations. Upon increasing the toluene concentration, ρ decreases while Λ shows a volcano type behavior. When varying the oxygen concentration in the reactants steam, an optimum oxygen concentration of ~2% was observed where ρ is maximized, while Λ monotonically decreases with oxygen concentration.[280,305,306]

4.7.1.2. CO_2 Hydrogenation. Elimination or valorization of CO_2 is a crucial objective to limit CO_2 emissions responsible for the global warming. During the last five years, the concept of EPOC has been applied to implement gas-phase CO_2 hydrogenation in presence of H_2. Theleritis et al.[202] recently used Ru/YSZ electrochemical catalysts for electrochemically promoting this reaction at 200−300 °C. As d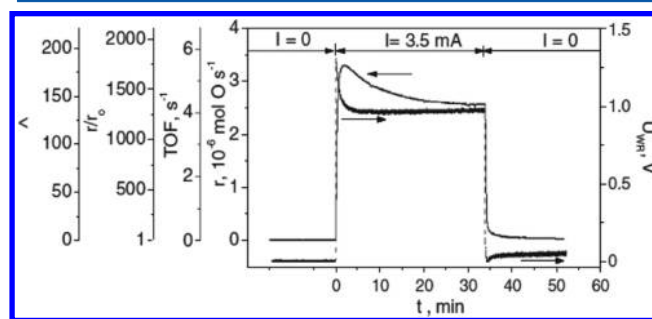escribed in section 4.2.1, product selectivity can be also affected by electrochemical promotion. It was found that O^{2-} supply to the Ru surface (positive polarization) causes a significant increase in the CH_4 formation rate and selectivity, accompanied by a significant decrease in the rate of CO formation. The opposite effect was observed by negative potential application (Figure 17).

Bebelis et al.[307,308] investigated the electrochemical promotion of CO_2 hydrogenation on Rh/YSZ and Pd/YSZ electrochemical catalysts prepared by organometallic paste deposition. Figure 48 shows the effect of ohmic drop-free catalyst potential variations on the rate of CH_4 and CO production in the temperature range 400−468 °C and for a P_{H2}/P_{CO2} ratio equal to 1.5. The methane formation rate increased by a factor of 2.7 with increasing Rh catalyst potential (electrophobic behavior), while the CO formation rate was increased by up to 1.7 times with decreasing catalyst potential (electrophilic behavior). The Λ values were
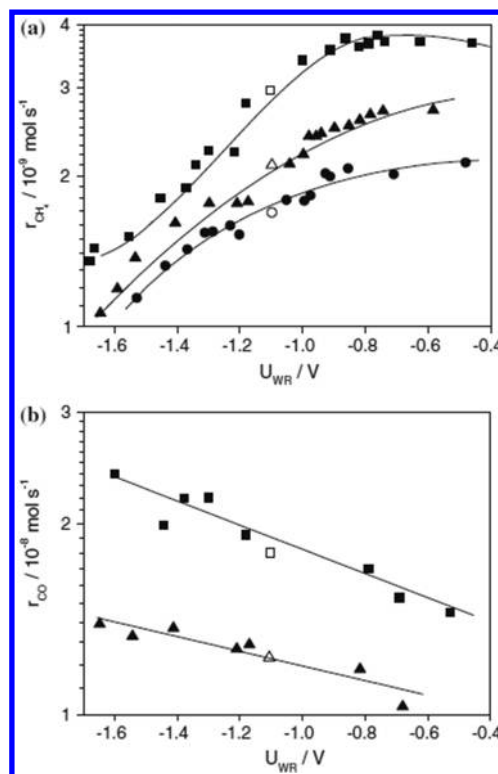
Figure 48. Effect of catalyst potential on the CH_4 production rate (a) and on the CO production rate (b) for the electrochemical catalyst Rh/YSZ. Open symbols correspond to open-circuit conditions. P_{CO2} = 1 kPa, P_{H2} = 1.5 kPa. (●) 400 °C (flow rate 27 cm³ (STP) min⁻¹), (▲) 451 °C (flow rate 38 cm³ (STP) min⁻¹), (■) 468 °C (flow rate 38.5 cm³ (STP) min⁻¹).[307] Reprinted with permission from ref 307. Copyright 2008 Springer Science and Business Media.

210 and 215 for CH_4 and CO, respectively. The observed EPOC behavior was attributed to the preferential formation, on the Rh surface, of electron donor hydrogenated carbonylic species upon positive polarization. These species promote the production of CH_4. Simultaneously, the catalyst potential increase drops the coverage of more electron acceptor carbonylic species resulting in CO formation.[307] Using Pd/YSZ electrochemical catalysts, experiments were carried out in H_2-rich gas mixtures at the temperature range of 533−605 °C. CO and H_2O were the only detected products. CO formation was enhanced by up to approximately 6 times by applying either negative or positive overpotentials (inverted volcano behavior). The observed rate changes were up to 150 times larger than the corresponding pumping rate of oxygen ions.[308]

The electrochemical promotion of CO_2 hydrogenation was also studied by Jimenez et al.[309] on composite Ni or Ru impregnated carbon nanofiber catalyst−electrodes deposited on YSZ, at 200−440 °C in H_2-rich atmosphere. Methane and CO were the carbon-containing products obtained both under open circuit and electropromoted conditions. It was found that negative polarization enhances mildly the hydrogenation rate (ρ = 3) and methane selectivity (from 15% to 35% at 310 °C) of the Ni-based materials, while for the case of the Ru-based materials only slight enhancement in the catalytic rate was observed (ρ = 1.1) without modification of the CH_4 selectivity.

4.7.1.3. H_2 Production. Souentie et al.[212] investigated the effect of EPOC for the water−gas shift (WGS) reaction over porous Pt catalyst electrodes interfaced with YSZ, using a fuel cell type electrochemical reactor at temperatures 300−400 °C, under
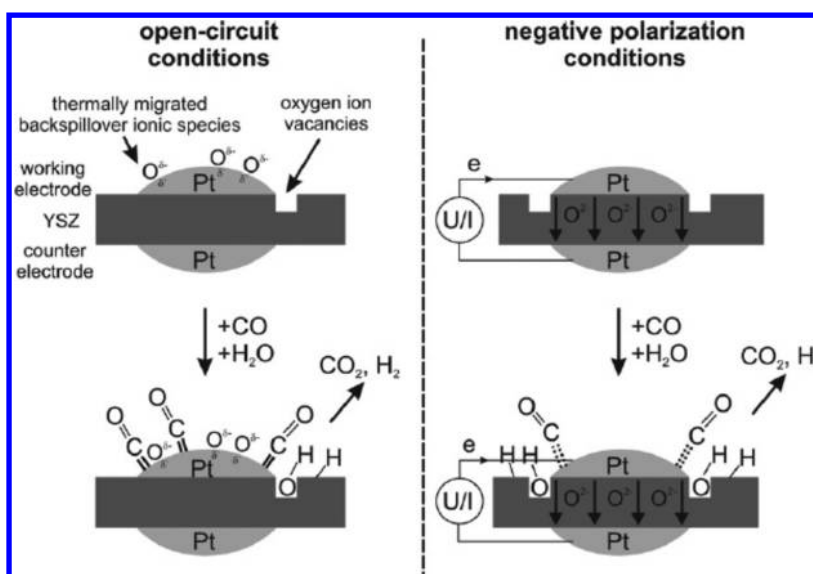
Figure 49. Schematic of a possible electrochemical promotion mechanism for the WGS reaction. Reprinted with permission from ref 212. Copyright 2012 Elsevier.

P_{H2O}/P_{CO} ratio values from 2.85 to 31. Both under unpromoted and electropromoted conditions, a negative order dependence of the catalytic reaction rate on P_{CO} and a positive one on P_{H2O} was found. Positive potential application (O^{2-} supply to the catalyst surface) caused a small decrease in the catalytic reaction rate, while negative potential application resulted in a pronounced rate increase, up to 200%, with Λ values up to 110.

The proposed mechanism for the electrochemical promotion of the WGS reaction is shown schematically in Figure 49. Hydroxyl groups on the YSZ surface react with CO, adsorbed on Pt, to form intermediate formates. The latter decompose to H_2 and CO_2, leaving oxygen vacancies that are filled by hydroxyl groups. The surface oxygen ion vacancies can be created due to O^{2-} thermal migration and backspillover onto the Pt surface, but also by partial reduction of the oxide support in the presence of CO. Negative polarization can lead to a weakening of the Pt−CO bond strength, but also to an increase in surface concentration of oxygen ion vacancies near the Pt−gas−support three-phase boundaries necessary for water dissociation.[212]

Caravaca et al.[310] reported the possibility of coupling the phenomenon of EPOC and the steam electrolysis process for the simultaneous production of H_2 in a single chamber solid electrolyte cell (Pt-YSZ/YSZ/Au). Their system was studied under methane partial oxidation, steam electrolysis, and methane autothermal reforming conditions at 600 °C. Application of negative currents under autothermal reforming conditions allows for the reduction of H_2O on the Pt catalyst−working electrode, producing H_2 and O^{2-} ions. Simultaneously, the electrochemically supplied O^{2-} ions act as electrochemical promoters on the active Pt catalyst film, generating an additional amount of H_2 by an intrinsic NEMCA effect in the methane steam reforming reaction.

4.7.1.4. NO_x Abatement. The abatement of NO_x (NO and NO_2) contained in the exhausts of lean-burn mobile engines is still a topic under investigation. For instance, in Europe, there is a strong development of the diesel cars market because of their lower fuel consumptions as compared to gasoline vehicles. The future EURO 6 legislation, from 2014, will require extremely low emission levels of NO_x decreasing from 180 mg/km (actual EURO 5 standard) to 80 mg/km. The challenge addressed to the

scientific catalysis community is to find smart catalysts able to selectively reduce NO_x into environmentally benign N_2 in a gaseous environment containing high excesses of oxygen and trace amounts of reducing agents (unburnt hydrocarbons and carbon monoxide). An ambitious solution is to selectively reduce NO_x into N_2 by using the unburnt hydrocarbons present in the exhaust.[311]

In this direction, the NO reduction by propene in the presence of oxygen on Pt/YSZ elctrochemical catalysts was investigated by Lintanf et al.[282,311] using Pt films prepared by the electrostatic spray deposition (ESD) technique. The catalytic activity was significantly enhanced (ρ values for CO_2 and N_2 are 2.3 and 2.0 respectively at 400 °C under application of −2 V). Dense ESD coatings were found to be more appropriate for EPOC applications because (i) low loadings of platinum with relatively high Pt dispersion are sufficient to achieve high activity and (ii) the microstructure was slightly altered after aging leading to a stable catalyst.

Constantinou et al.[312] used Rh catalyst−electrodes deposited by organometallic paste application on YSZ to study EPOC of NO reduction by propene at the temperature range of 320−450 °C, in a wide range of oxygen and propene partial pressures. Inverted volcano behavior was obtained. Catalytic rate enhancement was obtained both with positive and with negative potential or current application. The electropromotion was more pronounced under low oxygen concentration reaction mixtures. They observed up to 60-fold enhancement in the catalytic activity of NO reduction to N_2 (for p_{C3H6}/p_{O2} = 0.2).

A comparison of the activity between the electropromoted Rh paste electrochemical catalyst and highly dispersed (77%) Rh/YSZ (0.5% wt) was also given in this study. It was observed that the TOF values of the dispersed Rh/YSZ catalyst fall between those of unpromoted and electropromoted Rh/YSZ electrochemical catalyst. This implies that the dispersed catalysts are, to some extent, partially promoted due to thermal migration of the promoting O^{2-} species from YSZ to the dispersed catalytic surface. However, this thermal migration seems to be not sufficient to reach the catalytic activity of a fully electropromoted catalyst. This is another result, which shows that with EPOC it is

possible to accelerate the kinetic of a reaction, in levels higher than with conventional dispersed catalyst.[312]

4.7.2. New Findings with Alkaline Conductors. Alkaline promoters play a crucial role in heterogeneous catalysis. Their use is of paramount importance in the design of successful commercial catalysts. A typical example of alkali promotion is the chemical addition of potassium into industrial Fe-based catalyst for the ammonia synthesis reaction.[313] Coadsorbed potassium (in the form of K_2O) significantly enhances the dissociative adsorption of N_2, which is the rate-limiting step. From the pioneering work, carried out in 1991, on ethylene oxidation on Pt/βAl$_2$O$_3$ electrochemical catalysts,[314] EPOC phenomena have also been extensively studied in the literature by using alkaline ionic conducting materials (see section 3.2) as electro-active catalyst supports. The majority of these studies have been carried out with sodium or potassium β-alumina phase and NASICON (sodium super-ionic conductor)-based materials. The main advantage of the use of alkali cationic conductors in EPOC versus the more common anionic conductors (YSZ) used as solid electrolyte is their superior ionic conductivity at low temperatures (below 300 °C) where a great number of industrial and environmental catalytic reactions occur. The possibility of in situ supplying this kind of alkaline ionic promoters under operating conditions has allowed new applications of EPOC, which are not possible by the use of conventional heterogeneous alkali modified catalysts.

For instance, the use of this kind of alkali electrochemically promoted systems allows one to:

- Supply the optimum alkali promoter concentration at various reaction conditions, which is of great importance for non-stationary processes, for example, automotive catalysis.[315]

- Attenuate the effect of poisoning species on catalyst surfaces.[315] For instance, depending on the reaction conditions, the competitive adsorption of poisoning molecules with reactants can be controlled and avoided.

- Regenerate a catalyst from carbon deposition at fixed reaction conditions.[316] EPOC is a suitable tool to remove, at fixed reaction conditions, the carbon fragments typically deposited during hydrocarbon reforming reactions.

- Promote and store produced compounds on the catalyst surface by the formation of alkaline derived species.[317] This is very important for cyclic processes such as NO_x storage/reduction catalyst (NSR technology for NO_x abatement).

These possibilities offered by alkali-electropromoted systems along with other recent related studies are briefly described below and classified depending on the nature of the catalytic reaction.

4.7.2.1. NO_x and N_2O Abatement. EPOC applications with alkaline ionic conductors in NO_x removal have been extensively studied mainly through selective catalytic reaction (SCR) by unburnt hydrocarbons on wide variety of metal catalyst films.

One of the most relevant recent studies comes from the group of Vernoux and his collaborators[318] in the selective catalytic reduction (SCR) of NO by propene on Pt films deposited on NASICON (Na$_3$Zr$_2$Si$_2$PO$_{12}$), a Na$^+$ conducting solid electrolyte. In such a system, electrochemical promotion was shown to strongly enhance both the catalytic activity and the selectivity to N_2 under lean burn reaction conditions (under realistic oxidizing conditions). Such an improvement was obtained using low overpotentials, applying −100 mV to the Pt catalyst−electrode,

which enhanced the selectivity to N_2 from 41% to 61%. Additionally, the use of the NASICON material allowed operation at quite low temperatures (~300 °C) compatible with the treatment of automotive exhausts emissions.

A more recent study carried out by de Lucas-Consuegra et al.[214] also evidenced improvement of the catalytic performance of Pt/K$^+$-β Al$_2$O$_3$ electrochemical catalyst for NO SCR by propene under wet reaction conditions (i.e., large excess of steam) at 200−400 °C (temperature window suitable with a diesel engine working in an urban cycle). The application of positive potentials at low temperatures and more negative ones at higher temperatures allowed the control of the competitive adsorption of different reactants versus H_2O molecules, which poisoned the catalytic active sites.

NO_x abatement in diesel exhausts can also be performed by using NO_x storage-reduction (NSR) catalysts, which are operated in cyclic gas-composition conditions. During the first step (lean phase), NSR materials store emitted NO_x as nitrates until the surface reaches the saturation threshold. A pulse of fuel postinjection then triggers the short second step (rich phase), during which the reducing conditions lead to nitrate decomposition and release as well as subsequent NO_x reduction into N_2 and surface regeneration. This kind of material is commonly composed of Pt nanoparticles to activate NO oxidation into NO_2 in the lean phase, a storage basic compound (typically Ba or K) to form nitrates from NO_2, Rh nanoparticles to reduce NO_x into N_2 in the rich phase, and an oxide support. De Lucas-Consuegra et al.[317] have proposed the use of a tubular Pt/K-β''Al$_2$O$_3$ electrochemical catalyst to implement NO_x storage/reduction process. The proposed system operated in a cyclical manner between negative and positive polarizations under an oxidizing and reducing atmosphere, respectively. In this system, potassium ions electrochemically transferred to the Pt catalyst played a double role in the NSR process, first promoting the NO oxidation reaction (rate-determining step for the NO_x storage) and then acting as storage sites through the formation of potassium nitrates species. Under negative polarization and lean burn conditions, NO_x was stored on the catalyst surface in form of potassium nitrates species. In a second step, under positive polarizations and reducing atmosphere, the catalyst was regenerated, and the stored nitrates were efficiently desorbed and reduced into N_2. The variation of the current under the applied polarizations allowed monitoring the progress of both the storing and the regeneration phases, and thus the optimization of the duration of both sequences in a technically feasible manner. In addition, the possibility of electrochemical regeneration of the catalyst surface allowed operation under a fixed lean gas composition, which implies an important technological advance for the NSR process versus the conventional use of potassium and barium modified heterogeneous catalysts.

Even if N_2O is not a concern of EURO5 and 6 legislations, it is a powerful greenhouse gas that must be also removed from the exhausts. In a recent study,[215] it was explored the ability of EPOC to improve the performance of a Pt catalyst for the reduction of N_2O by C_3H_6 using K$^+$-βAl$_2$O$_3$ as a solid electrolyte. Electrochemical pumping of K$^+$ to the Pt catalyst working electrode strongly increased the N_2O reduction rate, activating the catalyst at lower temperatures. Additionally, the presence of K$^+$ on the Pt catalyst strongly decreased the inhibiting effect of steam, increasing the N_2O reduction rate by more than 7 times. N_2O abatement was also performed on Pd/K$^+$-βAl$_2$O$_3$[319] with different hydrocarbons (alkanes and alkenes). EPOC experi-

ments were used to design optimally promoted conventional catalysts, suitable for N_2O abatement. Close similarities were found between the two different concepts of catalyst promotion, confirming the usefulness of EPOC as a rapid research tool to design effective catalyst formulations.

4.7.2.2. Hydrocarbon and CO Oxidation. Hydrocarbons (ethylene, propene, propane) and CO oxidation were also performed on alkaline conductors (Na^+ and K^+)-based electrochemical catalysts. For instance, Petrolekas et al.[320] have investigated the electrochemical promotion of ethylene combustion on a Pt/NASICON electrochemical catalyst. At 430 °C, electrochemical Na^+ supply to the Pt catalyst under near-stoichiometric ethylene-to-oxygen ratios causes an up to 10-fold catalytic rate enhancement for Na coverages of 0.03−0.08. The observed promotional role of sodium was attributed to enhanced oxygen chemisorption on the Pt catalyst−electrode surface.

Vernoux et al.[321] used a similar Pt/NASICON electrochemical catalyst for propene oxidation under both large excess of oxygen (for volatile organic contaminants, VOCs, abatement) and near the stoichiometry (for energy production) oxygen conditions. In agreement with the basic rules of promotion,[322] they found that near the C_3H_6/O_2 stoichiometric ratio, a strong promotional effect was observed for negative overpotentials (electrophilic NEMCA effect with $\rho CO_2 = 3$), which was attributed to the coverage increase of electron acceptor oxygen species. However, when oxygen was in large excess, such promotional effect was no longer observed due to an excess of O_2 chemisorbed on the catalyst surface.

Kotsionopoulos and Bebelis[224] have also recently studied EPOC of propane combustion over a Pt film catalyst deposited on Na^+-β''-Al_2O_3, in the temperature range 320−440 °C. For a stoichiometric oxygen to propane ratio, the system exhibited electrophobic behavior; that is, addition of sodium resulted in decrease of the CO_2 production rate. Relative changes in the catalytic rate by up to 60 times larger than the corresponding change in sodium coverage were measured.

Using a K^+-β'' Al_2O_3 solid electrolyte,[323] a very strong promotional effect of K^+ was evidenced on Pt impregnated film for C_3H_6 oxidation at temperatures below 300 °C. For instance, under C_3H_6/O_2 2000 ppm/7% at 200 °C, a rate enhancement ratio (ρCO_2) of 7 was achieved under application of $V_{WR} = -2$ V, increasing propene conversion from 10% to 70%. In addition, results showed permanent NEMCA effect, which was attributed to the formation of very stable promoting species (potassium oxides and super oxides) under reaction conditions. Another paper of the same group pointed out the interest of using K^+-β Al_2O_3 to promote CO oxidation on Pt films.[279] Temperature-programmed reaction experiments demonstrated the utilization of EPOC for activating a catalyst at lower reaction temperatures. The effect of catalyst polarization drastically increased the catalytic rate more than 11 times in CO removal rates, decreasing at the same time the light-off temperatures by ∼40 °C. These results are of great interest because the exhaust released from a car engine during the first minutes after a "cold-start" is a critical issue for the performance of catalytic converters, especially at high CO concentrations. A more recent study has also demonstrated the possibility to simultaneous promote C_3H_6 and CO oxidations[281] on a Pt−C catalyst film interfaced to K^+-β Al_2O_3. The simulated gas stream with large excess of CO_2 demonstrated again the interest of the EPOC phenomena for the removal of VOCs in automotive exhaust emissions.

4.7.2.3. Hydrogen Production and Purification Processes. The EPOC phenomenon with alkaline ionic conductors was also

applied in catalytic H_2 production and purification processes. De Lucas-Consuegra et al.[316] have explored the H_2 production from methane via steam reforming, partial oxidation, and autothermal steam reforming over a (Pt−Pt/YSZ/Na^+-β'' Al_2O_3) electrochemical catalyst. Among the different explored reaction compositions, the autothermal steam reforming process seems to be the most suitable one for the operation of the electrochemical catalyst under cyclic positive and negative polarizations. Figure 50 shows variations of H_2, CO, and CO_2
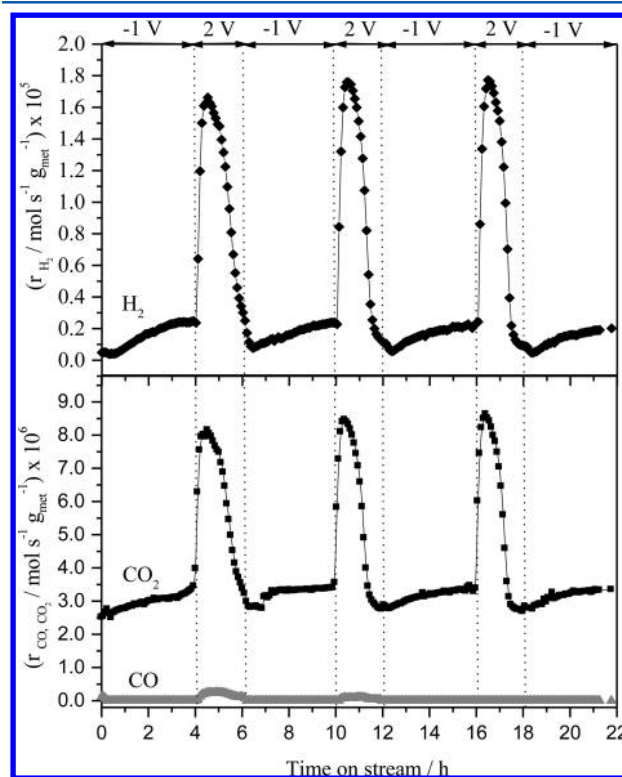
Figure 50. Influence of the applied potential on H_2, CO, and CO_2 production rates during the reproducibility experiment under ATR conditions at 500 °C. Reprinted with permission from ref 316. Copyright 2012 Elsevier.

production rates with time on stream under different cycles of positive and negative potentials. This experiment was carried out under autothermal steam reforming conditions ($CH_4/H_2O/O_2$: 1/4/0.2%) between negative (−1 V for 4 h) and positive polarizations (+2 V for 2 h). Under positive polarization, the electrochemical catalyst produced a high amount of H_2 coming mainly from CH_4 decomposition process (with almost no CO production). However, it was deactivated due to a strong increase in the CH_4-derived chemisorption species, which led to carbon deposition. Nevertheless, the subsequent application of negative polarization led to a strong increase in the coverage of O_2- and H_2O-derived molecules that caused the removal of the deposited carbon and, hence, the regeneration of the catalyst. The results are of great technological importance and demonstrate that EPOC can be used to regenerate, in an unlimited way, the catalytic performance of the system from carbon deposition under fixed reaction conditions.

A more recent study carried out from the same group has also demonstrated the possibility of the alkaline EPOC systems to enhance significantly the H_2 production activity and selectivity via partial oxidation of methanol.[324] The use of a Pt/K^+-β-Al_2O_3

electrochemical catalyst allows enhancement up to 6 times in the H_2 production rate on a dense Pt film prepared by cathodic arc deposition.

Concerning H_2 purification processes, the use of alkaline electro-active catalyst supports has been shown to enhance the catalytic properties of different metals for the preferential CO oxidation reaction in H_2-rich streams[325] and in the water–gas shift reaction.[211] CO conversion on a non-noble metal catalyst (Ni) can be electrochemically promoted, increasing the conversion from 18% to 50%, under the optimal potential conditions.

4.7.2.4. Other Related Industrial Processes. Alkaline conductor-based electrochemical catalysts were widely applied to other catalytic reactions of great industrial interest. One of the earliest results came from the group of Vayenas in the silver-catalyzed epoxidation of ethylene.[326] It was found that the catalytic activity and selectivity of polycrystalline Ag for the epoxidation and complete oxidation of ethylene could be affected in a pronounced and reversible manner by the use of Na-β''-Al_2O_3 solid electrolyte and in the presence or absence of traces of chlorinated hydrocarbons in the gas phase. In a more recent study,[327] the use of a potassium conductor was explored on the Ag-catalyzed propene and ethylene epoxidation in the presence of moderators such as NO and chlorine.

The group of Vayenas also investigated, in the past, the ammonia decomposition reaction over $Fe/K_2YZr(PO_4)_3$ (a K^+ ionic conductor).[328] At temperatures around 500 °C, it was found that the electrochemical supply of moderate amounts of potassium ions can cause an enhancement in the catalytic rate.

In another study of the same group,[286] it was investigated the acetylene selective hydrogenation on Pd films deposited on Na-β''-Al_2O_3, at low temperatures (60–100 °C) and GHSV from 10^3 to 10^4 h^{-1}, that is, under conditions similar to those used in industrial processes. It was shown that the β''-Al_2O_3 can act as an active catalyst support causing enhanced performance of the Pd catalyst. Acetylene conversion and hydrogenation selectivity values up to 90% and 95%, respectively, were obtained.

More recent studies coming from the group of Lambert[329,330] have also explored EPOC of the same catalytic reaction using sodium and potassium conductors on Pt- and Pd-based electrochemical catalysts with several important findings from an industrial interest. Specifically, Tracey et al.[331] investigated the applicability of EPOC to the Pt-catalyzed acetylene hydrogenation to ethylene and ethane using as the electrolyte β'' alumina with Na^+ conductivity and Williams et al.[332] using as the electrolyte β'' alumina with K^+ conductivity. Using the Na^+ conductor, in hydrogen-rich atmospheres at temperatures below 230 °C, electrochemical promotion by 0.02 monolayer Na converts Pt from a poor catalyst to an active and selective one (ethylene selectivity was increased from 4% on the Na-free surface to 78% at a catalyst potential of −400 mV, at which point the acetylene conversion is 54%). At higher temperatures (above 230 °C) and in an acetylene-rich environment, deposition of carbon or carbonaceous species became significant, causing a reduction in the activity, increase in selectivity, and decrease in the promoting effect of Na.[319] Using the K^+ conductor, ethylene selectivity was increased from 10% (unpromoted catalyst) to 90% (under imposition of −400 mV) at 157 °C in a hydrogen-rich atmosphere.[320] Comparing the results of both studies (Na$^+$ and K$^+$ conducting supports), it is obvious that there is no important difference between these two alkalis with regard to promoting efficiency.

The same group has widely explored EPOC with alkaline ionic conductors (Na^+ and K^+ conductors) for the Fischer–Tropsch synthesis reaction under low and high pressure conditions.[331,332] It was shown that Rh catalytic activity could be strongly promoted by potassium ions.[331] At 200 °C and 14 bar, 43 products were detected, comprising alkanes, alkenes, and primary alcohols. By electrochemicaly supplying K^+, the selectivity toward alkenes and primary alcohols increased as a result of the actual increases in the rates of formation of these products, while alkane formation was progressively suppressed.

Finally, it is also interesting to note one of the most recent studies on CO_2 hydrogenation on Pd/Na^+-β-Al_2O_3 electrochemical catalyst carried out by Bebelis et al.[312] It was shown that the CO formation rate increased by supplying sodium ions to the catalyst–electrode, enhancing the CO production up to 6.7 times. All of these results demonstrated the ability of alkaline EPOC systems to strongly promote a wide variety of catalytic reactions of great industrial importance.

4.7.3. New Findings with Protonic Conductors.
4.7.3.1. Ceramic Proton Conductive Membranes. Since the discovery of NEMCA, high temperature ceramic proton conductors have been used for the electrochemical promotion of various reactions. Kokkofitis et al. have provided a recent comprehensive review of EPOC studies carried out on ceramic proton conductive based electrochemical catalysts.[71] Recent findings during EPOC investigations with proton conductors are presented in this section.

Liu et al.[333] used fluorite-type structure oxide ceramics $Ce_{0.8}M_{0.2}O_{2-\delta}$ (M = La, Y, Gd, Sm) with protonic conductivity, in hydrogen-containing atmospheres, to electrochemically promote the ammonia synthesis reaction on Ag–Pd catalysts at 400–800 °C. Their results showed that the NEMCA effect can play a key role in synthesizing ammonia electrochemically. The electrochemically induced increase in the rate of NH_3 synthesis was up to a factor of 13 higher than the unpromoted catalytic rate (ρ = 13) and up to a factor of 6 higher than the rate of supply of protons to the catalyst, that is, from the maximum rate anticipated from Faraday's Law for a purely electrochemical reaction (Λ = 6). The NEMCA effect was significant at lower potential and poisoned with increasing potential.

Stoukides and his co-workers have used a strontia–zirconia–yttria perovskite (SZY, $SrZr_{0.95}Y_{0.05}O_{3-a}$) solid electrolyte and studied the electrochemical promotion of ammonia synthesis and water gas shift.[71,334,335] The catalytic activity of an industrial Fe-based ammonia synthesis catalyst can be electrochemically promoted at 450–700 °C and at atmospheric total pressure. Up to an 80% increase in the reaction rate was observed when protons were electrochemically supplied to the catalyst, although the observed NEMCA behavior was relatively moderate with values of Faradaic efficiency, Λ, and of the rate enhancement ρ below 3 and 2, respectively.[334] The case of electrochemically promoting the water gas shift reaction was studied at 600–750 °C and atmospheric total pressure using a polycrystalline Pd film as the catalyst. It was found that when protons are pumped away from the catalyst, the rate of H_2 formation increased to a moderate extent. Faradaic efficiency values up to 8 were reported, while the highest rate enhancement ratio measured was 2.[335]

Kalimeri et al.[336] used a double chamber proton conducting membrane reactor $Pd/SrZr_{0.95}Y_{0.05}O_{3-a}/Ag$ at 500–750 °C to study NO_x reduction. Water was supplied to the one chamber of the reactor, where H_2 was efficiently produced by steam electrolysis on the Ag film. NO, NO_2, or N_2O was supplied to the second chamber of the reactor on the Pd film. The in situ

produced hydrogen on the Ag film was used to selectively reduce nitrogen oxides into N_2 on the Pd film. Apparently 100% selectivity was observed in all of the experiments. Non-Faradaic N_2O decomposition was also observed under cathodic over-potentials. When only N_2O was supplied to the Pd catalyst, the electrochemical activation was found to be less pronounced, with values of ρ and Λ in the range of 1.08−1.33 and 1.2−3, respectively. More pronounced electropromotion was achieved when propane and oxygen were supplied together with N_2O on Pd film (values for ρ up to 1.45 and for Λ up to 15 were reported). This was attributed to the participation of hydrogen ad-species not only to the oxygen scavenging process but also the reverse water−gas shift reaction. Under open circuit, Pd was essentially inactive toward NO dissociation. However, when protons were electrochemically supplied to the catalyst, Pd showed catalytic activity even if this effect was purely Faradaic because Λ values were equal to unity.[336]

The recently discovered high temperature proton conductor, $La_{0.99}Sr_{0.01}NbO_{4−\delta}$, was used as a support for Pt catalyst in the electrochemical promotion of ethylene oxidation at 350−450 °C by Poulidi et al.[337] Moderate non-Faradaic rate modification occurred under negative polarization, while some permanent promotion was also observed. In oxidative atmospheres, both the oxygen partial pressure and the temperature influenced the type and magnitude of the observed rate modification. Rate-enhancement values of up to $\rho = 1.4$ and Faradaic-efficiency values approaching $\Lambda = −100$ were obtained under negative polarization at low oxygen partial pressures. Under dry and mildly oxidizing conditions, the reaction showed inverted volcano behavior with a more pronounced effect for positive overpotentials, suggesting that some oxygen ion conductivity may occur under these conditions.

The same group[338] has studied the use of $BaZr_{0.9}Y_{0.1}O_{3−\alpha}$ (BZY) for the electrochemical promotion of ethylene oxidation on Pt catalyst at 300−450 °C. Although BZY is known for its protonic conductivity, it was reported[338] that under appropriate conditions it can act also as oxygen ion conductor. Under open-circuit conditions, BZY behaves in principle as a protonic conductor, while under polarization the conductivity is controlled by the gaseous atmosphere. In oxygen containing atmospheres, oxide ion conductivity is predominant, while in reducing conditions (such as C_2H_4) proton conduction takes place. It was found that electrochemical promotion of such a system is significantly influenced by the oxygen to ethylene ratio in the reaction mixture. In excess of ethylene, an inverted volcano behavior was observed exhibiting a minimum under open-circuit conditions. According to EPOC literature, ethylene oxidation on Pt catalyst is promoted by positive polarization on an oxide support (electrophobic behavior) and by negative polarization on a proton conducting suppoer (electrophilic behavior). In the case of BZY electrolyte, in excess of ethylene and under negative polarization, protons were removed and protonic conduction is favored, while positive polarization led to oxide ion conduction. In both cases, the reaction was promoted in agreement with the EPOC rules. Rate enhancement ratio, ρ, values up to 1.5 were obtained under positive polarization and up to 1.7 under negative polarization.

4.7.3.2. Polymeric Proton Conductive Membranes. The phenomenon of EPOC is not limited only to ceramic electrolytes, which are the topic of this Review. Polymeric membrane electrolytes with protonic conductivity are very promising materials for implementing EPOC at temperatures much lower (below 100 °C) than ceramic electrolytes.

Therefore, this section gives a short overview of EPOC on polymeric electrolytes.

Smotkin and his group[205,339] were the first to report electrochemical promotion of non-redox, unimolecular catalytic reactions (isomerization of alkenes) on high surface area Pd/C cathodes of polymer electrolyte fuel cell reactor units with Nafion membrane as the electrolyte. Recently, Salazar and Smotkin[340] extended these studies of promoting isomerization reactions to substituted olefins to investigate the possibility of effecting skeletal rearrangement reactions in solvent-free systems at low temperature (70 °C). They found that the isomerization of 2,3-dimethyl-1-butene to 2,3-dimethyl-2-butene can be enhanced over 1000-fold (vs open-circuit value) by spillover protons generated by low currents on carbon supported Pd catalysts in a polymer electrolyte fuel cell ($\rho = 1230$). With 3,3-dimethyl-1-butene, the proton spillover catalyzed methyl shift occurred at low levels, and 2,2-dimethyl-butane was the primary product from the simple reaction. The skeletal rearrangement product, 2,3-dimethyl-butane, and the demethylated product, 2-methyl-butane, were found at relatively low levels. Thus, although the spillover promoted isomerization of the substituted olefin, 2,3-dimethyl- 1-butene, was dramatic, the proton spillover promoted skeletal rearrangement reaction of 3,3-dimethyl-1-butene remains elusive. The reduced product of a skeletal rearrangement reaction was observed at potentials substantially negative to the current onset potential. The evidence for NEMCA promoted skeletal arrangement is very weak, while the primary product resulting from the simple reduction of the double bond of the starting material essentially tracked the current potential characteristics of the fuel cell.

Petrushina and co-workers[218,341,342] have explored EPOC using Pt and Pt−Ru carbon supported catalysts in fuel cell type reactor units, using an electrolytic membrane of polybenzimidazole (PBI) doped with H_3PO_4. Several reactions were implemented such as methane oxidation, NO reduction with hydrogen, and CO hydrogenation. Recently,[343] they have investigated the electrochemical promotion of NO reduction in the presence of methane.

In this study,[343] one compartment of the fuel cell reactor (anodic) was supplied with NO, CH_4, and Ar, while the other one (cathodic) was exposed to H_2 and Ar. Experiments were performed at 135 and 165 °C. It was found that NO can be electrochemically reduced at the anode by protons or electro-chemically produced hydrogen. In the presence of methane, NO reduction mainly proceeded chemically by methane. The maximum Faradaic part of NO conversion reached 3.4% of the overall conversion under polarization. When the cell was polarized negatively (i.e., protons supplied to the working electrode−anode), the NO reduction rate was affected. At low values of overpotential, the methane conversion decrease was attributed to the competition with the electrochemical NO reduction by protons. However, when larger negative over-potentials were applied to the cell, CH_4 conversion increased from 14% under open-circuit conditions to 22.4%. This promotion effect was irreversible; the methane conversion increased after each negative polarization run, reaching after three successive runs of polarization a maximum of 46.5% at 135 °C. Upon these large negative overpotentials, the electro-chemical reduction of the protonic membrane took place, which produced hydrogen that can remove chemisorbed oxygen species and then alter the coverage of both NO and CH_4. No significant effect of the temperature was observed between 135 to

165 °C on NO reduction by methane, while the rate of NO electrochemical reduction decreased.

The possibility of electrochemically promoting catalytic reactions taking place on carbon supported anodes in polymer electrolyte membrane fuel cell units has been also investigated by the group of Vayenas.[344−346] It was pointed out that EPOC can be successfully applied for the removal of CO from H_2-rich hydrogen mixtures such as methanol reformates at low temperatures (30−80 °C). Carbon supported Pt, Pt−Cu, and Au catalysts were used as anodes in fuel cell reactors with Nafion electrolytic membranes, to study the electrochemical promotion of CO conversion into CO_2 via the preferential oxidation of CO in excess of hydrogen and the water−gas shift reaction. It was found that the magnitude of electrochemical promotion strongly depends on the kind of the anodic electrocatalyst (Pt, PtCu, or Au), on the CO/H_2 concentration ratio in the reaction mixture, on the operating temperature, and on the presence of oxygen in the cathode side of the cell (reference side). Pronounced electropromotion was reported in the presence of CO-rich anode environments ($\rho = 18$, $\Lambda = 40$).

4.7.4. Alternative Materials. Innovative works using alternative materials for electrolytes and catalysts have been recently carried out.[347,348]

Implementing new materials have two main objectives:

(a) to demonstrate EPOC at low temperatures by using new electrolytes that show higher ionic conductivity than YSZ, and

(b) to strongly reduce or to remove the utilization of noble metals.

A BITAVOX dense membrane was used[347] to implement EPOC at low temperatures, because the ionic conductivity of BIMEVOX is much higher than that of YSZ (see section 3.1.3.). The catalytic performances of a Pt/BITAVOX electrochemical catalyst were evaluated for NO_x reduction by propene. Unfortunately, it was found that the Pt catalytic film is gradually poisoned by the formation of $Bi_xPt_{1−x}$ alloy due to the slight reduction of the electrolyte even under lean-burn conditions. Therefore, a new geometry was proposed with the insertion of a YSZ barrier layer of a few nanometers between the catalyst and the electrolyte. Electrochemical promotion was demonstrated for this system at low temperature (200−300 °C) under lean-burn conditions for NO_x reduction by propene (Λ values up to 580) and propene deep oxidation. In the case of propene combustion, electrochemical promotion was maintained even in the presence of steam (Λ values up to 8).

Karoum et al.[348] have carried out EPOC experiments using CGO ($Ce_{0.9}Gd_{0.1}O_{2−\delta}$) as the electrolyte, which also exhibits higher conductivity than YSZ. In this study, electrochemical promotion of propene deep oxidation was performed on sputter-deposited Pt, with a large quantity of steam in the feed and extremely low loading of Pt (32 μg cm$^{−2}$). NEMCA effect was observed at temperatures lower than 200 °C even in the presence of steam in the feed. Activation of propene conversion was evidenced both under stoichiometric and under lean-burn conditions with Λ values slightly higher than unity. Still in the presence of large quantity of steam and also in the presence of excess oxygen, promotion of the propene oxidation was observed both with positive ($\Lambda = 6$) and with negative polarizations ($\Lambda = -2$).

A new design of electrochemical catalysts was also developed[338] by adding a sputtered interlayer of strontium-doped lanthanum manganites between the CGO dense support and an ultrathin coating of Pt (2 μg cm$^{−2}$). The catalytic activity of this ultrathin layer of Pt deposited on the electronically

conducting interlayer of perovskite can be electropromoted even in the presence of steam in the feed. This result is of great interest for future industrial applications of EPOC.

The interlayer configuration of electrochemical catalysts was first pioneered by Baranova et al.[349,350] and Wutrich et al.[351] by using titania deposited between Rh catalyst electrodes and a YSZ dense membrane. This study and subsequent ones by Baranova et al.[352,353] showed that the presence of the porous TiO_2 interlayer enhances the open-circuit catalytic rate for CH_4 and C_2H_4 oxidation on Rh and also stabilizes the electrochemically promoted highly active Rh catalyst state. This pronounced effect was attributed to a self-driven wireless-EPOC mechanism, where $O^{2−}$ promoting species are supplied from TiO_2 to Rh particles due to TiO_2−Rh work function difference and the subsequent charge transfer from TiO_2 to Rh via a self-driven EPOC $O^{2−}$ transport mechanism.

More recently, the effect of a TiO_2 interlayer was examined by Papaioannou et al.[354] on the catalytic activity and EPOC behavior of C_2H_4 oxidation on Pt by comparing a Pt/YSZ catalyst electrode and a Pt/TiO_2/YSZ catalyst electrode under similar operating conditions in O_2 excess. It has been found that the presence of the dispersed TiO_2 interlayer results in a very significant increase in the magnitude of the electrochemical promotion effect upon anodic polarizations. The rate enhancement ratio and the apparent faradaic efficiency values were found to be a factor of 2.5 and 4, respectively, larger than those measured on conventional Pt/YSZ electrochemical catalyst.

To fully remove the utilization of noble metals, Roche et al.[355,356] investigated the case of using doped lanthanum manganites ($La_{0.7}Sr_{0.3}MnO_3$) as catalysts for EPOC applications. Propane deep oxidation was selected as a model reaction. It was found that, at 300 °C, it was possible to observe an influence of the polarization on the binding strength of propane on LSM, which could slightly increase the propane coverage on LSM and then the catalytic activity. A rate enhancement ratio of 1.25 was reported with a corresponding Faradaic efficiency of the order of 5 (25% conversion gain).

4.8. Energy Efficiency

At this stage, the EPOC process efficiency can only be evaluated at the laboratory scale. Indeed, most of the studies involve samples based on solid electrolyte disks with diameters in the range 10−20 mm, that is, with areas of catalyst−electrode in the range 1−3 cm^2. Table 3 summarizes the electrical power used in recent EPOC studies on alkane deep oxidation.

The maximum power density required to obtain significant electropromoted states is 0.5 mW per cm^2 of catalyst−electrode. Considering typical operating conditions of the studies reported in Table 3 (overall flow: 10 L/h, reactants diluted in He, a monatomic gas), the energy required for heating the gaseous stream can be estimated at around 1.54 mW/K. This value is underestimated because heat losses surely occur.

The practical interest of EPOC in alkane combustion is to decrease the light-off temperature, that is, the temperature value at 50% of conversion. Considering that this light-off temperature is lowered by 10 °C, which is widely obtained with around 2 cm^2 of catalyst−electrode, the heat energy gain is around 15.4 mW as compared to 1 mW (for 2 cm^2) consumed for the electrical polarization. This example gives an idea of the expected energy gains of EPOC processes. Nevertheless, the development of suitable EPOC reactors as well as of highly dispersed electropromoted catalysts is required to demonstrate this energy efficiency at a larger scale.
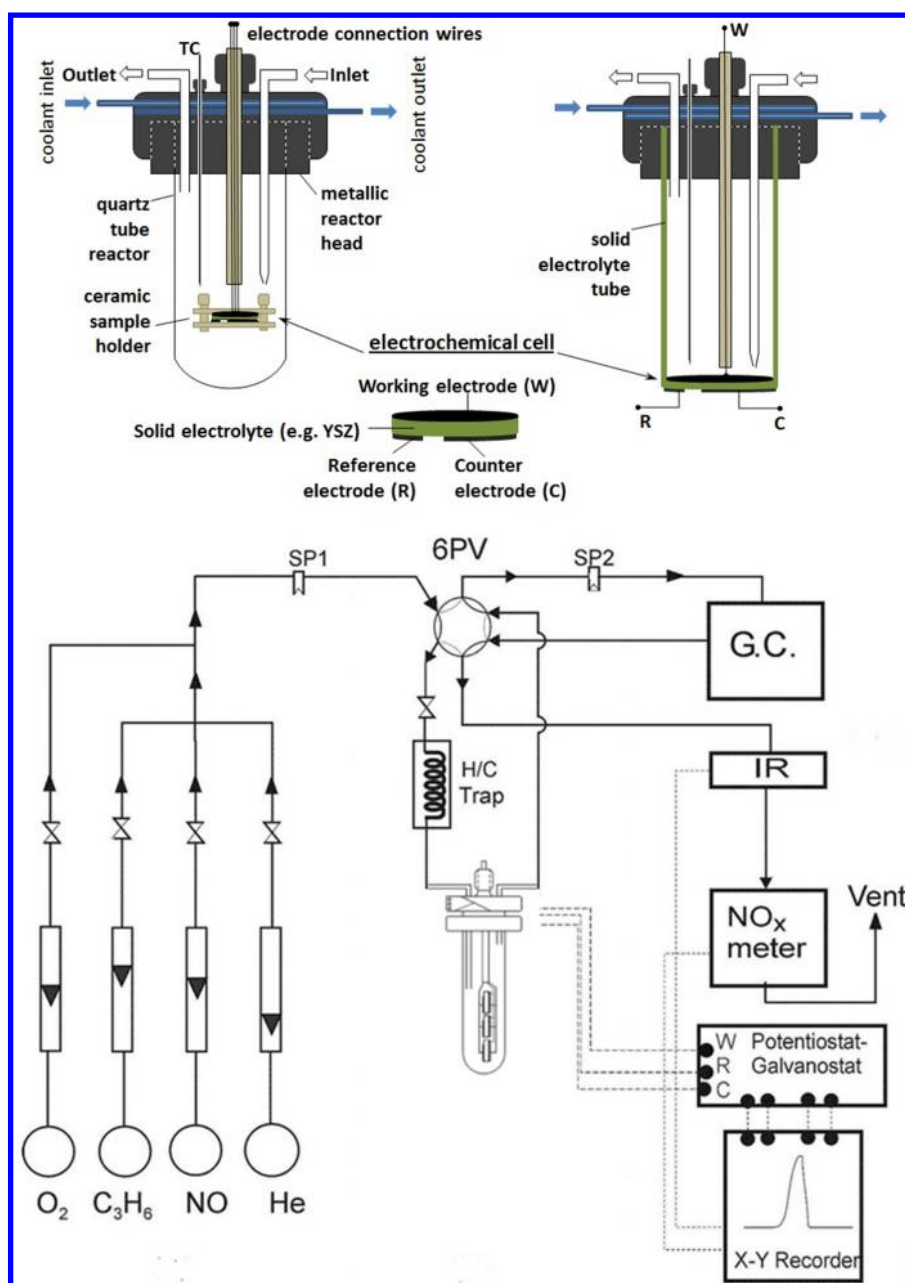
Figure 51. (Top) Typical reactor designs used in electrochemical promotion studies: single-chamber design (left) and fuel cell type design (right). (Bottom) Typical apparatus for electrochemical promotion studies using a three-pellet single chamber reactor.

4.9. EPOC Reactors

The reactors used so far to investigate EPOC can be divided into two general categories. The laboratory reactors focus on establishing well-characterized flow fields (CSTR or differentially tubular), low conversion, and isothermality so that reliable kinetic data can be obtained, not affected by mass or heat transport effects. A typical electrochemical catalyst sample consists of a dense pellet of electrolyte (around 20 mm diameter). The catalytic layer is deposited on one side (working electrode), while the counter-electrode and the reference are deposited on the other side. The scale-up multiplate and multipellet reactors aim for high conversions and aim directly in developing practical systems.

4.9.1. Laboratory Reactors. A typical apparatus for electrochemical promotion experiments consists of three parts: (a) the gas feed and mixing system, (b) the reactor, and (c) the

analysis and electrochemical measurements system. A detailed schematic of the experimental apparatus is shown in Figure 51, where the three parts are clearly shown.

The gas feed and mixing system mainly consists of glass flowmeters or electronic mass flowmeters connected to gas bottles. For reactants that are in liquid state at room conditions (e.g., methanol or toluene), a saturator is normally used through which a carrier gas (e.g., He, N_2) is sparged and then mixed with the other reactants. In this case, all lines connected to the reactor are heated to avoid condensation in the lines. In certain cases, the gases from the bottles should be pretreated to avoid contamination of the catalyst. For example, a heated (at $T > 300$ °C) trap for the decomposition of carbonyls is used in the case of CO feed, as iron carbonyls poison the metal catalysts. Check-valves and on−off valves are used in the gas feed and mixing system for safety reasons and for better control of the

system. In most cases, the reactant mixture is fed to the reactor through a 6-port valve. This allows for analysis of the reactants or products without interruption of the flow of reactants to the reactor. A 4-port valve can also be used for switching between the analysis of reactants and products. In this case, when selecting the analysis of reactants, the reactor works in a batch mode, which may be undesirable in some cases, for example, in catalytic systems where the steady state is slowly attained.[23]

Two types of continuous flow reactors are commonly used in electrochemical promotion experiments.[23] The "single chamber" reactor depicted in Figure 51 is made of a quartz tube closed at one end. The open end of the tube is mounted on a stainless steel cap, which has provisions for the introduction of reactants and removal of products as well as for the insertion of a thermocouple and connecting wires to the electrodes of the cell. A solid electrolyte disk, with three porous electrodes deposited on it, is appropriately clamped inside the reactor. Hence, in this configuration, the three electrodes (working, counter, and reference) are exposed to the same reactant-product atmosphere. Au wires are normally used to connect the catalyst−working electrode as well as the two Au auxiliary electrodes with the external circuit. These wires are mechanically pressed onto the corresponding electrodes, using an appropriate ceramic holder. A thermocouple, inserted in a closed-end quartz tube, is used to measure the temperature of the solid electrolyte pellet.

The second type of reactor is the "fuel cell type" reactor (Figure 51), which is similar to conventional fuel cells. It consists of a closed-end solid electrolyte tube appropriately mounted on a stainless steel cap, similar to the one in the single pellet reactor. The tube usually sits on an appropriately machined (Macor) base, which facilitates wire attachment to the counter and reference electrode and allows for ambient air circulation over these electrodes. The porous electrodes are deposited on both sides of the bottom of the solid electrolyte tube, the working electrode in the inner side, exposed to the reaction mixture, and the counter and reference electrodes on the outer side, exposed to ambient air. The auxiliary electrodes in this case are usually porous Pt or Ag films, as there is no need to be inert. Ag electrodes offer the advantage of low polarizability of the auxiliary electrode/solid electrolyte interface. However, Pt auxiliary electrodes are comparatively more stable and can be used at higher temperatures; thus they are normally the preferred choice. It has to be emphasized that the reference electrodes in electrochemical promotion studies (as in many cases in solid-state electrochemistry) do not correspond necessarily to inherently non-polarizable interfaces. However, they can be used as reference electrodes as long as the current passing through them during the measurements is negligible. The main advantage of the "single-chamber" type reactor is its simplicity and the ability to use cheaper solid electrolyte elements (disks instead of tubes). However, in this case, the open-circuit potential measurements and their dependence on gas-phase composition and temperature do not offer the precise information that can be acquired from similar measurements in the "fuel cell type" reactor, where the gas-phase electrode is exposed to a reference gas-phase mixture (e.g., ambient air).

The analysis commonly comprises line gas chromatography and, if available, by mass spectrometry and/or IR spectroscopy. The products from the reactor or, alternatively, the reactants (selection is made by switching a 4-port or 6-port valve) are directed to the gas chromatograph via a 6-port valve. This valve allows for sampling of certain gas volume and subsequent injection into one of the columns of the gas chromatograph. The

selection between the two columns of the gas chromatograph is made via a 4-port valve. A cheaper alternative to the use of the 6-port sampling valve and the use of the 4- or 6-port valve for selection between the analysis of reactants and products is the use of a gas syringe of certain volume (e.g., 2 mL) and the provision for sampling ports (e.g., a tee fitting with the sampling port capped with a septum) in the lines of reactants and products. As discussed below, this solution is not applicable in the case of condensable reactants or products.[23]

The mass spectrometer sampling capillary or the dispersive infrared analyzers used for continuous analysis and monitoring of the gas-phase composition are situated between the reactor and the sampling valve, as close to the reactor as possible, to avoid any delay in the recording of changes in the composition of reactants or products. This delay should be taken into account when plotting simultaneously the time dependence of catalyst potential or current and gas-phase concentration of the reactants or products.[23]

An alternative design of the "single chamber" reactor has been developed in recent years[357,358] and is depicted in Figure 52. In
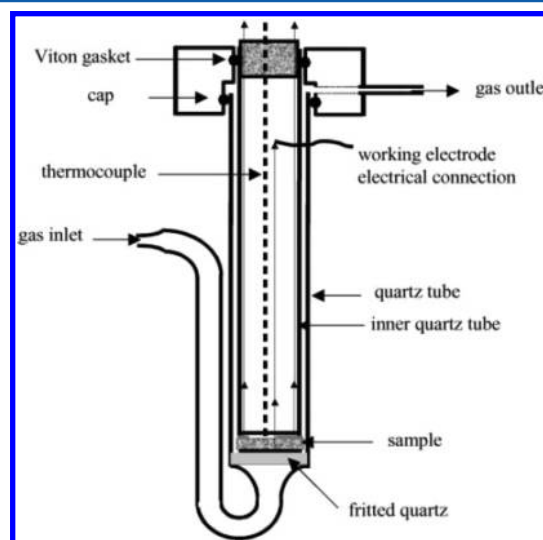
Figure 52. Alternative design for single-chamber reactor used in electrochemical promotion studies. Reprinted with permission from ref 357. Copyright 2012 Elsevier.

this configuration, the electrolyte pellet is placed on a fritted quartz, with the catalyst−electrode side facing the fritted quartz. The gas flow passes through the porous disk from below and then diffuses to the catalyst surface. An inner quartz tube is pressed onto the YSZ pellet to ensure electrical contacts. The Viton gaskets, placed in a polypropylene cap, ensure the air-tightness between the two quartz tubes. For the current collection, a gold mesh is placed between the quartz porous disk and the working electrode, while one gold wire is welded onto the gold mesh and two others are attached to the reference and counter electrodes.[357]

Particular attention must be paid to avoid mass and heat transfer limitations during the kinetic measurements. This is particularly important when carrying out NEMCA experiments under high vacuum.[234,359,360]

4.9.2. Scale-Up: Multipellet, Multiplate, and Bipolar EPOC Reactors.
In recent years, there has been considerable effort for the development of multipellet or multiplate and
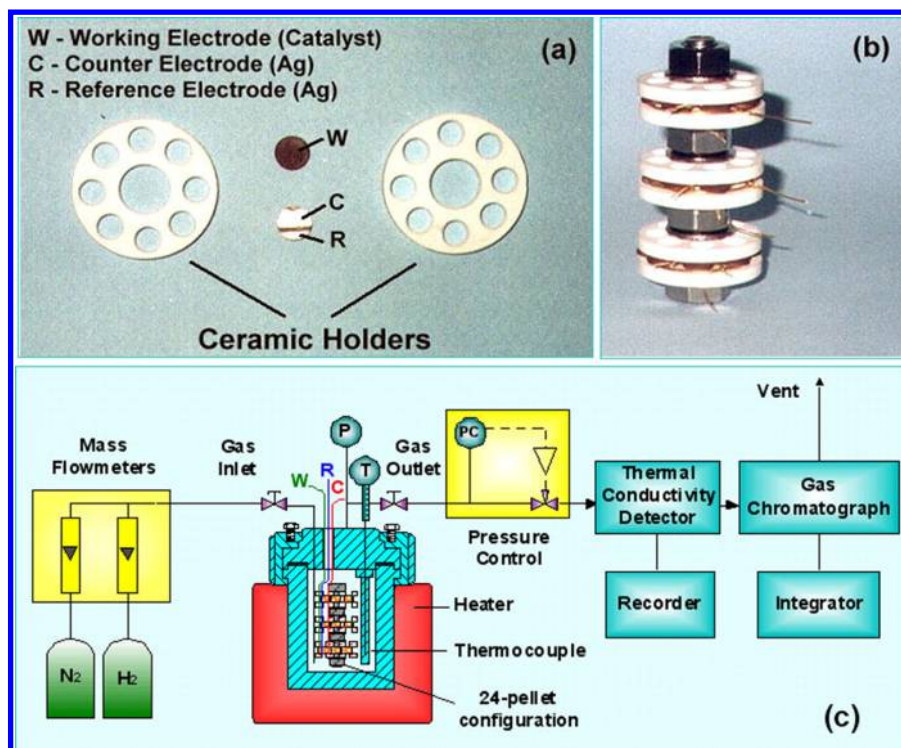
Figure 53. Experimental setup: (a) Machinable ceramic holders and two proton conducting pellets showing the location of catalyst, counter, and reference electrodes. (b) Twenty four pellet unit. (c) High-pressure reactor, gas feed, and analysis unit. Reprinted with permission from ref 361. Copyright 2012 American Chemical Society.

bipolar reactors, which could be scaled up for practical applications. Some of these studies are summarized here.

4.9.2.1. Multipellet EPOC Reactor for the Electrochemical Promotion of NH$_3$ Synthesis. One of the first attempts to electropromote a commercial catalyst was reported by Yiokari et al.[361] for the NH$_3$ synthesis. The catalytic synthesis of ammonia from its elements via the Haber−Bosch process is of major industrial importance, and the high pressure synthesis is commonly catalyzed by Fe promoted with K$_2$O, CaO, and Al$_2$O$_3$. In that study, a commercial fully promoted Fe-based catalyst (BASF S6-10RED) was used, deposited on CaZr$_{0.9}$In$_{0.1}$O$_{3-\alpha}$, a proton conducting solid electrolyte. The catalyst was milled and deposited via a slurry. Because the commercial Fe-based catalyst is electronically conducting, as it is not supported on an insulating support (e.g., SiO$_2$, Al$_2$O$_3$), it was found that this catalyst film deposited on the H$^+$ conductor had sufficient conductivity to also act as an electrode of the solid electrolyte cell.

This electrochemical promotion study was novel in three respects: (a) the catalyst−electrode was a fully promoted industrial catalyst, (b) the study was carried out at high pressure (50 atm), and (c) this was the first attempt for the scale-up of an electrochemically promoted reactor since 24 CaZr$_{0.9}$In$_{0.1}$O$_{3-\alpha}$ cell-pellets, electrically connected in parallel, were placed in the high pressure reactor (Figure 53).[361]

The rate of ammonia production was enhanced by more than 1100% in the nitrogen-rich regime (Figure 54), upon potential application of −1 V between the working electrode and the Ag reference electrode. The extent of the NEMCA effect depends strongly on the kinetic regime of the reaction. Very pronounced non-Faradaic behavior is observed in the region $0.33 \leq$ H$_2$/N$_2 \leq$ 0.67 where ρ values of 12 or more are obtained (Figure 54).
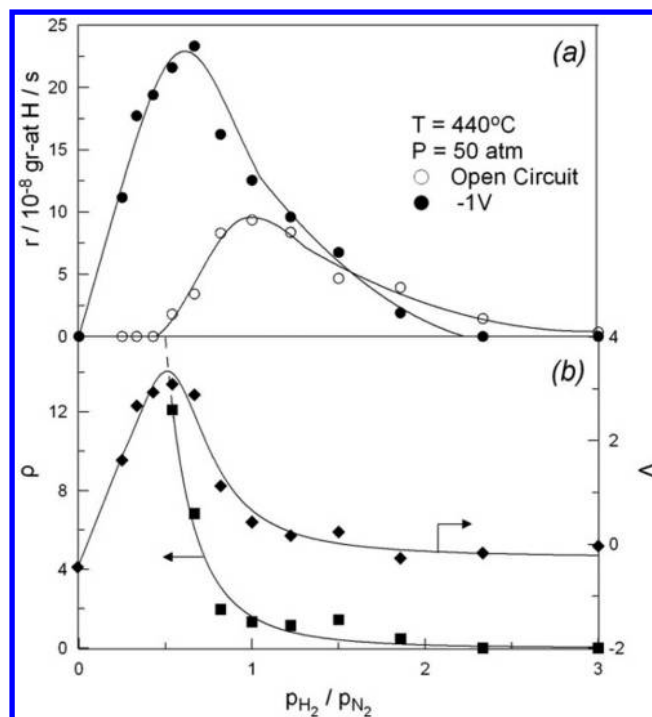
Figure 54. (a) Effect of inlet H$_2$/N$_2$ ratio on the rate of NH$_3$ synthesis over promoted Fe/CaZr$_{0.9}$In$_{0.1}$O$_{3-\alpha}$ under open-circuit (O) and for $U_{WR} = -1.0$ V (●). (b) Corresponding ρ (r/r_0) (■) and Λ (=$\Delta r_H/(-I/F)$) (◆) values. Reprinted with permission from ref 361. Copyright 2012 American Chemical Society.

In this case, the enhancement in the catalytic activity is due to the electrochemical supply of H$^+$ to the catalyst, which decreases the catalyst work function and thus strengthens the chem-

isorptive bond of electron acceptor N while at the same time weakening the bonds of electron donor H and NH_3.

4.9.2.2. Electropromotion of Thin Sputtered Metal Catalysts and Development of the Novel Monolithic Electrochemically Promoted Reactor (MEPR). A major thrust toward practical utilization of electrochemical promotion was realized through the confirmation of the feasibility of electropromotion of thin sputtered metal films[275,362] and the development of the monolithic electrochemically promoted reactor (MEPR).[275] Sputtered metal films on untreated YSZ surfaces, with a thickness of 40−50 nm, were reported to have a metal dispersion higher than 10−20%,[275] which is comparable to that of state-of-the-art conventional supported catalysts. The performance of these films is remarkable not only in terms of electrochemical promotion efficiency but also in reference to long-term stability and endurance.

On the other hand, the recently developed MEPR[275] provides a practical structured electrochemically promoted reactor, which allows, in principle, the transition from laboratory studies to practical applications. The MEPR can be considered as a hybrid between a classical monolithic honeycomb reactor and a planar solid oxide fuel cell. The core of the MEPR is a ceramic casing, made of machinable glass ceramic (MacorTM) (Figure 55). The
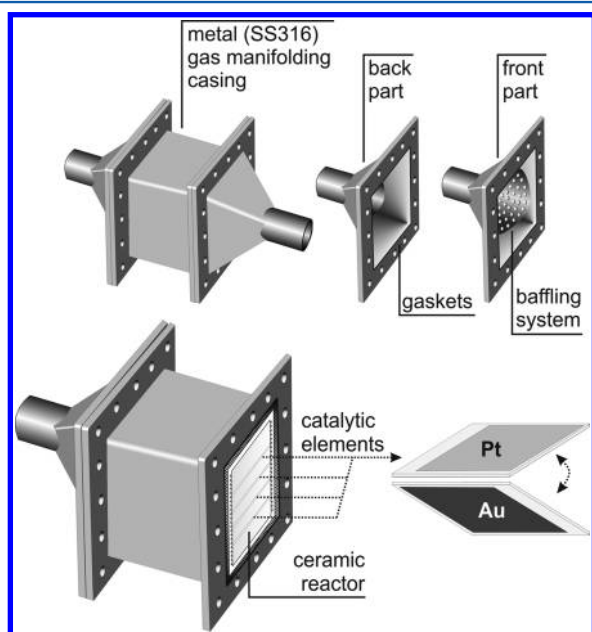
Figure 55. Schematic of the assembled monolithic electropromoted reactor (MEPR). Reprinted with permission from ref 275. Copyright 2012 Elsevier.

internal faces of the two opposing reactor walls have appropriately machined parallel grooves where a number of solid electrolyte plates are inserted. These surfaces are also used to create the two necessary current collectors, one establishing electrical contact with all catalyst films deposited on the top side of the plates, while the other current collector establishes electrical contact with all catalyst films deposited on the bottom side of the plates. In this way, a significant practical simplification is realized as both the top and the bottom catalyst films can be electrochemically promoted (with reverse polarity) via only two external connecting wires. The reactor is enclosed in a suitable metal casing of stainless steel with a baffling system at the gas entrance aiming to achieve as uniform a gas flow distribution as

possible at the gas entrance. A schematic of the assembled MEPR is shown in Figure 55.

The MEPR is a simple device that permits easy practical utilization of electrochemical promotion. It accomplishes an efficient and compact reactor design, which can be assembled and dismantled at will. In addition, the MEPR has only two external connecting wires, and its catalytic plates can be replaced whenever necessary. It exhibits excellent mechanical and thermal stability, enabling its use under harsh environments, such as in a car engine exhaust. Furthermore, it is possible to use one of the plates as a gas sensor element and utilize the potential signal generated by this element to dynamically control the current or potential applied to the electropromoted catalytic plates.

The electropromoted reactor has already been evaluated successfully for hydrocarbon oxidation and NO reduction by C_2H_4 or C_3H_6 in the presence of O_2 using both conventional thick films and thin sputtered noble metal electrodes.[275,362−370] Specifically, the MEPR with 22 Rh/YSZ/Pt parallel plate elements was found to promote selective catalytic reduction (SCR) of NO by 450% with near 100% selectivity to N_2, even in high excess of O_2 (10%) at temperatures 200−300 °C (Figure 56).[364] The corresponding Λ_{NO} and Λ_{CO_2} values were up to 2.4
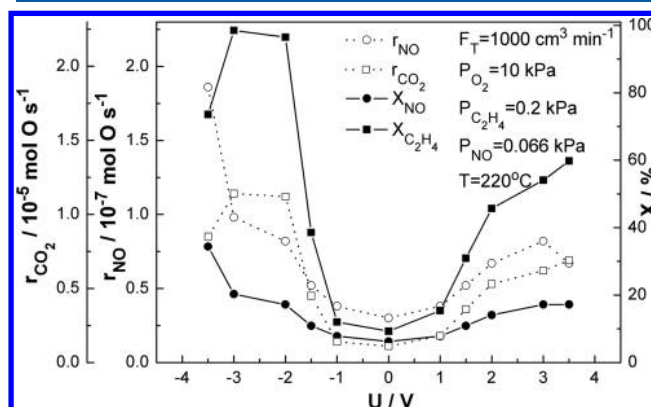
Figure 56. Steady-state effect of the applied potential on the NO conversion rate (r_{NO}), on the CO_2 formation rate (r_{CO_2}), and on the conversion of NO and C_2H_4 (x_{NO}, x_{C2H4}) at T = 220 °C, and highly oxidizing conditions.[364] Reproduced with permission from ref 364. Copyright 2008 Springer Science and Business Media.

and 350, respectively, and the rate enhancement ratio of complete C_2H_4 oxidation was up to 900%.[364] The monolithic electropromoted reactor was also tested under real conditions for the treatment of automotive exhaust gas of a diesel engine, demonstrating excellent mechanical and thermal stability after prolonged operation.[365] When HC exhaust port-injection was utilized, NO_x reduction was enhanced by electropromotion (ρ_{NO} = 0.7, Λ_{NO} = 3).[365] This advance appears to be promising for the use of MEPR in automotive exhaust pollution control.

Moreover, the MEPR was successfully operated and EPOC of ethylene oxidation was induced on active skeletal-Pt-catalysts at flow rates as high as 56 L min^{-1} (Λ = 30), mean gas residence times of 0.34 s, and reactor space velocities up to 2.7×10^4 h^{-1}, showing the strong potential of this reactor for practical applications.[366]

MEPR units with up to 22 thin Rh/YSZ/Pt or Cu/TiO$_2$/YSZ/Au plate cells were used to investigate the hydrogenation of CO_2 at atmospheric pressure and temperatures 220−380 °C. The Rh/YSZ/Pt cells led to CO and CH_4 formation, and the open-circuit selectivity to CH_4 was less than 5%. Both positive and negative
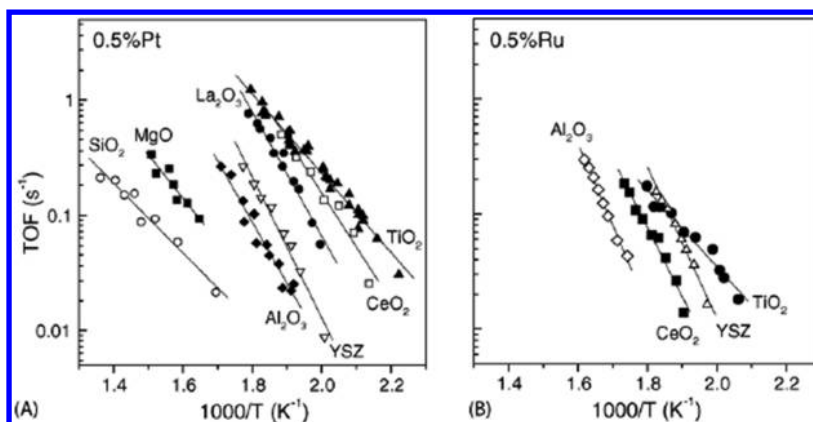
Figure 57. Effect of the nature of the support on the turnover frequency of CO conversion of (A) Pt and (B) Ru catalysts (0.5 wt %) supported on the indicated metal oxide powders. Reprinted with permission from ref 378. Copyright 2012 Elsevier.

applied potentials significantly enhanced the total hydrogenation rate, but the selectivity to CH_4 remains below 12%. The Cu/TiO_2/YSZ/Au cells produced CO, CH_4, and C_2H_4 with selectivities to CH_4 and C_2H_4 up to 80% and 2%, respectively. Both positive and negative applied potential significantly enhanced the hydrogenation rate and the selectivity to C_2H_4. It was found that the addition of small (ca. 0.5 kPa) amounts of CH_3OH in the feed had a pronounced promotional effect on the reaction rate and selectivity.[369] The effect of electrochemical promotion of catalysis on the SO_2 oxidation reaction was investigated over thin (<40 nm) Pt catalyst electrodes interfaced with YSZ, in a MEPR equipped with 5 or 22 electrocatalytic plates. A mildly oxidizing gas mixture was used at temperatures from 330 to 370 °C and flow rates between 1 and 30 L min^{-1}. It was found that positive potential applications can cause an increase of up to 200% in the catalytic oxidation rate of SO_2 with Faradaic efficiency values up to 30 at flow rates as high as 30 L min^{-1}, which corresponds to 3×10^4 h^{-1} space velocity or 0.1 s residence time.[370] The MEPR can, conceptually, be scaled-up (or scaled-down) following a stack design and can, in principle, be used for many practical applications in exhaust treatment units and in chemical destruction or synthesis processes.[371]

## 5. IONIC CONDUCTING CERAMIC SUPPORTS FOR CONVENTIONAL DISPERSED CATALYSTS

5.1. Key Characteristics of Metal Support Interactions (MSI)

This section gives a short overview of the phenomenon of metal−support interactions (MSI), which can play a key role in the design of successful commercial finely dispersed nanoparticle catalysts. It also discusses the similarities between MSI and EPOC, which have been demonstrated by several studies.

It is well established that many supports of heterogeneous catalysts, besides altering physical properties of the catalytic system, such as providing high dispersion and surface area for the catalyst, have also a chemical role in catalysis and are not inert as initially thought. Even when the active phase has the same dispersion or average crystallite size, the support can have a dramatic effect on the catalytic activity or selectivity due to the phenomenon of metal−support interactions.[1,8,372−377] This phenomenon is known as Schwab effect of the second kind or, more commonly, metal−support interactions (MSI) and refers to the effect of the support on the catalytic properties of the supported metal. In contrast, the effect of a supported metal on the catalytic properties of a metal oxide is known as Schwab effect of the first kind. Although geometric factors are known to have an

important effect on some of these systems, it is generally accepted since the works of Volkenstein, Schwab, and Solymosi that electronic effects are more important. A typical recent example of MSI is given in Figure 57.

In this study, Panagiotopoulou and Kondarides[378] used Pt and Ru catalysts with the same metal loading (0.5 wt %) supported on a variety of commercial oxide powders for the water−gas shift (WGS) reaction. Figure 57 shows the effect of the nature of the oxide carrier on the catalytic performance of these catalysts. The authors have concluded that both Pt and Ru catalysts exhibit significantly higher activities when supported on "reducible" (TiO_2, CeO_2, La_2O_3, and YSZ) rather than on "irreducible" oxides (Al_2O_3, MgO, and SiO_2). When noble metals are dispersed on "reducible" oxides, such as CeO_2 and TiO_2, the apparent activation energy of the reaction was found not to depend on the nature of the metallic phase but only on the nature of the support. Their results are in accordance with a Mars−van Krevelen type mechanism for the WGS reaction, where CO molecules adsorbed on the metal are oxidized by oxygen originating from the support, which in turn is oxidized by water. Let us note that in this study the oxygen mobility of the support is discussed in terms of the oxide reducibility. However, another way to look at Figure 57 is to note that the supports with the higher anionic conducting (YSZ) or mixed anionic−electronic conductivity (CeO_2, TiO_2, La_2O_3) are the best.

The nature of metal−support interactions has been the focal point of extensive research and dispute particularly after the discovery by Tauster[183] of the phenomenon of SMSI.

In his early work,[183] Tauster and his co-workers used different group VIII metal particles (Ru, Pt, Pd, Ir, Rh, Os) supported on TiO_2 and investigated their capacity to chemisorb H_2 and CO after reduction at 200 and 500 °C. Their results showed that the chemisorption properties of the metals are strongly related to the reduction degree of the support, providing evidence for a strong interaction between the noble metal and TiO_2.[183] On the basis of these observations, Tauster and Fung[379] studied further the SMSI effect by examining the chemisorption properties of Ir catalysts supported on numerous oxides. Correlation was provided between MSI activity and reducibility among saturated transition metal oxides, highlighting the need for using reducible, transition metal oxide supports.[183,379]

Since the discovery of the effect of SMSI, it was proposed by Tauster[183,379] that its mechanism does not involve encapsulation or deposition of impurities. Two possible mechanisms were discussed by Tauster[380] in terms of (a) metal−metal bonding

between the noble metal and the titanium cations, that is, charge transfer from the Ti^{3+} cations of the support to the Pt metal can disturb the electronic density on the metal particle surface and thus modify its ability to adsorb reactive gases; and (b) the formation of intermetallic compounds (e.g., of the type of Pt_3Ti or Ir_3Ti).

Up to date, the origin of the SMSI effect is still not fully clarified. The thorough understanding of metal–support interactions is one of the greatest challenges in heterogeneous catalysis.

Two main schools of thought existed, which focused on the following:

(i) the particle-size effects and electronic interactions (charge transfer) between the metal particles and the support, and

(ii) the migration of oxide species from the support onto the catalyst particle surface, known as "decoration".[184]

Meriaudeau et al.[381] embraced the Fermi level adjustment theory and attributed SMSI to the formation of intermetallic bonds with charge transfer from the support to the metal crystallites. According to this model, after strong reduction of the TiO_2 support, its Fermi level becomes higher than this of the metal. When the metal particles are in contact with reduced TiO_2, an adjustment of the Fermi level occurs at the metal–support interface (i.e., electrons are transferred from the reduced support toward the metal, and therefore the metal particles are negatively charged).

From another point of view, MSI was related to the formation of suboxides (e.g., TiO_x), and their diffusion on the surface of the bulk metal can cause perturbation in the relative competition between the reactant gases for chemisorptions sites and thus alter the catalytic rate.[184,382,383] Many investigators have shown that the geometric decoration model can be responsible for the SMSI state.

Relation between MSI and structural changes of the catalyst has been also proposed,[384] suggesting that the 3D-structure of the metal crystallites can be altered due to chemical transformations of the support during reduction and that this structural modification can affect the adsorption characteristics and thus catalytic activity.

Oxygen vacancies in the support[385] have been also credited to be responsible for the MSI effect due to their possible interaction with metal particles. This model introduces the possibility of metal particle decoration by oxygen ions ($O^{\delta-}$) and the participation of these ions on the chemisorptive properties of the catalysts. Even if the origin of MSI is not fully clarified, recent studies were performed to compare the magnitude of MSI with that of EPOC by using metal-supported catalyst on oxygen ionic conductors such as TiO_2. These experiments seem to demonstrate that the two phenomena can be explained by a similar process, that is, the backspillover of O^{2-} ionic species onto the metallic particles. The self-driven NEMCA mechanism,[23] recently confirmed using $^{18}O_2$ isotopic tracer experiments,[233,293] which describes the electrochemical promotion of the catalytic activity of a metallic nanoparticle in contact with a grain of ionically conducting support, without any electrical polarization, finally merges EPOC and MSI at the nanometric scale.

5.1.1. Comparison between EPOC and Metal–Support Interactions. A link between EPOC and metal–support interactions was first established in 1993 by Cavalca, Larsen, Vayenas, and Haller.[384] These authors have investigated the electrochemical promotion of methanol oxidation on Pt deposited on YSZ in a single chamber reactor (Figure 58). The presence of a negative self-created potential (electromotive
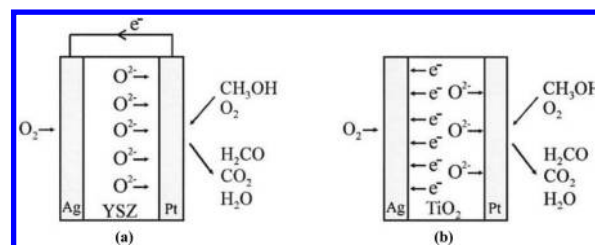

Figure 58. Self-driven electrochemical promotion of CH_3OH oxidation on Pt using O^{2-} conductor (YSZ) with external catalyst–counterelectrode short-circuiting (a) and mixed ionic (O^{2-})–electronic conductor (TiO_2) with internal short-circuiting. Reprinted with permission from ref 386. Copyright 2012 American Chemical Society.

force) ($U_{WR} \approx -0.3$ V) between the Pt catalyst and the Ag counter and reference electrodes under open-circuit conditions (as one observes in any electrochemical promotion study using the single-chamber reactor) was noticed, which is due to faster oxygen consumption by the catalytic methanol oxidation on Pt than on Ag. This property is, for instance, utilized in the concept of single-chamber fuel cells.[387]

This electromotive force together with the electrophobic behavior of methanol oxidation on Pt (i.e., this reaction is promoted by O^{2-} supply to the catalyst) motivated the authors to develop a self-driven NEMCA system, simply by short-circuiting the catalyst and the counter electrode without using any external power source (galvanostat or potentiostat).[386]

Upon short-circuiting, the Fermi levels of the Pt catalyst and of the Ag counter electrode become equal and O^{2-} are continuously supplied to the Pt catalyst to equilibrate the oxygen chemical potentials on Pt and Ag. Because the catalytic reaction on Pt is very fast, this equilibration cannot be established, causing a continuous and stable O^{2-} flux to the Pt catalyst and also a continuous replenishment of the spent O^{2-} by gaseous O_2 at the Ag counter electrode. The electrical circuit is complete, because electronic current flows through the short-circuiting wire and compensates the O^{2-} flux (Figure 58a). Positive currents, that is, O^{2-} pumping to the Pt catalyst, can cause up to 2-fold increase in the rate of H_2CO formation and on the selectivity to H_2CO. The measured Λ values are of the order of 100. The changes in the CO_2 production are negligible. This self-driven NEMCA system is suitable for promoting any electrophobic reaction.[384]

The authors suggested the replacement YSZ by TiO_2, which presents both ionic (O^{2-}) and electronic conductivity, widely used in MSI. In this case, there is no need for a short-circuiting wire, because electronic current can pass through the TiO_2 pellet itself. Under these conditions, there is no net current flowing in the TiO_2 pellet, electrons migrate from the Pt to the Ag electrode, while O^{2-} migrate onto the Pt catalyst surface to electropromote the reaction (i.e., the O^{2-} current in TiO_2 is equal and opposite to the electronic current as depicted in Figure 58b).[8]

The experiments of self-driven NEMCA without any electrical polarization demonstrate that supported dispersed catalysts can also be electropromoted if the support is an ionic conductor. Because O^{2-} backspillover can take place over micrometer distances on the porous Pt films used for EPOC studies with YSZ and TiO_2, it can certainly take place over nanometer distances on the supported Pt nanoparticles of commercial highly dispersed YSZ and TiO_2-supported catalysts. The experiments by Cavalca et al. in conjunction with the XPS studies[8,23] presented in section 4.2.3 seem to indicate that the mechanism of metal–support interaction promotion of catalytic oxidations can be similar to the

mechanism of self-driven electrochemical promotion systems and is based on self-induced migration of promoting O^{2-} species on the nanoparticle catalyst surface. Such self-driven NEMCA (or metal–ionically conducting support interaction supported) effects[8] can be implemented:

(i) with the usual distribution of nanoparticles in commercial ZrO_2- or TiO_2- or CeO_2-supported noble metal catalysts, where each two dissimilar size crystallites create a small local galvanic cell able to electrochemically promote one of the two nanoparticles,

(ii) with mixed conducting supports (TiO_2, CeO_2) but also on doped ZrO_2, where direct replenishment of O^{2-} by gaseous O_2 is rather efficient.

A recent example of self-driven NEMCA effect on metallic nanoparticles was presented by Vernoux et al.,[388] who investigated the catalytic performance for propane deep oxidation of nanodispersed catalyst powder of Pt/YSZ under various thermal pretreatments. It was shown that thermally induced migration of O^{2-} ionic species from YSZ to the Pt surface can promote strongly the propane combustion.

Figure 59a shows the O_2-TPD spectra recorded after adsorption of oxygen
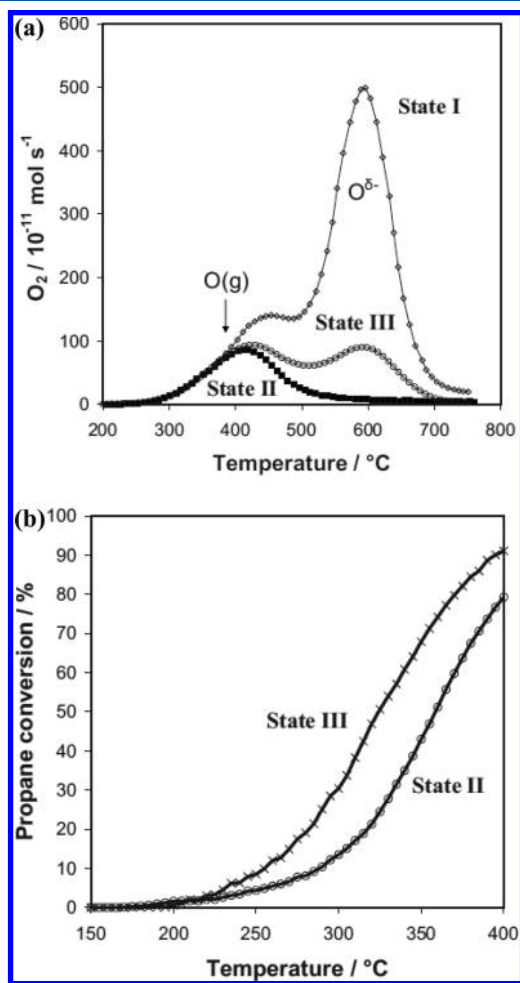

Figure 59. (a) O_2-TPD spectra recorded after adsorption of oxygen on the Pt/YSZ powder catalyst at states I, II, and III. (b) Comparison of the catalytic activity for propane combustion of Pt/YSZ nanodispersed catalysts at states II and III. Reproduced with permission from ref 388. Copyright 2012 The Electrochemical Society.

(i) at 300 °C for 1 h on the fresh Pt/YSZ-supported catalyst (denoted as state I),

(ii) at 300 °C for 1 h on the Pt/YSZ-supported catalyst after the first TPD (denoted as state II), and

(iii) at 500 °C for 1 h on the Pt/YSZ-supported catalyst after the second TPD (denoted as state III).

Two distinct oxygen desorption peaks were observed in the first and third TPD spectra, while only one was in the second one (Figure 59a). The presence of two peaks on Pt-supported catalysts is unusual and was attributed to O_2 desorption from the Pt accessible surface, which clearly demonstrates the coexistence of two different binding strengths of chemisorbed oxygen on the Pt surface, suggesting two O adsorption states. As was already shown in Figure 30, the first peak is due to gaseous chemisorbed oxygen and the second one is due to migration of oxygen ionic species from the YSZ bulk. The TPD spectrum of state II exhibited only one oxygen desorption peak corresponding to gaseous chemisorbed oxygen, as after the first TPD, YSZ was practically depleted, and no more non-stoichiometric oxygen species existed in the bulk. Therefore, the migration of ionic species became impossible. The pretreatment at 500 °C under oxygen was effective for replenishing the YSZ bulk and thus revealing the second peak in the TPD spectrum.

Figure 59b shows the catalytic performance of propane deep oxidation with Pt/YSZ catalysts at states II and III. Above 220 °C, the catalytic activity of state III was higher than that of state II. As the two states possessed similar Pt dispersion, that is, 13%, the only difference between the two catalysts was their ability to induce thermal migration of O^{2-} species from YSZ.[388]

This confirms that O^{2-} ionic species are effective promoters for alkane deep oxidation, which is in agreement with the findings of EPOC experiments,[23] described in section 4 in which a Pt/YSZ electrochemical catalyst can be activated by a positive polarization, that is, by electrochemically supplying O^{2-} species on Pt. These results provide evidence that EPOC can be induced without any electrical polarization by using nanoparticles of metallic catalysts supported on ionic conducting ceramics,[388] as in MSI processes.

In another study, Nicole et al.[257−259,263,264] used the ethylene oxidation as a model reaction in three independent catalytic systems to compare EPOC and MSI (Figure 60). This study examined:

(i) The open-circuit and NEMCA-induced catalytic activity of IrO_2 and of mixed IrO_2−TiO_2 catalytic films deposited on a YSZ dense membrane (Figure 60a). The latter catalyst consists of nanoparticles of IrO_2 (active phase) in intimate contact with micrometric grains of TiO_2 (inert support) with different loadings of IrO_2.

(ii) The unpromoted (open-circuit) and NEMCA-induced (under polarization) catalytic activity of Pt films deposited on YSZ and on TiO_2 (Figure 60b).

(iii) The enhancement in catalytic activity of Rh catalysts induced by EPOC via the electrochemical supply of O^{2-} from YSZ to a Rh catalyst film (polarization, Figure 59c, left) and via metal–support interactions (Figure 60c, right) between dispersed Rh nanoparticles (with 0.5 wt % metal loading) on various porous high surface supports (TiO_2, SiO_2, γ-Al_2O_3, YSZ, and TiO_2 doped with 4 mol % WO_3).

First, let us consider the study of the electrochemical promotion of ethylene oxidation on IrO_2−TiO_2 catalytic films interfaced on a YSZ dense membrane. Different compositions of
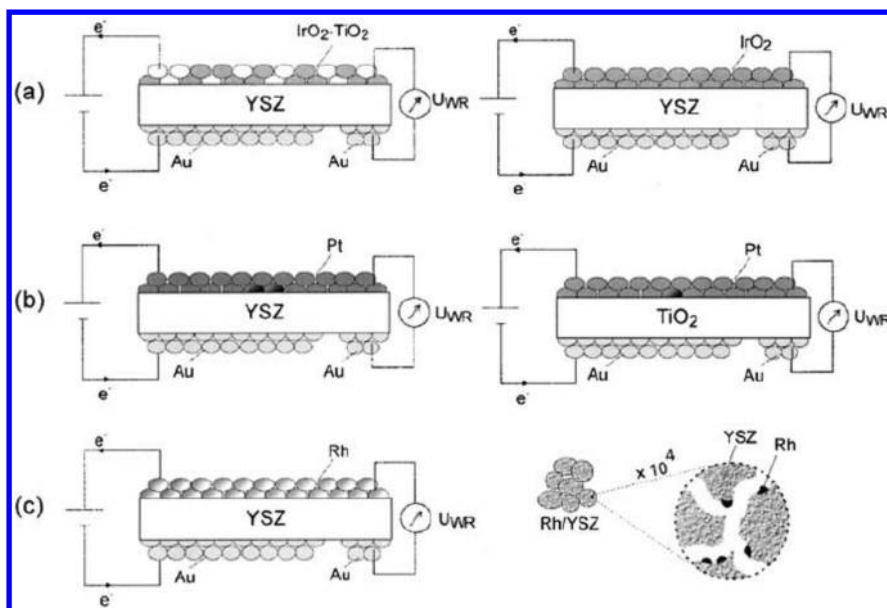
Figure 60. Schematic of the experimental setup used (a) to induce electrochemical promotion (via YSZ) on IrO_2 and IrO_2-TiO_2 porous catalyst films, (b) to compare the electrochemical promotion induced on Pt via YSZ and via TiO_2, and (c) to compare the electrochemical promotion behavior induced by varying U_{WR} on a Rh porous catalyst film (left) and on a fully dispersed Rh catalyst supported on porous (80 m^2/g) YSZ support. Reprinted with permission from ref 264. Copyright 2012 Elsevier.

films were prepared to investigate the EPOC magnitude (under positive polarization) as a function of the TiO_2 content in the film (0, 25, 50, 75, 100 mol %). Note that pure TiO_2 (X_{IrO2} = 0) is always inactive (Figure 61). The maximum EPOC enhancement was observed with pure IrO_2 (X_{IrO2} = 100%) catalyst, when application of +200 μA leads to 11-fold increase in the catalytic rate (Figure 61).[264] As was also shown in Figure 61, there is no significant electrochemical promotion (ρ < 1.5) of the mixed IrO_2-TiO_2 catalyst whatever the IrO_2 loading. This suggests that
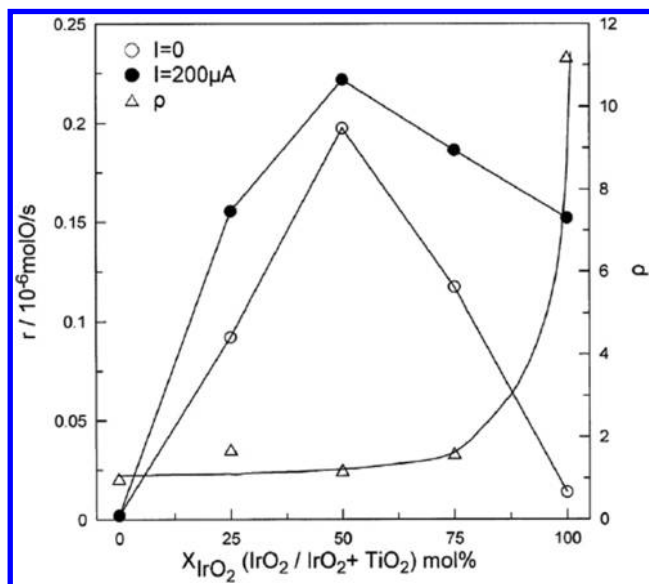
Figure 61. Effect of the mole fraction, X_{IrO2}, of IrO_2 in the IrO_2-TiO_2 catalyst film on the rate of C_2H_4 oxidation under open-circuit conditions (○) and under electrochemical promotion conditions (●) via application of I = 200 μA, T = 380 °C, p_{C2H4} = 0.15 kPa, p_{O2} = 20 kPa. The "△" indicate the corresponding electrochemical promotion rate enhancement ratio r values. Reprinted with permission from ref 264. Copyright 2012 Elsevier.

IrO_2 in the IrO_2-TiO_2 catalyst is already in an electrochemically promoted state due to MSI.

The authors proceeded to quantify the magnitude of the MSI effect on the catalytic rate by defining a rate enhancement ratio in a manner similar to that of EPOC. Therefore, the parameter ρ_{MSI} was defined from:

$$\rho_{MSI} = r/r_u \tag{41}$$

where r_u was the unpromoted catalytic rate (when no MSI takes place) per unit mass of the active catalyst and r was the same (promoted) catalytic rate enhanced due to the metal−support interaction. For this system, the authors have considered r_u as equal to the rate measured on pure IrO_2.

In view of this equation, the maximum enhancement via MSI is observed (Figure 61) at X_{IrO2} = 50%. The maximum value of ρ_{MSI} was equal to 13, very close to the EPOC rate enhancement ratio observed upon polarization with the pure IrO_2 film. Nevertheless, even the higly efficient catalyst (50 mol % IrO_2/50 mol % TiO_2) can be slightly electropromoted (ρ = 1.1).

The authors also explored EPOC on Pt films deposited on YSZ and TiO_2. Similar electrochemical promotion behavior was obtained with both systems.[8,263] The presence of similar O^{2-} backspillover mechanism on Pt from YSZ and TiO_2 was confirmed by in vacuum XPS. As expected, the application of a positive current caused a pronounced increase in the catalytic rate (25-fold increase for Pt/YSZ and 22-fold increase for Pt/TiO_2). The values of the Faradaic efficiency were 74 × 10^3 for Pt/YSZ and only 1.88 × 10^3 for Pt/TiO_2, implying that only a fraction of about 2.5% of the current in TiO_2 is anionic (O^{2-}) and the rest is electronic, in good agreement with the literature.[219]

As is shown in Figure 60c, a detailed comparative study was carried between electropromoted Rh/YSZ catalysts (films of Rh deposited on a dense YSZ pellet) and conventional catalysts (Rh nanoparticles dispersed on various supports). The kinetics of C_2H_4 oxidation were investigated on Rh films interfaced with YSZ at various imposed potentials and thus imposed work function values, Φ (i.e., under conditions of electrochemical

promotion). In parallel, the impact of the work function of the oxide support on the catalytic activity of finely dispersed Rh catalysts was examined by using the same operating conditions. The different supports were TiO_2 (undoped and doped with WO_3), γ-Al_2O_3, YSZ, and SiO_2 (Figure 62).[264]

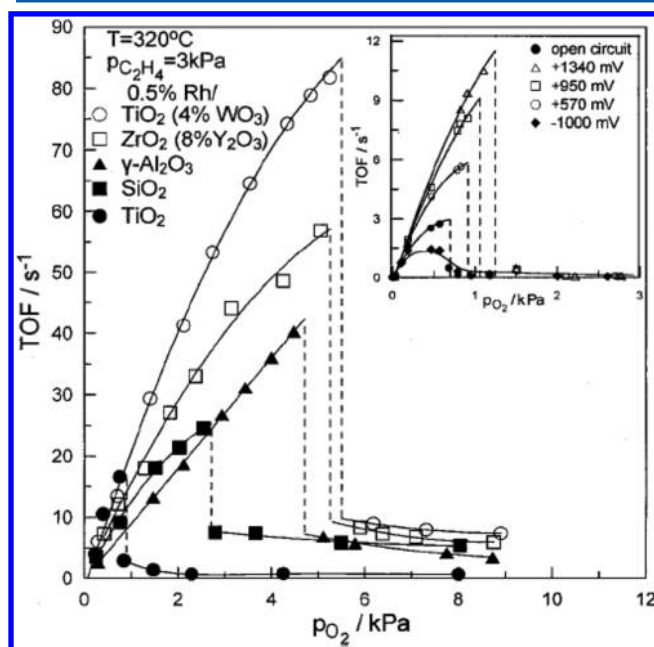**Figure 62.** Effect of p_{O_2} on the rate of C_2H_4 oxidation on Rh supported on five supports of increasing Φ. Catalyst loading 0.5 wt %. Inset: Electrochemical promotion of a Rh catalyst film deposited on YSZ. Effect of potentiostatically imposed catalyst potential U_{WR} on the rate and TOF dependence on p_{O_2} at fixed P_{C2H4}. Reprinted with permission from ref 264. Copyright 2012 Elsevier.

It was established that the reaction kinetics are affected in the same way upon varying the work function of the Rh film via electrical polarization of the Rh/YSZ interface (EPOC) or upon varying the work function of the support of the dispersed Rh catalysts (MSI) (Figure 62). The observations of this study give a clear demonstration of the equivalence of the promoting mechanism of MSI and electrochemical promotion (i.e., O^{2-} migration onto the catalyst surface). The carrier can continuously supply promoting oxygen ionic species to the catalyst surface, while spent oxygen in the support can be continuously replenished by gaseous oxygen.

It appears that the mechanism of MSI on various supports is similar to that of EPOC without the need of electrical polarization. For this process (backspillover of oxygen ions from the support material to the surface of the metal crystallites) to be effective, the support material must possess sufficient ionic conductivity. Stated differently, EPOC can be considered as an electrically controlled MSI. It also appears that at least certain types of metal−support interactions are induced by reverse spillover of oxygen anions from the carrier onto the surface of the metal crystallites as shown schematically in Figure 63.[264] A difference between the two phenomena of MSI and EPOC is that in EPOC experiments the spillover−backspillover rate can be accurately measured and controlled by simply measuring the imposed current or potential.

5.2. Comparison between Chemical and Electrochemical Promotion of Catalysis

The performance of dispersed metal catalysts can be improved by addition of promoters that enhance either activity, selectivity, or both.[389,390] Alkali metal compounds are commonly employed as promoters of metal catalysts. Therefore, alkali adsorption using single crystal model systems has been investigated by the methods of surface science.[391]

Most of these single crystal studies are carried out under conditions of ultrahigh vacuum. Although in favorable cases such data[390] can be directly related to the behavior of practical catalysts working at atmospheric pressure,[393] in general the linkage between the two is more tenuous.

Lambert and co-workers have used EPOC to investigate the efficacy of Na^+ as a promoter of Pt for reactions of environmental importance, such as CO oxidation,[394] NO reduction by CO,[213] and by propene.[382,383] It was shown, for all of these reactions, that Na^+ supplied electrochemically from a β''-Al_2O_3 solid electrolyte (a Na^+ ion conductor described in section 3.2) strongly affects both catalytic activity and selectivity of Pt catalyst films.[213,394−396]

Examples are presented in Figure 64 for the selective catalytic reduction of NO by propene.[395] The electrochemically supply of Na^+ on the catalyst surface, upon applying negative over-potential, promotes the production rates of N_2, N_2O, and CO_2. Unfortunately, the selectivity toward N_2 was not significantly modified. The authors reported that, in every case, the system was perfectly reversible and exhibited no hysteresis when switching between negative and positive catalyst potentials.

This group has also investigated the Na promotion, chemically added, of NO_x reduction by propene over conventional dispersed catalysts. In particular, they studied the $NO+C_3H_6$
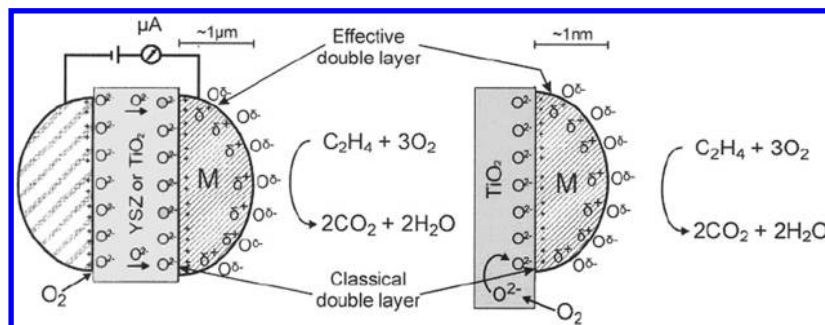
Figure 63. Schematic of a metal grain (μm) in a metal catalyst film deposited on YSZ or TiO_2 under electrochemical promotion conditions (left), of a metal nanoparticle (nnm) deposited on a porous TiO_2 support (right) showing the locations of the classical double layers formed at the metal−support interface, and of the effective double layers formed at the metal−gas interface. Reprinted with permission from ref 264. Copyright 2012 Elsevier.
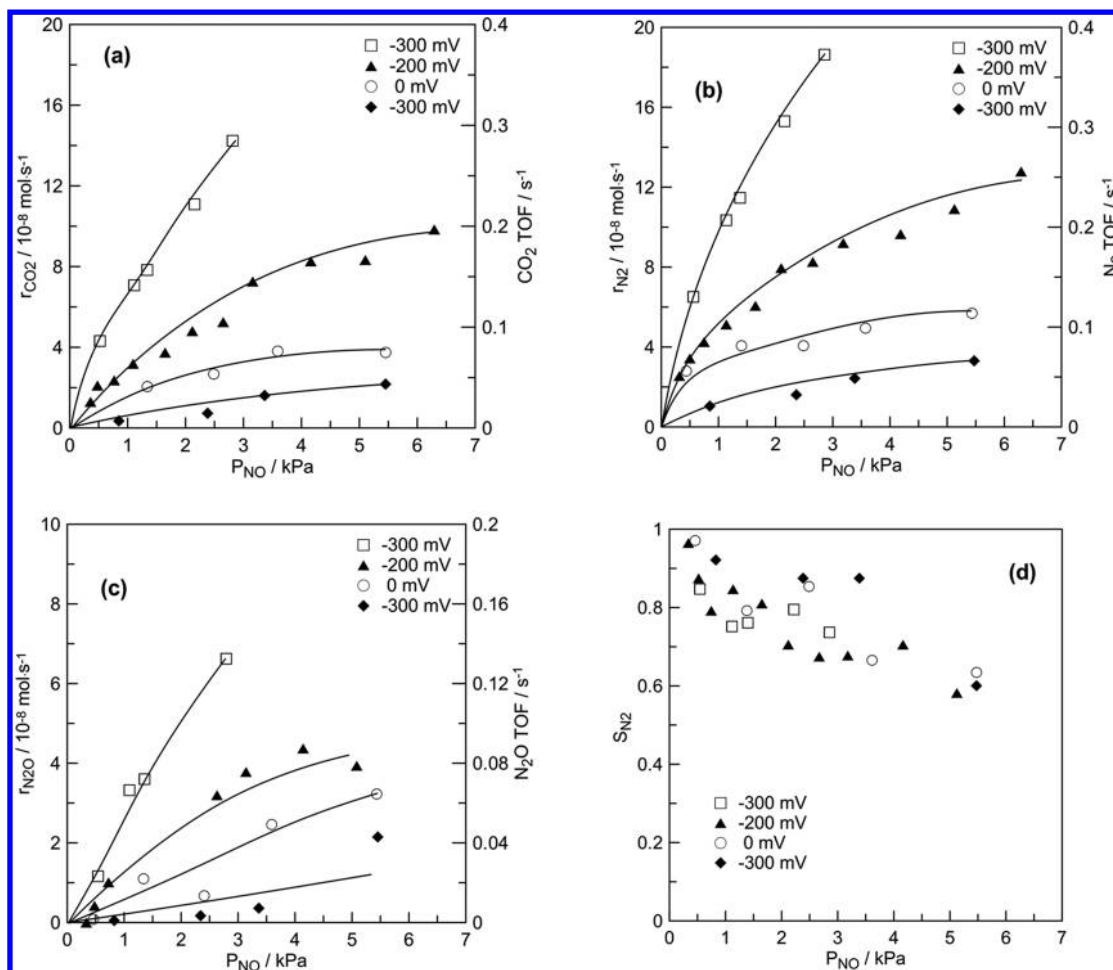
Figure 64. Effect of NO partial pressure (P_{NO}) on the rate of (a) CO_2, (b) N_2, (c) N_2O production as well as on N_2 selectivity denoted as S_{N2} (d) at different catalyst potentials U_{WR}. Electrochemical catalyst: Pt/β''-Al_2O_3. Conditions: P_{C3H6} = 0.27 kPa, T = 648 K, total flow rate, F_t = 1.3 × 10^{-4} mol/s. Reprinted with permission from ref 395. Copyright 2012 American Chemical Society.

reaction over catalysts in which the active phase (Pt) was dispersed on γ-Al_2O_3 carrier. This catalyst was doped by impregnation with different sodium loadings.[396] Figure 65 depicts the effect of the sodium loading on N_2, CO_2, and N_2O turnover rates. Promotion is maximized for a sodium content of 4 wt %. Further increase in the sodium loading (up to 10.4 wt %) leads to a slight inhibition of the rates. All rates exhibit an exponential increase with increasing sodium loading in the interval 0−4 wt % Na (Figure 65). Enhancement ratios, ρ, values as high as $\rho_{N2} \approx 300$, $\rho_{CO2} \approx 250$, $\rho_{N2O} \approx 7$ were found for the production of N_2, CO_2, and N_2O, respectively.[397]

Close similarities between electrochemically promoted catalysts (Pt film interfaced on a NASICON membrane, described in section 3.2.2)[318] and conventionally promoted highly dispersed catalysts (Pt/γ-Al_2O_3)[398] were also reported by Vernoux and co-workers for the same reaction but in the presence of large excess of oxygen. Application of negative overpotentials through a Pt/NASICON interface significantly improves the Pt catalytic performance in the oxygen-rich C_3H_6/NO/O_2 atmosphere. Negative potential application to a Pt film on NASICON leads to a spillover of Na ions from the electrolyte onto the Pt surface. At 295 °C, the authors observed that the application of −100 mV leads to the enhancement of NO and C_3H_6 conversions, while the selectivity to N_2 increases from 41% to 61%. The same promoting effect was observed for the case of highly dispersed catalysts. In particular, the selectivity to N_2

improved from 25% on the Na free Pt on γ-Al_2O_3 to 45% on the catalyst with 5 wt % Na.[398] Therefore, the two ways of Na addition to Pt (electrochemical or chemical) lead to similar improvements of the Pt catalytic performance.

The authors concluded that the promotion is mainly due to the electronic interactions of Na^+ with the platinum particles. The detailed comparison between the amounts of the electrochemical and chemical Na addition needed to cause the same effect on the catalytic rate suggests that during chemical addition a large fraction of the promoter is in contact with the support but not with Pt active sites, revealing the advantage of the electrochemical addition.[398] These promotional effects were explained on the basis of the variation of the work function (WF) of Pt according to the rules of classical and electrochemical promotion.[398] The consequence of applying a negative overpotential, when supplying Na^+ to Pt, is to weaken the Pt chemical bonds with electron-donor adsorbates, such as C_3H_6, and to strengthen those with electron-acceptor ones, such as O_2 and NO. Therefore, whatever the mode of Na addition (electrochemical or chemical), the tentative interpretation of the Na effects operates in the same direction, a strengthening of the Pt−O and Pt−NO bonds and a weakening of the Pt−C_3H_6 bond. This assumption is supported by the elegant use of XPS, by Lambert and co-workers,[399] in conjunction with electrochemical promotion with cationic conductors. These authors have shown that sodium introduced on Pt surfaces from the gas phase
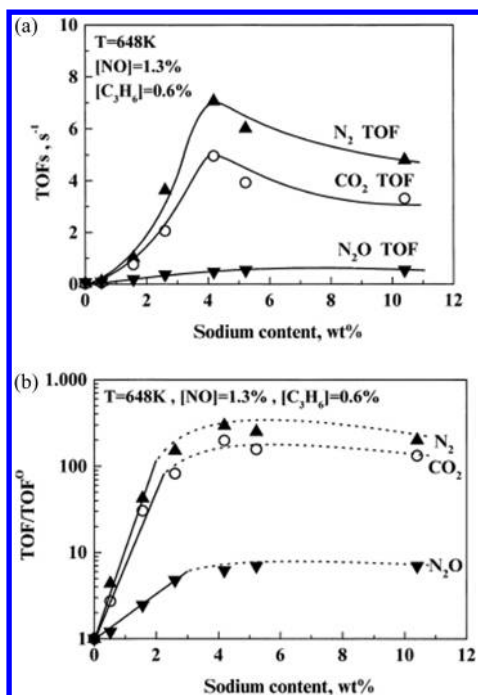
AY

dx.doi.org/10.1021/cr4000336 | Chem. Rev. XXXX, XXX, XXX−XXX

Figure 65. (a) The effect of sodium on (a) the turnover frequency (TOF) and on (b) rate enhancement ratios (TOF/TOF°) for N_2, CO_2, and N_2O productions. TOF and TOF° refer to turnover frequencies of Na-promoted catalyst and Na-free catalyst, respectively. Conventional dispersed catalysts: Pt/γ-Al_2O_3. Condition: T = 648 K, [NO] = 1.3%, [C_3H_6] = 0.6%. Concentrations refer to reactor outlet. Reprinted with permission from ref 397. Copyright 2013 Elsevier.

(classical promotion) is indistinguishable (for time scales shorter than that of a catalytic turnover, i.e., typically from 10^{-2} to 10^2 s) from sodium introduced on the same Pt surface via electrical current application between the Pt catalyst and a counter electrode deposited on the same β''-Al_2O_3 component (electrochemical promotion).

All of these studies demonstrate that the electrochemical[316,392−395] or chemical[397,398] supply of Na^+ on Pt-based catalysts leads to similar modifications in the catalytic activity, whatever the nature of the catalyst, that is, dispersed nanoparticles of Pt or percolated Pt films. Moreover, the rules developed for EPOC can be used to interpret the effects of a classical chemical promotion on the catalytic activity.

5.3. Overview of Recent Catalytic Studies Using O^{2-} Ionically Conducting Supports

The self-driven NEMCA concept described in the previous sections clearly creates several new possibilities for supported metal catalysts. Ionically conducting supports can provide promoting ionic species to metallic active sites. In addition, ionically conducting ceramics possess surface oxygen vacancies, which can also be considered as active sites in catalysis. This section gives an overview of recent selected catalytic studies using conventional dispersed catalysts supported on oxygen conducting ceramics. As the ionically conducting support is used as a reservoir of ionic promoting species, most of the studies are focused on oxygen conductors, which can be continuously replenished if oxygen (in the form of O_2, CO_2, or H_2O) is present in the reaction feed, as was commonly observed. Studies presented in this part were selected because the role of ionic conductivity and/or surface oxygen vacancies in the catalytic process was clearly proposed by the authors. Furthermore, metal−support interactions driven by the presence of oxygen vacancies and/or ionic mobility were observed and discussed. Moreover, we decided to not discuss the utilization of perovkistes in catalysis even though they are widely investigated because many factors affect their activity, not only their electrical properties.

5.3.1. Use as Catalysts. Oxygen ion conductors used in the fuel cell and oxygen sensor technology have also a significant role in catalysis. Gellings and Bouwmeester[39,400] have published in 1992 and in 2000 two comprehensive reviews of the catalytic studies on solid oxides, which display oxygen ion and mixed conductivity. In these papers, they tried to correlate the catalytic activity and selectivity with the electrical conducting properties of the oxides, which depend on their crystal and defect structures (Table 4).

In general, the intrinsic catalytic activity of O^{2-} conducting solid electrolyte, and of most other ceramics, is much lower than that of metals for most reactions at the same temperature, and thus high temperatures, typically above 500 °C, are necessary to reach practical reaction rate values.

Yttria-stabilized zirconia has received recent attention as a methane partial oxidation catalyst because of its substantial

Table 4. Recent Catalytic Studies Using O^{2-} Conducting Ceramics as Catalysts

catalytic system	reaction involved	T, °C	key parameter of the system	ref
YSZ	partial and total oxidation of CH_4	500−800	Mars van Krevelen mechanism	400
YSZ, ZrO_2	partial and total oxidation of CH_4	500−900	extrisnsic oxygen vacancies	402−405
CaO stabilized ZrO_2	partial and total oxidation of CH_4	545−710	high oxygen mobility	406
YSZ	C_3H_6 and C_7H_8 oxidation	25−450	oxygen vacancies	408
ZrO_2 doped with Y_2O_3 and CaO	CO and CO_2 hydrogenation	425	oxygen vacancy availability and ionic conductivity	410−412
ZrO_2 doped with Y_2O_3 and CeO_2	CO hydrogenation	400	redox properties and lattice oxygen mobility	413
CeO_2	CO oxidation	100−450	oxygen vacancies	414
CeO_2 doped Y_2O_3	CO oxidation	25−950	oxygen vacancies	416
CeO_2	dehydrogenation of alkenes	600	vacancy mobility	418
CeO_2-based materials	soot oxidation	200−600	reducibility and active oxygen lattice species	424
La doped CeO_2	soot oxidation	300−800	extrinsic oxygen vacancies	429
CeO_2−ZrO_2	soot oxidation	150−800	specific surface area and bulk oxygen mobility	430
$BiCuVO_x$ $BiCoVO_x$	oxidative dehydrodimerization of C_3H_6	300−550	migration of lattice oxygen	431
Bi_2O_3-GDC	CH_4 oxidation in absence of gas-phase oxygen	200−850	mobile oxygen species in Bi_2O_3 and surface lattice oxygen in GDC	432

selectivity to CO and H_2 in the presence of molecular oxygen.[401] The well-known oxygen ion conductors formed by substitution of zirconia with non-reducible cations such as calcium and yttrium are not thought of as reducible oxides (see section 3.1.1). The surface and bulk can behave differently; however, and Steighus and his co-workers[400] have shown that some bulk oxygen species from yttria-stabilized zirconia are available for CPOM (catalytic partial oxidation of methane). YSZ is able to catalyze CPOM ($CH_4 + O_2 \rightarrow CO + H_2 + H_2O$) from 550 °C. The full oxidation of methane to CO_2 and H_2O occurs as a primary reaction. The authors have concluded that the lattice oxygen is active for forming CO, CO_2, and H_2O and that both reactions follow the Mars–van Krevelen mechanism.

The Mars–van Krevelen redox mechanism was also proposed by Zhu et al.,[402−405] at relatively high temperatures (500−900 °C) on ZrO_2 and YSZ catalysts. As shown in Figure 66, the
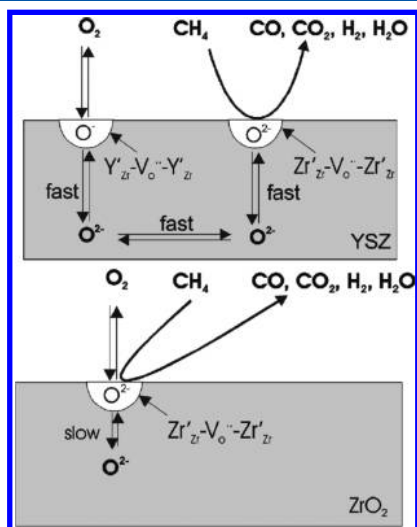

Figure 66. Reaction models of the catalytic partial oxidation of methane on YSZ (above) and ZrO_2 (below) catalysts. Reprinted with permission from ref 403. Copyright 2012 Elsevier.

catalytic rate on ZrO_2 is limited by the rate of reoxidation of the vacant sites by O_2. On the other hand, fast diffusion of oxygen in YSZ in conjunction with rapid oxygen activation at extrinsic oxygen vacancies at the surface provides an alternative pathway for replenishment of the oxygen consumed by methane. This difference in the catalytic performance of ZrO_2 and YSZ was attributed to the difference in the defect chemistry of these two catalysts, which is related to the generation of the extrinsic oxygen vacancies as described in section 3.1.1.[403]
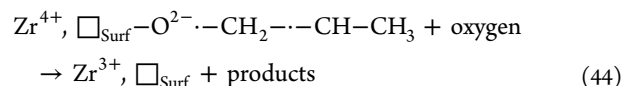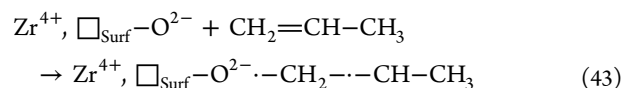
Moreover, these studies[404] demonstrated that the catalytic performance is determined by the composition of the surface rather than of the bulk of YSZ. As long as YSZ catalyst is not contaminated (by impurities such as CaO, TiO_2, and Na_2O), the composition of the outermost surface of calcined YSZ is independent of both the concentration of Y_2O_3 in the bulk and the calcination temperature; the surface always contains 12 ± 2 mol % Y_2O_3 due to segregation of Y_2O_3. Calcination at higher temperatures creates more active sites per square meter, while the catalyst loses surface area via sintering.

Similar properties were also obtained with high surface area calcia–zirconia catalysts,[406] where the surface reaction rate increases dramatically as the catalysts are reduced. The presence of a second smaller reservoir of oxygen species, which passivates the material against this rapid surface reduction until it is

exhausted, was also reported. This small reservoir of passivating oxygen equals approximately 0.01 surface layers. Its origin is not clear but could be special sites at the surface or could be associated with defects in the bulk, which are available to heal the surface because of the high mobility of oxygen in this material.

The catalytic performance for other oxidation processes has been related to the presence of oxygen vacancies in ionically conducting ceramics,[407] for example, the oxidation of propane on YSZ,[408] as well as the oxidative coupling of methane on Y_2O_3–CaO.[409]

Labaki et al.[408] have shown that anionic vacancies induced by the insertion of Y_2O_3 in the ZrO_2 structure can enhance the activity for both propene and toluene oxidation even if high CO production is evidenced. The proposed mechanism involves reactive O^{2-} ions that could be formed and chemisorbed on oxygen vacancies in relation with the existence of Zr^{3+} cations. The following expressions describe the mechanism for the case of propene oxidation ($\square_{Surf}$ is an anionic vacancy on a YSZ surface):

$$Zr^{3+}, \square_{Surf} + O_2 \rightarrow Zr^{4+}, \square_{Surf}-O^{2-} \tag{42}$$

$$Zr^{4+}, \square_{Surf}-O^{2-} + CH_2{=}CH-CH_3$$
$$\rightarrow Zr^{4+}, \square_{Surf}-O^{2-}\cdot-CH_2-\cdot-CH-CH_3 \tag{43}$$

$$Zr^{4+}, \square_{Surf}-O^{2-}\cdot-CH_2-\cdot-CH-CH_3 + oxygen$$
$$\rightarrow Zr^{3+}, \square_{Surf} + products \tag{44}$$

A relation between vacancy mobility in the support and catalytic activity and selectivity was also reported for hydrogenation reactions. Ekerdt et al. studied hydrocarbon synthesis on ZrO_2 stabilized with Y_2O_3 or CaO via the CO and CO_2 hydrogenation reactions[410−412] and proposed that vacancies of the crystal lattice of the catalysts play an important role in the reaction, because they are the active sites for the catalytic reaction. Doping of ZrO_2 with Y_2O_3 and CaO leads to enhanced catalytic properties due to increase in the oxygen vacancy availability and thus higher ionic conductivity. Similar observations appeared in the work of Li et al.[413] upon investigating the incorporation of CeO_2 or Y_2O_3 with ZrO_2 and its effect on catalytic activity for the selective synthesis of isobutene and isobutane (i-C4) from CO hydrogenation. Strong corelation between the catalytic performance in the isosynthesis reaction and the redox and acid–base properties of the ZrO_2-based catalysts was observed. The enhanced redox properties of doped zirconia-based catalysts, related to increased lattice oxygen mobility of the catalysts, were identified to be responsible for the condensation reaction leading to the production of C4 hydrocarbons. The ratio of base to acid sites was found to determine the percentage of n-C4 and i-C4 in total C4 hydrocarbons for the isosynthesis reaction.

Cerium oxides, which are also known oxygen ion conductors (section 3.1.1), have been used as catalysts for the CO oxidation reaction. Huang and Kung[414] showed that the surface oxygen vacancies of CeO_2 can be the active sites, while a significant increase in catalytic activity was observed as ceria was doped with La and Eu by Hernández et al.[415] Yang et al. also used doped ceria catalysts and observed that the amounts of the dopant (Y^{3+} in their case) determined the concentration, type, and distribution of oxygen vacancies in ceria, which in turn influenced the reducibility and catalytic activity in the CO oxidation reaction.[416] Cerium oxides have been also used to catalyze the methane

Table 5. Recent Catalytic Studies Using O^{2-} Conducting Ceramics as Supports

catalytic system	reaction involved	T, °C	key parameter of the system	ref
Pt and CuO supported on YSZ	CO oxidation	300–450	oxygen ions, vacancies	433–435
CuO supported on doped CeO_2	CO oxidation	200–1000	surface oxygen vacancies	417, 438, 439
CuO supported on $Ce_xZr_{1-x}O_2$	CO oxidation	25–250	catalyst reducibility	440
CuO supported on CeO_2	preferential oxidation of CO	100–300	redox properties, particle size, and ionic conductivity	441
Pd supported on TiO_2, CeO_2, and CeO_2–TiO_2	CO oxidation	25–250	oxygen mobility	442
Au supported on TiO_2, $Ce_{0.5}Zr_{0.5}O_2$	CO oxidation	25–450	oxygen vacancies	443
Pt supported on YSZ, C, and γ-Al_2O_3	CO oxidation	40–280	ionic conductivity	444
Rh supported on YSZ, α-Al_2O_3	dehydrogenation of C_2H_4	300–900	reducibility of the support	445
Pt supported on γ-Al_2O_3, doped CeO_2	partial oxidation of methane	25–800	availability and mobility of oxygen ions	446, 447
Pt supported on $Ln_{0.3}Ce_{0.35}Zr_{0.35}O_{2-y}$ (Ln = La, Pr, Gd)	partial oxidation of methane	650–800	oxygen mobility	448
PdO supported on ZrO_2	CH_4 oxidation	25–900	surface oxygen exchange	449
Pt supported on SiO_2, Al_2O_3, MgO_2, CeO_2, TiO_2, La_2O_3, MnO, ZrO_2	C_7H_8 oxidation	100–500	reducibility of the support	450
Au supported on CeO_2	C_3H_6 and C_7H_8 oxidation	50–350	oxygen mobility	451
BNHA supported on GDC	partial oxidation of n-tetradecane containing sulfur and aromatic compounds	400–900	oxygen ion conductivity	452
Pt supported on CeO_2–ZrO_2 doped with rare-earth cations	CH_4 dry reforming	500–850	oxygen mobility	453
Rh supported on YSZ, Al_2O_3	CH_4 reforming	650	lattice oxygen species	454, 455
Pt supported on ZrO_2	CO_2 reforming	700	oxygen exchange bewteen CO_2 and support	456
Pt supported on YSZ	CH_4/CO_2 reforming	600–750	oxygen vacancies	458
Pt supported on ZrO_2, γ-Al_2O_3	CH_4/CO_2 reforming	600	surface oxygen vacancies	459
Ni supported on doped CeO_2	CH_4/CO_2 reforming	400–550	oxygen ionic mobility	460
Ni supported on $Ca_{12}Al_{14}O_{33}$	biomass steam reforming	25–1000	oxygen restored properties of the support	461
Fe supported on MgO, Mg–Ce–O, Mg–Ce–Zr–O	C_6H_5OH steam reforming	600–650	oxygen exchange	462
Pt, Pd, Cu, Ni supported on CeO_2	WGS	150–300	oxygen vacancies	463, 464
Au supported on CeO_2	WGS	300–380	oxygen vacancies	465
Pt supported on CeO_2, Ca-doped CeO_2	WGS	200–300	oxygen mobility	466
Rh supported on ZrO_2 doped with trivalent metal oxide	N_2O decomposition	100–800	oxygen vacancies and ionic conductivity	467, 468
Rh supported on GDC	NO reduction by CO	200–800	oxygen vacancies	469
Ag supported on ZrO_2, CeO_2–ZrO_2, CeO_2, Al_2O_3	NO reduction by C_3H_6 in the presence of SO_2 and/or H_2O	400–800	oxygen ion conductivity diminishes sulfur contamination	470
Pt supported on ZrO_2, CeO_2–ZrO_2, Al_2O_3, La_2O_3	NO reduction by C_3H_6, C_3H_8 in the presence of O_2	25–550	oxygen ion conductors prevent the poisoning by carbon deposition	471

oxidation reaction[417] and the dehydrogenation of alkanes to alkenes with a posterior selective hydrogen oxidation,[418] demonstrating also the importance of the vacancy mobility in the catalytic material.

The oxygen mobility or support reducibility of ionically conducting ceramics is also utilized in soot oxidation process. Various families of catalysts are reported in the literature to be effective for soot oxidation by oxygen. Perovskites[419–421] and ceria-based oxides[422,423] are the most extensively investigated. Regarding the mechanism of soot oxidation with oxygen, it has been clearly established in the literature that lattice oxygen of the catalyst is active for soot oxidation.[422,424,425] In addition, soot oxidation predominantly takes place at the particulate/catalyst interface.[426–428] Ceria-based materials exhibit a Mars and van Krevelen mechanism. The reducibility of ceria (Ce^{4+} into Ce^{3+}) and its high oxygen storage capacity can generate mobile bulk species effective for soot oxidation. Substitution of ceria with various cations can improve their redox properties. For instance, it was shown that a partial substitution of Ce^{4+} by La^{3+} can enhance the catalytic performance for soot oxidation by increasing the reducibility and then the quantity of active lattice

oxygen species.[424] As was shown in Figure 9, the insertion of M^{3+} cations, such as La^{3+}, into the ceria strongly enhances its bulk oxygen mobility, but this parameter is rarely considered in catalytic studies. Nevertheless, comparing zirconium versus lanthanum substitution in a ceria solid solution, Katta et al.[429] have concluded that La-doped ceria is more active for soot combustion due to the extrinsic oxygen vacancies induced by La^{3+} substitution, which improve the oxygen mobility.

By using various compositions of ceria–zirconia solid solutions, Aneggi et al.[430] have confirmed that soot particles are oxidized by surface active oxygen donated by ceria–zirconia. The vacancy induced by the oxidation is refilled by gaseous oxygen and/or subsurface bulk oxygen. Therefore, the activity is linked with the specific surface area (quantity of Ce^{4+} cations on the surface) as well as with the bulk oxygen mobility characterized in this study by the oxygen storage capacity. A dual mechanism seems to occur on ceria-based catalysts by coupling a surface redox process (surface oxygen exchange) and a reverse-spillover of bulk oxygen species.

5.3.1.1. BIMEVOX Oxygen Ion Conductors. Ionic oxide conductors of the BIMEVOX family are also potentially

BB

dx.doi.org/10.1021/cr4000336 | Chem. Rev. XXXX, XXX, XXX–XXX

interesting catalysts for the selective oxidation of hydrocarbons in which the migration of lattice oxygen plays an important role (section 3.1.3). The catalytic performance of $Bi_2Cu_{0.1}V_{0.9}O_{5.35}$ (BICUVOX) and $Bi_2Co_{0.1}V_{0.9}O_{5.35}$ (BICOVOX) in the oxidative dehydrodimerization of propene has been studied by Chetouani et al.[431] The processes were proposed to occur as follows: at low temperatures (below 450 °C) weakly bonded oxygen is present, and deep oxidation of propene proceeds as long as gas O_2 is supplied to the gas phase. As BIMEVOX materials are very poor electronic conductors, there are few available electrons to promote the full reduction of O to O^{2-}, and then electrophilic species are formed on the catalyst and promote deep oxidation. When the reaction temperature is higher (500–550 °C), propene begins to reduce the solid and can produce oxygen vacancies $V_O^{\cdot\cdot}$, which can be replenished by diffusion of bulk O^{2-} and/or by gaseous oxygen chemisorption. If the ionic oxide conductivity is high enough, oxygen bulk diffusion is fast, and the two processes may occur at the same time.

Bismuth oxide is also a material that exhibits high oxygen–ion conductivity. This oxide, Bi_2O_3, also has applications as a catalyst for oxidation reactions. Huang and Li[432] used ceramic systems of Bi_2O_3 and gadolinia-doped ceria (GDC) solid mixture as catalysts for direct methane oxidation, in the absence of gas-phase oxygen at 780 °C. It was found that the Bi_2O_3–GDC system exhibits a synergistic effect, because of a combination of (a) the high catalytic activity of methane reaction with surface lattice oxygen on GDC and (b) the high content of mobile oxygen species in Bi_2O_3. The mixing of Bi_2O_3 with GDC also increases the self-decoking capability of the catalyst during direct methane oxidation due to the high content of mobile oxygen in Bi_2O_3.

5.3.2. Use as Supports for Oxidation Reactions. Metcalfe et al.[433] have reported that the YSZ support can enhance the catalytic activity of Pt for CO oxidation. They proposed[434] that oxygen ions and vacancies in the support lattice can interact with adsorbed species on the metal surface, resulting in oxygen transfer between support and metal. This study is another example of a self-driven NEMCA effect. This again highlights the common behavior between metal/support interactions at the nanoscale and EPOC at the microscale (Table 5).

Remarkable catalytic activity for CO oxidation was also reported when copper nanoparticles are supported on YSZ[435−437] and doped ceria,[417,438,439] due to the presence of surface oxygen vacancies. The authors have proposed a mechanism (Figure 67),[437] which involves the creation of active centers composed of an interfacial Cu^+ ion in interaction with a surface oxygen vacancy of YSZ. These interfacial active centers could provide a second reaction pathway for the reaction. Therefore, the turnover frequency is much higher than that of redox cycle mechanism operated on a CuO catalyst supported on the non-conducting γ-alumina.

Several studies have revealed that enhancement in the reactivity for CO oxidation over CuO catalysts on CeO_2-based supports can be significantly achieved by increasing the oxygen vacancies concentration in the support. For instance, doping of CeO_2 with Y_2O_3 and Gd_2O_3 has a beneficial effect on catalytic performance of CuO catalysts due to enhanced oxygen ionic conductivity.[417] However, when Y_2O_3 is introduced at concentrations higher than 10 mol %, surface segregation can occur and decrease the amount of the surface oxygen vacancies, leading to a decrease in the CO oxidation activity.[417] CuO supported on Pr- and Cu-doped CeO_2 also exhibits high catalytic activity,[438] associated with high oxygen vacancy concentration in
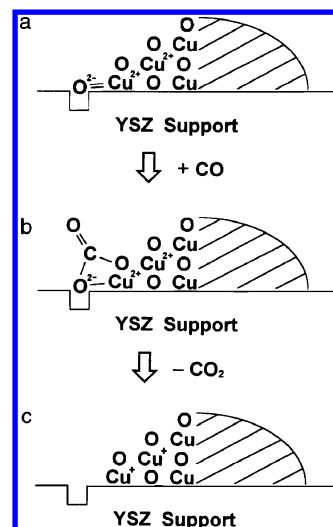
Figure 67. Scheme of interfacial center formation. (□) Surface oxygen vacancy of YSZ support; (diagonal stripe) copper oxide particle. Reprinted with permission from ref 437. Copyright 2012 Elsevier.

the catalyst. Similarly, doping CeO_2 with Sm_2O_3 (SDC) results in a significant light-off behavior (Figure 68) recorded on CuO
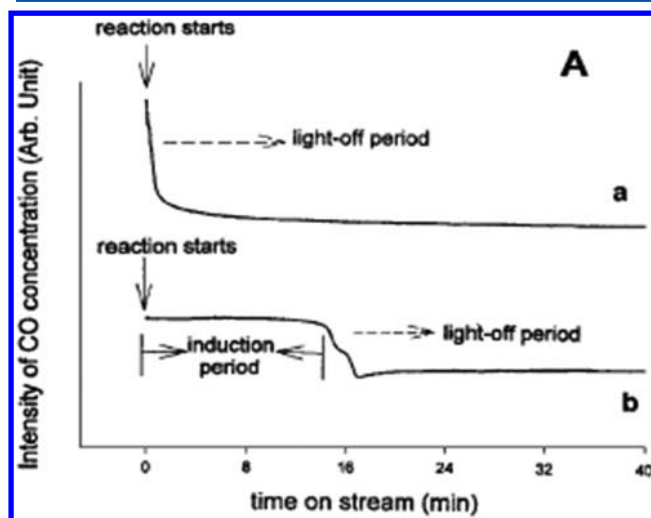
Figure 68. Variations of catalytic behavior exhibited by (a) CuO supported on an oxygen-ion-conducting material, SDC; and (b) pure CuO. All samples have the same loading of copper(II) oxide. Reprinted with permission from ref 439. Copyright 2012 Elsevier.

catalysts,[439] characterized by a negligible induction period and appreciable activity at low temperatures, still related to the surface oxygen vacancies of the support.

Figure 68 displays that the CuO/SDC-catalyzed CO oxidation behavior over time-on-stream is quite different from that catalyzed by unsupported CuO. Over CuO/SDC, no induction period existed, and the CO concentration dropped sharply soon after the reaction was started. According to the authors, these striking differences in catalytic behavior can be attributed to the effect of interfacial metal oxide–support interaction induced by the oxygen-ion-conducting support, SDC.

Catalytic systems formed by CuO supported on commercial $Ce_xZr_{1-x}O_2$ mixed oxides were also investigated for CO oxidation by Ayastuy et al.[440] According to this study, many factors can affect the activity, mainly related to close interactions

between ceria and copper species. Incorporation of Zr into the ceria lattice, resulting in a $Ce_xZr_{1-x}O_2$ solid solution, leads to improved bulk redox properties of the cerium oxide. At higher Zr concentrations, the oxygen mobility from the bulk to the surface of the ceria lattice is larger, at temperatures higher than 120 °C. A synergetic effect between Cu nanoparticles and the support, which decreases as the Zr content in the support increases, was reported. Figure 69 depicts this mechanism.

Figure 69. Mechanism of CO oxidation on CuO catalysts supported on $Ce_xZr_{1-x}O_2$. Reprinted with permission from ref 440. Copyright 2012 Elsevier.

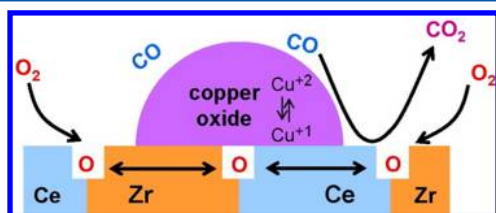The catalytic activity was correlated with the catalyst reducibility at temperatures below 170 °C. In this temperature range, copper species are more reducible because the copper–ceria interface is larger. The reducibility is often measured in catalytic studies by using temperature-programmed reduction (TPR) method. A flow of diluted hydrogen (1−5%) is introduced on the catalyst, and its consumption as a function of temperature, which is linearly increased, is measured. The peak position of H_2 consumption gives an indication of the reducibility of the sample. The lower is the temperature of the peak, the higher is the reducibility. This reducibility behavior is often linked in the catalysis community with the oxygen mobility on the surface. This property is quite different from that of bulk ionic conductivity discussed in the first section of this Review.

On this specific $Cu/Ce_xZr_{1-x}O_2$ catalyst,[440] the authors proposed that the active sites involved in the redox process are located at copper–support interface positions, and more precisely in the copper–ceria interface, whose concentration is related to the ceria content of the support. Higher zirconium content in the support reduces these active sites for the catalytic activity.

Maciel et al.[441] examined the effect of the properties of the CeO_2 support on the preferential CO oxidation reaction (PROX-CO) on CuO catalysts, by preparing the support with two different methods: hydrothermal and via precipitation. It was observed that the catalyst prepared with the hydrothermal method showed superior performance. Its higher activity and selectivity were attributed to a combination of different properties: (i) the morphology and the small crystallites size of this support, which increase the specific surface area, (ii) the enhanced redox properties and ionic conductivity of CeO_2 due to the higher mobility of the oxygen ions, important in the PROX-CO mechanism, and (iii) the favorable reduction of CuO on this catalyst as compared to the catalyst supported on the precipitated ceria. One can notice, in this publication, also the ambiguity between bulk ionic conductivity, which is not commonly measured in a catalytic study, and the oxygen mobility estimated from the reducibility (TPR).

The advantageous use of supports with high oxygen mobility during CO oxidation was also evidenced using noble metal catalysts.[442−444] Over Pd supported on TiO_2, CeO_2, and CeO_2–TiO_2, Zhu et al.[442] attributed the highest activity of Pd/CeO_2–

TiO_2 to the enhancement of CO activation caused by (a) the facilitated reduction of Pd^{2+} to Pd^0 and (b) oxygen activation through the improvement of the surface oxygen supply and oxygen vacancy formation. The Au-catalyzed CO oxidation was studied by Sanchez et al.[443] focusing on the effect of the nature of the support (prepared by a novel oil-in-water microemulsion reaction approach for the synthesis of mesoporous nanocrystalline oxides). The high performance observed with the TiO_2 supported catalyst was explained by an enhanced dispersion of the Au particles on the TiO_2 support, while the superior activity of $Ce_{0.5}Zr_{0.5}O_2$ as compared to the pure oxides was attributed to the increased number of oxygen vacancies in this material. Isaifan et al.[444] used Pt nanoparticles (synthesized via a modified polyol method) deposited on YSZ, carbon, and γ-Al_2O_3 for the catalytic CO oxidation. Best catalytic performance was obtained with the YSZ supported catalyst. YSZ is the only one among the studied supports having ionic conductivity, suggesting the promoting role of O^{2-} ionic species contained in YSZ on the catalytic activity of Pt for CO oxidation.

The effect of the reducibility of the support on the catalytic activity was investigated by Ferrizz et al.[445] using the temperature-programmed desorption (TPD) technique in a single ultrahigh vacuum surface analysis system. They studied the dehydrogenation of C_2H_4 on Rh particles supported on α-Al_2O_3, YSZ, and CeO_2 thin films deposited on YSZ and α-Al_2O_3 membranes. Their results suggest that both CeO_2 and YSZ supports are able to donate oxygen (provided by the reduction of the support) for reaction with carbon species, adsorbed on the supported Rh particles during the dehydrogenation reaction, to produce CO. This study underlines the relation often established between the reducibility of the support and its ability to give oxygen to metallic nanoparticles. However, the relationship with the bulk oxygen ionic conductivity of the support is difficult to establish. Indeed, the electrochemical impedance spectroscopy (EIS) technique widely used to measure the bulk ionic conductivity was developed for solid-state electrochemistry (described in section 2.4.1). The models used to interpret the impedance diagrams are valid for dense or slightly porous samples. Therefore, EIS cannot be used for the measurement of the ionic conductivity of powdered supports.

Ionically conducting ceramics are effective for CPOM as described in section 5.3.1. CPOM was also investigated over Pt catalysts supported on doped CeO_2 and γ-Al_2O_3. This study revealed that the ionic conductivity of the support can affect the amount of deposited carbon.[446,447] The higher availability and mobility of oxygen ions in doped CeO_2 as compared to γ-Al_2O_3 enhances the oxidation of the deposited carbon (Figure 70).[446,447] Addition of dopants to ceria can enhance the ionic conductivity, which results in a rapid oxidation of adsorbed carbon on the catalyst surface, confirming the efficiency of this kind of ceramics for soot oxidation.

CPOM at short contact times on Pt catalysts supported on $Ln_{0.3}Ce_{0.35}Zr_{0.35}O_{2-y}$ (Ln: La, Pr, Gd) was studied by Sadykov et al.[448] It was found that the reaction proceeds through direct route with oxygen-assisted methane activation on Pt. This is in contrast with conventional catalysts such as Pt deposited on support materials without significant oxygen mobility. The direct pathway postulates the formation of H_2 and CO as primary products further oxidized into CO_2 and H_2O depending on process conditions (contact time, O/C ratios, etc.). This mechanistic feature is related by the authors with the strong Pt–support interactions stabilizing highly dispersed oxidic Pt species, less active in methane and syngas combustion than
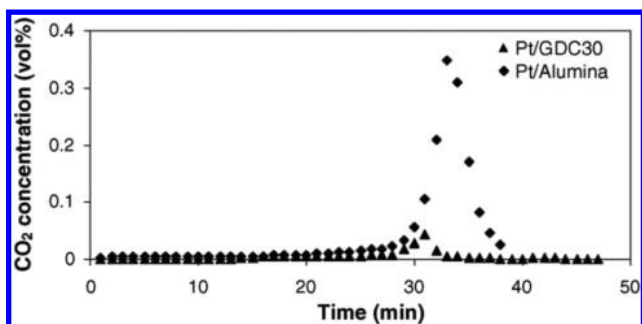
Figure 70. CO_2 concentration during burn off of carbon, postreaction of CPOM. Reprinted with permission from ref 446. Copyright 2012 Elsevier.

metallic clusters. The support activates oxygen molecules and supplies active oxygen species to Pt sites. The authors suggest that a high rate of oxygen diffusion both on the surface and in the bulk of the support, combining with Pt/support oxygen spillover, stabilizes Pt in a well-dispersed partially oxidized state. These properties could prevent coking at high methane concentrations in the feed.

Ciuparu et al.[449] used isotopically labeled reaction mixture pulsed experiments (i.e., the reaction mixture was periodically injected in helium stream that was flowing continuously over the catalyst) with pure unsupported PdO particles as compared to zirconia-supported PdO particles. It was concluded that ZrO_2 contributes significantly to the oxygen pool of the PdO phase available for the methane combustion, because the exchange of oxygen between zirconia and PdO is very fast. According to the authors, the catalyst surface is involved in the methane reaction mechanism by successive reduction/reoxidation cycles. The reoxidation step uses both oxygen from the bulk PdO and gas-phase oxygen and also oxygen from the support.

The reducibility of the support and its effect on catalytic performance for toluene oxidation were investigated by Saqer et al.[450] using Pt catalysts supported on a variety of metal oxides (M_xO_y), inert and reducible. Pt supported on inert metal oxides (SiO_2, Al_2O_3, MgO) exhibits practically the same activity, indicating that reaction rate over these samples is mainly determined by the dispersed metallic phase and does not depend on the nature on the support. In contrast, when Pt is supported on reducible metal oxides, the catalytic activity is strongly influenced by the nature of the support and decreases in the order of Pt/CeO_2 > Pt/TiO_2 > Pt/La_2O_3 > Pt/MnO. Regarding Pt/ZrO_2, its catalytic performance is similar to that of irreducible catalysts, although ZrO_2 is known to exhibit some redox characteristics. It should be noted that metal dispersion of Pt/M_xO_y catalysts varies significantly from one catalyst to another, and, therefore, the possibility of a particle size effect on TOF cannot be excluded.

Enhanced catalytic activity of Au nanoparticles supported on ceria for propene and toluene oxidation was also reported by Ousmane et al.,[451] showing that the oxygen vacancies present in the ceria defective structure act as nucleation sites for gold anchoring. They also contribute to enhance oxygen mobility and to increase catalytic activity in oxidation reactions.

Ni-substituted barium-hexaaluminate (BNHA) deposited onto gadolinium-doped ceria (GDC), an oxygen conductor, was prepared using different methods (incipient wetness impregnation and solid-state mixing). They were examined as catalysts for partial oxidation of n-tetradecane containing sulfur and aromatic compounds.[452] Both GDC-supported catalysts

demonstrated greatly reduced deactivation, with significantly reduced carbon formation, which was attributed to the oxygen-conducting property of the GDC.

5.3.3. Use as Support for Reforming Reactions. Pt catalysts supported on nanocrystalline ceria–zirconia samples doped with rare-earth (Gd, Pr, La) cations were used for the reaction of CH_4 dry reforming.[453] The results showed that at high temperatures (800 °C) the highest performance is demonstrated by the Pr-doped sample, which was correlated with its highest bulk oxygen mobility. Pr-doped ceria is a mixed ionic–electronic conductor as described in section 3.4.1. This study gave evidence that bulk mobility in complex fluorite-like oxide supports is also an important factor favoring coke precursors gasification by supplying oxygen-containing species to the Pt–support interface.

Steady-state tracing techniques were used by the group of Efstathiou to investigate the mechanistic aspects of CH_4 reforming to highlight the contribution of the support.[454,455] The surface coverage of active oxygen-containing species, which lead to the formation of CO, is found to be very small over both Rh/Al_2O_3 and Rh/YSZ catalysts. However, over the Rh/YSZ catalyst, a large reservoir of lattice oxygen species coming from the carrier can interact reversibly with gaseous CO_2 under reforming reaction conditions. A spillover of these lattice oxygen species onto the Rh surface seems to occur, contributing to the formation of CO and H_2O. This reaction route proceeds in parallel with the reforming reaction on the Rh surface.

The oxygen pathway of the reaction was confirmed from the transient responses (shown in Figure 71) of gaseous $C^{18}O$, $H_2^{18}O$, $C^{16}O^{18}O$, and $^{16}O^{18}O$ obtained under the last CH_4/$C^{16}O_2$/He switch of the following delivery sequence: CH_4/$C^{16}O_2$/He (650 °C, 2 h) → CH_4/$C^{18}O_2$/Ar/He (650 °C, 5 min) → CH_4/$C^{16}O_2$/He (650 °C, t). The transient responses containing ^{18}O shown in Figure 71a and b suggest that during
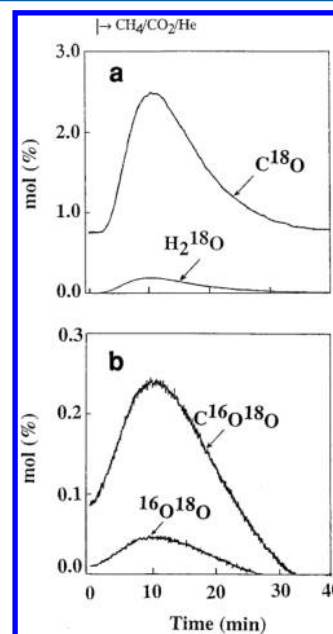
Figure 71. Steady-state tracing of the reforming reaction of CH_4 with CO_2 at 650 °C on Rh/YSZ. Delivery sequence: CH_4/$C^{16}O_2$/He (650 °C, 2 h) → CH_4/$C^{18}O_2$/Ar/He (650 °C, 5 min) → CH_4/$C^{16}O_2$/He (650 °C, t). Data shown in this figure correspond to the last CH_4/CO_2/He switch. Reprinted with permission from ref 455. Copyright 2012 Elsevier.

the 5 min treatment of the Rh/YSZ catalyst at 650 °C with $CH_4/C^{18}O_2/Ar/He$, a large reservoir of ^{18}O species was formed, which subsequently was depleted under $CH_4/C^{16}O_2/He$ treatment. Integration of all responses shown in Figure 71 provides an amount of 1500 mmol/gcat of oxygen species, which correspond to 75 monolayers of exposed Rh atoms. Thus, according to the authors, this result indicates that the corresponding quantity of oxygen species accumulated on the catalyst surface during the $CH_4/C^{16}O_2/He$ treatment cannot reside on the Rh surface, but must be on the YSZ support.[455]

Van Keulen et al.[456] found that during CO_2 reforming of methane reaction over the Pt/ZrO_2 catalysts, an oxygen pool is present on the material. CO_2 acts as an oxygen supplier, while CH_4 extracts the oxygen. The authors have not concluded about the nature of the pool. However, there is evidence that ZrO_2 can be partially reduced in presence of Pt at 700 °C. Tournayan et al.[457] explained this reduction of zirconia by the formation of a $Pt_{1-x}Zr_x$ alloy. This suggests that the oxygen pool used for the reactions is present in the vicinity of the Pt crystallites. Chen and co-workers also found that YSZ is a promising support for CH_4/CO_2 reforming on Pt.[458] The proposed mechanism involves CO_2 adsorption and activation on YSZ via the affinity of oxygen vacancies to the negative dipole of carbon dioxide, or through carbonate formation on YSZ, facilitating the reaction of $CH_x(a)$ and $CO_2(a)$.

The mechanism of the CO_2 reforming of methane reaction over the Pt/ZrO_2 catalyst was investigated and compared to the case of a Pt/γ-Al_2O_3 catalyst by O'Connor et al.[459] It was shown that over both catalysts, methane decomposition takes place over platinum. The main difference between the two catalysts was correlated with the carbon dioxide dissociation. Over Pt/γ-Al_2O_3, this step is proposed to be assisted by hydrogen, while over Pt/ZrO_2, it takes place over the zirconia support and involves surface oxygen vacancies.

The suggested reaction steps over Pt/ZrO_2 are the following ($\square_{Zr}$ is an oxygen vacancy at the zirconia surface, * is a Pt site, the Zr subscript denotes species adsorbed on a zirconia site, and O_{Zr} is an oxygen surface species):
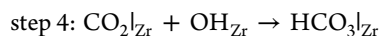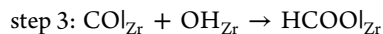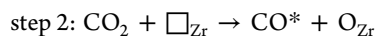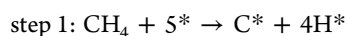
step 1: $CH_4 + 5* \rightarrow C* + 4H*$

step 2: $CO_2 + \square_{Zr} \rightarrow CO* + O_{Zr}$

step 3: $CO|_{Zr} + OH_{Zr} \rightarrow HCOO|_{Zr}$

step 4: $CO_2|_{Zr} + OH_{Zr} \rightarrow HCO_3|_{Zr}$

step 5: $HCO_3|_{Zr} + \square_{Zr} + * \rightarrow CO* + OH_{Zr} + O_{Zr}$

step 6: $C* + O_{Zr} \rightarrow CO* + \square_{Zr}$

step 7: $H* + O_{Zr} \rightarrow OH* + \square_{Zr}$

step 8: $H* + OH* \rightarrow H_2O$

step 9: $H* + H* \rightarrow H_2*$
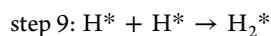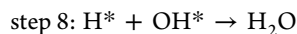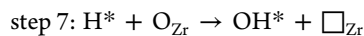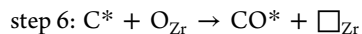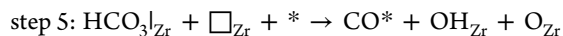
Huang et al.[460] proposed a similar mechanism for the CO_2 reforming of CH_4 over Sm_2O_3- and Gd_2O_3-doped CeO_2 supported catalysts. The authors also evidenced a very sensitive catalytic activity behavior to the oxygen-vacancy properties of the support. In this mechanism, CO_2 dissociation can occur on surface doped ceria vacancies, producing gaseous CO and atomic oxygen, which occupies an oxygen vacancy. The oxygen ionic mobility in the support can improve the conversion of the adsorbed carbon species, that is, CH_x, via the oxygen transport.

This greatly increases the CH_4 conversion, which produces hydrogen, and also lessens the carbon deposition.

Ni catalysts supported on mayenite ($Ca_{12}Al_{14}O_{33}$), an oxygen ion conductor, were used by Li et al.[461] for the catalytic biomass tar steam reforming, with toluene as tar destruction model compound. The observed high catalytic activity and carbon and sulfur tolerance were attributed to the high oxygen restored properties of the support.

Isotopic experiments have proved the contribution of oxygen vacancies or labile oxygen of the support on the catalytic activity for the steam reforming of phenol toward H_2 production over Rh and Fe supported on MgO, Mg−Ce−O, and Mg−Ce−Zr−O metal oxides.[462] It was shown that the major part of ^{18}O species was adsorbed on oxygen vacant sites and/or exchanged with labile oxygen of the support. These chemisorbed oxygen species then diffuse onto the metal and oxidize the deposited C_xH_y species derived from phenol decomposition.

This example underlines that high oxygen mobility combined with high rate of oxygen exchange can be very useful for high-temperature activation of biogas or biofuel.

Using CeO_2-based catalysts for the WGS, Deshpande and Madras[463] showed that lattice oxygen utilization occurs resulting in reduced ceria, which in turn gets oxidized by the utilization of oxygen from the reactants.[464] A cooperative redox reaction mechanism, involving oxidation of CO adsorbed on the metal cluster by oxygen supplied to the metal interface by ceria, followed by H_2O filling of the oxygen vacancy on ceria, was used to fit the kinetics. The crucial role in the dissociation of water during the WGS reaction on Au/CeO_2 catalysts was also supported by XPS analysis carried out by Rodriguez et al.[465] This analysis revealed that when Au nanoparticles are vapor deposited on CeO_2 (111), partial reduction of the support takes place. Thus, the admetals favor the formation of oxygen vacancies in ceria, and these vacancies enhance chemical reactivity of metal nanoparticles.

The effect of the ionic mobility of the support on the WGS reaction was also evidenced by Lincaniso et al.[466] using undoped and calcia-doped ceria supports to disperse Pt catalysts. The catalysts with Ca-doped support presented enhanced WGS activities as compared to the single-oxide catalysts, because Ca strains the zirconia lattice, improving the O-mobility, and, in turn, the mobility of O-bound intermediates, which are proposed to arise on the support, and migrate and decompose at the Pt−oxide interface.

5.3.4. Use as Supports for N_2O and NO_x Abatement. The oxygen mobility of the support is also discussed in N_2O decomposition. This reaction is, of course, important in inductrial plants (nitric acid production) to remove emissions of this strong greenhouse gas effect. According to Centi et al.,[467,468] the doping of zirconia with trivalent elements such as Ce^{3+}, Sb^{3+}, or Al^{3+} during the sol−gel preparation of the support makes it possible to obtain a further promotion of the reactivity of Rh catalysts in N_2O decomposition. Independently of the nature of the dopant, the authors observed that the amount of dopant has a volcano-type influence on the catalyst reactivity in the decomposition of N_2O. This observation was used to further confirm that the effect primarily must be attributed to the substitution of a trivalent ion for Zr^{4+} more than to a specific role of the dopant itself. This partial substitution creates oxygen vacancies and strongly improves the ionic conductivity of the support as was discussed in section 3. The volcano-type behavior can be linked with the variation of the ionic conductivity with the M^{3+} cation loading, as was shown in Figure 9.

Cho[469] has confirmed that the presence of oxygen vacancies in Gd_2O_3-doped CeO_2 support is related to the catalytic activity of Rh catalysts for the reduction of NO by CO. It was found that the oxygen uptakes of both unpoded and doped CeO_2 are an order of magnitude greater than that of γ-Al_2O_3.

The performance of zirconia, ceria−zirconia, ceria, and alumina supports was studied by Hickey et al.[470] during NO reduction by propylene in the presence of SO_2 and/or H_2O over Ag catalysts. The use of ZrO_2-based supports was shown to improve both the SO_x resistance and the ease of regeneration of the Ag-based catalysts. Moreover, inclusion of ceria in the ZrO_2-based support formulation was shown to favor the SO_x resistance behavior as ceria seems to act as a sulfur scavenger.

Interesting results were also obtained by Tanabe et al.[471] during operando X-ray absorption near edge structure (XANES) study on the HC (C_3H_6, C_3H_8)−NO−O_2 reaction in reducing conditions over Pt/γ-Al_2O_3, Pt/ZrO_2, Pt/CeO_2−ZrO_2, and Pt/La_2O_3 catalytic powders pressed into discs. In the case of CeO_2−ZrO_2 and ZrO_2, the catalytic start-up temperatures were lower than those with La_2O_3 and γ-Al_2O_3 support, demonstrating that the high activity of lattice oxygen in these oxides contributes to the catalytic reaction and suppresses the poisoning effect of carbonaceous species on Pt.

These two studies confirm the ability of oxygen conductors to regenerate metallic particles or prevent their poisoning against carbon deposition and sulfur contamination. This property of ionically conducting ceramics has be to deeply explored to design effective and stable catalysts for high temperature reactions involving severe operating conditions, in the presence of biogas or biofuel for instance.

6. CONCLUSIONS AND PROSPECTS

6.1. EPOC: Added Values to Catalysis?

6.1.1. Chemical and Electrochemical Promotion, Metal Support Interactions, Operational Differences. Chemical promotion, electrochemical promotion, and metal−support interactions observed on metal supported catalysts are, at a first glance, three independent phenomena that can affect catalyst activity and selectivity in a dramatic manner.[8,23] However, as discussed in section 5, promotion, electrochemical promotion, and metal−support interactions on ion-conducting and mixed-conducting supports are three different facets of a similar process. All three are linked with the addition of promoting species to the metallic active sites.[23] The origin of these three phenomena can be interpreted as the interaction of adsorbed reactants and intermediates with an effective double layer formed by promoting species at the metal−gas interface.

Classical promotion obtained with the addition of a chemical compound to a metal supported catalyst induces effects on the catalytic activity similar to those of electrochemically supplied corresponding ions. This has been clearly established in the literature for chemical promotion of catalysts with alkalis, supplied either chemically (NaOH) or electrochemically (Na$^+$ from an electrolyte). Similar would be the situation on a Pt surface decorated with O^{2-}, the only difference being the experimental difficulty of introducing O^{2-} with classical promotion and its short lifetime on the catalyst surface, that is, only Λ times longer than the catalytic turnover. Consequently, the proposed functional identity of classical promotion, electrochemical promotion, and metal−support interactions should not lead the reader to pessimistic conclusions regarding the practical usefulness of EPOC.[8,23] Operational differences exist between

the three phenomena, and it is useful to address and systematize them.

(1) The main operational difference is the ability of EPOC to continuously replenish the promoting species on the catalyst surface, allowing thus the use of short-lived ($10-10^3$ s) but extremely effective promoters such as $O^{\delta-}$, which is $10-10^5$ times less reactive than normally chemisorbed atomic oxygen and which was totally unknown from classical promotion studies.[23,273] This is because of its short lifetime, which makes it unsuitable for any classical promotion application, but, even more importantly, because it can only be introduced on metal catalyst surfaces interfaced with O^{2-}-conducting solid electrolytes (e.g., YSZ) or mixed O^{2-}-electronic conductors (e.g., TiO_2, CeO_2).

This is an important operational advantage of electrochemical promotion: it permits the use of a wide variety of sacrificial promoters (e.g., O^{2-}, H^+) that have too short lifetimes for classical promotion applications.

(2) It is very difficult to imagine how one can use metal−support interactions with conventional supports to promote electrophilic reactions or how one can use classical promotion to generate the strongest electronegative promoter, $O^{\delta-}$, on a catalyst surface. Furthermore, there is no reason to expect that a metal−support interaction-promoted catalyst is at its "best" electrochemically promoted state. Thus, the experimental problem of inducing electrochemical promotion on fully dispersed catalysts remains important.[23] Recent work[293] on this direction proved the feasibility of EPOC on highly dispersed nanoparticles.

(3) Last is the ability to control in situ, that is, during catalyst operation, the coverage of the promoting species on the catalyst surface, for achieving optimum catalyst performance.[23] This property can be of great interest in transient atmosphere such as car exhaust gas.

6.1.2. Rules of Promotion and Promoter Prediction. As was already discussed in section 4.4, careful classification and examination of the electrochemical promotion and classic promotion literature[273,274] has revealed four simple and rigorous experimental rules (G1−G4), which enable one to predict the rate versus work function, Φ, behavior of catalytic reactions (electrophobic, electrophilic, volcano, inverted volcano) on the basis of the rate dependence on the reactants on the unpromoted surface. These promotional rules lead to the following three practical rules, P1−P3, which dictate the choice of promoter type (electropositive or electronegative), with respect to rate maximization, on the basis of the nature (electron donor or acceptor) of the most strongly bonded reactant species.[273,274]

P1: If a catalyst surface is covered predominantly by an electron acceptor adsorbate, then an electron acceptor (electronegative) promoter is to be recommended.

P2: If a catalyst surface is covered predominantly by an electron donor adsorbate, then an electron donor (electropositive) promoter is to be recommended.

P3: If a catalyst surface has very low coverages of both electron acceptor and electron donor adsorbates, then both an electron acceptor and an electron donor promoter will enhance the rate.

These simple rules can provide useful guidelines for a rational first screening and selection of promoters for practical supported catalysts.

6.2. Ionic Conducting Ceramics: Growing Importance Supports for Heterogeneous Catalysis

Electrochemical promotion of catalysis has been discovered by using large metal particles deposited on dense O^{2-} conducting membranes, that is, with samples initially produced for solid-state electrochemistry experiments. The polarization of these model electrochemical catalysts allows the researchers to evidence the strong impact of O^{2-} ionic species on the catalytic activity of noble metals. The unusual scale of the metallic catalytic particles (around 1 μm), comparable to the spatial resolution of XPS, Kelvin probe, STEM, or PEEM (see section 4), was decisive because it permits one to prove the backspillover of oxygen ionic species and their strong interactions with the metal. Furthermore, large active particles combined with dense electrolytic supports limit or avoid the oxygen exchange process that commonly occurs between the gas phase and the redox support. This allows one to clearly evidence, by using temperature-programmed desorption measurements, the back-spillover of ionic oxygen species from the electrolyte onto the noble metal particles. Three decades of fundamental research involving few groups in the world have establish EPOC rules depending on the charge of ions, and nature of reactants and of the metal. This Review underlines that these rules can also be used to interpret metal—support interactions described in the literature on conventional dispersed catalysts.

Backspillover of ionic promoting species can also occur on dispersed catalysts, of course without any external electrical polarization. This migration of ionic species from the support to the metallic nanoparticles is described as the origin of metal—support interactions phenomena. The driving force of this backspillover at the nanoscale is not fully understood and could be induced by local gradients of work-function and/or chemical potential. This point must certainly be addressed in the future. Nevertheless, the consequence is that NEMCA effects observed on model electrochemical catalysts could be reproduced on highly dispersed catalysts by controlling metal—support interactions, that is, the ionic promoting species backspillover. Section 5 of this Review lists many reactions for which the utilization of an oxygen conductor support can promote the activity. In addition, these ceramics present surface oxygen vacancies able to chemisorb reactants and a remarkable thermal and chemical stability, inherent to the fluorite structure for zirconia and ceria oxides. In specific operating conditions, oxygen conducting ceramics can avoid or limit the poisoning of the metallic active sites against carbon deposition or sulfur contamination. This property could be particularly interesting for high temperature combustion or reforming of biogas and biofuel.

All of these properties explain the increase in the number of publications in heterogeneous catalysis involving supports based on zirconia or ceria supports. Figure 72 highlights this enhancement by plotting the ratio between the number of publications involving common SiO_2- or Al_2O_3-based supports and that using ZrO_2- or CeO_2-based supports. This ratio has strongly increased from less than 0.1 in 1990 to 0.7 in 2010. For specific reactions such as CO oxidation and WGS for which metal—support interactions have been often evidenced in literature data (see section 6), this ratio is now larger than 1 (Figure 73).

The multidisciplinary approach of EPOC combining solid-state electrochemistry, heterogeneous catalysis, and materials science has certainly contributed to the wide utilization of ionically conducting ceramics in catalysis. Nevertheless, a large
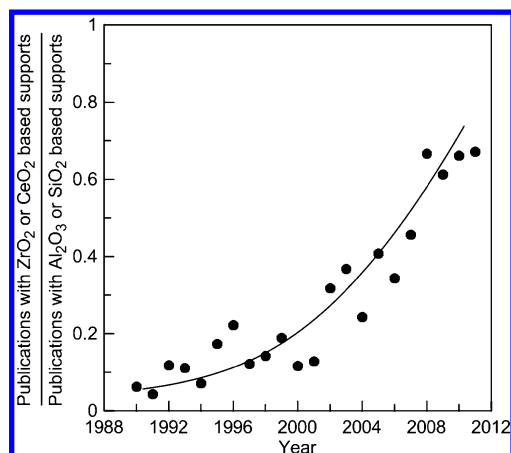
Figure 72. Ratio of number of publications on catalytic oxidation reactions using supports based on ZrO_2 or CeO_2 versus Al_2O_3 and SiO_2 during the last two decades. Source: Scopus 2012.
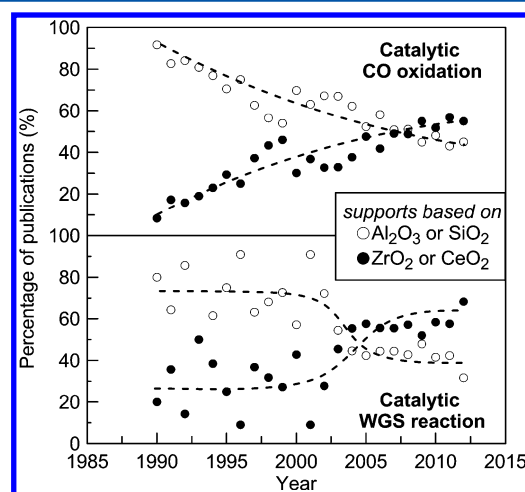
Figure 73. Evolution with time of the percentage of publications focused on CO oxidation and water—gas shift utilizing insulating supports (Al_2O_3 or SiO_2) and supports with finite ionic mobility (ZrO_2 or CeO_2). Source: Scopus 2012.

research effort will still be necessary to fully understand the interactions between metallic active sites and an ionically conducting support. The metal/support interactions control will necessary produce smart and efficient catalysts. EPOC is a precious tool to investigate these interactions. Furthermore, EPOC will lead to practical applications in the near future if the quest for highly dispersed electropromoted catalysts is achieved.

AUTHOR INFORMATION

Corresponding Author

*Phone: (33) (0)4 72 43 15 87. Fax: (33) (0)4 72 43 16 95. E-mail: philippe.vernoux@ircelyon.univ-lyon1.fr.

Notes

Biographies

Philippe Vernoux is a senior researcher at the Centre National de la Recherche Scientifique (CNRS). Philippe received his Ph.D. in Solid State Electrochemistry in 1998 from the University of Grenoble and then moved to the Laboratory of Electrochemistry of Chemical Analysis in Paris, as a postdoctoral fellow. In 2000, he joined CNRS as a researcher at the laboratory of Applied Chemistry for Environment in Lyon and obtained his habilitation in Catalysis in 2006 from the University of Lyon. From 2007, Philippe is the cohead with Dr. Christian George of the group "air cleaning, gas treatment, atmospheric chemistry" of the Institute of Researches on Catalysis and Environment in LYON (IRCELYON). His current research is mainly focused on car exhaust treatments, solid oxide fuel cells, and EPOC.

Leonardo Lizarraga received his Ph.D. degree from University of Buenos Aires, Argentina, in 2007. For his Ph.D., he studied the electro-chemomechanical properties of conducting polymers. He then completed a postdoctoral stance with Dr. Philippe Vernoux at IRCELYON CNRS, France, focused on car exhaust treatments, particulate matter detoxification, and studies of EPOC phenomenon. He is currently a postdoctoral research fellow at Georgia Institute of Technology working in the research group of Dr. L. A. Bottomley focused on force spectroscopy applied to polymers.

Mihalis Tsampas carried out his Ph.D. under the supervision of Prof. C. G. Vayenas at the University of Patras (Greece) in 2010. During his dissertation, he investigated the EPOC phenomenon on Proton Exchange Membrane fuel cell type reactors and the proton conductivity of NAFION polymeric membranes. After a postdoctoral period at University of Patras and The Cyprus Institute (Cyprus), he joined the group of Dr P. Vernoux at IRCELYON (France) in 2011. His current research is mainly focused on soot oxidation on ionically conducting supports and fundamental isotopical labeling EPOC studies.

Foteini M. Sapountzi received her Ph.D. in chemical engineering at the University of Patras (Greece) in 2009, under the supervision of Prof. C. G. Vayenas. After a period of being a postdoctoral researcher in the same group and a visiting Lecturer in the department of Materials Science at the same university, she moved to Spain and worked with Prof. J. L. Valverde (University of Castilla la Mancha). Currently, she is a postdoctoral researcher in IRCELYON (France) under the supervision of Dr. P. Vernoux. Her research is focused on catalytic and electrocatalytic processes on the frame of EPOC and on fuel cell technology.

BI

dx.doi.org/10.1021/cr4000336 | *Chem. Rev.* XXXX, XXX, XXX—XXX

Antonio de Lucas Consuegra is a lecturer of the Department of Chemical Engineering of University of Castilla La Mancha (Spain). Antonio received his Chemical Engineering degree after a research stay at the University of Kentucky (EEUU) under the supervision of prof. Mark Keane (2004). He then received his Ph.D. in Chemical Engineering at the University of Castilla La Mancha in 2008, under the supervision of Prof. J. L. Valverde. After a postdoctoral period at Laboratoire de Synthese et Fonctionnalisation des Ceramiques Saint-gobain-CNRS (France) under the supervision of Dr. Vernoux, he became a lecturer at the University of Castilla La Mancha. His research activities lie mainly in the areas of environmental catalysis, gas-phase electrocatalysis, hydrogen production, and electrochemical promotion of catalysis.

Jose Luis Valverde completed his graduate and Ph.D. studies with honors at the Complutense University of Madrid. In 1990, he joined the University of Castilla-La Mancha in Spain as an assistant professor. His research activities developed as a Full Professor of the University of Castilla-La Mancha (since 2003) have been focused on different subjects related to conventional catalysis, electrocatalysis, application of the electrochemical promotion of catalysis (EPOC), synthesis and uses of carbon nanostructures (graphene, carbon nanotubes, carbon nanofibers, and carbon nanospheres) as catalysts, synthesis of microcapsules containing PCMs, and simulation of chemical processes with home-made software and commercial packages. He has coauthored several book chapters, patents, and more than 170 research papers.

Stamatios Souentie received his Bachelor in Chemical Engineering from the University of Patras in 2005 and his Ph.D. under the supervision of Prof. C. G. Vayenas from the same institute in 2009. During his dissertation, he studied the practical utilization of EPOC phenomenon using novel reactors and thin catalyst films. After a postdoctoral period at University of Patras, EPFL and University of Lyon - IRCELYON, he joined the Research & Development Center of Saudi Aramco in

Dhahran, Saudi Arabia in 2012. His current research is mainly focused on CO_2 capture and novel application strategies.

Constantinos (Costas) Vayenas got his Ph.D. from the University of Rochester in 1976. He then taught as Assistant Professor at Yale (1976–77) and as Assistant and Associate Professor at MIT (1977–82) before returning to Greece as Professor at the University of Patras. He was then a Humboldt Fellow at the University of Karlsruhe, visiting Professor at Yale, EPFL, and the University of Lyon. His research interests focus on EPOC, electrocatalysis, fuel cells, heterogeneous catalysis, and mathematical modeling of chemical and physical phenomena. He is one of the Editors of *Modern Aspects of Electrochemistry* and has received the Dreyfous teacher-scholar award (1981), the Academy of Athens award in Chemistry (1992), the Wason medal of the American Concrete Institute (1994), and the Outstanding Achievement Award of the Electrochemical Society (1996). He is a Fellow of the ISE since 2005 and a member of the Academy of Athens since 2010.

Dimitrios Tsiplakides is Assistant Professor at the Chemistry Department of the Aristotle University of Thessaloniki and Visiting Professor at CPERI-CERTH. His research interests focus on electrocatalysis, fuel cells, heterogeneous catalysis, metal–support interactions, and electrochemical promotion of catalytic reactions. His most recent research activities are in the fields of fuel cells and integrated systems of regenerative fuel cells and on the practical utilisation of EPOC. He has authored 38 refereed publications, holds 1 international patent, and is coauthor of the "Electrochemical Activation of Catalysis" (Kluwer/Plenum 2001). He was awarded the Oronzio De Nora Foundation Prize of ISE on Electrochemical Technology and Engineering, 2004.

Stella Balomenou is a Research Scientist at CPERI-CERTH since 2006. Her expertise is in the areas of solid-state electrochemistry and fuel cell technologies, chemical and electrochemical kinetics, reactor design and engineering, and electrochemical promotion of catalysis. In this context, she has authored 18 papers in international, high impact refereed journals and holds 2 international patents in novel fuel cell architectures and electrochemically promoted reactor design. She is coinventor and patent holder of the Monolithic Electrochemically Promoted Reactor (MEPR) and Triode Fuel Cell concept.

Elena Baranova is an Assistant Professor in the Department of Chemical and Biological Engineering, Center for Catalysis Research and Innovation at the University of Ottawa. She received her M.Sc. degree in Chemical Engineering (1999) from the Ukrainian State University of Chemical Engineering (Ukraine). She pursued her studies at the Institute of Chemical Science and Engineering at École Polytechnique Fédérale de Lausanne (Switzerland), where she completed her Ph.D. under the supervision of Prof. Ch. Comninellis in 2005. During her Ph.D., she spent several months in the laboratory of Prof. C. G. Vayenas at the University of Patras (Greece). She became an NSERC postdoctoral fellow in 2005 and later a research associate with the National Research Council Canada. She subsequently worked as a senior scientist at Abbott Point of Care before joining the University of Ottawa in 2008. Her current research interests are in the area of electrocatalysis and EPOC.

REFERENCES

(1) Hegedus, L. L.; Aris, R.; Bell, A. T.; Boudart, M.; Chen, N. Y.; Gates, B. C.; Haag, W. O.; Somorjai, G. A.; Wei, J. *Catalyst Design: Progress and Perspectives*; John Wiley & Sons: New York, 1987.

(2) Ertl, G.; Knötzinger, H.; Weitcamp, J. *Handbook of Catalysis*; VCH Publishers: Weinheim, 1997.

(3) *Modern Electrochemistry: No. 2A Fundamentals of Electrodics, No. 2B Electrodics in Chemistry, Engineering, Biology, and Environmental Science*;

Bockris, J. O. M., Reddy, A. K. N., Gamboa-Aldeco, M., Eds.; Kluwer Academic/Plenum Publishers: New York, 2000.

(4) Hamann, C. H.; Hammett, A.; Vielstich, W. *Electrochemistry*; Wiley-VCH: Weinheim, 1998.

(5) Somorjai, G. A. *Chemistry in Two Dimensions: Surfaces*; Cornell University Press: Ithaca, NY, 1981.

(6) Engel, T.; Ertl, G. In *The Chemical Physics of Solid Surfaces and Heterogeneous Catalysis*; King, D. A., Woodruff, D. P., Eds.; Elsevier: Amsterdam, 1982; Vol. *4*.

(7) Wieckowski, A. *Interfacial Electrochemistry, Theory, Experiments and Applications*; Marcel Dekker: New York, 2000.

(8) Vayenas, C. G. *J. Solid State Electrochem.* **2011**, *15*, 1425.

(9) *Fuel Cell Science and Engineering*; Stolten, B., Emonds, B., Eds.; Wiley-VCH: Weinheim, 2012.

(10) Singhal, S. C. *Solid State Ionics* **2000**, *135*, 305.

(11) Fergus, J. W. Electrochemical Sensors: Fundamentals, Key Materials and Applications. In *Handbook of Solid State Electrochemistry*; V. V., K., Ed.; Wiley-VCH: New York, 2009.

(12) Wiedenmann, H.-M.; Hötzel, G.; Neumann, H.; Riegel, J.; Stanglmeier, F.; Weyl, H. Exhaust gas sensors. In *Automotive Electronics Handbook*, 2nd ed.; Jurgen, R. K., Ed.; McGraw-Hill: New York, 1999.

(13) Wiemhöfer, H. D.; Göpel, W. *Sens. Actuators, B* **1991**, *4*, 365.

(14) Ullman, H.; Teske, K. *Sens. Actuators, B* **1991**, *4*, 417.

(15) Alcock, C. B.; Li, B.; Fergus, J. W.; Wang, L. *Solid State Ionics* **1992**, *53−56*, 39.

(16) Xia, C. Electrolytes. In *Solid Oxide Fuel Cells: Materials Properties and Performance*; Fergus, J. W., Hui, R., Li, X., Wilkinson, D. P., Zhang, J., Eds.; CRC Press: New York, 2008.

(17) Holtappels, P.; Stimming, U. Solid Oxide Fuel Cells (SOFC). In *Handbook of Fuel Cells*; Vielstich, W., Lamm, A., Gasteiger, H. A., Eds.; Wiley: New York, 2010.

(18) Stoukides, M.; Vayenas, C. G. *J. Catal.* **1981**, *70*, 137.

(19) Vayenas, C. G.; Bebelis, S.; Neophytides, S. *J. Phys. Chem.* **1988**, *92*, 5083.

(20) Vayenas, C. G.; Bebelis, S.; Ladas, S. *Nature* **1990**, *343*, 625.

(21) Pritchard, J. *Nature* **1990**, *343*, 592.

(22) Vayenas, C. G.; Jaksic, M. M.; Bebelis, S. I.; Neophytides, S. G. *The Electrochemical Activation of Catalytic Reactions Modern Aspects in Electrochemistry*; Plenum: New York, 1996.

(23) Vayenas, C. G.; Bebelis, S.; Pliangos, C.; Brosda, S.; Tsiplakides, D. *Electrochemical Activation of Catalysis: Promotion, Electrochemical Promotion and Metal-Support Interaction*; Plenum Publishers: New York, 2001.

(24) Wagner, C.; Schottky, W. *Z. Phys. Chem.* **1930**, *B11*, 163.

(25) Rickert, H. *Electrochemistry of Solids: An Introduction*; Springer: Berlin, 1982.

(26) Gellings, P. J.; Bouwmeester, H. J. M. *The CRC Handbook of Solid State Electrochemistry*; CRC Press: Boca Raton, FL, 1997.

(27) Göpel, W. *Sens. Actuators, B* **1994**, *18−19*, 1.

(28) Lundström, I.; Van den Berg, A.; Van der Schoot, B.; Van den Vlekkert, H.; Armgarth, M.; Nylander, C. I. In *Sensors: a Comprehensive Survey*; Göpel, W., Hesse, H., Zemel, J. N., Eds.; VCH Publishers: Weinheim, Germany, 1991; Vol. *2*.

(29) Appleby, A. J.; Foulkes, F. R. *Fuel Cell Handbook*; Van Nostrand Reinhold: New York, 1989.

(30) Kiukkola, K.; Wagner, C. *J. Electrochem. Soc.* **1957**, *104*, 379.

(31) Garagounis, I.; Kyriakou, V.; Anagnostou, C.; Bourganis, V.; Papachristou, I.; Stoukides, M. *Ind. Eng. Chem. Res.* **2011**, *50*, 431.

(32) Pasciak, G.; Prociow, K.; Mielcarek, W.; Gornicka, B.; Mazurek, B. *J. Eur. Ceram. Soc.* **2001**, *21*, 1867.

(33) Etsell, T. H.; Flengas, S. N. *Chem. Rev.* **1970**, *70*, 339.

(34) Chebotin, V. N.; Perfilyev, M. V. *Electrochemistry of Solid Electrolytes*; Khimiya: Moscow, 1978.

(35) Frenkel, J. *Z. Phys.* **1926**, *35*, 652.

(36) Schottky, W. *Z. Phys. Chem.* **1935**, *B29*, 335.

(37) Pieraggi, B. In *Shreir's Corrosion*; Richardson, T. J. A., Ed.; Elsevier: Amsterdam, 2010; Vol. *1*.

(38) Kröger, F. A.; Vink, H. J. In *Solid State Physics: Advances in Research and Applications*; Seitz, F., Turnbull, D., Eds.; Academic Press: New York, 1956; Vol. 3.

(39) Gellings, P. J.; Bouwmeester, H. J. M. *Catal. Today* **1992**, *12*, 1.

(40) Shukla, A. K.; Ramdas, S.; Rao, C. N. R. *J. Phys. Chem. Solids* **1973**, *34*, 761.

(41) Strock, L. W. *Z. Phys. Chem.* **1934**, *25*, 441.

(42) Beevers, C. A.; Ross, M. A. *Z. Kristallogr.* **1937**, *97*, 59.

(43) Le Cars, Y.; Thery, J.; Collongues, R. *C. R. Acad. Sci.* **1972**, *C274*, 4.

(44) Yao, Y. F.; Kummer, J. T. *J. Inorg. Nucl. Chem.* **1967**, *29*, 2453.

(45) Toropov, H. A.; Stukalova, M. M. *Dokl. Acad. Nauk USSR* **1939**, *24*, 458.

(46) *Kirk-Othmer Encyclopedia of Chemical Technology*; John Wiley & Sons, Ltd.: Chichester, 2012.

(47) *Solid State Proton Conductors: Properties and Applications in Fuel Cells*; Knauth, P., Di Vona, M. L., Eds.; John Wiley & Sons, Ltd.: Chichester, 2012.

(48) Lidiard, A. B. *Phys. Rev.* **1954**, *94*, 29.

(49) Dreyfus, R. W.; Nowick, A. S. *J. Appl. Phys. Suppl.* **1962**, *33*, 473.

(50) Haven, Y. *J. Chem. Phys.* **1953**, *21*, 171.

(51) Funke, K. *Prog. Solid State Chem.* **1993**, *22*, 111.

(52) Funke, K.; Rolling, B.; Lange, M. *Solid State Ionics* **1998**, *105*, 195.

(53) Patterson, J. W. *J. Electrochem. Soc.* **1971**, *118*, 1033.

(54) *Perovskite Oxide for Solid Oxide Fuel Cells (Fuel Cells and Hydrogen Energy)*; Ishihara, T., Ed.; Springer: Berlin, 2009.

(55) *Impedance Spectroscopy Theory, Experiment, and Applications*, 2nd ed.; Barsoukov, E., Macdonald, J. R., Eds.; Wiley-Interscience: New York, 2005.

(56) Badwal, S. P. S.; Drennan, J. *J. Mater. Sci.* **1987**, *22*, 3231.

(57) Gibson, I. R.; Dransfield, G. P. *J. Mater. Sci.* **1998**, *33*, 4297.

(58) Yang, Y. L.; Chen, C. L.; Chen, S. Y.; Chu, C. W.; Jacobson, A. J. *J. Electrochem. Soc.* **2000**, *147*, 4001.

(59) Yang, Y.; Jacobson, A. J.; Chen, C. L.; Luo, G. P.; Ross, K. D.; Chu, C. W. *Appl. Phys. Lett.* **2001**, *79*, 776.

(60) Baranova, E. A.; Foti, G.; Jotterand, H.; Comninellis, Ch. *Top. Catal.* **2007**, *44*, 419.

(61) Baranova, E. A.; Kuznetsov, O. O. *Electrochem. Solid-State Lett.* **2011**, *15*, 2012.

(62) Vayenas, C. G. *Solid State Ionics* **1988**, *28–30*, 1521.

(63) Gellings, P. J.; Koopmans, H. J. A.; Burggraaf, A. J. *Appl. Catal.* **1988**, *39*, 1.

(64) Stoukides, M. *Ind. Eng. Chem. Res.* **1988**, *27*, 1745.

(65) Metcalfe, I. *Catal. Today* **1994**, *20*, 283.

(66) Vayenas, C. G.; Bebelis, S. I.; Yentekakis, I. V.; Lintz, H.-G. *Catal. Today* **1992**, *11*, 303.

(67) Iwahara, H.; Shimura, T.; Matsumoto, H. *Electrochemistry* **2000**, *68*, 154.

(68) Stoukides, M. *Catal. Rev.: Sci. Eng.* **2000**, *42*, 1.

(69) Sundmacher, K.; Rihko-Struckmann, L. K.; Galvita, V. *Catal. Today* **2005**, *104*, 185.

(70) Marnellos, G.; Stoukides, M. *Solid State Ionics* **2004**, *175*, 597.

(71) Kokkofitis, C.; Ouzounidou, M.; Skodra, A.; Stoukides, M. *Solid State Ionics* **2007**, *178*, 507.

(72) Athanassiou, C.; Pekridis, G.; Kaklidis, N.; Kalimeri, K.; Vartzoka, S.; Marnellos, G. *Int. J. Hydrogen Energy* **2007**, *32*, 38.

(73) Wagner, C. *Adv. Catal.* **1970**, *21*, 323.

(74) Vayenas, C. G.; Saltsburg, H. M. *J. Catal.* **1979**, *57*, 296.

(75) Vayenas, C. G.; Lee, B.; Michaels, J. N. *J. Catal.* **1980**, *36*, 18.

(76) Goodenough, J. B. *Annu. Rev. Mater. Res.* **2003**, *33*, 91.

(77) Huang, X. J.; Weppner, W. *J. Chem. Soc., Faraday Trans.* **1996**, *92*, 2173.

(78) Scott, H. G. *J. Mater. Sci.* **1975**, *10*, 1527.

(79) Smith, A. W.; Meszaros, F. W.; Kamata, C. D. *J. Am. Ceram. Soc.* **1996**, *9*, 240.

(80) Kitazawa, K.; Coble, R. L. *J. Am. Ceram. Soc.* **1974**, *57*, 360.

(81) Lu, B.; Lin, Y. S. *J. Mater. Sci.* **2011**, *46*, 7056.

(82) Malavasi, L.; Fisher, C. A. J.; Islam, M. S. *Chem. Soc. Rev.* **2010**, *39*, 4370.

(83) Hund, F. *Z. Phys. Chem.* **1952**, *199*, 142.

(84) Inaba, H.; Tagawa, H. *Solid State Ionics* **1996**, *83*, 1.

(85) *Fundamentals of Inorganic Membrane Science and Technology*; Burggraaf, A., Cot, L., Eds.; Elsevier: Amsterdam, 1996.

(86) Sammes, N. M.; Tompsett, G. A.; Nafe, H.; Aldinger, F. *J. Eur. Ceram. Soc.* **1999**, *19*, 1801.

(87) Mogensen, M.; Sammes, N. M.; Tompsett, G. A. *Solid State Ionics* **2000**, *129*, 63.

(88) *Solid State Electrochemistry I Fundamentals, Materials and Their Applications*; Vladislav, V. K., Ed.; Wiley-VCH Verlag GmbH & Co. KGaA: Weinheim, 2009.

(89) Kharton, V. V.; Marques, F. M. B.; Atkinson, A. *Solid State Ionics* **2004**, *174*, 135.

(90) Skinner, S. J.; Kilner, J. A. *Mater. Today* **2003**, *6*, 30.

(91) Hui, S. R.; Roller, J.; Zhang, X.; Deces-Petit, C.; Xie, Y.; Maric, R.; Ghosh, D. In *Solid Oxide Fuel Cells IX*, Mizusaki, J., Singhal, S. C., Eds.; The Electrochemical Society: NJ, 2005.

(92) Yahiro, H.; Eguchi, K.; Arai, H. *Solid State Ionics* **1989**, *36*, 71.

(93) Eguchi, K.; Setoguchi, T.; Inoue, T.; Arai, H. *Solid State Ionics* **1992**, *52*, 165.

(94) Yoshida, H.; Deguchi, H.; Miura, K.; Horiguchi, M.; Inagaki, T. *Solid State Ionics* **2001**, *140*, 191.

(95) Kilner, J. A. In *Solid State Chemistry*; Metselaar, R., Heijingers, H. J. M., Schoonmann, J., Eds.; Elsevier Science: Amsterdam, Netherlands, 1982.

(96) Kim, D. J. *J. Am. Chem. Soc.* **1989**, *72*, 1415.

(97) Kilner, J. A.; Brook, R. J. *Solid State Ionics* **1982**, *6*, 237.

(98) Catlow, C. R. A. *Solid State Ionics* **1984**, *12*, 67.

(99) Atkinson, A.; Kilner, J.; Skinner, S.; Brandon, N. P.; Brett, D. J. L. In *Energy Production and Storage: Inorganic chemical strategis for a warming world*; Crabtree, R. H., Ed.; Wiley and Sons, Chichester, UK, 2010.

(100) Badwal, S. P. S.; Ciacchi, F. T.; Milosevic, D. *Solid State Ionics* **2000**, *136–137*, 91.

(101) Mori, M.; Abe, T.; Itoh, H.; Yamomoto, O.; Takeda, Y.; Kawahara, T. *Solid State Ionics* **1994**, *74*, 157.

(102) Kharton, V. V.; Figueiredo, F. M.; Navarro, L.; Naumovich, E. N.; Kovalevsky, A. V.; Yaremchenko, A. A.; Viskup, A. P.; Carneiro, A.; Marques, F. M. B.; Frade, J. R. *J. Mater. Sci.* **2001**, *36*, 1105.

(103) Stevenson, J. W.; Hasinska, K.; Canfield, N. L.; Armstrong, T. R. *J. Electrochem. Soc.* **2000**, *147*, 3213. Kramer, S. A.; Tuller, H. L. *Solid State Ionics* **1995**, *82*, 15.

(104) Arikawa, H.; Nishiguchi, H.; Ishihara, T.; Takita, Y. *Solid State Ionics* **2000**, *136–137*, 31.

(105) Yaremchenko, A. A.; Avdeev, M.; Kharton, V. V.; Kovalevsky, A. V.; Naumovich, E. N.; Marques, F. M. B. *Mater. Chem. Phys.* **2002**, *77*, 552.

(106) Choudhary, T. V.; Benerjee, S.; Choudhary, V. R. *Appl. Catal., A* **2002**, *234*, 1.

(107) Petrović, S.; Terlecki-Baričević, A.; Karanović, Lj.; Kirilov-Stefanov, P.; Zdujic, M.; Dondur, V.; Paneva, D.; Mitov, I.; Rakić, V. *Appl. Catal., B* **2008**, *79*, 186.

(108) Tacson, J. M. D.; Mendioroz, S.; Tejuca, L. G. *J. Phys. Chem.* **1981**, *124*, 109.

(109) Niu, J.; Deng, J.; Liu, W.; Zhang, L.; Wang, G.; Dai, H.; He, H.; Zi, X. *Catal. Today* **2007**, *126*, 420.

(110) Kharton, V. V.; Patrakeev, M. V.; Waerenborgh, J. C.; Sobyanin, V. A.; Veniaminov, S. A.; Yaremchenko, A. A.; Gaczynski, P.; Belayev, V. D.; Semin, G. L.; Frade, J. R. *Solid State Sci.* **2005**, *7*, 1344.

(111) Levasseur, B.; Kaliaguine, S. *J. Solid State Chem.* **2008**, *181*, 2953.

(112) Taguchi, H.; Matsuura, K.; Takada, M.; Hirota, K. *J. Solid State Chem.* **2012**, *190*, 157.

(113) Villoria, J. A.; Mota, N.; Al-Sayari, S. A.; Alvarez-Galvan, M. C.; Navarro, R. M.; Fierro, J. L. G. *Micro Nanosyst.* **2012**, *4*, 231.

(114) Kucharczyk, B.; Tylus, W. *Appl. Catal., A* **2008**, *335*, 28.

(115) Royer, S.; Alamdari, H.; Duprez, D.; Kaliaguine, S. *Appl. Catal., B* **2005**, *58*, 273.

(116) Jiang, S. P. *J. Mater. Sci.* **2008**, *43*, 6799.

(117) Richter, J.; Holtappels, P.; Graule, T.; Nakamura, T.; Gauckmer, L. J. *Monatsh. Chem.* **2009**, *140*, 985.

(118) Skinner, S. J. *Int. J. Inorg. Mater.* **2001**, *3*, 113.

(119) Sun, C.; Stimming, U. *J. Power Sources* **2007**, *171*, 247.

(120) Mogensen, M.; Lybye, D.; Bonanos, N.; Hendriksen, P. V.; Poulsen, F. W. *Solid State Ionics* **2004**, *174*, 279.

(121) Hashimoto, T.; Ishiwaza, N.; Mizutani, N.; Kato, M. *J. Mater. Sci.* **1988**, *23*, 1102.

(122) Ishihara, T.; Matsuda, H.; Takata, Y. *J. Am. Chem. Soc.* **1994**, *116*, 3801.

(123) Feng, M.; Goodenough, J. B. *Eur. J. Solid State Inorg. Chem.* **1994**, *T31*, 663.

(124) Ishihara, T.; Akbay, T.; Furutani, H.; Takita, Y. *Solid State Ionics* **1998**, *113−115*, 585.

(125) Ishihara, T.; Matsuda, H.; Azmi, M.; Bustam, B.; Takita, Y. *Solid State Ionics* **1996**, *86−88*, 197.

(126) Sinha, A.; Nafe, H.; Sharma, B. P.; Gopalan, P. *J. Electrochem. Soc.* **2008**, *155*, B309.

(127) Lacorre, P.; Goutenoire, F.; Bohnke, O.; Retoux, R.; Laligant, Y. *Nature* **2000**, *404*, 856.

(128) Tealdi, C.; Malavasi, L.; Ritter, C.; Flor, G.; Costa, G. *J. Solid State Chem.* **2008**, *181*, 603.

(129) Kendrick, E.; Islam, M. S.; Slater, P. R. *J. Mater. Chem.* **2007**, *17*, 3104.

(130) Boysen, H.; Kaiser-Bischoff, I.; Lerch, M. *Diffus. Fundam.* **2008**, *8*, 2−1.

(131) Lacerda, M.; Irvine, J. T. S.; Glasser, F. P.; West, A. R. *Nature* **1988**, *332*, 525.

(132) Abraham, F.; Debreville-Gresse, M. F.; Mairesse, G.; Novogrocki, G. *Solid State Ionics* **1988**, *116*, 28.

(133) Boivin, J. C.; Mairesse, G. *Chem. Mater.* **1998**, *10*, 2870.

(134) Steil, M. C.; Fouletier, J.; Kleitz, M.; Labrune, P. *J. Eur. Ceram. Soc.* **1999**, *19*, 815.

(135) Vannier, R. N.; Mairesse, G.; Abraham, F.; Nowogrocki, G. *Solid State Ionics* **1994**, *70−71*, 248.

(136) Weber, N.; Kummer, J. T. *Proc. Ann. Power Sources Conf.* **1967**, *21*, 37.

(137) Yamaguchi, G.; Suzuki, K. *Bull. Chem. Soc. Jpn.* **1968**, *41*, 93.

(138) Lu, X.; Xia, G.; Lemmon, J. P.; Yang, Z. *J. Power Sources* **2010**, *195*, 2431.

(139) Hong, H. Y.-P. *Mater. Res. Bull.* **1976**, *11*, 173.

(140) Anantharamulu, N.; Koteswara-Rao, K.; Rambabu, G.; Vijaya-Kumar, B.; Radha, V.; Vithal, M. *J. Mater. Sci.* **2011**, *46*, 2821.

(141) Clearfield, A.; Subramanian, M. A.; Wang, W.; Jerus, P. *Solid State Ionics* **1983**, *9−10*, 895.

(142) Bruce, P. G.; West, A. R. *J. Electrochem. Soc.* **1983**, *130*, 662.

(143) Rabenau, R. *Solid State Ionics* **1981**, *6*, 267.

(144) Bell, M. F.; Breitschwerdt, A.; von Alpen, O. *Mater. Res. Bull.* **1981**, *16*, 267.

(145) Iwahara, H.; Uchida, H.; Ono, K.; Ogaki, K. *J. Electrochem. Soc.* **1988**, *135*, 529.

(146) Yajima, T.; Kazeoka, H.; Yogo, T.; Iwahara, H. *Solid State Ionics* **1991**, *47*, 271.

(147) Yajima, T.; Suzuki, H.; Yogo, T.; Iwahara, H. *Solid State Ionics* **1992**, *51*, 101.

(148) Iwahara, H. *Solid State Ionics* **1992**, *52*, 99.

(149) Iwahara, H.; Yajima, T.; Hibino, T.; Ozaki, K.; Suzuki, H. *Solid State Ionics* **1993**, *61*, 65.

(150) Islam, M. S. *J. Mater. Chem.* **2000**, *10*, 1027.

(151) Islam, M. S.; Slater, P. R. *MRS Bull.* **2009**, *34*, 935.

(152) Shin, S.; Huang, H. H.; Ishigame, M.; Iwahara, H. *Solid State Ionics* **1990**, *40*, 910.

(153) Tao, S.; Irvine, J. T. S. *J. Solid State Chem.* **2007**, *180*, 3493.

(154) Bohn, H. G.; Schober, T.; Mono, T.; Schilling, W. *Solid State Ionics* **1999**, *117*, 219.

(155) Goodenough, J. B.; Ruiz-Diaz, J. E.; Zhen, Y. S. *Solid State Ionics* **1990**, *44*, 21.

(156) Zhang, G. B.; Smyth, D. M. *Solid State Ionics* **1995**, *82*, 153.

(157) Norby, T. *Solid State Ionics* **1999**, *125*, 1.

(158) Norby, T.; Christiansen, N. *Solid State Ionics* **1995**, *77*, 240.

(159) Farrington, G. C.; Briant, J. L. *Science* **1979**, *204*, 1371.

(160) Ikawa, H.; Tsurumi, T.; Urabe, K.; Udagawa, S. *Solid State Ionics* **1986**, *20*, 1.

(161) *High Temperature Solid Oxide Fuel Cells: Fundamentals, Design and Applications*; Singhal, S. C.; Kendall, K., Eds. Elsevier: Oxford, 2002.

(162) Tuller, H. L.; Nowick, A. S. *J. Electrochem. Soc.* **1975**, *122*, 255.

(163) Kilner, J. A. *Chem. Lett.* **2008**, *37*, 1012.

(164) Wang, S.; Inaba, H.; Tagawa, H.; Dokiya, M.; Hashimoto, T. *Solid State Ionics* **1998**, *107*, 73.

(165) Trovarelli, A.; de Leitenburg, C.; Boaro, M.; Dolcetti, G. *Catal. Today* **1999**, *50*, 353.

(166) Campbell, C. T.; Peden, C. H. F. *Science* **2005**, *309*, 713.

(167) Aneggi, E.; Boaro, M.; de Leitenburg, C.; Dolcetti, G.; Trovarelli, A. *J. Alloys Compd.* **2006**, *408*, 1096.

(168) Yan, Z. P.; Chong, M. B.; Cheng, D. G.; Chen, F. Q.; Zhan, X. L. *Prog. Chem.* **2008**, *20*, 1037.

(169) Gorte, R. J. *AIChE J.* **2010**, *56*, 1126.

(170) Minh, N. Q.; Takahashi, T. *Science and Technology of Ceramic Fuel Cells*; Elsevier: Amsterdam, 1995.

(171) Yamamoto, O. *Electrochim. Acta* **2000**, *45*, 2423.

(172) Tsipis, E.; Kharton, V. V. *J. Solid State Electrochem.* **2008**, *12*, 1367.

(173) Kharton, V. V.; Yaremchenko, A. A.; Naumovich, E. N. *J. Solid State Electrochem.* **1999**, *3*, 303.

(174) Zinkevich, M.; Aldinger, F. *J. Alloys Compd.* **2004**, *375*, 147.

(175) Kofstad, P. *Non-stoichiometry, Diffusion and Electrical Conductivity of Binary Metal Oxides*; Wiley: New York, 1972.

(176) Matzke, H. J. *Non-stoichiometric Oxides*; Academic Press: New York, 1981.

(177) Barteau, M. A. *Chem. Rev.* **1996**, *96*, 1413.

(178) Li, M.; Chen, Y. *Sens. Actuators, B* **1992**, *15*, 48.

(179) Sharma, R. K.; Bhatnager, M. C.; Sharma, G. I. *Sens. Actuators, B* **1988**, *46*, 194.

(180) Akbar, S.; Yoankman, L. B. *J. Electrochem. Soc.* **1997**, *144*, 1750.

(181) Birkefeld, L. C.; Azad, A. M.; Akbar, S. *J. Am. Ceram. Soc.* **1992**, *75*, 2694.

(182) Jochen, W. Titanium Dioxide. *European Coatings Literature*; Vincentz Network: Hannover, 2003.

(183) Tauster, S. J.; Fung, S. C.; Garten, R. L. *J. Am. Chem. Soc.* **1978**, *100*, 170.

(184) Haller, G. L.; Resasco, D. E. *Adv. Catal.* **1989**, *36*, 173.

(185) Fouletier, J.; Mantel, E.; Kleitz, M. *Solid State Ionics* **1982**, *6*, 1.

(186) Asano, M.; Kuwano, J.; Kato, M. *J. Ceram. Soc. Jpn.* **1989**, *97*, 1253.

(187) Yamazoe, N.; Hisamoto, J.; Miura, N.; Kuwata, S. *Sens. Actuators* **1987**, *12*, 415.

(188) Owens, B. B. *Adv. Electrochem. Electrochem. Eng.* **1991**, *8*, 1.

(189) Liang, C. C. In *Fast Ion Transport in Solids*; van Gool, W., Ed.; North-Holland: Amsterdam, 1973.

(190) Julien, C. *Mater. Sci. Eng., B* **1990**, *6*, 9.

(191) Julien, C.; Nazri, G. A. *Solid State Batteries: Materials Design and Optimization*; Kluwer: Boston, MA, 1994.

(192) Pancharatnam, S.; Huggins, S. R. A.; Maso, D. M. *J. Electrochem. Soc.* **1975**, *122*, 869.

(193) Gür, T. M.; Huggins, R. A. *J. Electrochem. Soc.* **1979**, *126*, 1067.

(194) Wagner, C. Adsorbed Atomic Species as Intermediates in Heterogeneous Catalysis. In *Advances in Catalysis*; Eley, D.D., Paul, H. P., Eds.; Academic Press: New York, 1970; Vol. *21*.

(195) Baltruschat, H.; Anastasijevic, N. A.; Beltowska-Brzezinska, M.; Hambitzer, G.; Heitbaum, J. *Ber. Bunsen-Ges.* **1990**, *94*, 996.

(196) Politova, T. I.; Sobyanin, V. A.; Belyaev, V. D. *React. Kinet. Catal. Lett.* **1990**, *41*, 321.

(197) Anastasijevic, N. A.; Baltruschat, H.; Heitbaum, J. *Electrochim. Acta* **1993**, *38*, 1067.

(198) Bebelis, S.; Vayenas, C. G. *J. Catal.* **1989**, *118*, 125.

(199) Lambert, R. In *Catalysis and Electrocatalysis at Nanoparticles*; Wieckowski, A., Savinova, E. R., Vayenas, C. G., Eds.; Marcel Dekker, Inc.: New York, 2003.

(200) Nicole, J.; Comninellis, C. *J. Appl. Electrochem.* **1998**, *28*, 223.

(201) Makri, M.; Buekenhoudt, A.; Luyten, J.; Vayenas, C. G. *Ionics* **1996**, *2*, 282.

(202) Theleritis, D.; Souentie, S.; Siokou, A.; Katsaounis, A.; Vayenas, C. G. *ACS Catal.* **2012**, *2*, 770.

(203) Kokkofitis, C.; Karagiannakis, G.; Zisekas, S.; Stoukides, M. *J. Catal.* **2005**, *234*, 476.

(204) Kotsionopoulos, N.; Bebelis, S. *J. Appl. Electrochem.* **2005**, *35*, 1253.

(205) Ploense, L.; Salazar, M.; Gurau, B.; Smotkin, E. S. *J. Am. Ceram. Soc.* **1997**, *119*, 11550.

(206) Katsaounis, A. *J. Appl. Electrochem.* **2010**, *40*, 885.

(207) Tsiplakides, D.; Balomenou, S. *Chem. Ind. Chem. Eng. Q.* **2008**, *14*, 97.

(208) Vayenas, C. G.; Koutsodontis, C. G. *J. Chem. Phys.* **2008**, *128*, 182506.

(209) Lizarraga, L.; Guth, M.; Billard, A.; Vernoux, P. *Catal. Today* **2010**, *157*, 61.

(210) Lizarraga, L.; Souentie, S.; Mazri, L.; Billard, A.; Vernoux, P. *Electrochem. Commun.* **2010**, *12*, 1310.

(211) de Lucas-Consuegra, A.; Caravaca, A.; González-Cobos, J.; Valverde, J. L.; Dorado, F. *Catal. Commun.* **2011**, *15*, 6.

(212) Souentie, S.; Lizarraga, L.; Kambolis, A.; Alves-Fortunato, M.; Valverde, J. L.; Vernoux, P. *J. Catal.* **2011**, *283*, 124.

(213) Palermo, A.; Lambert, R. M.; Harkness, I. R.; Yentekakis, I. V.; Marina, O.; Vayenas, C. G. *J. Catal.* **1996**, *161*, 471.

(214) de Lucas-Consuegra, A.; Dorado, F.; Jiménez-Borja, C.; Caravaca, A.; Vernoux, P.; Valverde, J. L. *Catal. Today* **2009**, *146*, 293.

(215) de Lucas-Consuegra, A.; Dorado, F.; Jiménez-Borja, C.; Valverde, J. L. *Appl. Catal., B* **2008**, *78*, 222.

(216) Lamy-Pitara, E.; El Mouahid, S.; Barbier, J. *Electrochim. Acta* **2000**, *45*, 4299.

(217) Neophytides, S. G.; Tsiplakides, D.; Stonehart, P.; Jaksic, M. M.; Vayenas, C. G. *Nature* **1994**, *370*, 45.

(218) Petrushina, I. M.; Bandur, V. A.; Cappeln, F.; Bjerrum, N. J. *J. Electrochem. Soc.* **2000**, *147*, 3010.

(219) Pliangos, C.; Yentekakis, I. V.; Ladas, S.; Vayenas, C. G. *J. Catal.* **1996**, *159*, 189.

(220) Petrolekas, P. D.; Balomenou, S.; Vayenas, C. G. *J. Electrochem. Soc.* **1998**, *145*, 1202.

(221) Vayenas, C. G.; Ladas, S.; Bebelis, S.; Yentekakis, I. V.; Neophytides, S.; Yi, J.; Karavasilis, Ch.; Pliangos, C. *Electrochim. Acta* **1994**, *39*, 1849.

(222) Kaloyannis, A.; Vayenas, C. G. *J. Catal.* **1997**, *171*, 148.

(223) Tsampas, M. N.; Sapountzi, F. M.; Vayenas, C. G. *Catal. Today* **2009**, *146*, 351.

(224) Kotsionopoulos, N.; Bebelis, S. *Top. Catal.* **2007**, *44*, 379.

(225) Tsiplakides, D.; Vayenas, C. G. *J. Electrochem. Soc.* **2001**, *148*, E189.

(226) Zipprich, W.; Wiemhofer, H. D.; Vohrer, U.; Gopel, W. *Ber. Bunsen-Ges.* **1995**, *99*, 1406.

(227) Rath, D. L.; Kolb, D. M. *Surf. Sci.* **1981**, *109*, 641.

(228) Riess, I.; Vayenas, C. G. *Solid State Ionics* **2003**, *159*, 313.

(229) Tsampas, M. N.; Sapountzi, F. M.; Boreave, A.; Vernoux, P. *Electrochem. Commun.* **2013**, *26*, 13.

(230) Neophytides, S. G.; Vayenas, C. G. *J. Phys. Chem.* **1995**, *99*, 17063.

(231) Neophytides, S. G.; Tsiplakides, D.; Vayenas, C. G. *J. Catal.* **1998**, *178*, 414.

(232) Tsiplakides, D.; Vayenas, C. G. *J. Catal.* **1999**, *185*, 237.

(233) Katsaounis, A.; Nikopoulou, Z.; Verykios, X. E.; Vayenas, C. G. *J. Catal.* **2004**, *222*, 192.

(234) Katsaounis, A.; Nikopoulou, Z.; Verykios, X. E.; Vayenas, C. G. *J. Catal.* **2004**, *226*, 197.

(235) Li, X.; Gaillard, F.; Vernoux, P. *Top. Catal.* **2007**, *44*, 391.

(236) Ladas, S.; Kennou, S.; Bebelis, S.; Vayenas, C. G. *J. Phys. Chem.* **1993**, *97*, 8845.

(237) Arakawa, T.; Saito, A.; Shiokawa, J. *Appl. Surf. Sci.* **1983**, *16*, 365.

(238) Luerßen, B.; Günther, S.; Marbach, H.; Kiskinova, M.; Janek, J.; Imbihl, R. *Chem. Phys. Lett.* **2000**, *316*, 331.

(239) Makri, M.; Vayenas, C. G.; Bebelis, S.; Besocke, K. H.; Cavalca, C. *Surf. Sci.* **1996**, *369*, 351.

(240) Harkness, I. R.; Lambert, R. M. *J. Catal.* **1995**, *152*, 211.

(241) Vayenas, C. G.; Archonta, D.; Tsiplakides, D. *J. Electroanal. Chem.* **2003**, *554–555*, 301.

(242) Asakura, K.; Lauterbach, J.; Rotermund, H. H.; Ertl, G. *Surf. Sci.* **1997**, *374*, 125.

(243) Kelling, S.; Cerasari, S.; Rotermund, H. H.; Ertl, G.; King, D. A. *Chem. Phys. Lett.* **1998**, *293*, 325.

(244) Von Oertzen, A.; Mikhailov, A.; Rotermund, H. H.; Ertl, G. *Surf. Sci.* **1996**, *350*, 259.

(245) Colen, R. E. R.; Kolodziejczyk, M.; Delmon, B.; Block, J. H. *Surf. Sci.* **1998**, *412–413*, 447.

(246) Kolodzejczyk, M.; Colen, R. E. R.; Delmon, B.; Block, J. H. *Appl. Surf. Sci.* **1997**, *121–122*, 480.

(247) Poppe, J.; Schaak, A.; Janek, J.; Imblihl, R. *Ber. Bunsen-Ges.* **1998**, *102*, 1019.

(248) Poppe, J.; Völkening, S.; Schaak, A.; Schütz, E.; Janek, J.; Imbihl, R. *Phys. Chem. Chem. Phys.* **1999**, *1*, 5241.

(249) Imbihl, R.; Janek, J. *Solid State Ionics* **2000**, *136–137*, 699.

(250) Luerßen, B.; Janek, J.; Imbihl, R. *Solid State Ionics* **2001**, *141–142*, 701.

(251) Luerßen, B.; Mutoro, E.; Fischer, H.; Günther, S.; Imbihl, R.; Janek, J. *Angew. Chem., Int. Ed.* **2006**, *45*, 1473.

(252) Barth, J. V. *Surf. Sci. Rep.* **2000**, *40*, 75.

(253) Janek, J.; Luerßen, B.; Mutoro, E.; Fischer, H.; Günther, S. *Top. Catal.* **2007**, *44*, 399.

(254) Janek, J.; Rohnke, M.; Luerßen, B.; Imbihl, R. *Phys. Chem. Chem. Phys.* **2000**, *2*, 1935.

(255) Mutoro, E.; Hellwig, C.; Luerssen, B.; Guenther, S.; Bessler, W. G.; Janek, J. *Phys. Chem. Chem. Phys.* **2011**, *13*, 12798.

(256) Toghan, A.; Khodari, M.; Steinbach, F.; Imbihl, R. *Thin Solid Films* **2011**, *519*, 8139.

(257) Tsiplakides, D.; Nicole, J.; Vayenas, C. G.; Comninellis, C. *J. Electrochem. Soc.* **1998**, *145*, 905.

(258) Varkaraki, E.; Nicole, J.; Plattner, E.; Comninellis, C.; Vayenas, C. G. *J. Appl. Electrochem.* **1995**, *25*, 978.

(259) Nicole, J.; Tsiplakides, D.; Wodiunig, S.; Comninellis, Ch. *J. Electrochem. Soc.* **1997**, *144*, L312.

(260) Wodiunig, S.; Patsis, V.; Comninellis, Ch. *Solid State Ionics* **2000**, *136*, 813.

(261) Falgairette, C.; Jaccoud, A.; Fóti, G.; Comninellis, C. *J. Appl. Electrochem.* **2008**, *38*, 1075.

(262) Falgairette, C.; Li, Y.; Foti, G.; Comninellis, C.; Harbich, W. *Appl. Catal., B* **2012**, *113–114*, 250.

(263) Nicole, J. Ph.D. Thesis, EPFL, 1999.

(264) Nicole, J.; Tsiplakides, D.; Pliangos, C.; Verykios, X. E.; Comninellis, C.; Vayenas, C. G. *J. Catal.* **2001**, *204*, 23.

(265) Pliangos, C.; Raptis, C.; Badas, T.; Vayenas, C. G. *Solid State Ionics* **2000**, *136–137*, 767.

(266) Pliangos, C.; Raptis, C.; Badas, T.; Vayenas, C. G. *Ionics* **2000**, *6*, 119.

(267) Foti, G.; Lavanchy, O.; Comninellis, Ch. *J. Appl. Electrochem.* **2000**, *30*, 1223.

(268) Pliangos, C.; Yentekakis, I. V.; Verykios, X. E.; Vayenas, C. G. *J. Catal.* **1995**, *154*, 124.

(269) Souentie, S.; Xia, C.; Falgairette, C.; Li, Y. D.; Comninellis, C. *Electrochem. Commun.* **2010**, *12*, 323.

(270) Souentie, S.; Lizarraga, L.; Papaioannou, E.; Vayenas, C. G.; Vernoux, P. *Electrochem. Commun.* **2010**, *12*, 1133.

(271) Poulidi, D.; Rivas, M. E.; Metcalfe, I. S. *J. Catal.* **2011**, *281*, 188.

(272) Mutoro, E.; Koutsodontis, C.; Luerßen, B.; Brosda, S.; Vayenas, C. G.; Janek, J. *Appl. Catal., B* **2010**, *100*, 328.

(273) Vayenas, C. G.; Brosda, S.; Pliangos, C. *J. Catal.* **2001**, *203*, 329.

(274) Brosda, S.; Vayenas, C. G.; Wei, J. *Appl. Catal., B* **2006**, *68*, 109.

(275) Balomenou, S.; Tsiplakides, D.; Katsaounis, A.; Thiemann-Handler, S.; Cramer, B.; Foti, G.; Comninellis, C.; Vayenas, C. G. *Appl. Catal., B* **2004**, *52*, 181.

(276) Vernoux, P.; Gaillard, F.; Karoum, R.; Billard, A. *Appl. Catal., B* **2007**, *73*, 73.

(277) Marwood, M.; Vayenas, C. G. *J. Catal.* **1998**, *178*, 429.

(278) Dorado, F.; de Lucas-Consuegra, A.; Vernoux, P.; Valverde, J. L. *Appl. Catal., B* **2007**, *73*, 42.

(279) de Lucas-Consuegra, A.; Dorado, F.; Valverde, J. L.; Karoum, R.; Vernoux, P. *Catal. Commun.* **2008**, *9*, 17.

(280) Gaillard, F.; Li, N. *Catal. Today* **2009**, *146*, 345.

(281) de Lucas-Consuegra, A.; Princivalle, A.; Caravaca, A.; Dorado, F.; Marouf, A.; Guizard, C.; Valverde, J. L.; Vernoux, P. *Appl. Catal., A* **2009**, *365*, 274.

(282) Lintanf, A.; Djurado, E.; Vernoux, P. *Solid State Ionics* **2008**, *178*, 1998.

(283) Constantinou, I.; Bolzonella, I.; Pliangos, C.; Comninellis, C.; Vayenas, C. G. *Catal. Lett.* **2005**, *100*, 125.

(284) Comninellis, C.; Vercesi, G. P. *J. Appl. Electrochem.* **1991**, *21*, 136.

(285) Marwood, M.; Vayenas, C. G. *J. Catal.* **1997**, *168*, 538.

(286) Balomenou, S.; Pitselis, G.; Polydoros, D.; Giannikos, A.; Vradis, A.; Frenzel, A.; Pliangos, C.; Pütter, H.; Vayenas, C. G. *Solid State Ionics* **2000**, *136−137*, 857.

(287) Pliangos, C.; Raptis, C.; Bolzonella, I.; Comninellis, C.; Vayenas, C. *Ionics* **2002**, *8*, 372.

(288) Xia, C.; Hugentobler, M.; Li, Y.; Foti, G.; Comninellis, C.; Harbich, W. *Electrochem. Commun.* **2010**, *13*, 99.

(289) Xia, C.; Hugentobler, M.; Li, Y.; Comninellis, C.; Harbich, W. *Electrochem. Commun.* **2010**, *12*, 1551.

(290) Wodiunig, S.; Bokeloh, F.; Nicole, J.; Comninellis, Ch. *Electrochem. Solid-State Lett.* **1999**, *2*, 281.

(291) Wodiunig, S.; Bokeloh, F.; Comninellis, Ch. *Electrochim. Acta* **2000**, *46*, 357.

(292) Roche, V.; Revel, R.; Vernoux, P. *Catal. Commun.* **2010**, *11*, 1076.

(293) Kambolis, A.; Lizarraga, L.; Tsampas, M. N.; Burel, L.; Rieu, M.; Viricelle, J. P.; Vernoux, P. *Electrochem. Commun.* **2012**, *19*, 5.

(294) Poulidi, D.; Mather, G. C.; Metcalfe, I. S. *Solid State Ionics* **2007**, *178*, 675.

(295) Poulidi, D.; Thursfield, A.; Metcalfe, I. S. *Top. Catal.* **2007**, *44*, 435.

(296) Poulidi, D.; Metcalfe, I. *J. Appl. Electrochem.* **2008**, *38*, 1121.

(297) Jimenez-Borja, C.; Dorado, F.; de Lucas-Consuegra, A.; Garcia-Vargas, J. M.; Valverde, J. L. *Catal. Today* **2009**, *146*, 326.

(298) Jimenez-Borja, C.; Dorado, F.; de Lucas-Consuegra, A.; Garcia-Vargas, J. M.; Valverde, J. L. *Fuel Cells* **2011**, *11*, 131.

(299) Jimenez-Borja, C.; Brosda, S.; Matei, F.; Makri, M.; Delgado, B.; Sapountzi, F.; Ciuparu, D.; Dorado, F.; Valverde, J. L.; Vayenas, C. G. *Appl. Catal., B* **2012**, *128*, 48.

(300) Jimenez-Borja, C.; Brosda, S.; Makri, M.; Sapountzi, F.; Dorado, F.; Valverde, J. L.; Vayenas, C. G. *Solid State Ionics* **2012**, *225*, 376.

(301) Roche, V.; Karoum, R.; Billard, A.; Revel, R.; Vernoux, P. *J. Appl. Electrochem.* **2008**, *38*, 1111.

(302) Nakos, A.; Souentie, S.; Katsaounis, A. *Appl. Catal., B* **2010**, *101*, 31.

(303) Bebelis, S.; Kotsionopoulos, N. *Solid State Ionics* **2006**, *177*, 2205.

(304) Kokkofitis, C.; Karagiannakis, G.; Stoukides, M. *Top. Catal.* **2007**, *44*, 361.

(305) Li, N.; Gaillard, F. *Appl. Catal., B* **2009**, *88*, 152.

(306) Li, N.; Gaillard, F.; Boreave, A. *Catal. Commun.* **2008**, *9*, 1439.

(307) Bebelis, S.; Karasali, H.; Vayenas, C. G. *J. Appl. Electrochem.* **2008**, *38*, 1127.

(308) Bebelis, S.; Karasali, H.; Vayenas, C. G. *Solid State Ionics* **2008**, *179*, 1391.

(309) Jimenez, V.; Jimenez-Borja, C.; Sanchez, P.; Romero, A.; Papaioannou, E. I.; Theleritis, D.; Souentie, S.; Brosda, S.; Valverde, J. L. *Appl. Catal., B* **2011**, *107*, 210.

(310) Caravaca, A.; de Lucas-Consuegra, A.; Molina-Mora, C.; Valverde, J. L.; Dorado, F. *Appl. Catal., B* **2011**, *106*, 54.

(311) Lintanf, A. Ph.D. Thesis, UJF, 2008.

(312) Constantinou, I.; Archonta, D.; Brosda, S.; Lepage, M.; Sakamoto, Y.; Vayenas, C. G. *J. Catal.* **2007**, *251*, 400.

(313) Campbell, I. M. *Catalysis at Surfaces*; Chapman and Hall: New York, 1988.

(314) Vayenas, C. G.; Bebelis, S.; Despotopoulou, S. *J. Catal.* **1991**, *128*, 415.

(315) de Lucas-Consuegra, A.; Caravaca, A.; Dorado, F.; Valverde, J. L. *Catal. Today* **2009**, *146*, 330.

(316) de Lucas-Consuegra, A.; Caravaca, A.; Martínez, P. J.; Endrino, J. L.; Dorado, F.; Valverde, J. L. *J. Catal.* **2010**, *274*, 251.

(317) de Lucas-Consuegra, A.; Caravaca, A.; Sanchez, P.; Dorado, F.; Valverde, J. L. *J. Catal.* **2008**, *259*, 54.

(318) Vernoux, P.; Gaillard, F.; Lopez, C.; Siebert, E. *J. Catal.* **2003**, *217*, 203.

(319) Pekridis, G.; Kaklidis, N.; Konsolakis, M.; Athanasiou, C.; Yentekakis, I. V.; Marnellos, G. E. *Solid State Ionics* **2011**, *192*, 653.

(320) Petrolekas, P. D.; Brosda, S.; Vayenas, C. G. *J. Electrochem. Soc.* **1998**, *145*, 1469.

(321) Vernoux, P.; Gaillard, F.; Lopez, C.; Siebert, E. *Solid State Ionics* **2004**, *175*, 609.

(322) Vayenas, C. G.; Brosda, S. *Solid State Ionics* **2002**, *8*, 243.

(323) de Lucas-Consuegra, A.; Dorado, F.; Valverde, J. L.; Karoum, R.; Vernoux, P. *J. Catal.* **2007**, *251*, 474.

(324) de Lucas-Consuegra, A.; González-Cobos, J.; García-Rodríguez, Y.; Mosquera, A.; Endrino, J. L.; Valverde, J. L. *J. Catal.* **2012**, *293*, 149.

(325) de Lucas-Consuegra, A.; Princivalle, A.; Caravaca, A.; Dorado, F.; Guizard, C.; Valverde, J. L.; Vernoux, P. *Appl. Catal., B* **2010**, *94*, 281.

(326) Karavasilis, C.; Bebelis, S.; Vayenas, C. G. *Ionics* **1995**, *1*, 85.

(327) Palermo, A.; Husain, A.; Tikhov, M. S.; Lambert, R. M. *J. Catal.* **2002**, *207*, 331.

(328) Pitselis, G. E.; Petrolekas, P. D.; Vayenas, C. G. *Ionics* **1997**, *3*, 110.

(329) Tracey, S.; Palermo, A.; Vazquez, J. P. H.; Lambert, R. M. *J. Catal.* **1998**, *179*, 231.

(330) Williams, F. J.; Palermo, A.; Tracey, S.; Tikhov, M. S.; Lambert, R. M. *J. Phys. Chem. B* **2002**, *106*, 5668.

(331) Urquhart, A. J.; Keel, J. M.; Williams, F. J.; Lambert, R. M. *J. Phys. Chem. B* **2003**, *107*, 10591.

(332) Williams, F. J.; Lambert, R. M. *Catal. Lett.* **2000**, *70*, 9.

(333) Liu, R. Q.; Xie, Y. H.; Wang, J. D.; Li, Z. J.; Wang, B. H. *Solid State Ionics* **2006**, *177*, 73.

(334) Ouzounidou, M.; Skodra, A.; Kokkofitis, C.; Stoukides, M. *Solid State Ionics* **2007**, *178*, 153.

(335) Kokkofitis, C.; Ouzounidou, M.; Skodra, A.; Stoukides, M. *Solid State Ionics* **2007**, *178*, 475.

(336) Kalimeri, K. K.; Athanasiou, C. I.; Marnellos, G. E. *Solid State Ionics* **2010**, *181*, 223.

(337) Poulidi, D.; Mather, G. C.; Tabacaru, C. N.; Thursfield, A.; Metcalfe, I. S. *Catal. Today* **2009**, *146*, 279.

(338) Poulidi, D.; Metcalfe, I. S. *Solid State Ionics* **2006**, *177*, 2211.

(339) Ploense, L.; Salazar, M.; Gurau, B.; Smotkin, E. S. *Solid State Ionics* **2000**, *136−137*, 713.

(340) Salazar, M.; Smotkin, E. *J. Appl. Electrochem.* **2006**, *36*, 1237.

(341) Petrushina, I. M.; Bandur, V. A.; Bjerrum, N. J.; Cappeln, F.; Qingfeng, L. *J. Electrochem. Soc.* **2002**, *149*, D143.

(342) Petrushina, I. M.; Bandur, V. A.; Cappeln, F.; Bjerrum, N. J.; Sorensen, R. Z.; Refshauge, R.; Qingfeng, L. *J. Electrochem. Soc.* **2003**, *150*, D87.

(343) Petrushina, I. M.; Cleemann, L. N.; Refshauge, R.; Bjerrum, N. J.; Bandur, V. A. *J. Electrochem. Soc.* **2007**, *154*, E84.

(344) Sapountzi, F. M.; Tsampas, M. N.; Vayenas, C. G. *Top. Catal.* **2007**, *44*, 461.

(345) Sapountzi, F. M.; Tsampas, M. N.; Vayenas, C. G. *Catal. Today* **2007**, *127*, 295.

(346) Sapountzi, F. M.; Tsampas, M. N.; Vayenas, C. G. *Catal. Today* **2007**, *146*, 319.

(347) Karoum, R.; Pirovano, C.; Vannier, R. N.; Vernoux, P.; Billard, A. *Catal. Today* **2009**, *146*, 359.

(348) Karoum, R.; Roche, V.; Pirovano, C.; Vannier, R. N.; Billard, A.; Vernoux, P. *J. Appl. Electrochem.* **2010**, *40*, 1867.

(349) Baranova, E.; Foti, G.; Comninellis, C. *Electrochem. Commun.* **2004**, *6*, 389.

(350) Baranova, E.; Foti, G.; Comninellis, C. *Electrochem. Commun.* **2004**, *6*, 170.

(351) Wuthrich, R.; Baranova, E.; Bleuler, H.; Comninellis, C. *Electrochem. Commun.* **2004**, *6*, 1199.

(352) Baranova, E. A.; Thursfield, A.; Brosda, S.; Fóti, G.; Comninellis, C.; Vayenas, C. G. *J. Electrochem. Soc.* **2005**, *152*, E40.

(353) Baranova, E. A.; Thursfield, A.; Brosda, S.; Foti, G.; Comninellis, C.; Vayenas, C. G. *Catal. Lett.* **2005**, *105*, 15.

(354) Papaioannou, E. I.; Souentie, S.; Sapountzi, F. M.; Hammad, A.; Labou, D.; Brosda, S.; Vayenas, C. G. *J. Appl. Electrochem.* **2010**, *40*, 1859.

(355) Roche, V.; Siebert, E.; Steil, M. C.; Deloume, J. P.; Roux, C.; Pagnier, T.; Revel, R.; Vernoux, P. *Ionics* **2008**, *14*, 235.

(356) Roche, V.; Hadjar, A.; Deloume, J. P.; Pagnier, T.; Revel, R.; Roux, C.; Siebert, E.; Vernoux, P. *Catal. Today* **2009**, *146*, 266.

(357) Vernoux, P.; Gaillard, F.; Bultel, L.; Siebert, E.; Primet, M. *J. Catal.* **2002**, *208*, 412.

(358) Dorado, F.; de Lucas Consuegra, A.; Jimenez, C.; Valverde, J. L. *Appl. Catal., A* **2007**, *321*, 86.

(359) Toghan, A.; Rösken, L. M.; Imbihl, R. *ChemPhysChem* **2010**, *11*, 1452.

(360) Vayenas, C. G.; Vernoux, P. *ChemPhysChem* **2011**, *12*, 1761.

(361) Yiokari, C. G.; Pitselis, G. E.; Polydoros, D. G.; Katsaounis, A. D.; Vayenas, C. G. *J. Phys. Chem. A* **2000**, *104*, 10600.

(362) Balomenou, S. P.; Tsiplakides, D.; Katsaounis, A.; Brosda, S.; Hammad, A.; Fóti, G.; Comninellis, C.; Thiemann-Handler, S.; Cramer, B.; Vayenas, C. G. *Solid State Ionics* **2006**, *177*, 2201.

(363) Tsiplakides, D.; Balomenou, S.; Katsaounis, A.; Archonta, D.; Koutsodontis, C.; Vayenas, C. G. *Catal. Today* **2005**, *100*, 133.

(364) Souentie, S.; Hammad, A.; Brosda, S.; Foti, G.; Vayenas, C. G. *J. Appl. Electrochem.* **2008**, *38*, 1159.

(365) Balomenou, S. P.; Tsiplakides, D.; Vayenas, C. G.; Poulston, S.; Houel, V.; Collier, P.; Konstandopoulos, A. G.; Agrafiotis, C. *Top. Catal.* **2007**, *44*, 481.

(366) Hammad, A.; Souentie, S.; Balomenou, S.; Tsiplakides, D.; Figueroa, J. C.; Cavalca, C.; Pereira, C. J.; Vayenas, C. G. *J. Appl. Electrochem.* **2008**, *38*, 1171.

(367) Koutsodontis, C.; Hammad, A.; Lepage, M.; Sakamoto, Y.; Foti, G.; Vayenas, C. G. *Top. Catal.* **2008**, *50*, 192.

(368) Souentie, S.; Hammad, A.; Vayenas, C. G. *Catal. Today* **2009**, *146*, 285.

(369) Papaioannou, E. I.; Souentie, S.; Hammad, A.; Vayenas, C. G. *Catal. Today* **2009**, *146*, 336.

(370) Hammad, A.; Souentie, S.; Papaioannou, E. I.; Balomenou, S.; Tsiplakides, D.; Figueroa, G. C.; Cavalca, C.; Pereira, C. J. *Appl. Catal., B* **2011**, *103*, 336.

(371) Tsiplakides, D.; Balomenou, S. *Catal. Today* **2009**, *146*, 312.

(372) Yoshida, A.; Mori, Y.; Ikeda, T.; Azemoto, K.; Naito, S. *Catal. Today* **2012**, DOI: 10.1016/j.cattod.2012.04.020.

(373) Bradford, M.C. J.; Vannice, M. A. *Catal. Today* **1999**, *50*, 87.

(374) Barton, D. G.; Shtein, M.; Wilson, R. D.; Soled, S. L.; Iglesia, E. *J. Phys. Chem. B* **1999**, *103*, 630.

(375) Meitzner, G.; Iglesia, E. *Catal. Today* **1999**, *53*, 433.

(376) Linsmeier, C.; Taglauer, E. *Appl. Catal., A* **2011**, *391*, 175.

(377) Bidaoui, M.; Especel, C.; Bouchenafa-Saib, N.; Duprez, N.; Mohammedib, O.; Royer, S. *Appl. Catal., A* **2012**, DOI: 10.1016/j.apcata.2012.07.023.

(378) Panagiotopoulou, P.; Kondarides, D. I. *Catal. Today* **2006**, *112*, 49.

(379) Tauster, S. J.; Fung, S. C. *J. Catal.* **1978**, *55*, 29.

(380) Tauster, S. J. *Acc. Chem. Res.* **1987**, *20*, 11.

(381) Meriaudeau, P.; Ellestad, O. H.; Dufaux, M.; Naccache, C. *J. Catal.* **1982**, *75*, 243.

(382) Burch, R. In *Hydrogen Effects in Catalysis*; Paal, Z., Menon, P. G., Eds.; Marcel Dekker: New York, 1988.

(383) Bond, G. C.; Rajaram, R. R.; Birch, R. *J. Phys. Chem.* **1986**, *90*, 4877.

(384) Baker, R. T. K.; Prestridge, E. B.; Garten, R. L. *J. Catal.* **1979**, *56*, 390.

(385) Sanchez, M. G.; Gazquez, J. L. *J. Catal.* **1987**, *1*, 120.

(386) Cavalca, C.; Larsen, G.; Vayenas, C. G.; Haller, G. *J. Phys. Chem.* **1993**, *97*, 6115.

(387) Kuhn, M.; Nappom, T. W. *Energies* **2010**, *3*, 57.

(388) Vernoux, P.; Guth, M.; Li, X. *Electrochem. Solid-State Lett.* **2009**, *12*, E9.

(389) Kiskinova, M. P. *Poisoning and Promotion in Catalysis Based on Surface Science Concepts and Experiments*; Elsevier: Amsterdam, 1992.

(390) Niemantsverdriet, J. W. *Appl. Phys. A: Mater. Sci. Process.* **1995**, *61*, 506.

(391) Thomson, S. J. *J. Chem. Soc., Faraday Trans.* **1987**, *83*, 2001.

(392) Ormerod, R. M.; Lambert, R. M. In *Surface Reactions in Springer Series in Surface Science*; Madix, R. J., Ed.; Springer: Berlin, 1994; Vol. *34*.

(393) Lee, A. F.; Baddeley, C. J.; Hardcre, C.; Ormerod, R. M.; Lambert, R. M.; Schmid, G.; West, H. *J. Phys. Chem.* **1995**, *99*, 6096.

(394) Yentekakis, I. V.; Moggridge, G.; Vayenas, C. G.; Lambert, R. M. *J. Catal.* **1994**, *146*, 292.

(395) Yentekakis, I. V.; Palermo, A.; Filkin, N. C.; Tikhov, M. S.; Lambert, R. M. *J. Phys. Chem. B* **1997**, *101*, 3759.

(396) Yentekakis, I. V.; Palermo, A.; Filkin, N. C.; Tikhov, M. S.; Lambert, R. M. *Stud. Surf. Sci. Catal.* **1998**, *116*, 255.

(397) Yentekakis, I. V.; Konsolakis, M.; Lambert, R. M.; Mcleod, N.; Nalbantian, L. *Appl. Catal., B* **1999**, *22*, 123.

(398) Yentekakis, I. V.; Konsolakis, M.; Lambert, R. M.; Palermo, A.; Tikhov, M. *Solid State Ionics* **2000**, *134-137*, 783.

(399) Yentekakis, I. V.; Lambert, R. M.; Tikhov, M. S.; Konsolakis, M.; Kiousis, V. *J. Catal.* **1998**, *176*, 82.

(400) Gellings, P. J.; Bouwmeester, H. J. M. *Catal. Today* **2000**, *58*, l.

(401) Steghuis, A. G.; Van Ommen, J. G.; Seshan, K.; Lercher, J. A. *Stud. Surf. Sci. Catal.* **1997**, *107*, 403.

(402) Steghuis, A. G.; Van Ommen, J. G.; Lercher, J. A. *Catal. Today* **1998**, *46*, 91.

(403) Zhu, J.; van Ommen, J. G.; Bouwmeester, H. J. M.; Lefferts, L. *J. Catal.* **2005**, *233*, 434.

(404) Zhu, J.; van Ommen, J. G.; Knoester, A.; Lefferts, L. *J. Catal.* **2005**, *230*, 291.

(405) Zhu, J.; Mujeebur Rahuman, M. S. M.; van Ommen, J. G.; Lefferts, L. *Appl. Catal., A* **2004**, *259*, 95.

(406) Mims, C. A. *Catal. Lett.* **2000**, *68*, 203.

(407) Voskresenskaya, E. N.; Roguleva, V. G.; Anshits, A. G. *Catal. Rev.: Sci. Eng.* **1995**, *37*, 101.

(408) Labaki, M.; Siffert, S.; Lamonier, J. F.; Zhilinskaya, E. A.; Aboukais, A. *Appl. Catal., B* **2003**, *43*, 261.

(409) Osada, Y.; Koike, S.; Fukushima, T.; Ogasawara, S.; Shikada, T.; Ikariya, T. *Appl. Catal.* **1990**, *59*, 59.

(410) He, M. Y.; Ekerdt, J. G. *J. Catal.* **1984**, *87*, 238.

(411) Jackson, N. B.; Ekerdt, J. G. *J. Catal.* **1990**, *126*, 31.

(412) Jackson, N. B.; Ekerdt, J. G. *J. Catal.* **1990**, *126*, 46.

(413) Li, Y.; He, D.; Zhu, Q.; Zhang, X.; Xu, B. *J. Catal.* **2004**, *221*, 584.

(414) Huang, T. J.; Kung, Y.-C. *Catal. Lett.* **2003**, *85*, 49.

(415) Hernández, W. Y.; Laguna, O. H.; Centeno, M. A.; Odriozola, J. A. *J. Solid State Chem.* **2011**, *184*, 3014.

(416) Yang, D.; Wang, L.; Sun, Y.; Zhou, K. *J. Phys. Chem. C* **2010**, *114*, 8926.

(417) Huang, T. J.; Wang, C. H. *J. Power Sources* **2006**, *163*, 309.

(418) Rothenberg, G.; de Graaf, E. A. B.; Bliek, A. *Angew. Chem., Int. Ed.* **2003**, *42*, 3366.

(419) Fino, D.; Russo, N.; Saracco, G.; Specchia, V. *J. Catal.* **2003**, *217*, 367.

(420) Russo, N.; Fino, D.; Saracco, G.; Specchia, V. *J. Catal.* **2005**, *229*, 459.

(421) Sakadane, M.; Asanuma, T.; Kubo, J.; Ueda, W. *Chem. Mater.* **2005**, *17*, 3546.

(422) Krishna, K.; Bueno-Lopez, A.; Makkee, M.; Moulijn, J. A. *Appl. Catal., B* **2007**, *75*, 189.

(423) Atribak, I.; Bueno-Lopez, A.; Garcia-Garcia, A. *Mol. Catal. A* **2009**, *300*, 103.

(424) Bueno-Lopez, A.; Krishna, K.; Makkee, M.; Moulijn, J. A. *J. Catal.* **2005**, *230*, 237.

(425) Guilhame, N.; Bassou, B.; Bergeret, G.; Bianchi, D.; Bosselet, F.; Desmartin-Chomel, A.; Jouguet, B.; Mirodatos, C. *Appl. Catal., B* **2012**, *119−120*, 287.

(426) Simonsen, S. B.; Dahl, S.; Johnson, E.; Helveg, S. *J. Catal.* **2008**, *255*, 1.

(427) Bassou, B.; Guilhame, N.; Lombaert, K.; Mirodatos, C.; Bianchi, D. *Energy Fuels* **2010**, *24*, 4766.

(428) Bassou, B.; Guilhame, N.; Lombaert, K.; Mirodatos, C.; Bianchi, D. *Energy Fuels* **2010**, *24*, 4781.

(429) Katta, L.; Sudarsanam, P.; Thrimurthulu, G.; Reddy, B. M. *Appl. Catal., B* **2010**, *101*, 101.

(430) Aneggi, E.; de Leitenburg, C.; Trovarelli, A. *Catal. Today* **2012**, *181*, 108.

(431) Chetouani, A.; Taouk, B.; Bordes-Richard, E. *Catal. Today* **2004**, *91−92*, 73.

(432) Huang, T. J.; Li, J. F. *J. Power Sources* **2008**, *181*, 62.

(433) Metcalfe, I. S. *Catal. Today* **1991**, *9*, 145.

(434) Metcalfe, I. S.; Sundaresan, S. *AIChE J.* **1988**, *34*, 195.

(435) Dow, W. P.; Huang, T. J. *J. Catal.* **1994**, *147*, 322.

(436) Dow, W. P.; Huang, T. J. *J. Catal.* **1996**, *160*, 171.

(437) Dow, W. P.; Wang, Y. P.; Huang, T. J. *J. Catal.* **1996**, *160*, 155.

(438) Pu, Z. Y.; Liu, X. S.; Jia, A. P.; Xie, Y. L.; Lu, J. Q.; Luo, M. F. *J. Phys. Chem. C* **2008**, *112*, 15045.

(439) Wang, J. B.; Tsai, D. H.; Huang, T. J. *J. Catal.* **2002**, *208*, 370.

(440) Ayastuy, J. L.; Gurbani, A.; Gonzalez-Marcos, M. P.; Gutierrez-Ortiz, M. A. *Appl. Catal., A* **2010**, *387*, 119.

(441) Maciel, C. G.; de Freitas-Silva, T.; Hirooka, I.; Belgacem, M. N.; Assaf, J. M. *Fuel* **2012**, *97*, 245.

(442) Zhu, H.; Qin, Z.; Shan, W.; Shen, W.; Wang, J. *J. Catal.* **2005**, *233*, 41.

(443) Sanchez-Dominguez, M.; Liotta, L. F.; Carlo, G. D.; Pantaleo, G.; Venezia, A. M.; Solansa, C.; Boutonnet, M. *Catal. Today* **2010**, *158*, 35.

(444) Isaifan, R. J.; Dole, H. A. E.; Obeid, E.; Lizarraga, L.; Vernoux, P.; Baranova, E. *Electrochem. Solid State* **2012**, *15*, E14.

(445) Ferrizz, R. M.; Egami, T.; Vohs, J. M. *Surf. Sci.* **2000**, *465*, 127.

(446) Salazar-Villalpando, M. D.; Miller, A. C. *Chem. Eng. J.* **2011**, *166*, 738.

(447) Salazar-Villalpando, M. D.; Berry, D. A.; Gardner, T. H. *Int. J. Hydrogen Energy* **2008**, *33*, 2695.

(448) Sadykov, V. A.; Sazonova, N. N.; Bobin, A. S.; Muzykantov, V. S.; Gubanova, E. L.; Alikina, G. M.; Lukashevich, A. I.; Rogov, V. A.; Ermakova, E. N.; Sadovskaya, E. M.; Mezentseva, N. V.; Zevak, E. G.; Veniaminov, S. A.; Muhler, M.; Mirodatos, C.; Schuurman, Y.; van Veen, A. C. *Catal. Today* **2011**, *169*, 125.

(449) Ciuparu, D.; Altman, E.; Pfefferle, L. *J. Catal.* **2001**, *203*, 64.

(450) Saqer, S. M.; Kondarides, D. I.; Verykios, X. E. *Top. Catal.* **2009**, *52*, 517.

(451) Ousmane, M.; Liotta, L. F.; Carlo, G. D.; Pantaleo, G.; Venezia, A. M.; Deganello, G.; Retailleau, L.; Boreave, A.; Giroir-Fendler, A. *Appl. Catal., B* **2011**, *101*, 629.

(452) Smith, M. W.; Berry, D. A.; Shekhawat, D.; Haynes, D. J.; Spivey, J. J. *Fuel* **2010**, *89*, 1193.

(453) Sadykov, V. A.; Muzykantov, V. S.; Bobin, A.; Mezentseva, N. V.; Alikina, G. M.; Sazonova, N.; Sadovskaya, E. M.; Gubanova, E. L.; Lukashevich, A. I.; Mirodatos, C. *Catal. Today* **2010**, *157*, 55.

(454) Tsipouriari, V. A.; Efstathiou, A. M.; Zhang, Z. L.; Verykios, X. E. *Catal. Today* **1994**, *21*, 579.

(455) Efstathiou, A. M.; Kladi, A.; Tsipouriari, V. A.; Verykios, X. E. *J. Catal.* **1996**, *158*, 64.

(456) van Keulen, A. N. J.; Seshan, K.; Hoebink, J. H. B. J.; Ross, J. R. H. *J. Catal.* **1997**, *166*, 306.

(457) Tournayan, L.; Auroux, A.; Charcosset, H.; Szymanski, R. *Adsorpt. Sci. Technol.* **1985**, *2*, 55.

(458) Chen, Y. Z.; Liaw, B. J.; Kao, C. F.; Kuo, J. C. *Appl. Catal., A* **2001**, *217*, 23.

(459) O'Connor, A. M.; Schuurman, Y.; Ross, J. R. H.; Mirodatos, C. *Catal. Today* **2006**, *115*, 191.

(460) Huang, T. J.; Lin, H. J.; Yu, T. C. *Catal. Lett.* **2005**, *105*, 239.

(461) Li, C.; Hirabayashi, D.; Suzuki, K. *Appl. Catal., B* **2009**, *88*, 351.

(462) Polychronopoulou, K.; Costa, C. N.; Efstathiou, A. M. *Catal. Today* **2006**, *112*, 89.

(463) Deshpande, P. A.; Madras, G. *AIChE J.* **2010**, *56*, 2662.

(464) Li, Y.; Fu, Q.; Flytzani-Stephanopoulos, M. *Appl. Catal., B* **2000**, *27*, 179.

(465) Rodriguez, J. A.; Liu, P.; Hrbek, J.; Evans, J.; Perez, M. *Angew. Chem., Int. Ed.* **2007**, *46*, 1329.

(466) Linganiso, L. Z.; Jacobs, G.; Azzam, K. G.; Graham, U. M.; Davis, B. H.; Cronauer, D. C.; Kropf, A. J.; Marshall, C. L. *Appl. Catal., A* **2011**, *394*, 105.

(467) Centi, G.; Arena, G. E.; Perathoner, S. *J. Catal.* **2003**, *216*, 443.

(468) Centi, G.; Panzacchi, B.; Perathoner, S.; Pinna, F. *Stud. Surf. Sci. Catal.* **2000**, *130*, 2273.

(469) Cho, B. K. *J. Catal.* **1991**, *131*, 74.

(470) Hickey, N.; Boscarato, I.; Kaspar, J.; Bertinetti, L.; Botavin, M.; Martra, G. *Appl. Catal., B* **2010**, *100*, 102.

(471) Tanabe, T.; Nagai, Y.; Dohmaa, K.; Takagi, N.; Takahashi, N.; Matsumoto, S.; Shinjoh, H. *Appl. Catal., B* **2011**, *105*, 41.